

MODELING TEMPERATURE DEPENDENCE OF THE COMBINED DENSITY OF STATES IN HETEROSTRUCTURES WITH QUANTUM WELLS UNDER THE INFLUENCE OF A QUANTIZING MAGNETIC FIELD

✉Ulugbek I. Erkaboev^a, ✉Sherzodjon A. Ruzaliev^{b*}, ✉Rustamjon G. Rakhimov^a,
✉Nozimjon A. Sayidov^a

^aNamangan Institute of Engineering and Technology, 160115, Namangan, Uzbekistan

^bFergana State University, 150100, Fergana, Uzbekistan

*Corresponding Author e-mail: sherzodjonruzaiev@gmail.com

Received June 28, 2024; revised August 8, 2024; accepted August 15, 2024

In this work, the dependence of the oscillation of the combined density of states on a strong magnetic field in heterostructures based on a rectangular quantum well is studied. The effect of a quantizing magnetic field on the temperature dependence of the combined density of states in nanoscale straight-band heterostructures is investigated. A new mathematical model has been developed for calculating the temperature dependence of the two-dimensional combined density of quantum well states in quantizing magnetic fields. The proposed model explains the experimental results in nanoscale straight-band semiconductors with a parabolic dispersion law.

Keywords: *Semiconductor, Nanoscale semiconductor structures, Quantizing magnetic field, Quantum well, Oscillation, Density of energy states*

PACS: 73.63.Hs, 73.21.Fg, 73.21.-b

INTRODUCTION

As is known, the influence of external factors (temperature, magnetic field and pressure) on quantum-dimensional heterostructures leads to a change in the position of the energy levels of charge carriers and, consequently, to a shift of the magneto-optical absorption edge [1-20]. The magneto-optical absorption spectrum of nanoscale semiconductors is determined by the energy distance between different minima of the sparse zone. Hence, the width of the forbidden zone of the quantum well can either decrease or increase due to external influences. Thus, the study of the magneto-optical absorption spectrum near the boundary of its absorption edge provides information about the structure of the energy spectrum of charge carriers near the lower edge of the conduction band and near the upper edge of the valence band of the quantum well, which is essential for determining the magnetic, optical and electrical properties of nanoscale semiconductors.

The combined densities of quantum well states play an important role in the oscillation of interband magneto-optical absorption. Therefore, in many cases, the matrix element (M) changes little within the Brillouin zone.

Consequently, the structure of the spectrum mainly determines the combined density of states in quantum-dimensional heterostructures. In works [1-3], a method was developed for calculating the oscillation of the combined density of states in a quantizing magnetic field with a non-quadratic law of dispersion under the influence of temperature and hydrostatic pressure. This method is used in the study of magnetic absorption in narrow-band semiconductors with a nonparabolic dispersion law. A fan diagram of the magnetic absorption spectrum in narrow-band semiconductors is constructed. However, these papers do not consider the temperature dependence of the two-dimensional combined density of states in the allowed zone of a quantum well with a parabolic law of dispersion. That is, the resulting method is applicable only for bulk semiconductor materials.

In addition, in works [4,5], the spectrum of InGaN/AlGaIn/GaN heterostructures with quantum wells is emitted by an LED and analyzed on the basis of a two-dimensional combined density of states model. The considered model of approximation of the luminescence spectra of LEDs in these works was developed for complex heterostructures with multiple quantum wells. In work [6], a random walk in a two-dimensional space consisting of an energy parameter of the order and an energy correlation function was performed, and a two-dimensional combined density of quantum well states was obtained. The order parameter, susceptibility and correlation function are calculated from the two-dimensional combined density of quantum well states. Numerical calculations of the author show that for the purposes of determining the two-dimensional combined density of states in continuous models, the Wang-Landau transition matrix method can be considered as an alternative to the pure Wang-Landau method. In work [7], an exact mathematical expression is proposed that directly combines the density functions of the states of the resolved zone of a quantum well to create a two-dimensional combined density of states for direct transitions. Using both expressions, the absorption coefficient of the quantum well and the superlattice was calculated, which led to a positive coincidence with the experimental data. In the above literature, the temperature dependence of the oscillation of the two-dimensional combined density of quantum well states in a quantizing magnetic field are not discussed. Also, the work determines the oscillations of the combined density of quantum well states at constant temperatures in the absence of a magnetic field.

The purpose of this work is to determine the effect of a strong magnetic field on the combined density of states in heterostructures with quantum wells.

MODEL

Calculation of the oscillation of the combined density of states in heterostructures with quantum wells in the presence of a magnetic field

In the absence of a magnetic field, the dependence of the density of the energy states of the conduction band and the valence band in the quantum well on the energy spectrum of charge carriers are step functions (Fig.1a) [21]:

$$g_c(E) = \frac{m_n^e}{\hbar^2 \pi} \sum_n \theta(E - E_n),$$

$$g_v(E) = \frac{m_n^h}{\hbar^2 \pi} \sum_m \theta(E - E_m). \quad (1)$$

Here, m_n^e and m_n^h are the effective masses of electrons and holes in the dimensional quantization subband in a quantum well numbered n and m . $\theta(E)$ - Heaviside step function.

For direct interband transitions, the combined densities of states are a convolution in energy, which also has a step function in energy [21]:

$$N_{jds}^{2d}(E) = \frac{m_{mn}^*}{\hbar^2 \pi} \sum_{m,n} \theta(E - E_{mn}) \quad (2)$$

Here, m_{mn}^* is the reduced effective mass of charge carriers for the subzones of dimensional quantization n and m , which is calculated by the ratio: $(m_{mn}^*)^{-1} = (m_n^e)^{-1} + (m_m^h)^{-1}$.

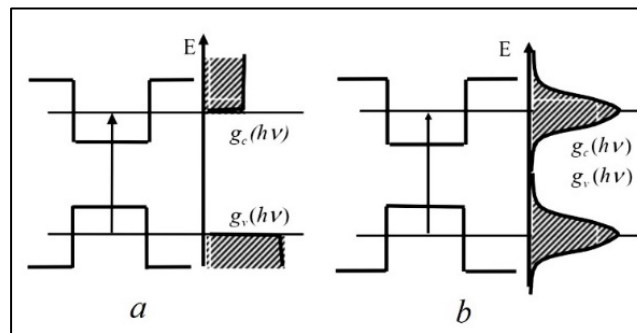


Figure 1. The energy distribution of the density of electronic states in quantum-dimensional GeSi/Si structures [21]: *a* - quantum well, *b* - quantum dot.

If the electronic and hole states in *GeSi* structures turn out to be size-quantized in all three quasi-momentum components, that is, they represent a quantum dot for charge carriers, then in this case the combined density of states in the allowed band of such a structure is a Gaussian function (Fig. 1b). Then, in the allowed zone there is a zero-dimensional combined density of states, which is a discrete non-decreasing function. In this case, the combined density of states is described using the so-called Dirac delta function $\delta(E)$:

$$N_{jds}^{0d}(E) = \sum_{l,m,n} \delta(E - E_{lmn}). \quad (3)$$

The combined density of states is a collection of infinitely narrow and high peaks (Fig.1b). All the results obtained above are valid for cases without the influence of quantization of the magnetic field, temperature and pressure. Specific questions arise: how to determine the combined density of states in quantum-dimensional direct transitions of heterostructures in the presence of a strong magnetic field? How does the dynamics of temperature rise affect this process?

Let's calculate the dependence of the combined density of states on the quantizing magnetic field in two-dimensional semiconductor materials with direct allowed transitions. In a quantizing magnetic field, the combined density of states is defined as an integral over all states in the conduction band with energies E_C and in the valence band with energies E_V of the quantum well, which satisfy the law of conservation of energy during the magneto-optical transition. Let us analyze the simplest model of a band structure near the edge of the band gap of a straight-band heterostructure with a quantum well under the influence of a strong magnetic field. That is, the valence band of the quantum well is completely filled with charge carriers, and the conduction band is empty. Here, the filling functions of the corresponding states are equal to $f_V=1, f_C=0$. In addition, in this model, the dependence of impurity levels on the combined density of quantum well states with the parabolic law of dispersion can be neglected. The magnetic field inductions are directed across (along the Z axis) and will be perpendicular to the XY plane. This is called a transverse quantum magnetic field.

Hence, in the presence of a strong magnetic field, the laws of dispersion energy are used to calculate the combined density of quantum well states, which can be written as follows:

$$\begin{aligned}
 E_c^{2d}(B, d, n_{cZ}) &= \left(N_L^c + \frac{1}{2} \right) \hbar \omega_c^c + \frac{\hbar^2 \pi^2}{2m_c^* d^2} n_{cZ}^2 + m_s^c g_c \mu_B H \\
 E_v^{2d}(B, d, n_{vZ}) &= - \left(N_L^v + \frac{1}{2} \right) \hbar \omega_c^v - \frac{\hbar^2 \pi^2}{2m_v^* d^2} n_{vZ}^2 - m_s^v g_v \mu_B H - E_g^{2d}(0)
 \end{aligned} \tag{4}$$

Here, N_L^c, N_L^v is the number of Landau levels of charge carriers in the allowed zone of the quantum well; ω_c^c, ω_c^v is the cyclotron frequency of the magnetic field in the conduction band and valence band of the quantum well; d is the thickness of the quantum well; n_{cZ}^2, n_{vZ}^2 is the number of the dimensional quantization subzone in the conduction band and in the valence band of the quantum well; n_{cZ}, n_{vZ} is the ordinal number of the quantization levels of electrons and holes along the Z axis, respectively.

Imagine that the electron and valence bands are symmetric, then the condition $n_{cZ} = n_{vZ} = n_Z$ is fulfilled. $m_s^c g_c \mu_B H, m_s^v g_v \mu_B H$ is the spin energy in the allowed zone; $E_g^{2d}(0)$ is the width of the forbidden zone of the quantum well at absolute zero temperature; B is the induction of the magnetic field.

For $E_c^{2d}(B, d, n_Z)$ and $E_v^{2d}(B, d, n_Z)$, without taking into account spin, magneto-optical transitions will correspond to the law of conservation of energy

$$\begin{aligned}
 E_{cv}^{2d}(B, d, n_Z) &= E_c^{2d}(B, d, n_Z) - E_v^{2d}(B, d, n_Z), \\
 E_{cv}^{2d}(B, d, n_Z) &= E_g^{2d}(0) + \left(N_L^c + \frac{1}{2} \right) \hbar \omega_c^c + \left(N_L^v + \frac{1}{2} \right) \hbar \omega_c^v + \frac{\hbar^2 \pi^2}{2m_{cv}^* d^2} n_Z^2, \\
 h\nu &\geq E_{cv}^{2d}(B, d, n_Z).
 \end{aligned} \tag{5}$$

Where, $h\nu$ is the absorbed photon energy, ν is the frequency of light, $\frac{1}{m_{cv}^*} = \frac{1}{m_c^*} + \frac{1}{m_v^*}$ is the combined (reduced) effective mass.

In the Z direction, a strong magnetic field does not change the relationship between the energy and the wave vector for the movement of charge carriers. However, for the movement of charge carriers in the direction of perpendicular magnetic induction (in the XY plane), the former quasi-continuous series of energy levels is replaced by a system of discrete Landau levels. Since the effective mass of electrons and holes is assumed to be constant, the distance between the Landau levels does not depend on the quantum number, which is $\hbar \omega_c$. Hence, in the conduction band and the valence band of the quantum well, the movement of free electrons and holes in all three directions is limited. When exposed to a quantizing magnetic field, a quantum well becomes an analogue of a quantum dot. And also, the energy spectrum of charge carriers will be entirely discrete. According to equation (3), when replacing E with $h\nu$ and E_{lmn} with $E_{cv}^{2d}(B, d, n_Z)$ in the argument $\delta(E - E_{lmn})$, we have:

$$N_{jds}^{2d}(h\nu, E_{cv}^{2d}(B, d, N_L^{cv}, n_Z)) = \frac{eB}{\pi \hbar} \sum_{N_L^c, N_L^v, n_Z} \delta(h\nu - E_{cv}^{2d}(B, d, N_L^{cv}, n_Z)). \tag{6}$$

Thus, under the influence of a quantizing magnetic field, the equation (6) can be used to determine the combined density of quantum well states. However, such equations do not take into account the influence of temperature and pressure on the discrete Landau levels of electrons and holes for straight-band quantum wells.

Effects of the quantizing magnetic field on the temperature dependence of the combined density of states in nanoscale straight-band heterostructures

The magneto-optical assimilation range could be a key prerequisite for many volumetric and low-dimensional optoelectronic devices. The method of magneto-optical retention in straight-band heterostructures with quantum wells and $\alpha_B^{2d}(h\nu, B, d)$ can be communicated as a function of the combined thickness of states. When uncovered to a quantizing attractive field, the combined thickness of states gives a degree of the number of permitted magneto-optical moves between the electronic states of the filled valence band and the vacant electronic states of the conduction band isolated by the photon vitality $h\nu$. In well-known logical writing, a few endeavors have been detailed to relate the densities of the vitality states of the allowed zone with the combined thickness of states within the nonattendance and nearness of a attractive field. [4-7]. Be that as it may, all the experimental and rearranged expressions of the combined thickness of states gotten were restricted by the nonappearance of weight and at moo temperatures.

From equation (6) it is clear that for $h\nu > E_{cv}^{2d}(B, d, N_L^{cv}, n_Z)$, the form of the combined density of states as a function of energies reflects the nature of deltoidness. When exposed to a quantizing magnetic field, the two-dimensional combined density of states $N_{jds}^{2d}(h\nu, E_{cv}^{2d}(B, d, N_L^{cv}, n_Z))$ it is determined by the energy spectrum of charge carriers in the allowed zone of the quantum well. Experiments show that the density of states of electrons and holes depends on temperature. The temperature dependence of the density of states of electrons and holes in a quantum well is explained

by the thermal blurring of discrete Landau levels [22-25]. As shown in works [23,24], the density of electron states in the conduction band of a quantum well at sufficiently high temperatures transforms from discrete Landau levels into a continuous energy spectrum. And at low temperatures, the quantizing magnetic field strongly affects the densities of states in the resolved zone of the quantum well, whereas the continuous energy spectrum decomposes into discrete Landau levels. In this case, as the temperature increases, collisions of charge carriers and thermal motions lubricate the discrete Landau levels, turning it into a continuous spectrum of the density of quantum well states. Hence, the temperature dependence of discrete Landau levels of charge carriers can be described by decomposing the combined density of quantum well states into a series of delta-shaped functions. The temperature dependence of the oscillation of the interband magneto-optical absorption in heterostructures with quantum wells was explained by a study using the delta-shaped functions of two-dimensional combined densities of states. The temperature dependence of the two-dimensional combined density of states is determined by thermal broadening of discrete Landau levels of charge carriers in the allowed zone of the quantum well.

At $T=0$, the Gaussian distribution function is delta-shaped and is defined by the following expression [26]:

$$Gauss(E, T) = \frac{1}{kT} \cdot \exp\left(-\frac{(E - E_i)^2}{(kT)^2}\right). \quad (7)$$

In addition, to describe the interband magneto-optical absorption, it is usually assumed that each energy spectrum of a quantum well is blurred according to the Gaussian law with a blurring parameter. This approach can be described by the temperature dependence of the two-dimensional combined density of states in a quantum well. Hence, the deep filled discrete Landau levels of charge carriers in a quantum well depend exponentially on the two-dimensional combined density of states. To calculate the temperature dependence of the two-dimensional combined density of states $N_{jds}^{2d}(h\nu, E_{cv}^{2d}(B, d, n_z))$ we assume that $N_{jds}^{2d}(h\nu, E_{cv}^{2d}(B, d, N_L^{cv}, n_z))$ for $T=0$ equal to the known energy functions $E_{cv}^{2d}(B, d, N_L^{cv}, n_z)$. For a heterostructure with quantum wells, in a strong magnetic field, the two-dimensional combined density of states is calculated by the equation (6). With increasing temperature, each combined density of states in the allowed zone of the quantum well with the energy of the conduction band and the valence band $E_{cv}^{2d}(B, d, N_L^{cv}, n_z)$ is eroded. Thermal blur $N_{jds}^{2d}(h\nu, E_{cv}^{2d}(B, d, N_L^{cv}, n_z))$ with energy $E_{cv}^{2d}(B, d, N_L^{cv}, n_z)$ is calculated by the Shockley-Reed-Hall statistics [27]. Thus, under the influence of a quantizing magnetic field, in the permitted zone of the quantum well, the resulting two-dimensional combined density of states, taking into account the contribution of thermal blurring of all states, will be determined by the sum of all blurring. Hence, at a finite temperature T , this reduces to the decomposition into a series $N_{jds}^{2d}(h\nu, E_{cv}^{2d}(B, d, N_L^{cv}, n_z))$ by Gaussian functions, for nanoscale semiconductor structures.

The equation (6) does not take into account thermal blurring of the two-dimensional combined density of states. If we decompose $N_{jds}^{2d}(h\nu, E_{cv}^{2d}(B, d, N_L^{cv}, n_z))$ in a row according to equations (7), then it is possible to take into account the temperature dependence of the two-dimensional combined density of states in the allowed zone of the quantum well. In a strong magnetic field, temperature blurring of the combined density of quantum well states lead to smoothing of discrete Landau levels of charge carriers, and thermal blurring is calculated using the equation (7). At $T=0$, the equation (7) turns into a delta-like function of the form:

$$Gauss(E, E_i, T) \xrightarrow{T \rightarrow 0} \delta(E - E_i). \quad (8)$$

Thus, it follows from equations (5), (6) and (7) that under the influence of a quantizing magnetic field, the temperature dependence of the combined density of quantum well states is reduced to the following analytical expression:

$$N_{jds}^{2d}(h\nu, E_{cv}^{2d}(B, T, d, N_L^{cv}, n_z)) = \frac{eB}{\pi\hbar} \frac{1}{kT} \sum_{N_L^c, N_L^v, n_z} \exp\left[-\frac{\left(h\nu - \left(E_g^{2d}(0) + \left(N_L^c + \frac{1}{2}\right)\hbar\omega_c^e + \left(N_L^v + \frac{1}{2}\right)\hbar\omega_c^v + \frac{\hbar^2\pi^2}{2m_{cv}^*d^2}n_z^2\right)\right)^2}{(kT)^2}\right] \quad (9)$$

Where, $N_{jds}^{2d}(h\nu, E_{cv}^{2d}(B, T, d, N_L^{cv}, n_z))$ - temperature dependence of the oscillation of the combined density of states in the allowed zone of the quantum well in the presence of a strong magnetic field. B is the induction of a transverse quantizing magnetic field.

This new analytical equation expresses the effect of the quantizing magnetic field on the temperature dependence of the two-dimensional combined density of states in heterostructures with quantum wells. The obtained expression is convenient for processing experimental data on the oscillation of interband magneto-optical absorption in quantum wells at various magnetic fields and temperatures. Thus, a mathematical model describing the effects of external factors (temperature and magnetic field) on the two-dimensional combined density of states in nanoscale semiconductor structures has been obtained.

RESULTS AND DISCUSSION

The results obtained on the new reduced model and its discussion.

Now, for specific straight-band heterostructures based on quantum wells, we consider the temperature dependence of the two-dimensional combined density of states in a quantizing magnetic field. In work [28], a high-quality heterostructure with a GaAs/AlGaAs quantum well with a width of 14 nm with a small concentration of aluminum (3%) in the barrier layers was investigated. Heterostructures with a GaAs/AlGaAs quantum well were studied at a temperature of 4 K. In the absence of a magnetic field, the band gap of the GaAs quantum well is equal to 1.464 eV (Fig. 2). Fig. 2 shows the dependence of the two-dimensional combined density of states on the absorbing photon energy for a GaAs quantum well $d=14$ nm ($n_z=1$) at a temperature $T=4$ K and a quantizing magnetic field $B = 9$ T. This graph was created by numerical calculation based on equation (9). In Fig.2, the number of discrete Landau levels of charge carriers is fourteen. These peaks (discrete Landau levels of charge carriers ($N_L^{cv}=14$)) are observed in the allowed band of the GaAs quantum well. It shows the two-dimensional combined density of states in a quantizing magnetic field $\hbar\omega_c = 0,02$ eV at $T = 4$ K, $kT = 4 \cdot 10^{-4}$, $\frac{\hbar\omega_c}{kT} = 50$, $kT \ll \hbar\omega_c$. In this case, the thermal smearing of the Landau levels of charge carriers is very weak and the two-dimensional combined density of states does not feel any deviation from the ideal shape. In this plot, the valence band and conduction band are chosen as symmetrical energy spectra. Then, from the first discrete Landau level of holes ($N_{L(v)}=0$) to $N_{L(v)}=6$, they are located higher from the beginning of the ceiling of the valence band of the quantum well. As well as other discrete Landau levels of electrons are located above the bottom of the conduction band of the quantum well.

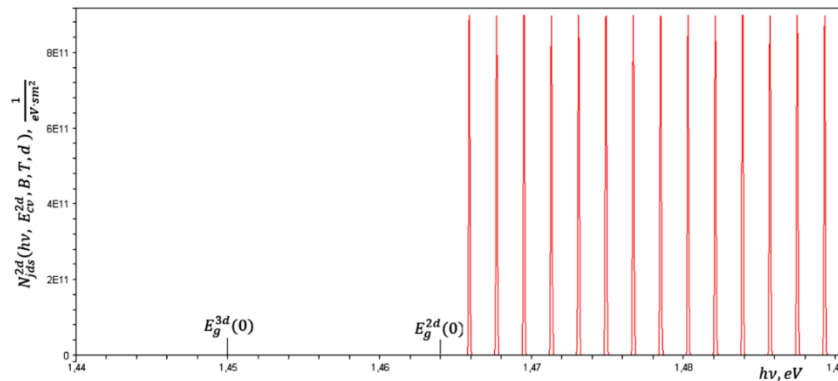


Figure 2. Dependence of the two-dimensional combined density of states on the absorbing photon energy in direct-gap heterostructures with GaAs/AlGaAs quantum wells ($d = 14$ nm) at a temperature $T = 4$ K and a quantizing magnetic field $B = 9$ T.

Fig. 3 appears the impact of temperature on the reliance of the two-dimensional combined thickness of states on the retaining photon vitality in direct-gap heterostructures with GaAs/AlGaAs quantum wells ($d=14$ nm) beneath the activity of a quantizing attractive field.

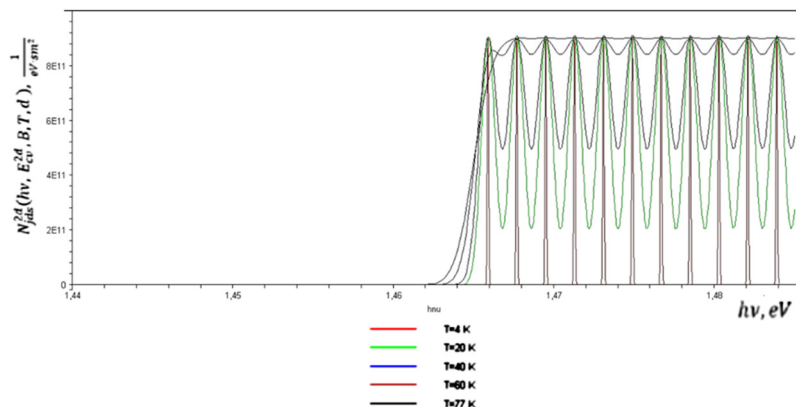


Figure 3. Effects of temperature on the dependence of the two-dimensional combined density of states on the absorbing photon energy in direct-gap heterostructures with GaAs/AlGaAs quantum wells ($d = 14$ nm) under the influence of a quantizing magnetic field $B=9$ T.

Here, the sum of acceptance of the quantizing attractive field is 9 T and plots of $N_{jds}^{2d}(\hbar\nu, E_{cv}^{2d}(B, T, d, N_L^{cv}, n_z))$ are made for temperatures of 4 K, 20 K, 40 K, 60K, 77 K. It can be seen from Fig.3 that with expanding temperature, the sharp crests of the Landau levels start to smooth out, and at adequately tall temperatures the discrete vitality densities of states turn into nonstop vitality spectra. These comes about were gotten for a steady quantum well thickness and attractive field. With expanding temperature, the sharp crests of the Landau levels of charge carriers start to smooth out (Fig. 3) and at

$kT \approx \hbar\omega_c^{cv}$ steadily vanish. Additionally, at adequately tall temperatures $kT > \hbar\omega_c^{cv} N_{jds}^{2d}(\hbar\nu, E_{cv}^{2d}(B, T, d, N_L^{cv}, n_Z))$ they turn into a persistent combined thickness of states of the quantum well and there will be no feel the impact of a quantizing attractive field. In expansion, as the temperature increments, the sharp crests within the Landau levels of charge carriers, due to the quantization of the energy levels of electrons and gaps within the permitted quantum well, steadily smooth out. This leads to the reality that at the temperature $T=40$ K, $kT=3,5 \cdot 10^{-3}$, $kT \approx \hbar\omega_c^{cv}$ discrete Landau levels of quantum well charge carriers gotten to be invisible. At a temperature of 77 K, the discrete Landau levels within the permitted band of the GaAs/AlGaAs quantum well are nearly imperceptible and coincide with the two-dimensional combined thickness of states within the nonappearance of a magnetic field. Consequently, the two-dimensional combined thickness of states within the conduction band and within the valence band of the quantum well are watched at temperatures $kT < \hbar\omega_c^{cv}$. Beginning from temperatures of the arrange of $0.5kT \sim \hbar\omega_c^{cv}$, the two-dimensional combined densities of states due to Landau quantization within the permitted band of the quantum well are not watched.

In this case, the measurements give a continuous spectrum of the two-dimensional combined density of states. Changing the cyclotron frequency of the magnetic field ω_c^{cv} changes the energy distance between discrete Landau levels of charge carriers in the quantum well (Fig.4). On Fig. 4 shows graphs of the two-dimensional combined density of states in direct-gap heterostructures with GaAs/AlGaAs quantum wells ($d=14$ nm) at various magnetic fields $B=9$ T and 12 T. As can be seen from these figures, with an increase in the induction of the quantizing magnetic field, we obtain a change in the discrete peaks of the Landau levels of charge carriers.

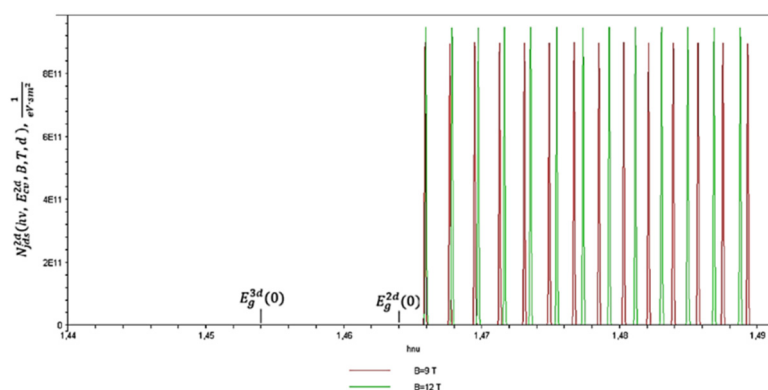


Figure 4. Influence of a quantizing magnetic field on the dependence of the two-dimensional combined density of states upon absorption of photon energy in direct-gap heterostructures with GaAs/AlGaAs ($d=14$ nm) quantum wells at a temperature of $T=4$ K.

Comparison of theory with experimental results in the absence and presence of a quantizing magnetic field

As is shown from work [29], the impact of a quantizing magnetic field on two-dimensional electron systems will illustrate exceptionally curiously physical properties emerging from the quantum imprisonment of charge carriers in a quantum well. Since this quantum imperative, the 2D combined thickness of states of charge carriers in a quantum well shows Van Hove singularities, where within the case of a perfect unbounded zero-dimensional cross section (quantum dab), the combined thickness of states tends to boundlessness for well-defined vitality values. Restricting a expansive number of 2D combined densities of states to a single vitality esteem leads to striking physical properties such as greatly tall magneto-optical assimilation, expanded thermoelectric control, quantized electronic conductivity, etc. Applications based on these properties seem lead to imperative unused nanotechnological gadgets and optoelectronic devices.

In particular, in work [30], two-dimensional combined densities of states of heterostructures based on an InGaN/GaN quantum well with different radiation wavelengths (violet, blue, and green) operating at different currents were studied. The results show that the blue shift of the emission with increasing current is associated with a change in the two-dimensional combined density of states. In this work, the dependence of the two-dimensional combined density of states of the InGaN/GaN quantum well on the absorbing photon energy in the absence of a magnetic field ($B=0$) and at temperatures $T=300$ K (Fig.5) was obtained. Here, the band gap of the InGaN/GaN quantum well is $E_g(0)=3.2$ eV, and the thickness of the quantum well is $d=10$ nm.

Now, let's apply the proposed model to the InGaN/GaN material. Fig.6 shows the influence of the quantizing magnetic field on the dependence of the two-dimensional combined density of states of the InGaN/GaN quantum well on the energy-absorbing photon at different temperatures. Here, $B=10$ T, $T=300$ K, 77 K and 5 K. Figures 5 and 6 show similar results with and without a magnetic field at room temperature. At room temperature, the influence of the magnetic field is not felt when the photon energy of the two-dimensional combined density of states is absorbed, since $kT \gg \hbar\omega_c$. The combined density of states behaves as if there is no magnetic field.

It follows from this that the proposed model obeys certain laws, and this indicates the correctness of the model.

Using equation (9), one can observe oscillations of the two-dimensional combined density of states (6) at different low temperatures. Also, a new analytical expression (the proposed new model) allows one to obtain the results of changes in the thickness of the quantum well associated with the combined density of states. This leads to a theoretical analysis of a number of experimental data.

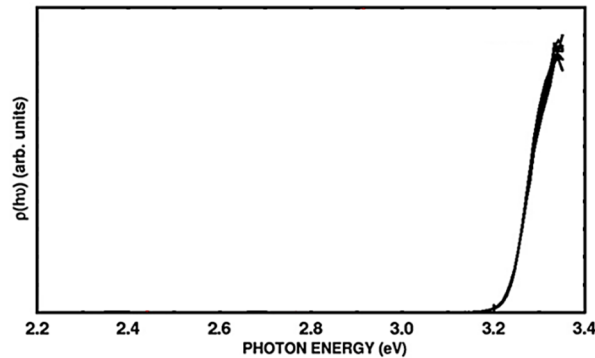


Figure 5. Dependence of the two-dimensional combined density of states on the energy-absorbing photon in direct-gap heterostructures based on an InGaN/GaN quantum well in the presence of a magnetic field and at room temperature [30].

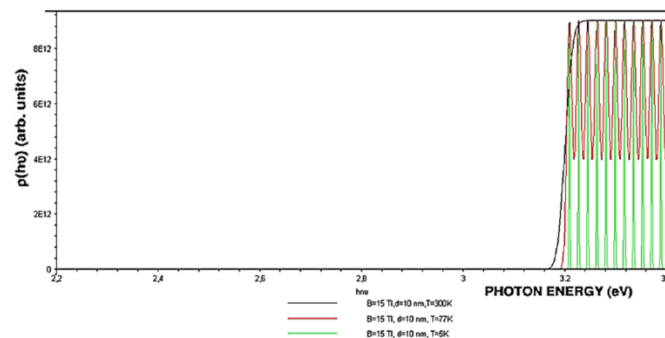


Figure 6. Influence of temperature and quantizing magnetic field on the two-dimensional combined density of states in direct-gap heterostructures based on the InGaN/GaN quantum well. Calculated using the model.

CONCLUSION

Based on the work carried out, the following conclusions can be drawn: An analytical expression is obtained for the oscillations of the two-dimensional combined density of states in the allowed band of a quantum well under the action of a quantizing magnetic field. A new model has been developed for calculating the effect of a quantizing magnetic field on the temperature dependence of the two-dimensional combined density of states in direct-gap heterostructures with quantum wells. The temperature dependence of the oscillations of the two-dimensional combined density of states of the quantum well is explained by the thermal smearing of the Gaussian distribution function in a strong magnetic field. Based on the proposed new models, the Landau levels of charge carriers in a direct-gap quantum well are determined in a wide temperature range. The experimental results were interpreted using the oscillations of the combined density of states of the quantum well in a quantizing magnetic field. The calculation results were compared with experimental results obtained for heterostructures based on an InGaN/GaN quantum well in a quantizing magnetic field at various temperatures.

ORCID

©Ulugbek I. Erkaboev, <https://orcid.org/0000-0002-6841-8214>; ©Sherzodjon A. Ruzaliev, <https://orcid.org/0009-0002-4270-7293>
©Rustamjon G. Rakhimov, <https://orcid.org/0000-0003-0850-1398>; ©Nozimjon A. Sayidov, <https://orcid.org/0000-0001-9382-8779>

REFERENCES

- [1] U.I. Erkaboev, R.G. Rakhimov, J.I. Mirzaev, N.A. Sayidov, and U.M. Negmatov, *East Eur. J. Phys.* (1), 485fghj (2024). <https://doi.org/10.26565/2312-4334-2024-1-53>
- [2] U.I. Erkaboev, and R.G. Rakhimov, *J. Comput. Electron.* **23**(2), (2024). <https://doi.org/10.1007/s10825-024-02130-3>
- [3] L.R. Mohan, and P.A. Wolff, *Phys. Rev.* **26**, 6711 (1982). <https://doi.org/10.1103/PhysRevB.26.6711>
- [4] M.L. Badgutdinov, and A.É. Yunovich, *Semiconductors*, **42**, 429 (2008). <http://dx.doi.org/10.1134/S1063782608040106>
- [5] V.E. Kudryashov, A.N. Turkin, A.E. Yunovich, A.N. Kovalev, and F.I. Manyakhin, *Semiconductors*, **33**, 429 (1999). <https://doi.org/10.1134/1.1187707>
- [6] Sh. Bhar, and S.K. Roy, *Comp. Phys. Commun.* **184**, 1387 (2013). <https://doi.org/10.1016/j.cpc.2013.01.004>
- [7] C.I. Cabrera, D.A. Contreras-Solorio, and L. Hernández, *Phys. E*, **76**, 103 (2016). <https://doi.org/10.1016/j.physe.2015.10.013>
- [8] J. Hwang, and J.D. Phillips, *Phys. Rev. B*, **83**, 195327-1 (2011). <http://dx.doi.org/10.1103/PhysRevB.83.195327>
- [9] J. Lee, H.N. Spector, W.Ch. Chou, and Y.Sh. Huang, *Phys. Rev. B*, **72**, 125329 (2005). <http://dx.doi.org/10.1103/PhysRevB.72.125329>
- [10] D. Shen, J. Dong, J. Shen, Y. Zhang, B. Xie, G. Wu, X. Chen, *et al.*, *J. Phys. Chem. Solids*, **69**, 2975 (2008). <https://doi.org/10.1016/j.jpcs.2008.06.072>
- [11] T.S. Moss, G.J. Burrell, and B. Ellis, *Semiconductor opto-electronics*, (Butterworth & Co. Ltd, England, 1973). <https://doi.org/10.1016/C2013-0-04197-7>
- [12] N.F. Mott, and E.A. Davis, *Electronic processes in non-crystalline materials*, (Clarendon Press, Oxford, 1971). <https://doi.org/10.1063/1.3071145>

- [13] A. Kulkarni, D. Guney, and A. Vora, *Nanomaterials*, **2013**, 504341 (2013). <http://dx.doi.org/10.1155/2013/504341>
- [14] U.I. Erkaboev, G. Gulyamov, and R.G. Rakhimov, *Indian J. Phys.* **96**, 2359 (2022). <https://doi.org/10.1007/s12648-021-02180-4>
- [15] U.I. Erkaboev, U.M. Negmatov, R.G. Rakhimov, J.I. Mirzaev, and N.A. Sayidov, *Int. J. Appl. Sci. Eng.* **19**, 2021123 (2022). [https://doi.org/10.6703/IJASE.202206_19\(2\).004](https://doi.org/10.6703/IJASE.202206_19(2).004)
- [16] U.I. Erkaboev, and R.G. Rakhimov, *East Eur. J. Phys.* **3**, 133 (2023). <https://doi.org/10.26565/2312-4334-2023-3-10>
- [17] U.I. Erkaboev and R.G. Rakhimov, *e-Prime - Advances in Electrical Engineering, Electronics and Energy*, **5**, 100236 (2023). <https://doi.org/10.1016/j.prime.2023.100236>
- [18] U.I. Erkaboev, N.A. Sayidov, U.M. Negmatov, J.I. Mirzaev, and R.G. Rakhimov, *E3S Web Conf.* **401**, 01090 (2023). <https://doi.org/10.1051/e3sconf/202340101090>
- [19] U.I. Erkaboev, N.A. Sayidov, U.M. Negmatov, J.I. Mirzaev, and R.G. Rakhimov, *E3S Web Conf.* **401**, 04042 (2023). <https://doi.org/10.1051/e3sconf/202340104042>
- [20] U.I. Erkaboev, R.G. Rakhimov, J.I. Mirzaev, N.A. Sayidov, U.M. Negmatov, and M. Abduxalimov. *AIP Conf. Proc.* **2789**, 040055 (2023). <https://doi.org/10.1063/5.0145554>
- [21] L.V. Grigoriev, *Silicon photonics* (ITMO University, St. Petersburg, 2016). (in Russian)
- [22] U.I. Erkaboev, R.G. Rakhimov, J.I. Mirzaev, N.A. Sayidov, U.M. Negmatov, and A. Mashrapov, *AIP Conf. Proc.* **2789**, 040056 (2023). <https://doi.org/10.1063/5.0145556>
- [23] U.I. Erkaboev, R.G. Rakhimov, J.I. Mirzaev, U.M. Negmatov and N.A. Sayidov, *Ind. J. Phys.* **98**, 189 (2024). <https://doi.org/10.1007/s12648-023-02803-y>
- [24] U.I. Erkaboev, R.G. Rakhimov, J.I. Mirzaev, U.M. Negmatov, and N.A. Sayidov, *Int. J. Mod. Phys. B.* **38**, 2450185 (2024). <https://doi.org/10.1142/S0217979224501856>
- [25] G. Gulyamov, U.I. Erkaboev, R.G. Rakhimov, J.I. Mirzaev and N.A. Sayidov, *Mod. Phys. Lett. B.* **37**, 2350015 (2023), <https://doi.org/10.1142/S021798492350015X>
- [26] D. Schoenberg, *Magnetic oscillations in metals*, (Wiley, New York, 1986). <http://dx.doi.org/10.1017/CBO9780511897870>
- [27] L.S. Stilbans, *Physics of semiconductors*, (Soviet Radio, Moscow, 1967). (in Russian)
- [28] A.V. Mikhailov, A.V. Trifonov, O.S. Sultanov, I.Yu. Yugova, and I.V. Ignatiev, *Semiconductors*, **56**, 672 (2022).
- [29] U.I. Erkaboev, R.G. Rakhimov, N.A. Sayidov, and J.I. Mirzaev, *Indian J. Phys.* **2022**, (2022). <https://doi.org/10.1007/s12648-022-02435-8>
- [30] Yu. Wang, N. Chen, Ch. Lu, and J. Chen, *Phys. B*, **406**, 4300 (2011). <https://doi.org/10.1016/j.physb.2011.08.071>

**МОДЕЛЮВАННЯ ТЕМПЕРАТУРНОЇ ЗАЛЕЖНОСТІ КОМБІНОВАНОЇ ГУСТИНИ СТАНІВ
В ГЕТЕРОСТРУКТУРАХ З КВАНТОВИМИ ЯМАМИ ПІД ВПЛИВОМ КВАНТУЮЧОГО МАГНІТНОГО ПОЛЯ**

Улугбек І. Єркабєв^а, Шерзоджон А. Рузалєв^б, Рустамжон Г. Рахімов^а, Нозімжон А. Саїдов^а

^аНаманганський інженерно-технологічний інститут, 160115, Наманган, Узбекистан

^бФерганський державний університет, 150100, Фергана, Узбекистан

У даній роботі досліджено залежність осциляцій комбінованої густини станів від сильного магнітного поля в гетероструктурах на основі прямокутної квантової ями. Досліджено вплив квантуючого магнітного поля на температурну залежність комбінованої густини станів у нанорозмірних прямокутних гетероструктурах. Розроблено нову математичну модель для розрахунку температурної залежності двовимірної комбінованої щільності станів квантових ям у квантуючих магнітних полях. Запропонована модель пояснює експериментальні результати в нанорозмірних прямокутних напівпровідниках з параболічним законом дисперсії.

Ключові слова: напівпровідник; нанорозмірні напівпровідникові структури; квантуюче магнітне поле; квантова яма; осциляції, щільність енергетичних станів

STUDY OF OPTICAL, ELECTROPHOTOGRAPHIC AND HOLOGRAPHIC PARAMETERS OF As-Se CONDENSATES FROM THE PREHISTORY OF THE ORIGINAL BULK MATERIALS

Sharifa B. Utamuradova^a, Zakirjan T. Azamatov^a, A.I. Popov^a, Mira R. Bekchanova^a,
Murodjon A. Yuldoshev^{b*}, Abror B. Bakhromov^a

^aInstitute of Semiconductor Physics and Microelectronics, National University of Uzbekistan,
20 Yangi Almozor st., Tashkent, 100057, Uzbekistan

^bTuran International University, 10D Q. Mamarasulov st., Namangan, Uzbekistan

*Corresponding Author e-mail: murod.yuldoshev1993@gmail.com

Received May 5, 2024; revised July 3, 2024; in final form August 15, 2024; accepted August 17, 2024

The results of a study of the optical, electrophotographic and holographic parameters of As-Se condensates from the prehistory of the original bulk materials are presented. It has been established that the electrophotographic parameters of freshly deposited As₄₀Se₆₀ layers change significantly with temperature; the dependences of the maximum charging potential (U_0) and the half-decay time of the potential ($\tau_{1/2}$) of electrophotographic As₄₀Se₆₀ layers in the dark on the processing temperature of the melt of the starting material are shown. The dependence of the half-life of the potential in the dark, as well as the properties of bulk samples, has an extremum in the region of $T_{\text{sub}} \sim 500^\circ\text{C}$. The correlation between the dependences of the properties of bulk samples and the electrophotographic parameters of the layers on T_{sub} indicates that the structural features of the source material in the deposition mode used affect the structure of the films.

Keywords: Chalcogenide glassy glasses; As-Se systems; Charging potential; Potential half-time; Diffraction efficiency; Optical transmittance

PACS: 68.37.Hk, 78.55.Ap, 42.25.Bs, 61.46.Km

INTRODUCTION

Currently, the development of modern science and technology in the world, which requires a significant increase in the volume of recording, storage and processing of information, necessitates the development and improvement of recording methods based on the use of various information media [1-5]. Promising materials for these purposes are chalcogenide glassy semiconductors (CHGS) [6-9].

Due to their high photoelectric sensitivity and low electrical conductivity, layers of glassy arsenic chalcogenides have found wide application in electrophotography, photothermoplastic recording of information, and also as active elements of transmitting television tubes – vidicons [10,11].

Factors that currently hinder the widespread use of chalcogenide glassy semiconductors in optical information recording devices are the limited methods for controlling the properties of these materials and their condensates, as well as the insufficiently high reproducibility of their properties. In this regard, an urgent task is to determine the influence of external influences on the structure of glassy arsenic chalcogenides and to develop methods for controlling their properties.

It is known that there is a relationship between the structure of bulk materials and the composition of vapor during their evaporation. We present the results of a study of the dependence of the properties of condensates on the prehistory of the initial bulk materials, carried out on materials of As-Se systems that are of practical importance for types of recording optical information.

EXPERIMENTAL PART

To determine the diffraction efficiency of holograms recorded on As - Se samples, an optical setup was used, the diagram of which is shown in Fig. 1. The recorded holograms were the interference of two flat beams. Angle of convergence $\cong 30^\circ$. The radiation source was an LG-38 He-Ne laser.

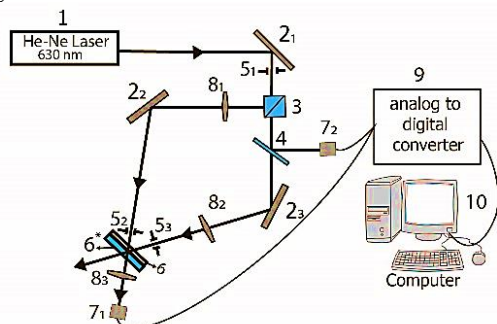


Figure 1. Experimental scheme for studying the holographic characteristics of CHGS films: 1-laser; 2₁, 2₂, 2₃-flat mirrors; 3-cubic prism; 4-translucent plate; 5₁, 5₂-diaphragm mask; 6-sample, 6*-substrate; 7₁, 7₂-registering devices; 8₁, 8₂, 8₃-shutters

The laser beam (Fig. 1) (1) is divided on a cubic prism (5) into two beams, which are then converged on the surface of the sample (6). The hologram obtained in this way is a diffraction grating, the frequency of the lines of which depends on the installation parameters and can be adjusted. For our case, $\nu=1000$ lines/mm. To obtain maximum contrast of the stripes, a filter (5_1) was introduced that aligns the beams in intensity. Masks ($5_2, 5_3$) serve to reduce errors associated with the inhomogeneity of the laser beam and inaccuracy of adjustment. Photosensors and associated recording devices ($8_1, 8_2, 8_3$) serve to measure the diffraction efficiency η , of the sample transparency coefficient T and the energy characteristics of the recording. The recording device is calibrated taking into account the diaphragmatic effect of the masks ($5_1, 5_2, 5_3$). The diffraction efficiency was assessed by the ratio of the radiation power of the reference beam, diffracted to the 1st order when reconstructing holograms, to the radiation power of the reference beam itself.

RESULTS AND DISCUSSION

Depending on the processing temperature of bulk CHGS, the microhardness of these materials, the ratio of the height of the crystallization peak to its width, the heat of crystallization, and the type of kinetic curves of differential solubility change [12,14]. As a rule, the dependences of the properties of $As_{40}Se_{60}$ CHGS on the melt processing temperature are of an extreme nature with the extremum located in the region of $T_{smp} \sim 500^\circ C$, and the critical temperature of the melt, up to which structural modification is effective, for this material under the processing modes in this work is $\sim 550 \div 600^\circ C$. To study the influence of the prehistory of bulk $As_{40}Se_{60}$ samples on the electrophotographic characteristics of their condensates, film samples (from bulk materials with different melt processing temperatures) were sawed onto aluminum substrates at $T_{sub}=70$ and $150^\circ C$. The condensation rate was chosen to be $3 \mu m/min$ ($T_{smp} \sim 380 \div 400^\circ C$), since it is known that the electrophotographic properties of $As_{40}Se_{60}$ layers at rates of $3 \div 6 \mu m/min$ do not depend on the condensation rate.

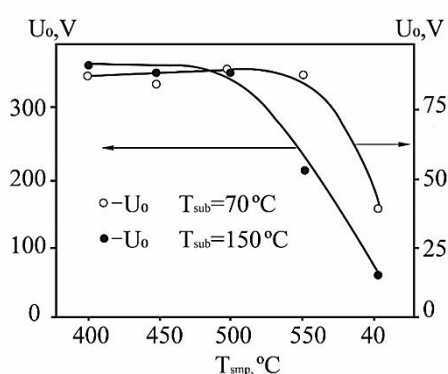


Figure 2. Dependence of the maximum charging potential U_0 of $As_{40}Se_{60}$ layers on the processing temperature of the melt of the starting material

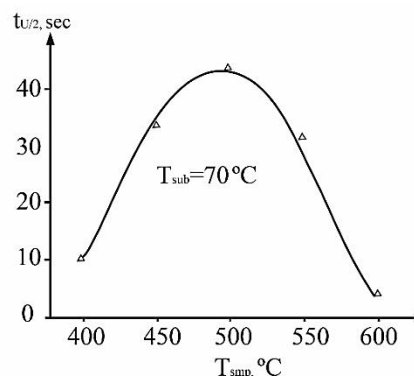


Figure 3. Dependence of the potential half-life in the dark ($t_{1/2}$) of $As_{40}Se_{60}$ layers on the processing temperature of the melt of the starting material

In the course of research, it was established that the electrophotographic parameters of freshly deposited $As_{40}Se_{60}$ layers change significantly with T_{smp} . In Fig. 2. The dependences of the maximum charging potential (U_0) and in Fig. 3. the half-decay time of the potential ($\tau_{1/2}$) of electrophotographic layers of $As_{40}Se_{60}$ in the dark on the processing temperature of the melt of the starting material are presented. The dependence of the half-life of the potential in the dark, as well as the properties of bulk samples, has an extremum in the region of $T_{smp} \sim 500^\circ C$. The correlation between the dependences of the properties of bulk samples and the electrophotographic parameters of the layers on T_{smp} indicates that the structural features of the source material in the deposition mode used affect the structure of the films. The form of these dependencies changes when the condensation conditions change, however, their connection with the prehistory of the source materials is preserved. As can be seen from Fig. 2. the electrophotographic parameters of the layers obtained by condensation onto a substrate heated to $70^\circ C$ deteriorate with an increase in the volumetric material T_{ab} above $500^\circ C$ (there is a decrease in the specific charging potential and its half-life in the dark). An increase in T_{sub} to $150^\circ C$ leads to an increase in the absolute values of U_0 and a slight shift of the entire curve to the region of higher processing temperatures.

Since the dark discharge of positively charged electrophotographic layers is caused by the generation of current carriers in the volume of the layer [13], the rate of potential decay in the dark (and, consequently, the half-life) will depend on the degree of structural disorder of the material, on the type and concentration of defects in him.

$As_{40}Se_{60}$ is characterized by the presence of various types of structural defects, such as pairs with variable valence formed on arsenic and selenium atoms, quasi-molecular defects and homopolar As-As, Se-Se bonds. The results of the differential solubility of bulk samples in a 10% KOH solution indicate different concentrations of defects such as "wrong bonds" in samples with different histories, which, as a rule, decreases with increasing T_{sub} . At the same time, with an increase in T_{sub} , the concentration of a pair with a variable valence in the melt increases exponentially and, under certain quenching conditions, is retained in the glass. A more complex situation occurs in the case of temperature

dependence of the concentration of quasi-molecular defects. The implementation of different ratios between the concentrations of the listed types of defects contributes to the formation of different thermodynamic properties in materials of the same chemical composition and, as a consequence, the formation of condensates (under identical conditions for their production) with different properties, using samples from different batches as an example. Obviously, in the case of film samples the situation is more complicated compared to bulk materials, since the evaporation process itself, being a powerful effect on the structure of the material, in some cases can lead to “erasing” of the prehistory. However, the conducted studies indicate a significant dependence of some parameters of condensates on the processing temperature of the source material under evaporation modes adopted in the production of devices [13,14].

The study of the effect of heat treatment of bulk materials on the optical and holographic parameters of $As_{40}Se_{60}$ condensates [15] was carried out on film samples with a thickness of 0,3 μm to 1 μm . Sputtering was carried out at $T_{\text{sub}} \sim 400^{\circ}\text{C}$ in a vacuum of no worse than 10^{-5} Torr on unheated glass substrates 1 mm thick. Freshly deposited films were irradiated with a He-Ne laser ($\lambda=0,63 \mu\text{m}$) until maximum darkening. Transmission spectra were taken from irradiated and unirradiated areas in the wavelength range (0,3+1) μm . In the same interval, the spectra of the annealed samples were taken. To determine the diffraction efficiency of holograms recorded on $As_{40}Se_{60}$ samples, an optical setup was used, the diagram of which is shown in Fig. 1. The diffraction efficiency was assessed by the ratio of the radiation power of the reference beam, diffracted to the 1st order when reconstructing holograms, to the radiation power of the reference beam itself. The determined relative values of the diffraction efficiency η and the shift of the optical transmission edge $\Delta\lambda$ in the 1st recording cycle are shown in Fig. 4. The spread of their values is obviously due to some heterogeneity of film thicknesses.

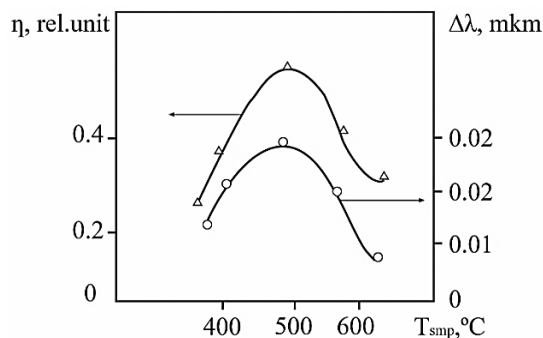


Figure 4. Changes in absorption edge ($\Delta\lambda$) of $As_{40}Se_{60}$ films obtained from bulk materials with diffraction efficiency (η) and shift of the optical different histories

CONCLUSION

Thus, the experimental results obtained indicate a significant influence of the prehistory of bulk materials both on the absolute values of the parameters of their condensates and on the degree of change in these parameters in the process of external influences. This gives grounds to assume a more complex dependence of the function $U(R)$. Metastable states are known that correspond to the structure of a freshly deposited, annealed, irradiated film with quanta of various energies (electrons, optical and X-rays). In addition, each structural state of a film obtained from a bulk material with a certain history obviously corresponds to a certain metastable state and the corresponding minimum of the potential function $U(R)$. The smooth nature of the change in the properties of materials, determined by their prehistory, can be explained by assuming the complex nature of the structure of the very minimum of the function $U(R)$, in particular, the presence in it of a number of shallower potential wells.

ORCID

✉ Sharifa B. Utamuradova, <https://orcid.org/0000-0002-1718-1122>; ✉ Zakirjan T. Azamatov, <https://orcid.org/0000-0001-7074-9437>
✉ Murodjon A. Yuldoshev, <https://orcid.org/0000-0002-9722-9439>; ✉ Abror B. Bakhromov, <https://orcid.org/0000-0001-8148-2467>

REFERENCES

- [1] Sh.B. Utamuradova, Z.T. Azamatov, M.A. Yuldoshev, N.N. Bazarbayev, and A.B. Bakhromov, East Eur. J. Phys. (4), 147 (2023), <https://doi.org/10.26565/2312-4334-2023-4-15>
- [2] Z.T. Azamatov, M.A. Yuldoshev, N.N. Bazarbayev, and A.B. Bakhromov, Physics AUC, **33**, 139 (2023). https://cis01.central.ucv.ro/pauc/vol/2023_33/13_PAUC_2023_139_145.pdf
- [3] V.A. Barachevsky, Opt. Spectrosc. **124**, 373–407 (2018), <http://dx.doi.org/10.1134/S0030400X18030062>
- [4] Z.T. Azamatov, V.E. Gaponov, A.A. Jeenbekov, and A.B. Bakhromov, Russian Microelectronics, **52**, Suppl 1, S263 (2023). <https://doi.org/10.1134/S106373972360019X>
- [5] Sh.B. Utamuradova, Z.T. Azamatov, V.E. Gaponov, N.N. Bazarbaev, and A.B. Bakhromov, Applied Physics, (4), 115 (2023). https://applphys.orion-ir.ru/appl-23/23-4/PF-23-4-115_RU.pdf
- [6] M. Iovu, S. Sergeev, O. Iaseniuc, Optoelectron. Adv. Mat. **12**(7-8), 377 (2018).
- [7] O. Iaseniuc, I. Cojocaru, A. Prisacar, A. Nastas, and M. Iovu, Journal of Optics and Spectroscopy, **121**(1), 1128 (2016). <https://doi.org/10.1134/S0030400X16070237>
- [8] Z.T. Azamatov, Sh.B. Utamuradova, M.A. Yuldoshev, and N.N. Bazarbaev, East Eur. J. Phys. (2), 187 (2023). <https://doi.org/10.26565/2312-4334-2023-2-19>

- [9] E. Achimova, A. Stronski, V. Abaskin, A. Meshalkin, A. Paiuk, A. Prisacar, P. Oleksenko, G. Triduh, *Optical Materials* **47**, 566 (2015); <https://doi.org/10.1016/j.optmat.2015.06.044>
- [10] G.E. Snopatin, V.S. Shiryayev, V.G. Plotnichenko, E.M. Dianov, and M.F. Churbanov, *Inorg. Mater.* **45**, 1439 (2009). <https://doi.org/10.1134/S0020168509130019>
- [11] M.F. Churbanov, and V.G. Plotnichenko, *Semiconductors and Semimetals*, **80**, 209 (2004). [https://doi.org/10.1016/S0080-8784\(04\)80029-2](https://doi.org/10.1016/S0080-8784(04)80029-2)
- [12] H. Takebe, T. Hirakawa, T. Ichiki, and K. Morinaga, *J. Ceram. Soc. Jpn.* **111**(8), 572 (2003). <https://doi.org/10.2109/jcersj.111.572>
- [13] K. Tanaka, and K. Shimakawa, *Amorphous Chalcogenide Semiconductors and Related Materials*, (Springer, New York, 2011).
- [14] J. Qin, Y. Chen, R. Wang, X. Shen, and T. Xu, *Journal of Non-Crystalline Solids*, **532**(15), 119888 (2020). <https://doi.org/10.1016/j.jnoncrysol.2020.119888>
- [15] L. Pan, B. Song, N. Mao, C. Xiao, C. Lin, P. Zhang, X. Shen, and S. Dai, *Optics Communications* **496**, 127123 (2021). <https://doi.org/10.1016/j.optcom.2021.127123>

**ДОСЛІДЖЕННЯ ОПТИЧНИХ, ЕЛЕКТРОФОТОГРАФІЧНИХ І ГОЛОГРАФІЧНИХ ПАРАМЕТРІВ
КОНДЕНСАТІВ As-Se ВІД ПЕРЕДІСТОРІЇ ВИХІДНИХ ОБ'ЄМНИХ МАТЕРІАЛІВ**

**Шаріфа Б. Утамурадова^а, Закірман Т. Азаматов^а, А.І. Попов^а, Міра Р. Бекчанова^а,
Муроджон А. Юлдошев^б, Аброр Б. Бахромов^а**

^а*Інститут фізики напівпровідників та мікроелектроніки Національного університету Узбекистану, Ташкент, Узбекистан*
^б*Міжнародний університет Туран, Наманган, Узбекистан*

Наведено результати дослідження оптичних, електрофотографічних та голографічних параметрів конденсатів As-Se від передісторії вихідних об'ємних матеріалів. Встановлено, що електрофотографічні параметри свіжонапиленних шарів As₄₀Se₆₀ істотно змінюються з T_{обр}, наведено залежності граничного потенціалу зарядки (U₀) і часу спаду потенціалу (τ_{1/2}) електрофотографічних шарів As₄₀Se₆₀ в темряві від температури обробки розплаву вихідного матеріалу. Залежність часу спаду потенціалу в темряві, як і властивості об'ємних зразків, має екстремум в області T_{обр}~500°C. Кореляція між залежностями властивостей об'ємних зразків та електрофотографічними параметрами шарів від T_{обр} про те, що структурні особливості вихідного матеріалу при використаному режимі напилення впливають на структуру плівок.

Ключові слова: халькогенідне склоподібне скло; системи As-Se; зарядний потенціал; напівчас спаду потенціалу; дифракційна ефективність; оптичний коефіцієнт пропускання

STRUCTURAL PROPERTIES OF Al-DOPED ZnO FILMS

 Sirajidin S. Zainabidinov^a,  Shakhriyor Kh. Yulchiev^b,  Akramjon Y. Boboev^{a,c},
 Bakhtiyor D. Gulomov^d,  Nuritdin Y. Yunusaliyev^a

^aAndijan state university named after Z.M. Babur, Andijan, Uzbekistan

^bAndijan state pedagogical institute, Andijan, Uzbekistan

^cInstitute of Semiconductor Physics and Microelectronics at the National University of Uzbekistan,
20 Yangi Almazar st., Tashkent, 100057, Uzbekistan

^dAndijan Machine-Building Institute, Andijan, 170119, Uzbekistan

*Corresponding Author e-mail: aboboevscp@gmail.com

Received June 30, 2024; revised July 25, 2024; accepted August 5, 2024

In this study, the results of the investigation of the influence of Al atoms on the structural characteristics of ZnO films obtained by the sol-gel method are presented. It has been determined that the glass substrates consist of subcrystallites with dimensions of 28.6 nm, having cubic unit cells with lattice parameters $a = 0.3336$ nm, and their surfaces belong to the crystallographic orientation (111). It has been identified that the grown thin ZnO films consist of subcrystallites with dimensions of 39.5 nm, having a wurtzite structure with lattice parameters $a = b = 0.3265$ nm and $c = 0.5212$ nm, respectively. It has been determined that at the boundaries of the division of these subcrystallites, polycrystalline regions with sizes of 12.6 nm, 28.3 nm, 30 nm, and 33 nm are formed. Additionally, nanocrystallites with sizes of 56.8 nm self-assemble on the surface areas of the deposited films. The increase in the values of the “c” axis of the hexagonal crystal lattice of ZnO films by 0.0009 nm when doping Al atoms from 1% to 5% is explained by the shift of the main structural line (002) at small angles ($\Delta\theta=0.12^\circ$). It has been established that nanocrystallites with lattice parameters $a_n = 0.5791$ nm, belonging to the spatial group $Fd\bar{3}m$, self-assemble on the surface areas of ZnO:Al films. The curve due to the presence of a monoenergetic level of fast surface states at the heterojunction.

Keywords: Borosilicate glass; Sol-gel method; Metal oxide; ZnO thin film; X-ray diffraction; Subcrystallite; Nanocrystal

PACS: 78.30.Am

INTRODUCTION

Currently, due to the rapid development of optoelectronics and nanoelectronics, thin films of ZnO with their sufficiently wide band gap (3.37 eV) are of great interest to both researchers and manufacturers of optoelectronic equipment. In addition to the simplicity and well-studied synthesis technology, the relatively low prices of the raw materials allow for the wide application of ZnO in production. Research shows that the unique physical and chemical properties of thin layers of ZnO open up the possibility of their wide application in many micro and nanoelectronic devices such as gas sensors, optical and magnetic storage devices, solar cells, piezoelectric conductors, photodiodes, photodetectors, etc. [1,2].

In addition, the possibility of controlling the electrical and photoconductivity of ZnO thin films by doping with various impurity atoms is attractive. Films of ZnO were grown using centrifugation, magnetron sputtering, and spray pyrolysis methods in works [3-5], and the optimal doping conditions of Al impurity atoms in these films were determined, as well as their piezoelectric and optoelectronic properties were studied. However, reliable results on the influence of different concentrations of impurity atoms on the structural properties of ZnO films are still lacking, which is an important issue for the stable functioning of devices. Therefore, this study presents the results of investigating the influence of Al impurity atoms on the structural characteristics of ZnO films obtained by the sol-gel method using the immersion technique.

MATERIALS AND METHODS

To prepare the required sol-gel solution, zinc acetate ($Zn(CH_3COO)_2 \cdot 2H_2O$) was used as a precursor, isopropyl alcohol ($CH_3CH(OH)CH_3$) as a solvent, diethylamine ($C_4H_{11}N$) as a stabilizer, and aluminum nitrate ($Al(NO_3)_3 \cdot 9H_2O$) as an additive. Zinc acetate (3.23 grams) and aluminum nitrate (0.047-0.265 grams), dissolved in isopropyl alcohol (100 ml), were slowly added dropwise with diethylamine (0.33 ml) to increase solubility. The mixture was stirred using a magnetic stirrer at 60°C and a speed of 1500 rpm until the solution became clear. To convert the prepared sol-gel solution into a gel, it was incubated in a special cabinet at room temperature for 168 to 240 hours. In the deposition setup, the optimal repeatability of processes was about 20 times when growing thin layers of ZnO, both pure and doped with aluminum atoms (from 1% to 5%). To remove any undissolved gel from the surface of the grown films, they were subjected to thermal treatment at 500°C for 10 minutes in a drying oven. X-ray diffraction studies of the grown films were conducted using an XRD-6100 X-ray diffractometer [6]. To determine the resistivity, concentration and the mobility of the majority charge carriers in the grown films, the Van der Pauw method was used on a HMS-7000 Hall effect measurement unit [7].

RESULTS AND DISCUSSION

Figure 1 shows the X-ray diffraction pattern of the borosilicate glass substrates used in our study. The diffraction pattern at a scattering angle of $2\theta = 47.1^\circ$ with $d/n = 0.1926$ nm exhibits a structural reflex with a crystallographic orientation of (111). This indicates that the majority of atoms in the substrate are arranged in a crystallographic orientation of (111) and its surface also belongs to this plane. Furthermore, based on the experimental values of the structural reflection (111), the lattice parameter (a_s) of the substrate was determined to be 0.3336 nm using the Nelson-Riley extrapolation function [8-10]. Based on the width of the crystallographic orientation (111), the size of the blocks (subcrystallites) was determined to be 28.6 nm. The fact that the structural reflection (111) has a width of 5.5×10^{-3} radians and a high intensity (~ 104 imp s $^{-1}$) indicates a high degree of crystallinity of the borosilicate substrate [11]. Furthermore, the diffraction pattern showed structural reflections corresponding to crystallographic directions (200) at an angle of $2\theta = 55.031^\circ$ with $d/n = 0.1668$ nm, (210) at an angle of $2\theta = 62.13^\circ$ with $d/n = 0.1492$ nm, and (211) at an angle of $2\theta = 68.57^\circ$ with $d/n = 0.1362$ nm. Analysis of these experimental results showed that the sizes of the corresponding crystallites, according to expression (3), were approximately 20 nm. The observation of such structural lines suggests the presence of polycrystalline regions at the boundaries of subcrystallites of the borosilicate substrate [12]. The observed structural reflection corresponding to the crystallographic direction (110) at a scattering angle of $2\theta = 38.1^\circ$ with d -spacing $d/n = 0.2359$ nm indicates the presence of nanopores sized 81.5 nm on the substrate surface [13]. Additionally, at a low angle of approximately $2\theta \approx 15^\circ$, the X-ray diffraction pattern shows broad diffuse reflection caused by structural fragments of SiO_x on the surface layers, which contain unsaturated bonds of silicon and oxygen atoms. The half-width ($\beta = 1.25 \times 10^{-1}$ rad) of this reflection indicates small sizes of the SiO_x structural fragment and the absence of long-range order in their arrangement. Thus, these SiO_x structural fragments represent atomic clusters rather than nanocrystallites, with characteristic sizes of approximately 1.2 nm [14].

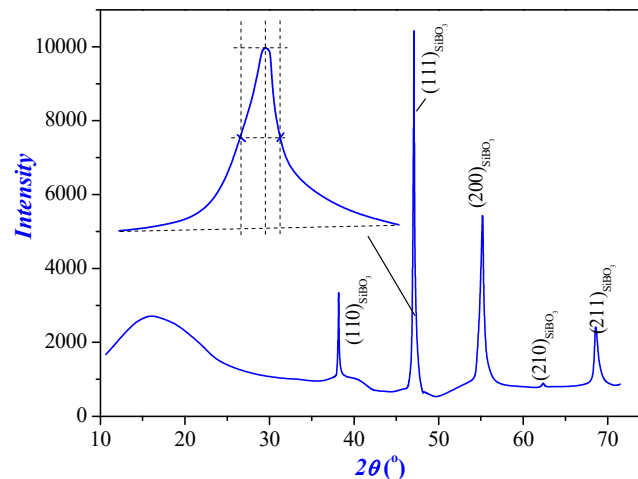


Figure 1. X-ray diffraction pattern of borosilicate glass

In Figure 2 (black curve), the X-ray diffraction pattern of ZnO films is shown, which significantly differs from the substrate's diffraction pattern.

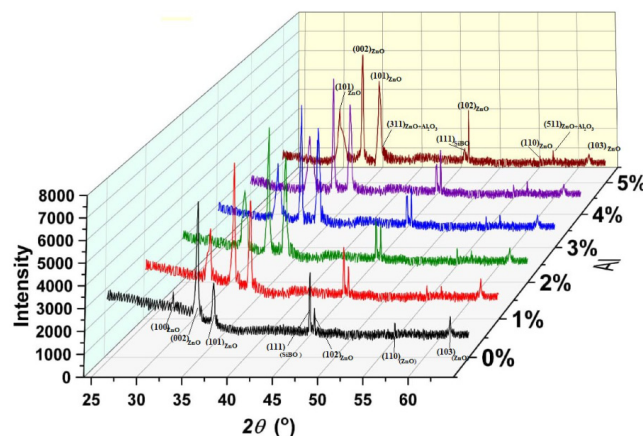


Figure 2. X-ray diffraction patterns of (a) undoped and (b-1%, c-2%, d-3%, e-4%, and f-5%) Al doped ZnO films.

It can be observed that at low-angle scattering, diffuse reflection with three highly intensive selective structural reflexes is present, belonging to the crystallographic orientation (100) at a scattering angle of $2\theta = 31.42^\circ$ with $d/n = 0.2774$ nm, (002) at an angle of $2\theta = 34.48^\circ$ with $d/n = 0.2581$ nm, and (101) at a scattering angle of $2\theta = 36.34^\circ$

with $d/n = 0.249$ nm. Among these observed reflexes, the structural line corresponding to the crystallographic direction (002) has the highest intensity (~ 104 imp·c⁻¹) (Figure 2, black curve). Based on these experimental values, the calculated full width at half maximum of this reflection was 3.9×10^{-3} radians, indicating a relatively high degree of crystallinity of the grown film. Upon analysis of the experimental results of this reflection, the constant of the crystal lattice has been determined, which are equal to $a = b = 0.3265$ nm and $c = 0.5212$ nm, respectively. This, in turn, allows to determine that the ZnO layers have a wurtzite structure, belonging to the hexagonal crystal lattice of the spatial group C6/mmc, which is provided by the alternate placement of zinc and oxygen in the elementary cell of the crystal lattice [9]. Using expression (3), the sizes of subcrystallites in unalloyed ZnO films were determined from the experimental values of the (002) reflection shape, which were approximately 39.5 nm. Additionally, double structural reflections belonging to the crystallographic orientations (111) and (102) are observed on the X-ray diffraction pattern of the grown films in the scattering angle range of 47.0° to 47.48° , corresponding to the substrate and ZnO film, respectively (Fig. 3, black curve). The structural line (111) belongs to the borosilicate substrate, located deeper in the ZnO film with a thickness of 1 μm , thus appearing due to the rays returning from the substrate surface.

In addition to the structural lines observed in the X-ray diffraction pattern, which belong to the crystallographic orientations (110) at an angle of $2\theta = 56.67^\circ$ with $d/n = 0.1630$ nm, (103) at an angle of $2\theta = 62.93^\circ$ with $d/n = 0.1481$ nm, (200) at an angle of $2\theta = 66.37^\circ$ with $d/n = 0.1398$ nm, (212) at an angle of $2\theta = 66.52^\circ$ with $d/n = 0.1376$ nm, and (201) at an angle of $2\theta = 69.17^\circ$ with $d/n = 0.1327$ nm. This, in turn, indicates that polycrystalline regions of 12.6 nm, 28.3 nm, 30 nm, and 33 nm in size, with different shapes, as well as nanocrystallites of 56.8 nm in the near-surface layers of grown ZnO films, self-assemble at the boundaries of subcrystallites.

In Figure 2 (curves red, green, blue, violet, and brown), X-ray diffraction patterns of doped Al (from 1% to 5%) thin films of ZnO are presented, which significantly differ from the X-ray diffraction pattern of pure ZnO film. It can be observed that their elastic background level of diffuse reflection, observed at low-angle scattering, decreases with an increase in the amount of dopant atoms. This indicates that with an increase in the amount of Al dopant atoms in the grown films, the uneven distribution of oxygen from the main background impurities along the crystal lattice decreases [4]. Additionally, besides this diffuse reflection, reflections corresponding to the crystallographic orientations (100) are observed at an angular scattering angle of $2\theta = 31.7^\circ$ with d-spacing $d/n = 0.2774$ nm, and (101) at an angular scattering angle of $2\theta = 36.34^\circ$ with d-spacing $d/n = 0.249$ nm, shifted towards smaller angles by $\Delta\theta = 0.06^\circ$ and $\Delta\theta = 0.08^\circ$, respectively. Simultaneously, in the X-ray diffraction patterns of the film with aluminum alloying atoms up to 2%, their intensities increase to 28.1% for the structural line (100) and 37.8% for the structural line (101). However, with alloying atoms above 2%, their intensities decrease by 4.29% and 1.6%, respectively. This indicates that instead of the structural lines (100) and (101), new reflections appear belonging to the crystallographic directions (220) and (311) of the ZnO and Al₂O₃ compounds [15].

From Figure 3, it can be seen that the main structural reflex belonging to the crystallographic direction (002) on the X-ray diffraction pattern is shifted towards small angles (from $2\theta = 34.44^\circ$ to $2\theta = 34.32^\circ$), i.e. by $\Delta\theta = 0.12^\circ$ with an increase in the number of Al alloying atoms.

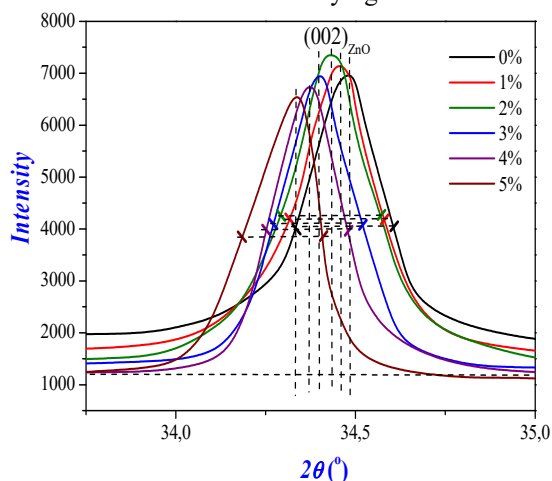


Figure 3. Reflex shape (002) of X-ray diffraction patterns of undoped and Al doped (from 1% to 5%) ZnO films

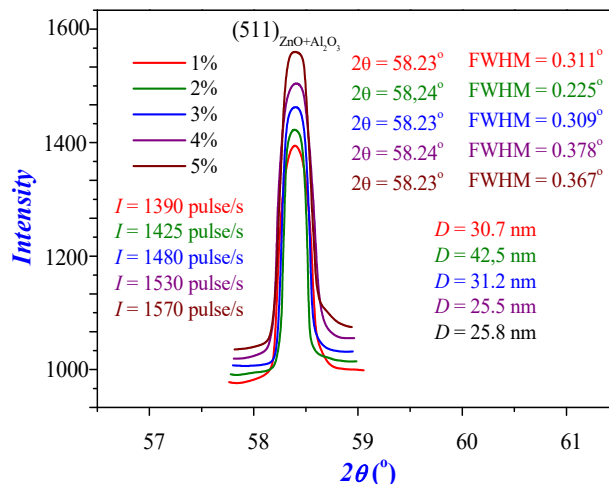


Figure 4. The forms of reflexes (511) of X-ray diffraction patterns of undoped and Al doped (from 1% to 5%) ZnO films

Their intensity increased to 5.2% for samples alloyed with Al up to 2% and decreased to 6.3% for samples with an Al content exceeding 2% (Figure 3, curves red, green, blue, violet, and brown). Analyzing the experimental results of these reflections using expression (4), it was established that the lattice parameter of the crystal at room temperature for films with Al alloying atoms is $a = b = 0.3265$ nm and $c = 0.5219$ nm, while the axes of the hexagonal crystal lattice increase by a small amount ($\Delta c = 0.0009$ nm). This indicates that in the crystal lattice of the film, Al⁺³ ions are replaced by Zn⁺² ions [15]. When determining the half-width (β) of these reflexes according to expression (2), they initially increased (doping with Al atoms up to 3%), and then decreased (doping with Al atoms more than 3%). This allows

determining the sizes of subcrystallites according to expression (3), which initially decreased (when doping with Al atoms up to 2%) ($D_{0\%Al:ZnO} = 39.5$ nm, $D_{1\%Al:ZnO} = 37.9$ nm, and $D_{2\%Al:ZnO} = 34.1$ nm), then increased when doping with Al atoms more than 2% ($D_{3\%Al:ZnO} = 34.4$ nm, $D_{4\%Al:ZnO} = 35.2$ nm, and $D_{5\%Al:ZnO} = 35.8$ nm). Based on the experimental values of these reflections, it can be concluded that doping ZnO with Al atoms up to 2% leads to an increase in the perfection of the crystal lattice of the films, while an increase in Al atoms more than 2% leads to their decrease [15]. Furthermore, the structural reflexes on the ZnO X-ray diffraction pattern increase when doped with Al atoms up to 2% and decrease with further increase in their concentration beyond 2%. Consequently, aluminum atoms incorporated into the ZnO crystal lattice up to 2% combine with oxygen, which acts as atoms of an uncontrolled background level, resulting in the organization of clusters corresponding to ZnO and Al_2O_3 compounds at an angle of $2\theta = 58.4^\circ$ with $d/n = 0.15740$ nm, leading to the emergence of new structural lines. Conversely, with an increase in doping of Al atoms above 2% in the crystal lattice, small microstrains are formed in the film. The structural lines corresponding to crystallographic orientations (110), (103), (200), (212), and (201) on the X-ray diffraction pattern change disproportionately with the increase in the number of added Al atoms. However, the sizes of these crystallites have partially decreased, forming various polycrystalline regions ranging in size from 11 nm to 30 nm.

As a result of the mutual substitution of ZnO and Al_2O_3 compounds, structural lines belonging to crystallographic directions (311) were observed on the X-ray diffraction pattern of ZnO films doped with Al atoms at a scattering angle of $2\theta = 58.23^\circ$ with d-spacing of 0.1574 nm (Fig. 4). Based on the experimental values of these structural lines using equations (1), (2), and (3), parameters of their lattices, full width at half maximum (β), and sizes of crystallites were determined.

The sizes of crystallites and the values of β varied with increasing amounts of Al dopant atoms (as a percentage: 1%, 2%, 3%, 4%, and 5%), specifically 31 nm, 42 nm, 31 nm, 25 nm, and 26 nm. Phase analysis of the experimental results of these reflections indicates that they originated from a phase different from the main phase, specifically from a phase with a cubic elementary cell belonging to space group $Fd\bar{3}m$ and with a lattice constant of 0.5791 nm. This, in turn, indicates the formation of distinct crystallographic nanocrystallites of a specific size and orientation in the (511) order in near-surface defect-prone regions of ZnO films doped with Al (from 1% to 5%).

Additionally, using the results of X-ray structural studies (relative analysis of structural reflections [16]), we determined the chemical composition of the grown films, and their calculated data are presented in Table 1.

Table 1. Proportions of grown film components

Components	Films	ZnO:Al				
	ZnO					
Zn, at%	49.89	29.93	29.47	28.17	27.55	26.52
O, at%	50.11	68.78	68.61	68.49	68.36	68.25
Al, at%	-	1.29	1.92	3.34	4.09	5.23

In accordance with the information provided, the proportion of Al atoms in relation to the total number of atoms in the films was 1.29%, 1.92%, 3.34%, 4.09%, and 5.22%, respectively.

CONCLUSION

Based on the conducted experimental research and analysis of the obtained results, the following conclusions can be drawn:

It has been established that the surface of the borosilicate substrate has a crystallographic orientation of (111) and consists of subcrystallites with a size of 28.6 nm, having a lattice constant as $= 0.3336$ nm, belonging to the space group $Pm\bar{3}m$. Additionally, the presence of polycrystalline regions approximately 20 nm in size at the boundaries between the subcrystallites of the substrate has been detected. Nanovoids with a size of ~ 81.5 nm is observed in its near-surface area, as well as structural fragments of SiO_x with dimensions of ~ 1.2 nm exhibiting amorphous properties.

It has been established that the surface of the grown ZnO films belongs to the crystallographic direction (002) and consists of blocks with dimensions of 39.5 nm, exhibiting a hexagonal crystalline lattice structure of wurtzite with lattice periods $a = b = 0.3265$ nm and $c = 0.5212$ nm, belonging to space group $C6/mmc$. It has also been determined that within the volume and on the surface of the films, self-organized polycrystalline regions of sizes 12.6 nm, 28.3 nm, 30 nm, and 33 nm, as well as nanocrystallites with a size of 56.8 nm, are formed.

It has been identified that Al^{+3} ions replace Zn^{+2} ions in the crystalline lattice forming the ZnO film, leading to a slight increase in the c-axis of the hexagonal crystalline lattice ($\Delta c = 0.0009$ nm), as determined by the slight shift of the main (002) crystallographic lines at small angles ($\Delta\theta = 0.12^\circ$).

ZnO films with Al atom concentrations (from 1% to 5%) exhibit nanocrystallites with a lattice constant of 0.5791 nm, forming in near-surface areas as compounds of ZnO and Al_2O_3 , belonging to the spatial group type $Fd\bar{3}m$.

Conflict of Interests

The authors declare that they have no conflict of interests

Funding

The work was carried out using project funds allocated according to the order of the rector of Andijan State University dated February 7, 2024, No. 04-12.

ORCID

- ©Sirajidin S. Zainabidinov, <https://orcid.org/0000-0003-2943-5844>; ©Shakhriyor Kh. Yulchiev, <https://orcid.org/0009-0007-2576-4276>
©Akramjon Y. Boboev, <https://orcid.org/0000-0002-3963-708X>; ©Bakhtiyor D. Gulomov, <https://orcid.org/0009-0005-8614-6311>
©Nuritdin Y. Yunusaliyev, <https://orcid.org/0000-0003-3766-5420>

REFERENCES

- [1] S. Zainabidinov, S.I. Rembeza, E.S. Rembeza, Sh.Kh. Yulchiev, "Applied Solar Energy," Academic Journal, **55**(1), 5 (2019). <https://doi.org/10.3103/S0003701X19010146>
- [2] Kh. J. Mansurov, A.Y. Boboyev, and J.A. Urinboev, "X-ray structural and photoelectric properties of SnO₂, ZnO, and Zn₂SnO₄ metal oxide films," East European Journal of Physics. (2), 336-340 (2024). <https://doi.org/10.26565/2312-4334-2024-2-39>
- [3] M. Laurenti, S. Stassi, M. Lorenzoni, M. Fontana, G. Canavese, V. Cauda, and C.F. Pirri, "Evaluation of the piezoelectric properties and voltage generation of flexible zinc oxide thin films," Nanotechnology, **26**(21), 1 (2019) <https://doi.org/10.1088/0957-4484/26/21/215704>
- [4] K. Chongsri, and W. Pecharapa, "UV Photodetector Based On Al-Doped ZnO Nanocrystalline Sol-Gel Derived Thin Films" Energy Procedia, **56**, 554–559 (2014). <https://doi.org/10.1016/j.egypro.2014.07.192>
- [5] P. Koralli, S.F. Varol, G. Mousdis, D.E. Mouzakis, Z. Merdan, M. Kompitsas, "Chemosensors. Comparative Studies of Undoped/Al-Doped/In-Doped ZnO Transparent Conducting Oxide Thin Films in Optoelectronic Applications," Chemosensors, **10**(5), 162 (2022). <https://doi.org/10.3390/chemosensors10050162>
- [6] F.I. Alreshedi, and J.E. Krzanowski, "X-ray Diffraction Investigation of Stainless Steel—Nitrogen Thin Films Deposited Using Reactive Sputter Deposition," Coatings, **10**, 984 (2020). <https://doi.org/10.3390/coatings10100984>
- [7] S.Z. Zainabidinov, A.Y. Boboev, and N.Y. Yunusaliyev, "Effect of γ -irradiation on structure and electrophysical properties of S-doped ZnO films," East European Journal of Physics, (2), 321-326 (2024). <https://doi.org/10.26565/2312-4334-2024-2-37>
- [8] S. Zainabidinov, Sh. Yuldashev, A. Boboev, and N. Yunusaliyev, "X-ray diffraction and electron microscopic studies of the ZnO(S) metal oxide films obtained by the ultrasonic spray pyrolysis method," Herald of the Bauman Moscow State Technical University, Series Natural Sciences, **1**(112), 78-92 (2024). <https://doi.org/10.18698/1812-3368-2024-1-78-92>
- [9] S.Z. Zainabidinov, Sh.B. Utamuradova, and A.Y. Boboev, "Structural Peculiarities of the (ZnSe)_{1-x-y}(Ge₂)_x(GaAs_{1- δ} Bi _{δ})_y Solid Solution with Various Nano-inclusions," Journal of Surface Investigation, Synchrotron and neutron techniques, 48-52 (2024). <https://doi.org/10.18698/1812-3368-2024-1-78-92>
- [10] V. Utyaganova, et al., "Controlling the porosity using exponential decay heat input regimes during electron beam wire-feed additive manufacturing of Al-Mg alloy," The International Journal of Advanced Manufacturing Technology, **108**, 2823–2838 (2020). <https://doi.org/10.1007/s00170-020-05539-9>
- [11] B. Parveena, M. Hassan, Z. Khalida, S. Riadz, and S. Naseem "Room-temperature ferromagnetism in Ni-doped TiO₂ diluted magnetic semiconductor thin films," Journal of Applied Research and Technology, JART, **15**(2), 132-139 (2017). <https://doi.org/10.1016/j.jart.2017.01.009>
- [12] L.S. Vasil'ev, I.L. Lomaev, and S.L. Lomaev, "On the Structure Of Segregations At Special Boundaries Of Polycrystalline Substitutional Alloys," Russian Physics Journal, **64**(10), 45-46 (2022). <https://doi.org/10.1007/s11182-022-02532-5>
- [13] M.F. Malek, M.H. Mamat, Z. Khusaimi, M.Z. Sahdan, M.Z. Musa, A.R. Zainun, A.B. Suriani, et al., "Sonicated sol-gel preparation of nanoparticulate ZnO thin films with various deposition speeds: The highly preferred c-axis (0 0 2) orientation enhances the final properties," Journal of Alloys and Compounds, **582**, 12-21(2014) <https://doi.org/10.1016/j.jallcom.2013.07.202>
- [14] V. Bratus, and V. Yukhimchuk, "Structural Transformations and Silicon Nanocrystallite Formation in SiO_x Films," FTP, **35**(7), 854–860 (2001). <https://doi.org/10.63-7826/01/3507-21.00>
- [15] A. Ghazai, E. Salman, and Z. Jabbar, "Effect of Aluminum Doping on Zinc Oxide Thin Film Properties Synthesis by Spin Coating Method," American Scientific Research Journal for Engineering Technology, and Sciences (ASRJETS), **26**(3), 202-203 (2016).
- [16] G. Fetisov, "X-ray diffraction methods for structural diagnostics of materials: progress and achievements," Physics - Uspekhi **63**(1), 2-32 (2020). <https://doi.org/10.3367/ufne.2018.10.038435>

СТРУКТУРНІ ВЛАСТИВОСТІ ПЛІВОК ZnO, ЛЕГОВАНИХ Al

Сіраїдін С. Зайнабідінов^a, Шахрїйор Х. Юльчїєв^b, Акрамжон Ю. Бобоев^{a,c},
Бахтїйор Д. Гуломов^d, Нурїдїн Ю. Юнусалїєв^a

^aАндижанський державний університет імені З.М. Бабура, Андижан, Узбекистан

^bАндижанський державний педагогічний інститут, Андижан, Узбекистан

^cІнститут фізики напівпровідників та мікроелектроніки Національного університету Узбекистану, Ташкент, Узбекистан

^dАндижанський машинобудівний інститут, Андижан, Узбекистан

У даній роботі наведено результати дослідження впливу атомів Al на структурні характеристики плівок ZnO, отриманих золь-гель методом. Встановлено, що скляні підкладки складаються з субкристалітів розміром 28,6 нм, які мають кубічні елементарні комірки з параметрами ґратки $a = 0,3336$ нм, а їх поверхні належать до кристалографічної орієнтації (111). Встановлено, що вирощені тонкі плівки ZnO складаються з субкристалітів розміром 39,5 нм, які мають структуру вюрциту з параметрами решітки $a = b = 0,3265$ нм і $c = 0,5212$ нм відповідно. Встановлено, що на межах поділу цих субкристалітів утворюються полікристалічні області з розмірами 12,6 нм, 28,3 нм, 30 нм і 33 нм. Крім того, нанокристаліти розміром 56,8 нм самоорганізуються на поверхнях нанесених плівок. Збільшення значень осі «с» гексагональної кристалічної ґратки плівок ZnO на 0,0009 нм при легуванні атомів Al від 1% до 5% пояснюється зміщенням основної структурної лінії (002) на малі кути ($\Delta\theta = 0,12^\circ$). Встановлено, що нанокристаліти з параметрами ґратки $a_p = 0,5791$ нм, що належать до просторової групи Fd3m, самоорганізуються на ділянках поверхні плівок ZnO:Al. крива через наявність моноенергетичного рівня швидких поверхневих станів на гетеропереході.

Ключові слова: боросилікатне скло; золь-гель метод; оксид металу; тонка плівка ZnO; рентгенівська дифракція; субкристаліт; нанокристал

THE MECHANISM OF CURRENT TRANSFER IN n-GaAs – p-(ZnSe)_{1-x-y}(Ge₂)_x(GaAs_{1-δ}Bi_δ)_y HETEROSTRUCTURES

✉ Sirajidin S. Zainabidinov^a, ✉ Khotamjon J. Mansurov^a, ✉ Akramjon Y. Boboev^{a,b},
✉ Jakhongir N. Usmonov^a

^aAndijan state university named after Z.M. Babur, Andijan, Uzbekistan

^bInstitute of Semiconductor Physics and Microelectronics at the National University of Uzbekistan,
20 Yangi Almazar st., Tashkent, 100057, Uzbekistan

*Corresponding Author e-mail: aboboevscp@gmail.com

Received June 30, 2024; revised July 25, 2024 accepted August 5, 2024

The I-V characteristics of heterostructures n-GaAs – p-(ZnSe)_{1-x-y}(Ge₂)_x(GaAs_{1-δ}Bi_δ) exhibit a characteristic quadratic law - $J \sim V^2$ I-V curve, followed by a sharp pre-breakdown current growth, which well explains the observed straight branch of the I-V characteristics and this regularity remains unchanged at different temperatures. The analysis of the I-V characteristics of n-GaAs-p-(ZnSe)_{1-x-y}(Ge₂)_x(GaAs_{1-δ}Bi_δ) heterostructures with an extended intermediate solid solution layer shows that the drift mechanism of charge transport predominates under forward bias conditions.

Keywords: Heterostructure; Substrate; Liquid phase epitaxy; Film; Solid solution; Compound; I-V characteristics; Drift mechanism; Charge transport; Temperature

PACS: 78.30.Am

INTRODUCTION

One of the current challenges of today is solving a range of technical problems related to expanding the capabilities of nano- and microelectronic systems and complexes, specifically the ability to simultaneously operate in a wide range of semiconductor device engineering. Although there are currently a large number of studies dedicated to this issue, many questions regarding the mechanisms of how different impurities affect the electrophysical properties of semiconductors and various physical processes occurring in non-equilibrium states are still far from being understood, due to the possibility of doping semiconductors with various impurities (atomic, molecular, isovalent). There is a scarcity of studies dedicated to the investigation of molecular dopants, the behavior of dopants in solid solutions depending on the composition of the base material, and the interaction of dopants in semiconductor materials.

The authors [1] obtained heterojunctions based on the A^{III}B^V-A^{II}B^{VI} compound through isovalent substitution and investigated the characteristics of the physical properties of such structures [2, 3]. The process of obtaining heterojunctions has a diffusion character. As a result of diffusion of isovalent atoms between the substrate and the diffusion heterolayer, a solid solution of variable composition is formed, which smoothes out the lattice parameter and the coefficient of thermal expansion, as well as eliminates the lattice mismatch between the contacting materials. In such structures, effective edge luminescence is achieved due to isovalent dopants. The concentration of isovalent dopants reaches $\sim 10^{19} \text{ cm}^{-3}$, without altering the width of the semiconductor's band gap. Isovalent substitution leads to a "cleaning" effect in the material, meaning that intrinsic defects, such as vacancies, are healed by the dopant atoms, resulting in a reduction in the concentration of non-radiative recombination centers [4].

The authors [5] have investigated monoatomic, triatomic, and cluster doping in the ZnSe - GaAs system using calculations of pseudopotential plane waves. Cluster doping (Zn-Se₄)³⁺ (as a donor) and (Se-Zn₄)³⁻ (as an acceptor) in GaAs, as well as (As-Ga₄)³⁺ (as a donor) and (Ga-As₄)³⁻ (as an acceptor) in ZnSe, will be stable at extremely extreme chemical potentials and will contribute to the introduction of a large number of free carriers. Cluster doping provides a lower level of acceptor or donor than monoatomic or triatomic doping. There is a strong tendency for Ga+As to cluster in ZnSe, compared to Zn+Se in GaAs, leading to an asymmetric dependence of the band gap on the composition of the solid solution. Specifically, the addition of a small amount of Ga+As to ZnSe results in a sharp decrease in the band gap width of the base material, whereas the addition of Zn+Se to GaAs does not significantly change the band gap width. [5].

The aim of this study is to investigate certain electrophysical properties of (ZnSe)_{1-x-y}(Ge₂)_x(GaAs_{1-δ}Bi_δ)_y solid solutions synthesized on silicon substrates using liquid-phase epitaxy.

MATERIALS AND METHODS

Epitaxial layers of n-GaAs – p-(ZnSe)_{1-x-y}(Ge₂)_x(GaAs_{1-δ}Bi_δ)_y were grown by liquid phase epitaxy method as described in reference [6]. Two horizontally positioned substrates – upper and lower – were secured in a vertical graphite cassette. Gallium arsenide substrates, cut from monocrystalline GaAs with a (100) orientation in the form of 20 mm diameter disks and a thickness of $\sim 350 \mu\text{m}$, had n-type conductivity with a carrier concentration of $5 \times 10^{17} \text{ cm}^{-3}$. The crystallization process of the thin film was carried out by forced cooling in a hydrogen atmosphere purified with palladium

from a tin solution melt. The composition of the melt solution was chosen based on data from [7, 8] and initial studies of the GaAs-Ge-ZnSe-Sn system. Samples were grown at various parameters of liquid-phase epitaxy. Films with predetermined physical properties were grown at a temperature range of crystallization of the bismuth-containing melt solution from 750 to 650°C and a substrate cooling rate of 1°C/min. The grown films had p-type conductivity and a thickness of 10 μm.

When investigating the current-voltage characteristics (I-V curves) of semiconductor heterostructures, special attention is given to selecting ohmic contacts. This means that carrier injection does not occur at the contact, and there is a linear relationship between current and voltage for any polarity. In practice, this implies that a contact can be considered ohmic if the voltage drop across it is much lower for any polarity compared to the voltage drop across the rest of the circuit. This is achieved in practice by creating a region of strong doping in the semiconductor between the metal and the bulk of the semiconductor. To obtain ohmic contacts to the heterostructures of n-GaAs – p-(ZnSe)_{1-x-y}(Ge₂)_x(GaAs_{1-δ}Bi_δ)_y, we used Au and Ag. The ohmicity of the obtained contacts was initially assessed on a profilometer, and subsequently verified by measuring the voltage drop and determining their resistance. For the hole conductivity type of semiconductor solid solutions (ZnSe)_{1-x-y}(Ge₂)_x(GaAs_{1-δ}Bi_δ)_y, contacts with the lowest specific resistance and good linearity were achieved by vacuum deposition of Au and Ag on the surface of epitaxial layers followed by annealing at a temperature of 150°C.

RESULTS AND DISCUSSION

To investigate the I-V characteristics of structures obtained by vacuum deposition, ohmic contacts were created - continuous ones on the back side and square-shaped ones, with an area of 6 mm² made of silver, on the side of the epitaxial layer. Volt-ampere characteristics were measured in the forward (when "+" was applied to p-(ZnSe)_{1-x-y}(Ge₂)_x(GaAs_{1-δ}Bi_δ)_y and reverse (when "-" was applied to n-GaAs) directions at various temperatures (Fig. 1).

Figure 1 shows the typical current-voltage characteristics (I-V curves) of multi-component heterostructures n-GaAs - p-(ZnSe)_{1-x-y}(Ge₂)_x(GaAs_{1-δ}Bi_δ). It can be observed that the structure exhibits excellent rectifying properties with a rectification coefficient determined as the ratio of forward current (J_{dir}) to reverse current (J_{rev}). At equal applied voltage values, the rectification coefficient $k = J_{dir}/J_{rev}$ ranges from 2000 to 2500 in the voltage range from 0.1 to 3 V. Additionally, in this voltage range, both in forward and reverse directions, there is no saturation of the current in the I-V characteristics at all temperatures, indicating a low density of surface states at the p-n junction interface [9]. Analysis shows that the I-V characteristics at all temperatures, plotted on a logarithmic scale, fit well to straight lines in the forward bias direction and are described by power-law dependencies of the form $-J = A \cdot V^\alpha$ with different values of the exponent α .

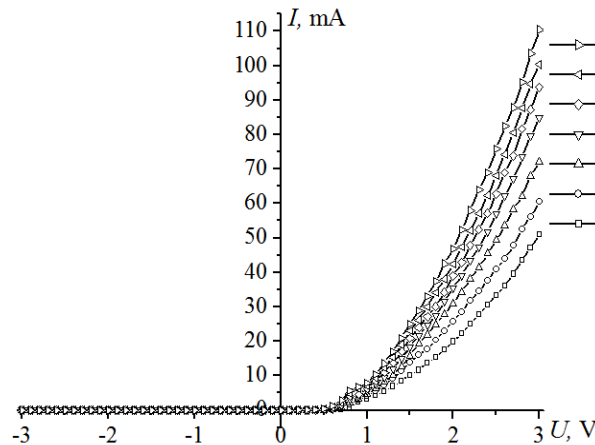


Figure 1. Typical current-voltage characteristics of n-GaAs – p-(ZnSe)_{1-x-y}(Ge₂)_x(GaAs_{1-δ}Bi_δ) heterostructures at various temperatures: 1 – 30°C, 2 – 50°C, 3 – 70°C, 4 – 90°C, 5 – 110°C, 6 – 130°C, 7 – 150°C

On the initial segment of the I-V curve from 0.1 to 0.3 V, a region of a spike is observed: $J \sim V^\alpha$ ($\alpha \approx 2$) (Figure 2). The conducted analysis indicates that such a dependence follows the regularity [10].

$$V = M(J)B_0\sqrt{\frac{J}{2}} \tag{1}$$

where $M(J)$ is calculated according to the following formula:

$$M(J) \approx 1 + 3m \left[2 + C \left(\alpha \tau_i / c_p \right) \sqrt{J} \right]^2, \tag{2}$$

$$m = 2\tau_i N_d V_p^* / 8b(b+1)n_p d,$$

and

$$C = [bn_p / qV_p^* (b + 1)]$$

In these relationships, V_p^* is a parameter determined by the non-ideal nature of the injecting contact [11].

The current-voltage characteristic in the form of (1) is manifested when the recombination velocity in the denominator of this expression has the form [11].

$$u_r = N_r \frac{c_n c_p (pn - n_i^2)}{c_n (n + n_1) + c_p (p + p_1) + \alpha \tau_i pn}, \tag{3}$$

where N_r is the concentration of recombination centers (complexes); n, p - are the concentrations of electrons and holes; n_i - is the intrinsic concentration in the semiconductor; c_n, c_p - are the capture coefficients of electrons and holes; n_1, p_1 - are the equilibrium concentrations of electrons and holes when the Fermi level coincides with the energy level of the impurity (the so-called static Shockley-Read factors); τ_i - is the time that takes into account various electron exchange processes within the recombination complex; α - is a coefficient depending on the type of defect complexes. A similar recombination mode is possible not only in the cases listed above but also in semiconductors with developed recombination-stimulated restructuring of metastable recombination complexes, such as negatively charged acceptor – positively charged dopant ion or positively charged donor - negatively charged vacancy.

At low excitation levels, i.e., $c_n (n + n_1) + c_p (p + p_1) \gg \alpha \tau_i pn$ when the contribution of the last term in the denominator of (3) becomes negligibly small, the recombination rate is described by the Shockley-Read statistics. In this case, the current-voltage characteristic (I-V curve) in drift carrier transport mode has a typical form corresponding to ohmic relaxation of bulk charge [12]:

$$V = \sqrt{\frac{8d^3 J}{9q\mu_p \mu_n \tau_p N_d}} = B_0 \sqrt{J}, \tag{4}$$

the definition was determined as follows.

Initially, the value of B_0 is determined from the slope of the experimental straight line $J = V^\alpha$, which in this case was $B_0 = 0.001 \text{ V} \cdot \text{A}^{(-1/2)}$ at room temperature. Then, using the expression

$$B_0 = \sqrt{\frac{8d^3}{9q\mu_p \mu_n \tau_p N_d}}, \tag{5}$$

using the experimental data for $d = 5 \text{ }\mu\text{m}$ and $\tau_p \approx 10^{-8} \text{ s}$, we find the value of N_d - the concentration of shallow donor impurity centers, which is equal to $1.2 \cdot 10^{15} \text{ cm}^{-3}$. The mobility of the main carriers – holes, determined by the Hall method, was $\mu_p = 300 \text{ cm}^2/\text{V}\cdot\text{s}$, and for estimation, the value of the mobility of minority carriers was taken as $\mu_n = b \cdot \mu_p = 1890 \text{ cm}^2/\text{V}\cdot\text{s}$, where b is the ratio of electron and hole mobilities, which according to our estimates was 6.3 [11].

The value of B_0 increases from $0.001 \text{ V} \cdot \text{A}^{(-1/2)}$ to $0.369 \text{ V} \cdot \text{A}^{(-1/2)}$ with increasing temperature, while the mobility μ_p and the lifetime τ_p of the main carriers, and consequently, the concentration of shallow donor impurity centers N_d , decrease. This apparently suggests that in this solid solution, the predominant role in the mobility mechanism is played by carrier scattering on ions of deep impurities [13].

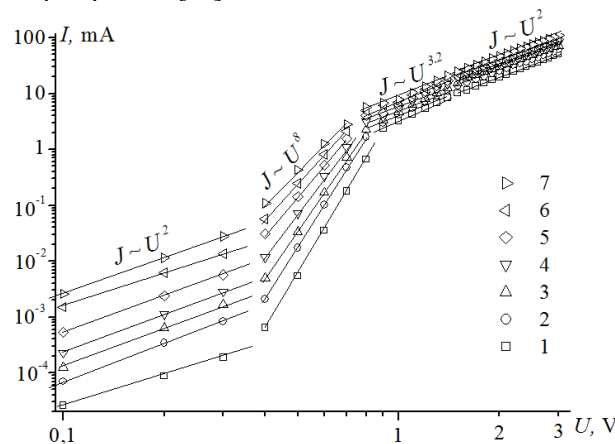


Figure 2. Volt-ampere characteristics of n-GaAs – p-(ZnSe)_{1-x-y}(Ge₂)_x(GaAs_{1-δ}Bi_δ)_y heterostructures in the forward direction in logarithmic scale at different temperatures: 1 – 30°C, 2 – 50°C, 3 – 70°C, 4 – 90°C, 5 – 110°C, 6 – 130°C, 7 – 150°C.

With further increase in voltage, as shown in Figure 2, starting from $V = 0.4 \text{ V}$, there is a sharp increase in the current $J = A \cdot V^\alpha$ with a power exponent $\alpha \approx 8$. This region is called pre-breakdown region. In this case, the third term in

the denominator of expression (3) for the recombination rate becomes significant, and the recombination rate no longer follows the Shockley-Read statistics, but acquires a completely different form [14]:

$$u_r = \frac{N_r}{\tau_i} \left(1 - \frac{2}{\tau_i c_p p} \right), \quad (6)$$

The current-voltage characteristic (I-V curve) –

$$J = \frac{q^2 (b+1)^2 N_r d^3}{\varepsilon \tau_i^2 c_p (V_0 - V)}, \quad (7)$$

where ε is the dielectric constant and

$$V_0 = \sqrt{\frac{q(b+1)N_r d^4}{2\varepsilon \tau_i \mu_p}} = const.$$

From (7), it can be observed that the denominator of this expression decreases with increasing voltage, indicating a rapid growth in current. The sharp increase in current within the voltage range $V = (0.4-0.8)$ V is described by this dependency [13].

According to the theory [15], the range from 0.9 to 1.5 V of the current-voltage characteristic is described by the expression $J = A \cdot V^{3.2}$ (Fig. 2) and occurs when the recombination of non-equilibrium charge carriers mainly occurs with a delay, i.e. with the participation of complexes where electronic exchange takes place inside. In this case, the inequality is realized in the denominator of expression (3)

$$c_n(n + n_1) + c_p(p + p_1) < \alpha \tau_i p n, \quad (8)$$

the analytical expression for I-V (curve) is as follows

$$V = \frac{(b+1)d^2 N_r}{N_d \mu_p \tau_i} + \frac{d}{q \mu_p (b+1)C} \sqrt{J} - \frac{2(b+1)N_r d^2 c_p}{N_d \mu_p \alpha \tau_i C} \frac{1}{\sqrt{J}} = A + B\sqrt{J} - \frac{D}{\sqrt{J}}. \quad (9)$$

Where A , B , and D are parameters dependent on the concentration of ionized atoms of deep impurities, the ratio of electron and hole mobilities, and the thickness of the interlayer transition, respectively, which can be determined from experimental data. To determine parameter A , two experimental points V_1, J_1 and V_2, J_2 are selected on the straight line of the $J \sim V^{3.2}$ dependence. The calculation results indicate that parameter A remains almost unchanged with increasing temperature (Table 1).

This indicates that in the first term of the expression (9), the ratios N_r/τ_i remain unchanged. Next, three experimental points (V_1, J_1) , (V_2, J_2) , (V_3, J_3) were selected to determine the parameters B and D from the section of rapid current growth. The calculation results are presented in Table 1, indicating that as the temperature increases, the parameter D increases while the value of B decreases. This could be a consequence of the increase in parameter “ C ” in equation (3), which is associated with the concentration of holes at the interface between the p-(ZnSe)_{1-x-y}(Ge₂)_x(GaAs_{1- δ} Bi _{δ}) film and the n-(GaAs) substrate, as well as the hole capture coefficients c_p .

Table 1. The values of parameters A , B , and D in expression (9) calculated from experimental I-V characteristics at various temperatures

t, °C	30	50	70	90	110	130	150
$A \cdot V$	0.69	0.7	0.705	0.711	0.717	0.723	0.73
$D \cdot V \cdot \text{mA}^{-1/2}$	1.38	2.12	2.44	2.94	4.16	5.58	7
$B \cdot V \cdot A^{1/2}$	0.0174	0.0156	0.0146	0.0134	0.0131	0.013	0.0128

Analysis has revealed that expression (9) enables describing the slope value of the volt-ampere characteristics of the $J \sim V^\alpha$ type, including the segment of sharp current increase.

After the section of sharp current growth $J \sim V^\alpha$, where $\alpha = 2$ (Fig. 2), when the last term in the denominator of expression (3) starts to play a decisive role and the recombination rate U_r reaches full saturation $U_r = N_r/\tau_i$, a second quadratic section appears and the I-V characteristic is described by the expression [13]:

$$V = \frac{(b+1)d^2 N_r}{2N_d \mu_p \tau_i} + \frac{d}{q \mu_p (b+1)C} \sqrt{J}. \quad (10)$$

The estimation of the value of N_r/τ_i for this segment is carried out similarly to the segment of sharp current growth. For two given experimental points, an equation of the straight line is constructed, from which the value of the constant corresponding to the value of the first term of the expression (10) is determined.

$$\frac{A}{2} = \frac{(b+1)d^2 N_r}{2N_d \mu_p \tau_i}$$

Substituting the known values of d , b , and N_d into (11), we obtain the quantity $N_{r/ti} = 5.2 \cdot 10^{18} \text{ cm}^{-3} \text{ s}^{-1}$

CONCLUSIONS

Thus, single-crystalline solid solutions of n-GaAs – p-(ZnSe)_{1-x-y}(Ge₂)_x(GaAs_{1-δ}Bi_δ)_y p-type conductivity were grown on single-crystalline n-GaAs substrates with (100) orientation by liquid phase epitaxy method. The volt-ampere characteristics of heterostructures n-GaAs – p-(ZnSe)_{1-x-y}(Ge₂)_x(GaAs_{1-δ}Bi_δ) exhibit a characteristic quadratic law $-J \sim V^2$ I-V curve, followed by a sharp pre-breakdown current growth, which well explains the observed straight branch of the I-V curve and this regularity remains unchanged at different temperatures. After the pre-test section, two characteristic sections are observed, which are described by expressions (10) and (11). The analysis of the current-voltage characteristics (I-V curve) of n-GaAs – p-(ZnSe)_{1-x-y}(Ge₂)_x(GaAs_{1-δ}Bi_δ) heterostructures with an extended intermediate solid solution layer shows that the drift mechanism of charge transport predominates under forward bias conditions.

Based on this data, it is possible to assume the successful implementation of the discussed heterostructures in voltage multiplication schemes and in converters (rectifiers) of direct voltage, where high requirements for frequency and time parameters of signals are not imposed, as well as in electronic and thermoelectronic devices.

Conflict of Interests

The authors declare that they have no conflict of interests

Funding

The work was carried out using project funds allocated according to the order of the rector of Andijan State University dated February 7, 2024, No. 04-12.

ORCID

©Sirajidin Z. Zainabidinov, <https://orcid.org/0000-0003-2943-5844>; ©Xhotamjon J. Mansurov, <https://orcid.org/0009-0006-4571-7795>
©Akramjon Y. Boboev, <https://orcid.org/0000-0002-3963-708X>; ©Jakhongir N. Usmonov, <https://orcid.org/0000-0002-7243-4938>

REFERENCES

- [1] V.P. Makhni, M.M. Sletov, and I.V. Tkachenko, "The nature of the green luminescence band in zinc selenide crystals," *Journal of Optical Technology*, **74**(6), 394-396 (2007). <https://doi.org/10.1364/JOT.74.000394>
- [2] V.P. Makhni, M.M. Sletov, and S.V. Khusnutdinov, "Preparation of ZnO Heterolayers on Zinc Chalcogenide Substrates," *Inorganic Materials*, **43**(12) 1304–1306 (2007). <https://doi.org/10.1134/S0020168507120096>
- [3] V.P. Makhniy, M.M. Sletov, and S.V. Khusnutdinov, "Luminescence of zinc oxide layers synthesized on zinc selenide substrates by the isovalent substitution method," *Russian Physics Journal*, **52**(2), 216-217 (2009).
- [4] A. Gangopadhyay, "Investigation of Strain Relaxation Mechanisms and Interfacial Defects in Lattice-mismatched GaAs(001)-based Heterostructures," PhD Thesis, Arizona State University, May 2021, pp.136.
- [5] L.G. Wang, and A.Z. Dilute, "Dilute nonisovalent (II-VI)-(III-V) semiconductor alloys: Monodoping, codoping, and cluster doping in ZnSe-GaAs," *Physical Review B*, **68**, 125211 (2003). <https://doi.org/10.1103/PhysRevB.68.125211>
- [6] A.Y. Boboev, "Structural features, electrophysical and photoelectric properties of n- (GaAs)-p-GaAs)_{1-x-y}(Ge₂)_x(ZnSe)_y heterostructures," PhD Thesis, Tashkent, IFPM, 2019, 128 p.
- [7] S. Zainabidinov, Sh. Utamuradova, and A. Boboev. "Structural Peculiarities of the (ZnSe)_{1-x-y}(Ge₂)_x(GaAs_{1-δ}Bi_δ)_y Solid Solution with Various Nano-inclusions," *Journal of Surface Investigation X-ray Synchrotron and Neutron Techniques*, **16**(6), 1130-1134 (2022). <https://doi.org/10.1134/S1027451022060593>
- [8] S. Zaynabidinov, A. Saidov, A. Boboev, and D. Abdurahimov, "Structure, Morphology and Photoelectric Properties of n-GaAs-p-(GaAs)_{1-x}(Ge₂)_x Heterostructure," *Herald of the Bauman Moscow State Technical University, Series Natural Sciences*, **100**(1), 72-87 (2022). <https://doi.org/10.18698/1812-3368-2022-1-72-87>
- [9] O.O. Mamatkarimov, O. Himmatkulov, and I.G. Tursunov, "Effect of Uniaxial Elastic Deformation on the Current–Voltage Characteristic of Surface-Barrier Sb–p-Si(Mn)–Au Diodes," *Semiconductors*, **54**(5), 563–566 (2020). <https://doi.org/10.1134/S1063782620050085>
- [10] A.S. Saidov, A.Yu. Leiderman, Sh.N. Usmonova, and U.P. Asatova, "Peculiarities of the Current–Voltage Characteristic of n-GaP–p-(InSb)_{1-x}(Sn₂)_x Heterostructures," *Technical Physics Letters*, **46**(11), 1124–1127 (2020). <https://doi.org/10.1134/S1063785020110279>
- [11] A.Yu. Leiderman, and M.K. Minbaev, "A mechanism of rapid growth of direct in semiconductor diode structures," *FTP*, **30**(10), 1729-1738 (1996). (in Russian)
- [12] Sh.A. Mirsagatov, A.Yu. Leiderman, and O.K. Ataboev. "Mechanism of Charge Transfer in Injection Photodiodes Based on the In–n+CdS–nCdS_xTe_{1-x}–pZn_xCd_{1-x}Te–Mo Structure," *Physics of the Solid State*, **55**(8), 1635–1646 (2013). <https://doi.org/10.1134/S1063783413080192>
- [13] A.Yu. Leiderman, and P.M. Karageorgiy-Alkalaev, "On the theory of sublinear current-voltage characteristics of semiconductor structures," *Solid State Communications*, **25**(10), 781-783 (1978). [https://doi.org/10.1016/0038-1098\(78\)90239-9](https://doi.org/10.1016/0038-1098(78)90239-9)
- [14] P.M. Karageorgiy-Alkalaev, and A.Yu. Leiderman, "Statistics of Inter-Impurity Recombination of Electrons and Holes in Semiconductors," *Physica status solidi (b)*, **26**(2), 419-428 (1968). <https://doi.org/10.1002/pssb.19680260204>
- [15] A.Yu. Leiderman. "Possible Influence of Nonequilibrium Carrier Recombination Rate Saturation on Photocell Operation," *Applied Solar Energy*, **44**(2), 79–81 (2008). <https://doi.org/10.3103/S0003701X08020035>

МЕХАНІЗМ ПЕРЕДАЧІ СТРУМУ В ГЕТЕРОСТРУКТУРАХ $n\text{-GaAs-p}(\text{ZnSe})_{1-x-y}(\text{Ge}_2)_x(\text{GaAs}_{1-\delta}\text{Bi}_\delta)$
Сіражідін С. Зайнабідінов^a, Хотамжон Дж. Мансуров^a, Акрамжон Ю. Бобоєв^{a,b}, Джахонгір Н. Усмонов^a

^aАндижанський державний університет імені З.М. Бабур, Андижан, Узбекистан

^bІнститут фізики напівпровідників та мікроелектроніки Національного університету Узбекистану,
100057, Ташкент, Узбекистан, вул. Янги Алмазар, 20

Вольт-амперні характеристики (ВАХ) гетероструктур $n\text{-GaAs-p}(\text{ZnSe})_{1-x-y}(\text{Ge}_2)_x(\text{GaAs}_{1-\delta}\text{Bi}_\delta)$ демонструють характерний квадратичний закон – ВАХ $J \sim V^2$ з різким зростанням передпробірного струму, що добре пояснює спостережувану пряму гілку ВАХ, і ця закономірність залишається незмінною при різних температурах. Аналіз ВАХ гетероструктур $n\text{-GaAs-p}(\text{ZnSe})_{1-x-y}(\text{Ge}_2)_x(\text{GaAs}_{1-\delta}\text{Bi}_\delta)$ з протяжним проміжним шаром твердого розчину показує, що при прямому зміщенні переважає дрейфовий механізм переносу заряду.

Ключові слова: гетероструктура; підкладка; рідкофазна епітаксія; плівка; твердий розчин; з'єднання; ВАХ; дрейфовий механізм; зарядний транспорт; температура

AN OPTIMIZED ULTRASONIC SPRAY PYROLYSIS DEVICE FOR THE PRODUCTION OF METAL OXIDE FILMS AND THEIR MORFOLOGY

✉ Sirajidin S. Zainabidinov^a, ✉ Akramjon Y. Boboev^{a,b}, ✉ Nuritdin Y. Yunusaliyev^a,
✉ Jakhongir N. Usmonov^a

^aAndijan State University named after Z.M. Babur, Andijan, Uzbekistan

^bInstitute of Semiconductor Physics and Microelectronics, National University of Uzbekistan, Tashkent, Uzbekistan

*Corresponding Author e-mail: aboboevscp@gmail.com

Received June 30, 2024; revised July 27, 2024; accepted August 1, 2024

In this work, we developed an optimized ultrasonic spray pyrolysis device for obtaining metal oxide films. The key benefit of this facility lies in its cost-effectiveness and its ability to consistently coat extensive surfaces without sacrificing the integrity of the semi-conductive films, thus streamlining the manufacturing process of semiconductor films. The resulting films exhibit the following attributes: the thickness of the deposited layer is approximately 400 nm, while the diameters of ZnO_{1-x}S_x nanocrystals range from 50 to 200 nm, oriented perpendicular to the crystallographic orientation (111). In the production of nanorods, the average height is estimated to be approximately 30-50 nm, with a density of $2.9 \times 10^{11} \text{ cm}^{-2}$ being indicated.

Keywords: Film; Space group; Subcrystal; Nanocrystal; Quantum size effect; Lattice parameter; Transparent electronics; Band gap
PACS: 78.30.Am

1. INTRODUCTION

Currently, wide-bandgap semiconductors such as zinc oxide (ZnO) and gallium nitride (GaN) are considered the most promising basic materials for the development of optoelectronic devices with predominant emission in the blue and ultraviolet spectral ranges. The bandgap energies (at 300 K) of $E_g \sim 3.37 \text{ eV}$ and 3.39 eV for ZnO and GaN, respectively, make them suitable for such applications [1,2]. GaN-based structures are already widely used for light sources (semiconductor light-emitting diodes and lasers) in the blue and ultraviolet regions of the optical spectrum. However, ZnO appears to be an equally promising semiconductor material for use in light-emitting devices as gallium nitride. It is known that ultraviolet emission in ZnO is due to excitonic recombination [3]. In the case of exciton photogeneration, ZnO allows for very low threshold power of optical pumping at 24 kW/cm^2 . For comparison, excitons in gallium nitride are thermally unstable at room temperature ($E_{exc.}, \text{ GaN} = 25 \text{ meV}$), and forced emission in the edge region is usually obtained through the recombination of electron-hole plasma, which results in significant threshold power values of optical pumping at 1.2 MW/cm^2 (almost 2 orders of magnitude higher than in ZnO), and as a result, the need to use micrometer-sized laser resonators. This is precisely why, in order to increase the exciton binding energy and reduce the generation threshold in the creation of semiconductor lasers and LEDs based on GaN (the main material for producing semiconductors in the short-wavelength range), more complex and expensive structures with quantum wells are used.

An important advantage of using ZnO structures is their low cost, as zinc makes up 0.1% of the Earth's crust, and the much lower toxicity of zinc compared to many other materials used in the semiconductor industry. The potential of using ZnO-based structures also lies in the possibility of expanding the optical emission range using solid solutions based on ZnO, such as ZnMgO and ZnCdO, etc. [4-5].

In this study, zinc oxide films were obtained using the ultrasonic spray pyrolysis method, and the optimal conditions of the technology were determined.

The conventional method of pulverization followed by pyrolysis has long been known and widely used. In this particular technique, the combination of pulverization with ultrasonic atomization, with the appropriate selection of synthesis conditions, substrate materials, and reagent concentrations, ensures the formation of ZnO films with acceptor-type doping [6-8]. Therefore, the most promising approaches currently considered are - the synthesis or doping of zinc oxide under significantly non-equilibrium conditions; annealing under a substance film with inadequate solubility of compound components; and annealing of crystals in an atmosphere of atomic halogen. In this case, to a certain extent, all three of these approaches are implemented. For example, during the pyrolysis of ultra-thin films of zinc nitrate and/or acetate solutions on the substrate surface, significantly non-equilibrium thermodynamic conditions arise, leading among other things to the formation of atomic oxygen and sulfur, as well as groups O-S, Zn-O-S, etc., aligning in the growing film. By using (selecting) substrates with different solubilities (or different diffusion coefficients) of ZnO and S atoms, it is possible, during post-annealing, to control the relative (and absolute) rates of "healing" of various defects. In this case, to a certain extent, all three of these approaches are implemented. For example, during the pyrolysis of ultra-thin films of zinc nitrate and/or acetate solutions on the substrate surface [9], significantly non-equilibrium thermodynamic conditions arise, leading among other things to the formation of atomic oxygen and sulfur, as well as O-S, Zn-O-S, and so on, groups that are arranged in the growing film. By using (selecting) substrates with different solubility (or different diffusion

coefficients) of ZnO and S atoms, it is possible, during the post-annealing process, to control the relative (and absolute) rates of "healing" of different defects.

2. DESCRIPTION OF AN OPTIMIZED ULTRASONIC SPRAY PYROLYSIS DEVICE

To verify the production of p-type ZnO, an ultrasonic setup was created for the synthesis of ZnO, as schematically shown in (Figure. 1). The setup consisted of an ultrasonic generator (1), evaporator (2), cylindrical quartz glass (3), double-layer cooling flask (4), additional liquid inlet pipe (5), gas inlet pipe (6), pump (7), gas outlet pipe (8), substrate (9), valve (for pump control) (10), valve (for pyrolysis time control) (11), tube clamp (12), stand with scale (for adjusting the distance between the spray head and the substrate) (13), heating platform (14), ring tube with holes at equal distances (15), water-filled container for filtration (16), thermocouple (17), glass transparent cover (18), cylindrical hollow body (19). Additionally, Figure 2 shows the diagram of the cylindrical hollow body device, where the water storage volume (20), spray head (21), and liquid outlet tube (22) are located.

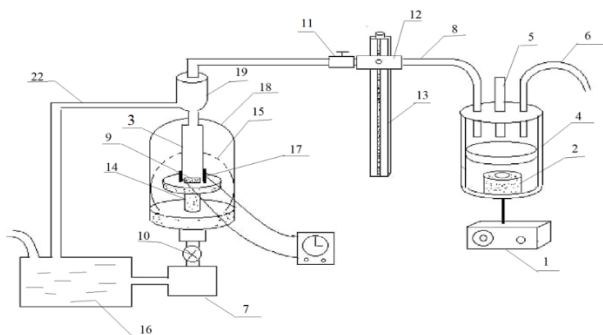


Figure 1. Optimized ultrasonic spray pyrolysis device for the production of metal oxide films

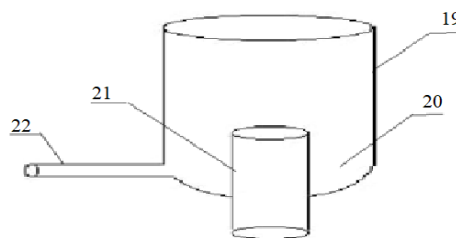


Figure 2 Diagram of the structure of a cylindrical hollow body

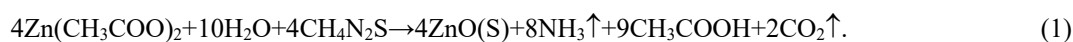
The ultrasonic generator emits a high-frequency pulse and sends it to the evaporator (ceramic or quartz piezoelectric material). As a result, the vibration is transmitted to the liquid (water) in the two-layer cooling flask. Upon the supply of the necessary chemical precursor through the additional outlet pipe (5) for the liquid into the two-layer cooling flask (4), the evaporation of the chemical precursor will begin. The pump (7) pulls the gas through the outlet pipe (8) to the substrate (9) from the vapor formed in the two-layer cooling flask (4) and the air passing through the gas inlet pipe (6) by means of a ring pipe with holes at equal distances (15). The captured air and chemical precursor vapors enter the cylindrical hollow housing (19) until they reach the substrate.

Through the use of a spray head (21), clean vapors are directed onto the substrate (9), while excess liquid, which negatively impacts the quality of the film, is collected in a water storage volume (20). The liquid collected in the water storage volume (20) is transferred through a liquid discharge pipe (22) into a container filled with water for filtration (16), where excess gases are also directed through a ring pipe with evenly spaced holes (15). Adjustments to the pump's (7) thrust force are made using a crane (10), while the dwell time and coating level are regulated with an additional valve (11). The distance between the substrate and the spray head is adjusted by vertically moving the gas exhaust pipe (8) on a stand with a scale (13), which is secured by a clamp (12). The substrate (9) and the vapors near it are heated by a heating platform (14). The necessary vapor is deposited as a layer on the substrate (9). Temperature is monitored and regulated by a thermocouple (17). The presence of a transparent glass cover (18) ensures that the process takes place in enclosed conditions.

Zinc acetate aqueous solutions were used as precursors for the deposition of ZnO films. To conduct doping, fatty elements were added to the zinc acetate aqueous solutions in the corresponding concentration, such as thiourea to obtain p-type conductivity ZnO or ammonium acetate to obtain n-type conductivity [10-12]. As a result of ultrasonic treatment of these solutions, the transition of the liquid to vapor occurred without significant heating of the liquid. The vapor formed as a result of ultrasonic treatment was deposited onto the substrate.

The substrate was heated to temperatures sufficient for the thermal decomposition of precursors, and on its surface, deposition occurred with the formation of ZnO film.

The formulas (1) represent the chemical reactions occurring during the synthesis of films:



3. MORPHOLOGY OF METAL OXIDE FILMS BY SPRAY PYROLYSIS DEVICE

To investigate the surface relief of ZnO_{1-x}S_x thin films, an atomic force microscope (AFM) "Solver-NEXT" SPM 9700HT (Shimadzu) was used. It is known that when calculating the profile obtained by the AFM method, the maximum depth of probe deviation is taken as zero. When studying a system with a low density of islands and a small filling coefficient of the heterostructure material, there is a high probability of the probe hitting the film surface and, therefore,

the correct choice of the zero level. The ratio of the average coating thickness calculated from the obtained AFM profile to the thickness measured in the experiment can be taken as a criterion for the correctness of determining the zero point. If the ratio is below one, it indicates the presence of a continuous sublayer with the zero-point positioned on it. Conversely, if the ratio exceeds one, there is an absence of a continuous sublayer, and the probable cause for this inconsistency lies in the unique characteristics of the AFM technique when assessing height differentials. While the height of a distinct protrusion on a level surface is ascertained with utmost precision, the depth of a minor crevice between islands is subject to considerable error due to the relatively large tip diameter and the occurrence of lateral flows around its edges.

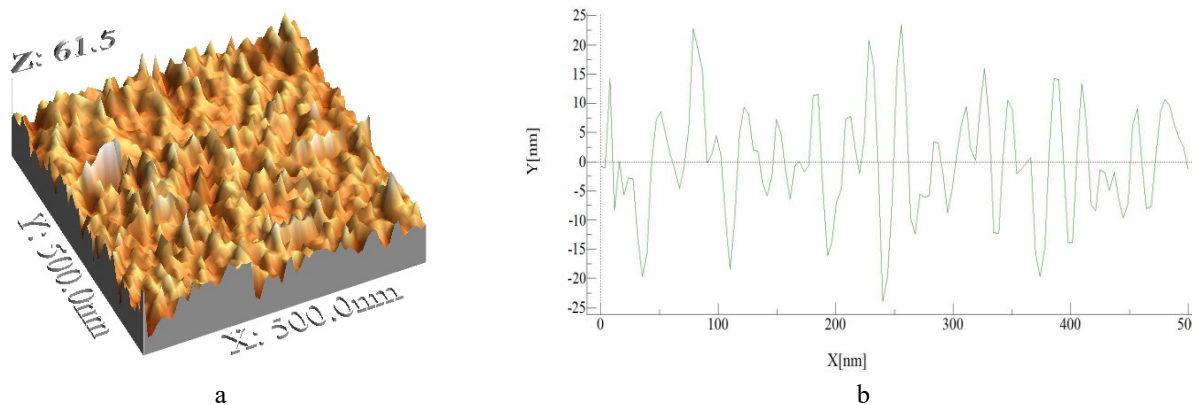


Figure 3. Topography and surface relief of metal oxide films ZnO_{1-x}S_x: a - 3D surface image and b - profile along the selected direction.

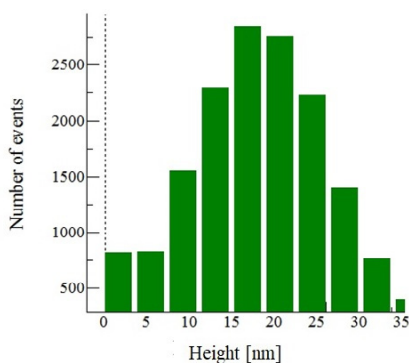


Figure 4. Distribution of islands by height in the array of nanoislands of ZnO_{1-x}S_x films.

Figure 3 illustrates three-dimensional (a) and one-dimensional (b) AFM images of nanostructures formation during the deposition process with an average height of nanostructures ranging from 30 to 50 nm. In Figure 3a, it can be observed that the film surface consists of an array of nanoislands, and the height distribution profile along the direction indicated by the line in Figure 3 is shown in Figure 4.

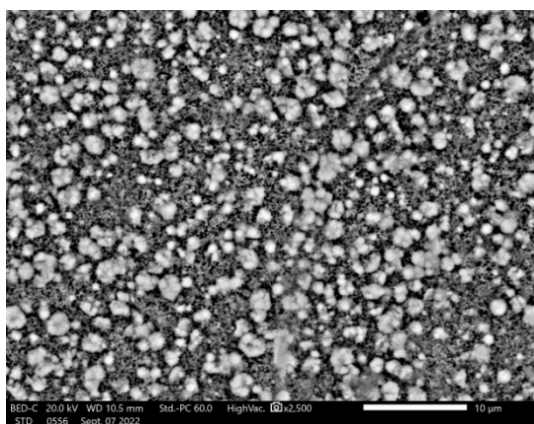


Figure 5. SEM image of the surface of the synthesized ZnO_{1-x}S_x films

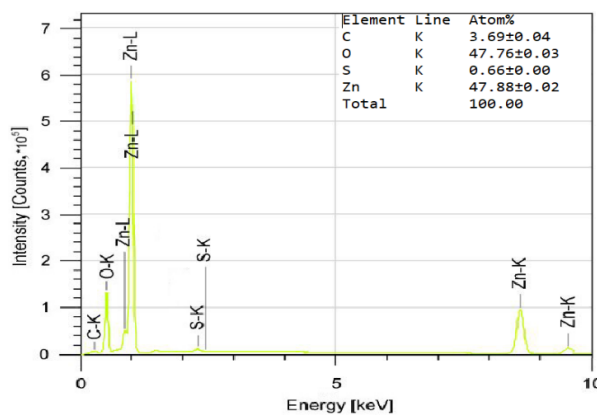


Figure 6. Energy dispersive spectroscopy (EDS) image of the synthesized ZnO_{1-x}S_x films

The distribution of nanoislands presented in Figure 4 reveals that approximately half of the nanostructures have heights ranging from 15 to 25 nm, indicating a significant uniformity of the islands. Furthermore, from the experimental results of the AFM studies, the average density of nanoislands was determined to be $2.9 \times 10^{11} \text{ cm}^{-2}$.

The relief and energy dispersive X-ray spectra (EDS) of the obtained $\text{ZnO}_{1-x}\text{S}_x$ metal oxide layers were investigated using scanning electron microscopy (SEM), JSM-IT200 (JEOL).

Figure 5 illustrates the SEM image of the surface of the obtained $\text{ZnO}_{1-x}\text{S}_x$ films. It is evident that the deposition of the films on Si results in the formation of densely packed nanocrystals of $\text{ZnO}_{1-x}\text{S}_x$ with various geometric shapes and sizes, possibly belonging to the F43m space group. The thickness of the grown layer is 400 nm, and the diameter of $\text{ZnO}_{1-x}\text{S}_x$ ZnO nanocrystals ranges from 50 to 200 nm. They grow perpendicular to the substrate along the z-axis, and the obtained ZnO films are highly ordered with a high degree of perfection (Fig. 5). The energy dispersive spectroscopy view of the film is presented in Fig. 6. From the analysis of these data, the atomic content of Zn, O, S, and C depending on the thickness of the obtained film has been determined. These show that the atomic content of Zn, O, S, and C has distributions in the following relative magnitudes of 0.4989, 0.4543, 0.0366, and 0.0101 in the near-surface region of the film, respectively.

4. CONCLUSIONS

Consequently, we have successfully fabricated thin films of zinc oxide doped with acceptor impurities consisting of cerium atoms on silicon substrates using the ultrasonic spray pyrolysis method. An advantage of this approach is its cost-effectiveness and the potential for a homogeneous deposition of semiconductor films across large areas without compromising quality, thereby facilitating the future utilization of this technique in semiconductor manufacturing. Atomic force microscopy studies of the metal-cased films showed that during the formation of nanoislands with an average height of about 30–50 nm and densities of $2.9 \times 10^{11} \text{ cm}^{-2}$. SEM data indicate that the thickness of the grown layer is approximately 400 nm, and the diameter of $\text{ZnO}_{1-x}\text{S}_x$ nanocrystals ranges from 50 to 200 nm, growing perpendicular to the substrate along the z-axis with a crystallographic orientation of (111). It has been determined that the atomic content of Zn, O, S, and C has distributions in the following relative magnitudes of 0.4989, 0.4543, 0.0366, and 0.0101 in the near-surface region of the film.

Conflict of Interests

The authors declare that they have no conflict of interests

Funding

The work was carried out using project funds allocated according to the order of the rector of Andijan State University dated February 7, 2024, No. 04-12.

ORCID

©Sirajidin S. Zainabidinov, <https://orcid.org/0000-0003-2943-5844>; ©A.Y. Boboev, <https://orcid.org/0000-0002-3963-708X>
©Nuritdin Y. Yunusaliyev, <https://orcid.org/0000-0003-3766-5420>; ©Jakhongir N. Usmonov, <https://orcid.org/0000-0002-7243-4938>

REFERENCES

- [1] S. Nandi, S. Kumar, and A. Misra, "Zinc oxide heterostructures: advances in devices from self-powered photodetectors to self-charging supercapacitors," *Mater. Adv.* **2**, 6768-6799 (2021). <https://doi.org/10.1039/D1MA00670C>
- [2] V. Karpyna *et al.*, "Zinc oxide – analogue of GaN with new perspective possibilities," *Cryst. Res. Technol.* **39**(11), 980-992 (2004). <https://doi.org/10.1002/crat.200310283>
- [3] P. Ščajev, and D. Gogova, "Long-lived excitons in thermally annealed hydrothermal ZnO," *Heliyon*, **10**(4), e26049 (2024). <https://doi.org/10.1016/j.heliyon.2024.e26049>
- [4] I. Ayoub, *et al.*, "Advances in ZnO: Manipulation of defects for enhancing their technological potentials," *Nanotechnology Reviews*, **11**(1), 575-619 (2022). <https://doi.org/10.1515/ntrev-2022-0035>
- [5] Sh.U. Yuldashev, R.A. Nusretov, I.V. Khvan, V.Sh. Yalishev, and T.W. Kang, "White light emission from ZnO/Zn_{0.9}Mg_{0.1}O heterostructures grown on Si substrates," *Japan. Appl. Phys.* **47**(17), 133-135 (2008). <https://doi.org/10.1143/JJAP.47.133>
- [6] S. Zaynabidinov, Sh. Yuldashev, A. Boboev, and N. Yunusaliyev, "X-ray diffraction and electron microscopic studies of the ZnO(S) metal oxide films obtained by the ultrasonic spray pyrolysis method," *Herald of the Bauman Moscow State Technical University, Series Natural Sciences*, **1**(112), 78-92 (2024). <https://doi.org/10.18698/1812-3368-2024-1-78-92>
- [7] J.M. Bian, X.M. Li, C.Y. Zhang, W.D. Yu, and X.D. Gao, "p-type ZnO films by monodoping of nitrogen and ZnO-based p-n homojunctions," *Appl. Phys. Lett.* **85**, 4070-4072 (2004). <https://doi.org/10.1063/1.1808229>
- [8] Y. Ryu, *et al.*, "Synthesis of p-type ZnO films," *Journal of Crystal Growth*, **216**(1), 330-334 (2000). [http://dx.doi.org/10.1016/S0022-0248\(00\)00437-1](http://dx.doi.org/10.1016/S0022-0248(00)00437-1)
- [9] K. Salima, and W. Azzaoui, "Physical properties of spray pyrolysed ZnO thin films obtained from nitrate, acetate and chloride precursors: Comparative study for Solar Cell Applications," *Revista Mexicana de Fisica*, **69**, 031002 (2023). <https://doi.org/10.31349/RevMexFis.69.031002>
- [10] R. Kumar, M. Sekhar, Raghvendra, R. Laha, and S. Pandey, "Comparative studies of ZnO thin films grown by electron beam evaporation, pulsed laser and RF sputtering technique for optoelectronics applications," *Applied Physics*, **126**, 859 (2020). <https://doi.org/10.1007/s00339-020-04046-8>
- [11] S.Z. Zaynabidinov, A.Y. Boboev, and N.Y. Yunusaliyev, "Effect of γ -irradiation on structure and electrophysical properties of S-doped ZnO films," *East European Journal of Physics*, (2), 321-326 (2024). <https://doi.org/10.26565/2312-4334-2024-2-37>
- [12] E. Ahmed, M. Samy, and L. Saad "Highly Conductive N-type Aluminum Doped Zinc Oxide for CZTS Kieserite Solar Cell," *Egypt. J. Chem.* **67**(4), 309-313 (2024). <https://doi.org/10.21608/ejchem.2023.241700.8724>

ОПТИМІЗОВАНИЙ ПРИСТРІЙ УЛЬТРАЗВУКОВОГО СПРЕЙ-ПІРОЛІЗУ ДЛЯ ВИРОБНИЦТВА МЕТАЛОКСИДНИХ ПЛІВОК ТА ЇХ МОРФОЛОГІЯ

Сіражідін С. Зайнабідінов^a, Акрамжон Ю. Бобосєв^{a,b}, Нурітдін Ю. Юнусалієв^a, Джахонгір Н. Усмонов^a

^aАндижанський державний університет імені З.М. Бабура, Андижан, Узбекистан

^bІнститут фізики напівпровідників та мікроелектроніки Національного університету Узбекистану, Ташкент, Узбекистан

У цій роботі ми розробили оптимізоване пристрій ультразвукового розпилувального піролізу для отримання плівок оксидів металів. Ключова перевага цього обладнання полягає в його економічній ефективності та здатності послідовно покривати великі поверхні без шкоди для цілісності напівпровідникових плівок, таким чином оптимізуючи процес виробництва напівпровідникових плівок. Отримані плівки демонструють такі властивості: товщина нанесеного шару становить приблизно 400 нм, тоді як діаметр нанокристалів ZnO_{1-x}S_x коливається від 50 до 200 нм, орієнтованих перпендикулярно до кристалографічної орієнтації (111). Під час виробництва нанострижнів середня висота оцінюється приблизно в 30-50 нм із зазначеною щільністю $2,9 \times 10^{11}$ см⁻².

Ключові слова: плівка; просторова група; субкристал; нанокристал; ефект квантового розміру; параметр решітки; прозора електроніка; щільна

PHOTOELECTRIC CHARACTERISTICS OF THE HETEROJUNCTION $n\text{-GaAs-p-(GaAs)}_{1-x-y}\text{(Ge}_2\text{)}_x\text{(ZnSe)}_y$

 Akramjon Y. Boboev^{a,b}

^aAndijan state university named after Z.M. Babur, Andijan, Uzbekistan

^bInstitute of Semiconductor Physics and Microelectronics at the National University of Uzbekistan,
20 Yangi Almazar st., Tashkent, 100057, Uzbekistan

Corresponding Author e-mail: e-mail: aboboevscp@gmail.com

Received April 18, 2024; revised June 29, 2024; accepted July 3, 2024

The photoelectric properties of $n\text{-GaAs-p-(GaAs)}_{1-x-y}\text{(Ge}_2\text{)}_x\text{(ZnSe)}_y$ heterostructures have been investigated both in photodiode and photovoltaic modes. It has been revealed that the spectral dependence of the photocurrent covers a wide range of energy intervals, ranging from 1.07 eV to 3 eV. It has been demonstrated that as the temperature of the crystallization onset (T_{oc}) increases, the peaks of the spectral dependencies of the photoelectromotive force (photo-EMF) shift towards shorter wavelengths. It has been observed that as the crystallization onset temperature (T_{oc}) of the solid solution layer $(\text{GaAs})_{1-x-y}\text{(Ge}_2\text{)}_x\text{(ZnSe)}_y$ increases, the lifetime of photo carriers increases from 10^{-7} s at $T_{oc}=650^\circ\text{C}$ to $5 \cdot 10^{-5}$ s at $T_{oc}=730^\circ\text{C}$. It is demonstrated that the peaks of the intrinsic photoluminescence band shift towards shorter wavelengths with an increase in the temperature of the crystallization onset. Additionally, the study of the intrinsic spectral region of photoluminescence in samples across the thickness of the epitaxial layer confirms the variability of the obtained structures.

Keywords: Solid solution; Heterostructure; Temperature; Photoelectric property; Photo-EM; Photoluminescence; Photo carriers; Varizon structure

PACS: 73.40. Lq, 78.20. -e, 81.05. Hd

INTRODUCTION

Semiconductors A^3B^5 and A^2B^6 are well known as promising materials for creating optoelectronic devices in the infrared and visible spectrums. Intensive research is being carried out to create various electronic devices based on GaP, GaAs, CdTe, ZnSe and their solid solutions [1-4]. Among these materials, GaAs-based compounds are of particular interest, as their electron and hole mobilities are much higher [5-9], thus enabling them to be used in high-speed optoelectronic devices. In addition, solid substitution solutions $(\text{GaAs})_{1-x-y}\text{(Ge}_2\text{)}_x\text{(ZnSe)}_y$ make it possible to expand the spectral range of functioning of structures based on them to 400 nm [10, 11]. However, the mass use of device structures made on the basis of the A^3B^5 compound is limited, on the one hand, by the economic inexpediency of large-scale use of such device structures, and on the other hand, by insufficient knowledge of the photoelectric properties of such materials and heterojunctions based on them.

In this regard, this work reports the results of studies of some photoelectric properties of the $n\text{-GaAs-p-(GaAs)}_{1-x-y}\text{(Ge}_2\text{)}_x\text{(ZnSe)}_y$ heterojunction, which was synthesized by growing epitaxial layers from solid solutions $(\text{GaAs})_{1-x-y}\text{(Ge}_2\text{)}_x\text{(ZnSe)}_y$ on an $n\text{-GaAs}$ substrate oriented in the (100) direction.

MATERIALS AND METHODS

The growth processes of epitaxial layers were carried out from a limited volume of tin solution-melt on a GaAs substrate using forced cooling method. The thicknesses of the resulting films varied within 10-15 μm depending on the size of the gap between the substrates and the growth mode. X-ray diffraction patterns of layers $(\text{GaAs})_{1-x-y}\text{(Ge}_2\text{)}_x\text{(ZnSe)}_y$, taken on a third-generation diffractometer of the Emyrean Malvern PANalytical L.T.D type, confirmed that the grown layers have a sphalerite crystal lattice and are characterized by the lowest mechanical stresses, both in volume and near the interface of the layers.

The lux-volt characteristics were measured on a setup that can simulate sunlight. A 150 W tungsten incandescent lamp was used as the radiation source. The illuminance measurements were conducted using a digital illuminance meter, MASTKCH LUXMETER MS6610.

An investigation was conducted to analyze the spectral sensitivity of the samples by employing an optical spectrometer that featured a CARLZEISJENA mirror monochromator with quartz optics. This sophisticated setup allowed for the examination of the samples within the photon energy range of 1 to 3 eV.

The photoluminescence spectrum of the samples was studied at the KSVU-23 installation. Optical pumping of the surface of the epitaxial layer at a temperature of 300 K was carried out by a mercury lamp, the signal was recorded on the SDL-2 installation.

RESULTS AND DISCUSSION

The surfaces of the epitaxial layers of $(\text{GaAs})_{1-x-y}\text{(Ge}_2\text{)}_x\text{(ZnSe)}_y$ solid solutions had p- type conductivity with Hall carrier concentrations $p=5 \cdot 10^{17} \text{ sm}^{-3}$. The literature highlights that the ZnSe epitaxial layer typically exhibits n-type

conductivity as a result of the self-compensation effect under standard conditions [12]. We successfully produced epitaxial films containing the chemical composition $(\text{GaAs})_{1-x-y}(\text{Ge}_2)_x(\text{ZnSe})_y$ that exhibited p-type conductivity. Based on quantum chemical concepts, the possibility of increasing the binding energy of selenium in the composition of the Se-Ge dumbbell structure located at the nodes of the crystal lattice of the $(\text{GaAs})_{1-x-y}(\text{Ge}_2)_x(\text{ZnSe})_y$ solid solution compared with the nodal position in the crystalline ZnSe lattice. This can lead to a significant reduction in the number of V_{Se} vacancies, which usually lead to the appearance of electronic conductivity in ZnSe. In addition, part of the vacancies in the selenium V_{Se} sublattice in solid solutions can be occupied by Ge atoms, which also leads to a decrease in the number of V_{Se} vacancies. It is assumed that the appearance of epitaxy layers of a solid solution of the $(\text{GaAs})_{1-x-y}(\text{Ge}_2)_x(\text{ZnSe})_y$ type during the formation of the $n\text{-GaAs-p-(GaAs)}_{1-x-y}(\text{Ge}_2)_x(\text{ZnSe})_y$ heterostructure is associated with partial dissolution GaAs substrates.

The photovoltaic properties of the obtained structures were studied by both photovoltaic and photodiode methods at a temperature of 300K. The surface was illuminated from the side of the solid solution. The lux-ampere characteristics of the structures, obtained under integral light illumination, have shown that the dependence of the short-circuit current (I_{sc}) on the illuminance exhibits a nonlinear relationship in the initial region. In other words, an increase in the incident light intensity leads to a wave-like increase in I_{sc} . This phenomenon may be attributed to changes in the parameters of the contacting semiconductors under the influence of the light flux, such as the lifetime of non-majority charge carriers and the diffusion length (Fig. 1). With increasing intensity of the incident light, the open-circuit EMF tended to saturate, reaching a value of 0.6 V, which may be due to the impossibility of reducing the thickness of the transition layer between the epitaxial film and the substrate under the influence of incident light.

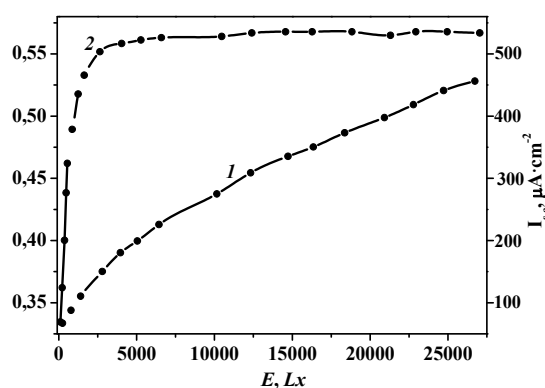


Figure 1. The dependence of the short-circuit current (1-curve) and the no-load EMF (2-curve) on the illumination by integral light

The lifetime of photocarriers in structures grown under various conditions is determined by the relaxation decay of the photo-EMF. The investigation revealed that as the temperature of the onset of crystallization (T_{oc}) of the $(\text{GaAs})_{1-x-y}(\text{Ge}_2)_x(\text{ZnSe})_y$ solid solution layer rose, the lifetime of photo carriers extended from 10^{-7} seconds at $T_{\text{oc}} = 650^\circ\text{C}$ to $5 \cdot 10^{-5}$ seconds at $T_{\text{oc}} = 730^\circ\text{C}$. The spectral characteristics of $I_{\text{s.c.}}$ (short-circuit current) and $U_{\text{o.c.}}$ (open-circuit voltage), as well as the photocurrent were measured in the photodiode mode. Monochromatic radiation was carried out from the solid solution $(\text{GaAs})_{1-x-y}(\text{Ge}_2)_x(\text{ZnSe})_y$. Measurement of the spectral dependence of photocurrent in photodiode mode (Fig. 2, curves *a* and *b*) showed that it covered a wide range of incident photon energies from 1.07 to 3.0 eV.

From Fig. 2, it can be seen that the spectrum of photodetectors in the energy range of 1-3 eV is characterized by six peaks with maximums at photon energies (eV): 1- at 1.37, 2-1.47, 3-1.65, 4-1.88, 5-2.3, 6-2.62 (Figure 2a).

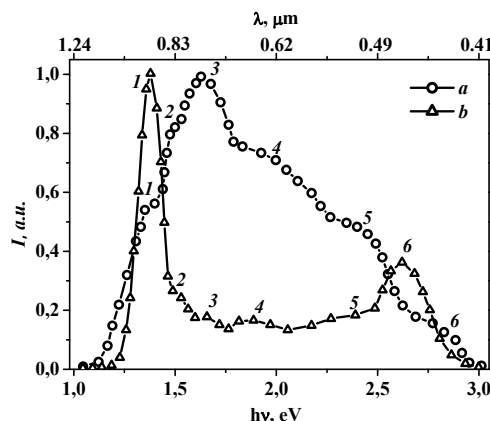


Figure 2. Spectral dependence of the photocurrent of the $n\text{-GaAs-p-(GaAs)}_{1-x-y}(\text{Ge}_2)_x(\text{ZnSe})_y$ structure obtained in photodiode mode at various crystallization onset temperatures: *a* - $T_{\text{oc}} = 730^\circ\text{C}$, *b* - $T_{\text{oc}} = 650^\circ\text{C}$.

In curve *b*, Figure 2. the spectrum begins at a photon energy of 1.07 eV, which may be due to the bonding energy of paired Ge atoms, which partially substitute some of the gallium arsenide molecules and create the corresponding energy

level [13]. Additionally, impurity germanium atoms self-organize into nanocrystals in defectable regions of the gallium arsenide lattice [10], forming their own energy level with an acceptor-like characteristics [10]. At a photon energy of 1.48 eV, a photopic corresponding to recombination from the conduction band to acceptor states in p-GaAs is observed [11]. The maximum of the spectral sensitivity dependence is observed at 1.64 eV, which may be due to the structural bandgap of the valence zone and isovalent impurities of Ge-Se compounds in the GaAs layer [14]. The following photopic peaks, curve *b*, Fig. 2, corresponding to photon energies of 1.89, 2.18, and 2.67 eV, may be attributed to compounds GaSe ($h\nu_{\max} = 1.88$ eV), ZnAs ($h\nu_{\max} = 2.15$ eV), and ZnSe ($h\nu_{\max} = 2.69$ eV) with deep levels in the valence zone of gallium arsenide [12].

The spectral dependencies of the photo-EMF of heterostructures n -GaAs – p -(GaAs) $_{1-x-y}$ (Ge) $_2$ (ZnSe) $_y$ are shown in Figure 3. It can be seen that the peaks of the spectral dependencies, characterized by the crystallization onset temperatures, shift towards the short-wavelength region with increasing displacement. Since carrier separation occurs in the solid solution (GaAs) $_{1-x-y}$ (Ge) $_2$ (ZnSe) $_y$ at the p - n junction, such mixing is likely associated with a decrease in the germanium content relative to ZnSe at the heterojunction boundary in the solid solution and an increase in the epitaxial onset temperature. Although the radiation falls on the side of the solid solution, some carriers generated from the surface of the solid solution at high energies of incident photons likely recombine without reaching the p - n junction boundary, where their separation occurs. Therefore, in almost all investigated cases of photo-EMF, a decrease in photosensitivity is observed in the short-wavelength region of the spectral dependence of photo-EMF. Some difference in the values of photosensitivity observed in the short-wavelength region for different samples can be explained by differences in film thickness.

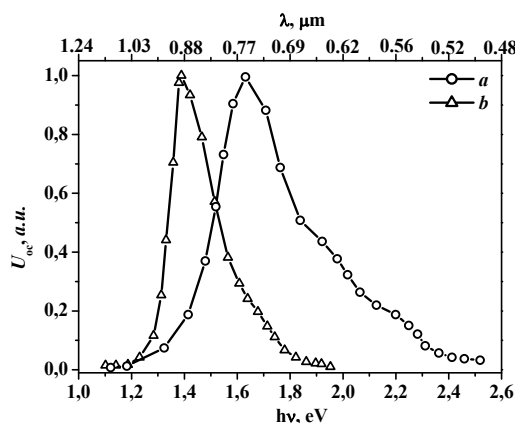


Figure 3. Spectral dependence of the open-circuit photo-EMF of the structures n -GaAs – p -(GaAs) $_{1-x-y}$ (Ge) $_2$ (ZnSe) $_y$ obtained at different crystallization onset temperatures: *a* - $T_{oc} = 730^\circ\text{C}$, *b* - $T_{oc} = 650^\circ\text{C}$.

Also, investigations of photoluminescence were conducted on the solid solutions (GaAs) $_{1-x-y}$ (Ge) $_2$ (ZnSe) $_y$ obtained by us in their intrinsic spectral range. Samples obtained at different crystallization onset temperatures were subjected to measurement. Scanning of the samples was performed on the surface of epitaxial layers. Optical pumping of the surface layers at a temperature of 300 K was performed using a mercury lamp.

Meanwhile, upon visual observation, luminescent glow ranging from green to blue was detected on the surface of epitaxial layers, depending on the sample conditions. By scanning the surface of the films in various directions, it was also possible to approximately visually assess the condition of the sample surfaces based on color and the uniformity of luminescence. In the photoluminescence spectra obtained by continuous recording (Figure 4 - *a* and *b*), it was found that the peaks of the intrinsic photoluminescence bands shift towards the short-wavelength region with increasing crystallization onset temperature.

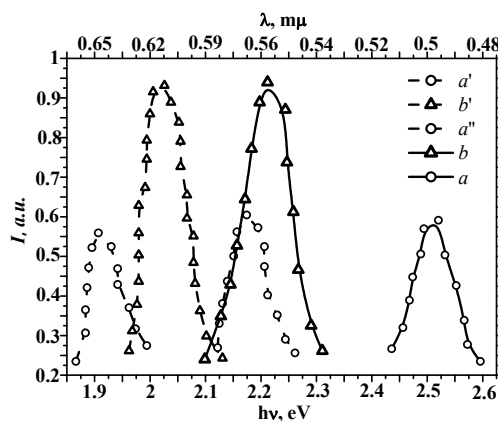


Figure 4. Intrinsic spectral range of photoluminescence spectra taken on the surface and upon sequential removal of the surface of epitaxial layers (*a'*, *a''*, *b'*): *a* - $T_{oc} = 730^\circ\text{C}$, *b* - $T_{oc} = 650^\circ\text{C}$.

Investigating the photoluminescence spectrum of the solid solution $(\text{GaAs})_{1-x-y}\text{(Ge}_2\text{)}_x\text{(ZnSe)}_y$ it was found that with the removal of surface layers, the peaks of the intrinsic band shift towards the long-wavelength region (Figure 4 - a' , a'' , and b'). The research [15] demonstrated that in the solid solution, the zinc selenide content increases along the growth direction, consequently leading to an increase in the width of the bandgap.

Thus, the dependence of the bandgap width on the composition of germanium and zinc selenide in the volume of solid solution has a non-monotonic character, and the obtained solid solutions exhibit varizon structures. The bandgap widths, estimated from the photoluminescence spectra for the two specified samples, were 2.51 and 2.21 eV.

CONCLUSIONS

Thus, the photoelectric properties of $n\text{-GaAs-p-(GaAs)}_{1-x-y}\text{(Ge}_2\text{)}_x\text{(ZnSe)}_y$ heterostructures have been investigated both in photodiode and photovoltaic modes. It has been found that the spectral dependence of the photo-current covers a wide range of energy intervals from 1.07 eV to 3 eV. It has been demonstrated that with an increase in the temperature of the crystallization onset (T_{oc}), the peaks of the spectral dependencies of the photo-electromotive force (photo-EMF) shift towards shorter wavelengths. It has been discovered that with an increase in the temperature of the crystallization onset (T_c) of the solid solution layer $(\text{GaAs})_{1-x-y}\text{(Ge}_2\text{)}_x\text{(ZnSe)}_y$, the lifetime of photo-carriers increases from 10^{-7} s at $T_{oc} = 650^\circ\text{C}$ to $5 \cdot 10^{-5}$ s at $T_{oc} = 730^\circ\text{C}$. Investigation of the photoluminescence on the surface of epitaxial layers $(\text{GaAs})_{1-x-y}\text{(Ge}_2\text{)}_x\text{(ZnSe)}_y$, it has been shown that the peaks of the intrinsic photoluminescence band shift towards shorter wavelengths with increasing crystallization onset temperature. Additionally, investigation of the intrinsic spectral range of photoluminescence in samples through the thickness of the epitaxial layer confirms the varizonality of the obtained structures.

Funding

The work was carried out using project funds allocated according to the order of the rector of Andijan State University dated February 7, 2024, No. 04-12.

ORCID

© Akramjon Y. Boboev, <https://orcid.org/0000-0002-3963-708X>

REFERENCES

- [1] W. Yang et al., "Pseudobinary Solid-Solution: An Alternative Way for the Bandgap Engineering of Semiconductor Nanowires in the Case of GaP–ZnSe," *Advanced Functional Materials*, **25**(17), 2543 (2015). <https://doi.org/10.1002/adfm.201404523>
- [2] A. Kosarev, V. Chaldysheva, V. Preobrazhenskii, M. Putyato, and B. Semyagin. "Effect of a Low-Temperature-Grown GaAs Layer on InAs Quantum-Dot Photoluminescence," *Semiconductors*, **50**(11), 1519 (2016). <https://doi.org/10.1134/S1063782616110154>
- [3] M. Szot, et al. "Experimental and Theoretical Analysis of PbTe–CdTe Solid Solution Grown by Physical Vapour Transport Method," *Acta Physica Polonica A*, **116**(5), 959 (2009).
- [4] A. Reznitskya, A. Klochikhina, and M. Eremenko. "Thermally Activated Resonance Tunneling in Asymmetric Systems of CdSe/ZnSe Double Quantum Wells with Self Assembled Quantum Dots," *Semiconductors*, **48**(3), 345 (2014). <https://doi.org/10.1134/S1063782614030221>
- [5] A. Sharma, and T. Das. "Electronic band structure and optical properties of GaAsSb/GaAs for optoelectronic device applications: A 14 band k.p study," *Optical Materials*, **112**, 110734 (2021). <https://doi.org/10.1016/j.optmat.2020.110734>
- [6] P. Sanmartin, F. Almonacid, M. Ceballos, A. Garcia-Loureiro, and E. Fernandez, "Wide-bandgap III-V materials for high efficiency air and underwater optical photovoltaic power transmission," *Solar Energy Materials and Solar Cells*, **266**, 112662 (2024). <https://doi.org/10.1016/j.solmat.2023.112662>
- [7] A. Yachmenev, S. Pushkarev, R. Reznik, R. Khabibullin, and D. Ponomarev, "Arsenides-and related III-V materials-based multilayered structures for terahertz applications: Various designs and growth technology," *Progress in Crystal Growth and Characterization of Materials*, **66**, 100485 (2020). <https://doi.org/10.1016/j.pcrysgrow.2020.100485> [Get rights and content](#)
- [8] N. Papez, R. Dallaev, S. Talu, and J. Kastyl. "Overview of the Current State of Gallium Arsenide-Based Solar Cells (Review)," *Materials*, **14**, 3075 (2021). <https://doi.org/10.3390/ma14113075>
- [9] J. Geisz, R. France, K. Schulte, M. Steiner, A. Norman, H. Guthrey, M. Young, et al., "Six-junction III–V solar cells with 47.1% under 143 Suns concentration," *Nat. Energy*, **5**(4), 326–335 (2020). <https://doi.org/10.1038/s41560-020-0598-5>
- [10] S. Zaynabidinov, A. Saidov, A. Boboev, and D. Abdurahimov, "Structure, Morphology and Photoelectric Properties of $n\text{-GaAs-p-(GaAs)}_{1-x}\text{(Ge}_2\text{)}_x$ Heterostructure," *Herald of the Bauman Moscow State Technical University, Series Natural Sciences*, **100**(1), 72-87 (2022). <https://doi.org/10.18698/1812-3368-2022-1-72-87>
- [11] S. Zainabidinov, A. Saidov, M. Kalanov, and A. Boboev, "Synthesis, Structure and Electro-Physical Properties $n\text{-GaAs-p-(GaAs)}_{1-x-y}\text{(Ge}_2\text{)}_x\text{(ZnSe)}_y$ Heterostructures (Review)". *Applied Solar Energy*, **55**, 291–308 (2019). <https://doi.org/10.1038/s41560-020-0598-510.3103/S0003701X1905013X>
- [12] S. Suprun, V. Sherstyakova, and E. Fedosenko. "Epitaxial Growth of ZnSe on GaAs with the Use of the ZnSe Compound as the Source". *Semiconductors*, **43**(11), 1526–1531 (2009) <https://doi.org/10.1134/S1063782609110220>
- [13] S. Khludkov, O. Tolbanov, M. Vilisova, and I. Prudaev, *Semiconductor devices based on gallium arsenide with deep impurity centers*, (Publishing House of Tomsk State University, Tomsk, 2016).
- [14] D. Bletskan, J. Madyar, and V. Kabaciy, "Effect of Nonstoichiometry and Doping on the Photoconductivity Spectra of GeSe Layered Crystals," *Semiconductors*, **40**(2), 137–142 (2006) <https://doi.org/10.1134/S1063782606020047>.
- [15] S. Zainabidinov, Sh. Utamuradova, and A. Boboev, "Structural Peculiarities of the $(\text{ZnSe})_{1-x-y}\text{(Ge}_2\text{)}_x\text{(GaAs}_{1-\delta}\text{Bi}_\delta\text{)}_y$ Solid Solution with Various Nano-inclusions," *Journal of Surface Investigation X-ray Synchrotron and Neutron Techniques*, **16**(6), 1130-1134 (2022). <https://doi.org/10.1134/S1027451022060593>

ФОТОЕЛЕКТРИЧНІ ХАРАКТЕРИСТИКИ ГЕТЕРОПЕРЕХОДУ $n\text{-GaAs-p-(GaAs)}_{1-x-y}\text{(Ge}_2\text{)}_x\text{(ZnSe)}_y$

Акрамжон Ю. Бобоєв^{a,b}



^aАндижанський державний університет імені З.М. Бабур, Андижан, Узбекистан

^bІнститут фізики напівпровідників та мікроелектроніки Національного університету Узбекистану,
100057, вул. Янги Алмазар, 20, Ташкент, Узбекистан

Досліджено фотоелектричні властивості гетероструктур $n\text{-GaAs-p-(GaAs)}_{1-x-y}\text{(Ge}_2\text{)}_x\text{(ZnSe)}_y$ як у фотодіодному, так і у фотоелектричному режимах. Виявлено, що спектральна залежність фотоструму охоплює широкий діапазон енергетичних інтервалів від 1,07 еВ до 3 еВ. Показано, що з підвищенням температури початку кристалізації (T_{oc}) піки спектральних залежностей фотоелектрорушійної сили (фото-ЕРС) зміщуються в бік коротших довжин хвиль. Було помічено, що зі збільшенням температури початку кристалізації (T_{oc}) шару твердого розчину $(\text{GaAs})_{1-x-y}\text{(Ge}_2\text{)}_x\text{(ZnSe)}_y$ час життя фотоносіїв збільшується з 10^{-7} с при $T_{oc}=650^\circ\text{C}$ до $5\cdot 10^{-5}$ с при $T_{oc}=730^\circ\text{C}$. Показано, що піки власної смуги фотолюмінесценції зміщуються в бік коротших довжин хвиль зі збільшенням температури початку кристалізації. Крім того, дослідження власної спектральної області фотолюмінесценції зразків по товщині епітаксійного шару підтверджує варіабельність отриманих структур.

Ключові слова: твердий розчин; гетероструктура; температура; фотоелектричні властивості; фото-ЕМ; фотолюмінесценція; фотоносії; варізонна структура

INFLUENCE OF MIXING VALENCE BAND STATES TO THE CONDUCTION BAND STATES ON TWO-QUANTUM LINEAR-CIRCULAR DICHROISM IN SEMICONDUCTORS

 Rustam Y. Rasulov^a,  Voxob R. Rasulov^{a*}, Nurillo U. Kodirov^a, Mardon Kh. Nasirov^a, Ikbol M. Eshboltaev^b

^a Fergana State University, Fergana, Uzbekistan

^b Kokand State pedagogical Institute, Kokand, Uzbekistan

*Corresponding Author e-mail: vrrasulov83@gmail.com

Received April 20, 2024; revised June 13, 2024; accepted June 17, 2024

A quantitative theory of two-photon linear-circular dichroism caused between the subbands of light and heavy holes of the valence band and conduction band is constructed, which takes into account the admixture of valence band states to the conduction band states and the temperature dependence of the band gap ($E_g(T)$) in semiconductors of tetrahedral symmetry in the multiband Kane model. It is shown that the type of oscillatory angular dependence or the amplitude values of the probabilities of two-photon optical transitions depend on the state of light polarization. This is due to the fact that, under the influence of linearly polarized light, alignment along the pulse occurs, and under the action of circularly polarized light, the moments of current carriers are oriented. It has been determined that the probability of two-photon optical transitions from the heavy hole subband to the conduction band of semiconductors at a fixed temperature increases with increasing frequency, passes through a maximum, and sharply decreases regardless of the degree of polarization of light, as well as the band gap.

Keywords: Probability of two-photon absorption of light; Frequency; Temperature; Oscillation dependence; Degree of polarization of light; Linear-circular dichroism; Semiconductor; Multiband Kane model

PACS: 71.20.-b, 71.28.+d

INTRODUCTION

Currently, the main research in the field of multiphoton (multi-quantum) light absorption is carried out in wide-gap semiconductors, as a number of their physicochemical properties have been studied in depth and in more detail. In this regard, multi-quantum effects occurring in narrow-gap crystals have been less studied in both theoretical and experimental aspects. The main reason for this is that the theoretical study of a number of optical phenomena in narrow-gap crystals requires the use of not only the Luttinger-Kohn approximation but also the Kane multiband approach.

The first work on two-quantum interband transitions in crystals was carried out in the early 60s, shortly after the advent of lasers [1-3]. When calculating the matrix elements of two-quantum transitions in crystals, perturbation theories based on the field of an unpolarized electromagnetic wave were used [2, 3], where the two-band Kane model was used.

In [4-11], linear-circular dichroism (LCD) of two- and three-quantum light absorption in crystals was studied both theoretically and experimentally. Nonlinear interband single-quantum absorption of polarized light in Weyl semimetals was studied in [12]. However, the question of the polarization and frequency-polarization dependence of two-quantum interband linear-circular dichroism in zinc blende crystals, caused between the subbands of light and heavy holes of the valence band and conduction band in the Kane approximation, taking into account the admixture of valence band states to the conduction band states, remained open to study, which this work is devoted to.

BASIC RELATIONS

It is known [4] that the coefficient of multi-quantum light absorption is determined by the probability of a N quantum optical transition from the $|n, \vec{k}\rangle$ state to the $|n', \vec{k}'\rangle$ state, determined by the relation

$$W^{(N)} = \frac{2\pi}{\hbar} \left\langle \sum_{n, n', \vec{k}} \left| M_{n\vec{k}, n'\vec{k}'}^{(N)} \right|^2 \right\rangle (f_{n\vec{k}} - f_{n'\vec{k}'}) \delta(E_{n'}(\vec{k}') - E_n(\vec{k}) - N\hbar\omega), \quad (1)$$

where $f_{n\vec{k}}$ ($f_{n'\vec{k}'}$) - is the equilibrium distribution function of current carriers in the initial (final) state, $M_{n\vec{k}, n'\vec{k}'}^{(N)}$ - is the composite matrix element of the N - quantum optical transition.

It can be seen that $W^{(N)}$, in turn, is assigned a value of $M_{n\vec{k}, n'\vec{k}'}^{(N)}$. In particular, to calculate the $M_{n\vec{k}, n'\vec{k}'}^{(N=1)}$ - composite matrix element of a single-quantum optical transition from the subband of light holes to the conduction band, one must know the Hamiltonian, since [13, 14]

$$M_{c,s; v, \Gamma_8, m}^{(1)} = \left(\frac{eA_0}{cm_0} \right) \vec{e} \cdot \vec{p}_{c,s; v, \Gamma_8, m}, \quad (2)$$

where $\vec{e} \cdot \vec{p}_{c,s;v,\Gamma_8,m} = \left(\frac{eA_0}{cm_0}\right) \frac{m_0}{\hbar} \frac{\partial}{\partial \vec{k}} [\hat{H}(\vec{k})]_{c,s;v,\Gamma_8,m}$ - is the matrix elements of the momentum operator, $\vec{e}(A_0)$ -is the polarization vector (amplitude value of the potential vector) of the light wave, $\hat{H}(\vec{k})$ - is the Hamiltonian of current carriers, the remaining quantities are well known. Note here that $\hat{H}(\vec{k})$ - is a quadratic matrix whose dimension depends on the choice of model. For example, in the Kane approximation, $\hat{H}(\vec{k})$ - can be represented as an 8x8 matrix, the form of which is given in [13, 14] in the Luttinger-Kohn approximation. However, in [13, 14], when calculating band matrix elements, the substitution of states of the valence band (Γ_8) to states of the conduction band (Γ_6) was not taken into account, taking this into account gives the following matrix elements of the momentum operator, presented in Tables 1 and 2.

Table 1. Interband matrix elements $\frac{m_0}{\hbar^2 k} \vec{e} \cdot \vec{p}_{m',m}^{(\Gamma_8)}$, calculated from $m', m = 3/2, +1/2, -1/2, -3/2$ taking into account the substitution of valence band states to conduction band states, where $p_{c,v} = \langle S | p_z | Z \rangle$, $e'_\pm = e'_x \pm ie'_y$, e'_x, e'_y, e'_z - are projections \vec{e} relative to the coordinate system x', y', z' , dependent on the direction of the wave vector of current carriers \vec{k} ($\vec{k} || z'$).

	$\langle hh, +3/2 $	$\langle lh, +1/2 $	$\langle lh, -1/2 $	$\langle hh, -3/2 $
$\langle c, +1/2 $	$-\frac{e'_+}{\sqrt{2}}$	$e'_z \sqrt{\frac{2}{3}}$	$\frac{e'_-}{\sqrt{6}}$	0
$\langle c, -1/2 $	0	$-\frac{e'_+}{\sqrt{6}}$	$e'_z \sqrt{\frac{2}{3}}$	$\frac{e'_-}{\sqrt{2}}$

Table 2. Intraband matrix elements of the momentum operator $[\vec{e} \cdot \vec{p}_{m',m}^{(\Gamma_8)} / (\hbar k)]$ for crystals of cubic symmetry. Here $\zeta_g = |p_{c,v}|^2 / (m_0 E_g)$, E_g - is the band gap.

	$\langle hh, +3/2 $	$\langle lh, +1/2 $	$\langle lh, -1/2 $	$\langle hh, -3/2 $
$\langle hh, +3/2 $	e'_z	$\zeta_g \frac{e'_-}{\sqrt{3}}$	0	0
$\langle lh, +1/2 $	$\zeta_g \frac{e'_+}{\sqrt{3}}$	$\left(1 - \frac{4}{3} \zeta_g\right) e'_z$	0	0
$\langle lh, -1/2 $	0	0	$\left(1 - \frac{4}{3} \zeta_g\right) e'_z$	$-\frac{\zeta_g e'_-}{\sqrt{3}}$
$\langle hh, -3/2 $	0	0	$-\frac{\zeta_g e'_+}{\sqrt{3}}$	e'_z

Let us note here that taking into account the substitution of valence band states for conduction band states leads to the following hole Hamiltonian:

$$H(\Gamma_8) = E_{\Gamma_8}^0 + \frac{\hbar^2 k^2}{2m_0} - \frac{\hbar^2 |p_{c,v}|^2}{m_0^2 E_g} \begin{bmatrix} \frac{k_1^2}{2} & -\frac{k_z k_-}{\sqrt{3}} & -\frac{k^2}{\sqrt{12}} & 0 \\ -\frac{k_z k_+}{\sqrt{3}} & \frac{2}{3} k_z^2 + \frac{k_1^2}{6} & 0 & -\frac{k^2}{\sqrt{12}} \\ -\frac{k_+^2}{\sqrt{12}} & 0 & \frac{2}{3} k_z^2 + \frac{k_1^2}{6} & \frac{k_z k_-}{\sqrt{3}} \\ 0 & -\frac{k_1^2}{\sqrt{12}} & \frac{k_z k_+}{\sqrt{3}} & \frac{k_1^2}{2} \end{bmatrix}, \tag{3}$$

which differs from the Luttinger-Kohn Hamiltonian (see, for example, formula (26.12) in monograph [13]).

Then the effective mass of electrons in the conduction band is expressed as

$$\frac{1}{m_c} = \frac{1}{m_0} + \frac{2}{3m_0^2} |p_{c,v}|^2 \left(\frac{2}{E_g} + \frac{1}{E_g + \Delta_{SO}} \right), \tag{4}$$

and the Kane parameter is determined by the relation

$$|p_{c,v}|^2 = \frac{3}{2} m_0 \frac{m_0 - m_c}{m_c} \frac{E_g (E_g + \Delta_{SO})}{2(E_g + \Delta_{SO}) + E_g}, \tag{5}$$

Δ_{SO} - is the width of the spin-orbit splitting of the valence band. In this case, the value that describes the substitution of valence band states to conduction band states $\zeta_g = 3m_0(m_{hh} - m_{lh}) / (4m_{hh}m_{lh}) \gg 1$ for a number of semiconductors (see Table 3), where $m_{hh}(m_{lh})$ - are heavy (light) holes. This means that taking into account the substitution of valence band states for conduction band states should lead to a significant contribution to the coefficient of both single and multi-quantum absorption of light, depending on the frequency of light and temperature, the study of which is the subject of this work.

Table 3. Numerical values of quantity ζ_g .

	InSb	InAs	GaAs
$\zeta_g = \frac{3m_0 m_{hh} - m_{lh}}{4 m_{hh} m_{lh}}$	46.5	25.5	6.18

To complete the problem, in further calculations we will take into account the dependence of band parameters, for example, the band gap on temperature $[E_g(T)]$, since the Kane parameter $p_{c,v} = (3Bm_0^2 E_g \hbar^{-2})^{1/2}$ and the effective masses of current carriers (see formulas (5) and (6)) also depend on $E_g(T)$. In particular, the $E_g(T)$ dependence is expressed by the Varshni formula [15]

$$E_g(T) = E_g(T = 0) - \gamma_T \frac{T^2}{T + T_V} \tag{6}$$

and Passler’s formula [16]

$$E_g(T) = E_g(T = 0) - \frac{\alpha \theta_p}{2} \left[\left(1 + \left(\frac{2T}{\theta_p} \right)^p \right)^{1/p} - 1 \right]. \tag{7}$$

Here γ_T , T_V , α , θ_p -are constant values depending on the physicochemical properties of the semiconductor, the numerical values of which are given in Tables 3 and 4.

$E_g(T)$ dependences determined by relations (6) and (7), it is clear that with increasing temperature, the band gap width described by the Varshni formula changes very slowly, and determined by the Passler formula decreases noticeably.

In particular, the temperature dependences of the effective masses of electrons $m_c(T)$ in the conduction band and holes $m_{SO}(T)$ in the spin-orbit splitting zone can be represented as [15]:

$$\frac{m_0}{m_{SO}(T)} = \gamma_1 - \frac{E_p \Delta_{SO}}{3E_g(E_g + \Delta_{SO})} \frac{m_0}{m_c(T)} = 1 + 2F + \frac{E_p(E_g + 2\Delta_{SO}/3)}{3E_g(E_g + \Delta_{SO})} \tag{8}$$

(see Fig. 2a and b). From Fig. 2 it can be seen that with increasing temperature, $m_c(T)$ for narrow (wide) band gap semiconductors decreases (increases), and $m_{SO}(T)$ increases in semiconductors with an arbitrary band structure, where the calculation is carried out using the Varshni formula. This temperature behavior of the effective masses leads to a noticeable change in the temperature and frequency dependence of the optical properties of semiconductors, for example, the light absorption coefficient. We will consider the analysis of this case later.

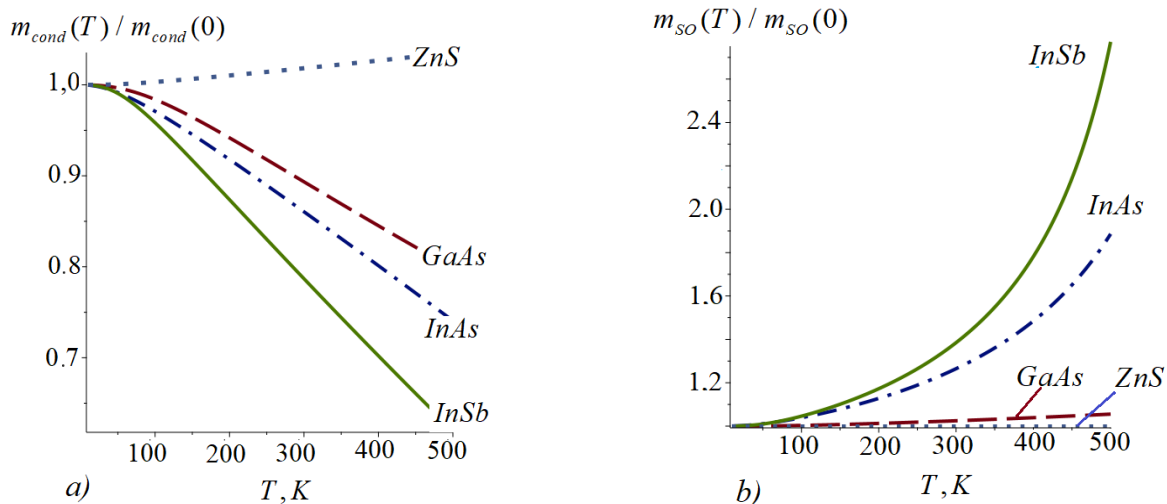


Figure 1. Temperature dependence of the effective masses of electrons (a) in the conduction band and holes (b) in the spin-orbit splitting zone of a semiconductor, calculated using the Varshni formula. Numerical values of zone parameters and thermoelectric quantities are obtained from Tables 3 and 4.

Table 3. Numerical values of band and thermoelectric quantities of some semiconductors [16]

Crystals	$E_g(T = 0), eV$	θ_p, K	$\alpha, meV/K$	p	θ_D, K
GaAs	1.519	230	0.472	2.44	360
InAs	0.414	143	0.281	2.1	262
InSb	0.234	136	0.250	2.68	205
ZnS	3.841	240	0.532	2.76	440

Table 4. Numerical values of band parameters of some semiconductors at T=0 K[2] [15].

	GaAs	InAs	InSb	ZnS
E_g, eV	1.519	0.417a	0.235a	3.54
Δ_{SO}, eV	0.34	0.39	0.81	0.06
E_p, eV	28.8	21.5	23.3	20.4
$\gamma_T, meV/K$	0.46	0.276	0.32	
T_V, K	204	93	170	
γ_1	6.98	20.0	34.8	
γ_2	2.06	8.5	15.5	
γ_3	2.93	9.2	16.5	
m_c/m_0	0.067	0.026	0.0135	
m_{SO}/m_0	0.172	0.14	0.11	
F	-1.94	-2.9	-0.23	

3. FREQUENCY, ANGULAR AND TEMPERATURE DEPENDENCES OF THE PROBABILITIES OF TWO-QUANTUM INTERBAND OPTICAL TRANSITIONS IN CRYSTALS OF TETRAHEDRAL SYMMETRY

Since the probability of optical transitions (see formula (1)) is determined by the composite matrix element, therefore, we will further calculate the matrix elements of the following two quantum optical transitions (without taking into account coherent saturation): a) the initial states of holes are in the heavy hole subband, where the conservation law written as $\delta(E_{cond} - E_{hh} - 2\hbar\omega)$, then the matrix elements of optical transitions of type $|V, \pm 3/2\rangle \rightarrow |m\rangle \rightarrow |c, \pm 1/2\rangle$ have the form $\left(\frac{eA_0}{ch}\right)^2 \frac{1}{\sqrt{2}} p_{c,v}^* \hbar k \frac{e'_{\pm} e'_{\pm z}}{(\pm\hbar\omega)} \left[1 + \frac{2}{3} \frac{\hbar\omega\zeta_g}{(E_{lh} - E_{hh} - \hbar\omega)}\right]$, and optical transitions of type $|V, \pm 3/2\rangle \rightarrow |m\rangle \rightarrow |c, \mp 1/2\rangle$ are prohibited; b) the initial states of holes are in the bottom of light holes, where the conservation law is written as $\delta(E_{cond} - E_{lh} - 2\hbar\omega)$, then the matrix elements of optical transitions of type $|V, \pm 1/2\rangle \rightarrow |m\rangle \rightarrow |c, \pm 1/2\rangle$ have the form $\left(\frac{eA_0}{ch}\right)^2 \hbar \frac{k}{\sqrt{6}(-\hbar\omega)} \left[\left(1 - \frac{4}{3}\zeta_g\right) e'_{\pm z} \pm \frac{\hbar\omega\zeta_g |e'_{\pm}|^2}{(E_{hh} - E_{lh} - \hbar\omega)}\right]$, and optical transitions of type $|V, \pm 1/2\rangle \rightarrow |m\rangle \rightarrow |c, \mp 1/2\rangle$ are prohibited.

Here $E_{cond} = \frac{\hbar^2 k^2}{2m_c} + E_g$ - is the energy spectrum of electrons in the conduction band, $E_L = -\frac{\hbar^2 k^2}{2m_L}$ - is the energy spectrum of holes in the valence band, $L = lh$ ($L = hh$) corresponds to light (heavy) holes, symbol \rightarrow describes a single-quantum optical transition. Then the composite matrix of a two-quantum interband optical transition $M_{L,\vec{k}; SO,\vec{k}}^{(2)}$, taking into account the admixture of valence states Γ_8 (valence band) and Γ_7 (spin-orbital splitting band) into the Γ_6 states (conduction band) is described by the following expression

$$M_{lh,\vec{k}; c,\vec{k}}^{(2)} = \frac{1}{3} \left(\frac{eA_0}{ch}\right)^4 \frac{|p_{c,v}^*|^2 \hbar^2 k^2}{(\hbar\omega)^2} \left[\left(1 - \frac{4}{3}\zeta_g\right)^2 e'_{\pm z}{}^4 - \left(\frac{\hbar\omega\zeta_g}{(E_{hh} - E_{lh} - \hbar\omega)}\right)^2 |e'_{\pm}|^4 \right], \quad (9)$$

$$M_{hh,\vec{k}; c,\vec{k}}^{(2)} = 3 \left(\frac{eA_0}{ch}\right)^4 \frac{|p_{c,v}^*|^2 \hbar^2 k^2}{(\hbar\omega)^2} \left(1 + \frac{2}{3} \frac{\hbar\omega\zeta_g}{(E_{lh} - E_{hh} - \hbar\omega)}\right)^2 e'_{\pm z}{}^2 e'_{\pm}{}^2, \quad (10)$$

where $\left(\frac{eA_0}{ch}\right)^2 = \frac{2\pi e^2}{n_{\omega} c} \frac{I}{(\hbar\omega)^2}$, $I(\omega)$ -is the intensity (frequency) of light, n_{ω} - is the refractive index of light at frequency ω , $p_{c,v} = (3Bm_0^2 E_g / \hbar^2)^{1/2}$ - is the Kane parameter, $B = \hbar^2(m_{hh} - m_{lh}) / (4m_{hh}m_{lh})$, $m_{hh}(m_{lh})$ -is the effective mass of light (heavy) holes.

Let us note here that if we do not take into account the admixture of valence states Γ_8 and Γ_7 to the Γ_6 states, then the results obtained are [14, 15]. Since the probabilities of intersubband two-quantum interband optical transitions are determined by relation (9) and (10), therefore, based on this expression, it is possible to calculate the frequency-temperature dependence of both the coefficients of two quantum light absorption and its linear-circular dichroism, taking into account the temperature dependence $m_c(T)$, $m_{SO}(T)$ and $E_g(T)$ [15]3. Then, by substituting (9) and (10) into (1), we can determine the frequency and polarization dependence of the probability of a two-quantum optical transition, where it is taken into account that to calculate the angular dependences of the optical parameters of a semiconductor it is convenient to use the following relations [4]: for linearly polarized light

$$|e'_{\pm z}|^2 = \cos^2(\vec{e} \cdot \vec{k}), \quad |e'_{\pm}|^2 = 1 - |e'_{\pm z}|^2 = 1 - \cos^2(\vec{e} \cdot \vec{k}), \quad (11)$$

and for circularly polarized light

$$|e'_{\pm z}|^2 = \frac{1}{2} \sin^2(\vec{q} \cdot \vec{k}), \quad |e'_{\pm}|^2 = \frac{1}{2} [1 + \cos^2(\vec{q} \cdot \vec{k})] \mp P_{circ} \cos(\vec{q} \cdot \vec{k}), \quad (12)$$

and also $\left(\frac{eA_0}{ch}\right)^2 = \frac{I}{\hbar\omega} \frac{e^2}{ch} \frac{2\pi}{n_{\omega}}$, where \vec{q} - is the wave vector of the photon, P_{circ} - is the degree of circular polarization, I - is the light intensity, n_{ω} - is the refractive index of the semiconductor at frequency ω .

In Fig. 2 shows the frequency-angular dependences $W_{linear}^{(2)}$ and $W_{circ}^{(2)}$ for light of linear (a, e) and circular (b, e) polarization for optical transitions from the heavy hole subband to the conduction band in GaAs. The results presented in Fig. 2a,b were obtained for $E_g(T = 0 \text{ K})$, and the results in Fig. 2d,c – for $E_g(T = 330 \text{ K})$. From these figures it is clear that the appearance of the graph, for example, the symmetry of oscillations of the angular dependence or the change in the amplitude values of $W_{linear}^{(2)}$ and $W_{circ}^{(2)}$, depends on the state of light polarization. This is due to the fact that since under the influence of linearly polarized light the alignment of pulses occurs, and under the action of circularly polarized light the moments of current carriers are oriented, and also taking into account dependencies $m_c(T)$, $m_{SO}(T)$ and $E_g(T)$ leads to the temperature dependence of the wave vector of photoexcited current carriers.

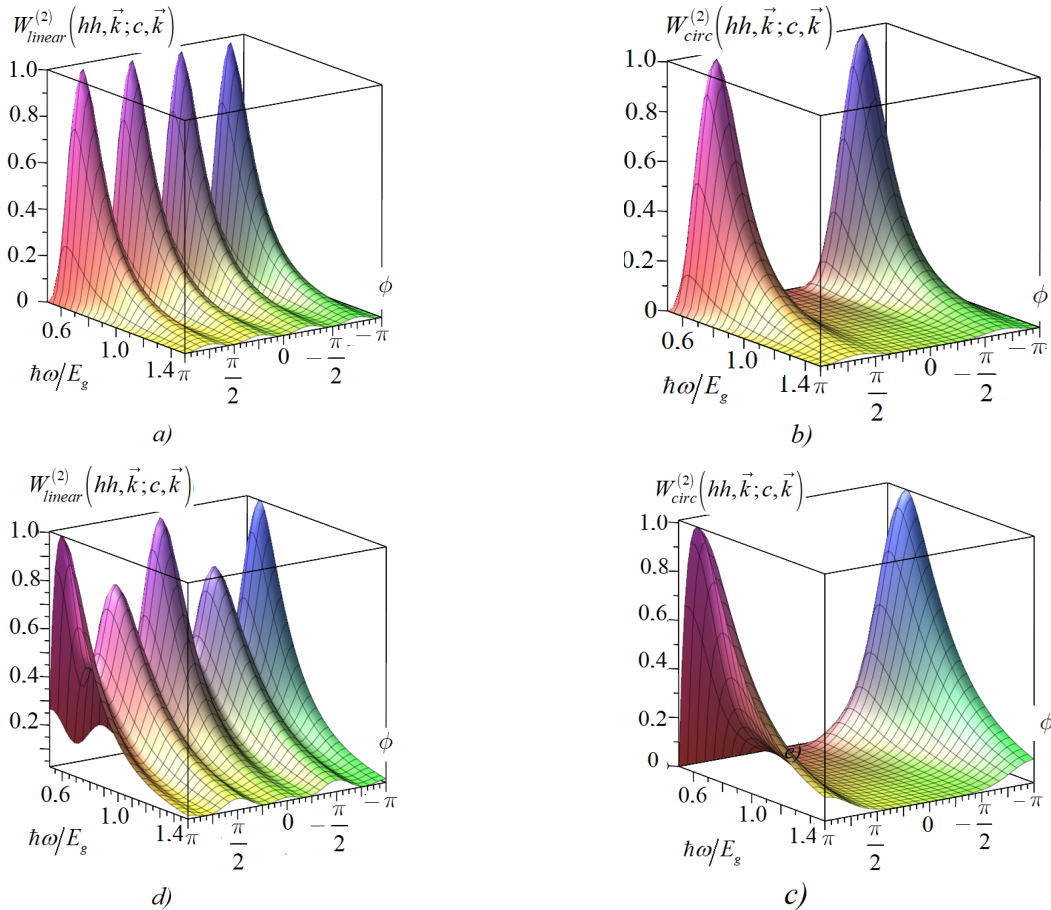


Figure 2. Frequency-angular dependences $W^{(2)}$ for light of linear $W_{linear}^{(2)}$ (a, d) and circular $W_{circ}^{(2)}$ (b, c) polarization for optical transitions from the heavy hole subband to the conduction band in GaAs. In figures a, b it was assumed that $E_g(T = 0 \text{ K})$, and in d, c - $E_g(T = 330 \text{ K})$.

In Fig. 3 shows the frequency-temperature dependences of the probability of $W_{circ}^{(2)}$ two-quantum optical transitions from the subband of light holes to the conduction band of semiconductors InSb (a), InAs (b), GaAs (c) under by the action of circularly polarized light, averaged over the solid angles of the wave vector of the current carriers, where the dependence $E_g(T)$ is taken into account (see Varshni's formula).

Calculations show that taking into account $E_g(T)$ leads to a sharp increase in $W_{circ}^{(2)}$ in low frequency regions and a transition through a maximum, then a hump-shaped dependence (see Fig. 3a) and b)) with increasing frequency at arbitrary temperatures. Note that the greater the width of the band gap, the greater the depth of the hump.

It should be noted that the probability of two-quantum optical transitions under the influence of linearly polarized light $W_{linear}^{(2)}$ exactly repeats the frequency-temperature dependence $W_{circ}^{(2)}$, but the amplitude value is four times smaller.

Calculations show that the probability of two-quantum optical transitions from the heavy hole subband to the conduction band of semiconductors at a fixed temperature increases with increasing frequency and passes through a maximum and sharply decreases regardless of the degree of polarization of light, as well as the band gap. This can be explained by a similar frequency-temperature dependence of the current carrier distribution functions.

It is known [4-10] that the coefficient of two-quantum linear dichroism of light absorption is determined by the probability ratio of $W_{circ}^{(2)}$ to $W_{linear}^{(2)}$, i.e. ratio $\eta^{(2)} = W_{circ}^{(2)}/W_{linear}^{(2)}$. In Fig. 4 shows the frequency-angular dependences $\eta^{(2)}$ caused by optical transitions from the branch of light holes to the conduction band of semiconductors InSb (a),

InAs (b), GaAs (c), where graphs 1 correspond to $E_g(T = 0\text{ K})$, and graphs 2 - $E_g(T = 30\text{ K})$ (graphs 2). From Fig. 4 it can be seen that at certain values of the angle $\eta^{(2)}$, regardless of the width of the band gap, it takes on a very large value, which, firstly, is due to the fact that these angles $W_{linear}^{(2)}$ have small values, and secondly, such an anomalous value decreases sharply at $\zeta_g = |p_{c,v}|^2 / (m_0 E_g) = 0$, i.e. when we do not take into account the admixture of valence band states to the conduction band states.

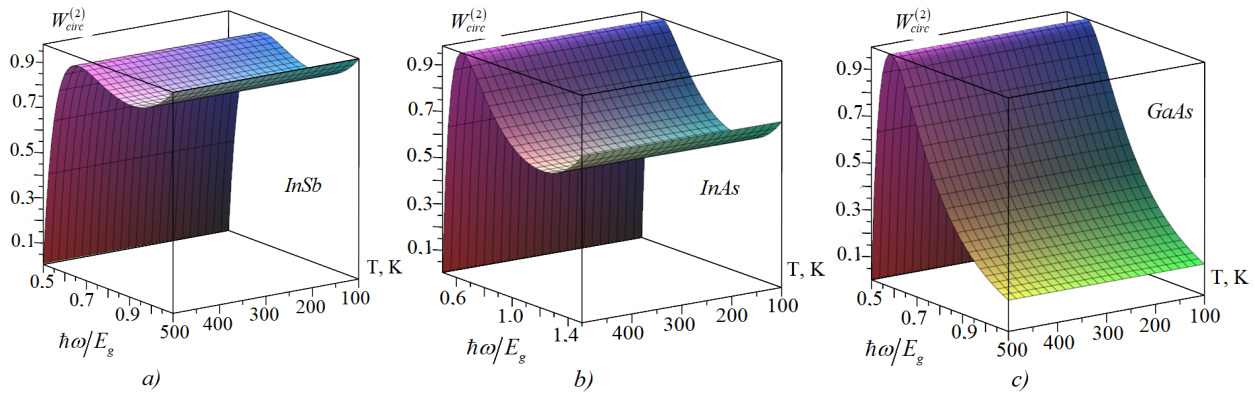


Figure 3. Frequency and temperature dependence of the probability of two-quantum optical transitions $W_{circ}^{(2)}$ from the light hole branch to the conduction band of semiconductors InSb (a), InAs (b), GaAs (c) under the influence of circularly polarized light. The calculations took into account the temperature dependence of the band gap.

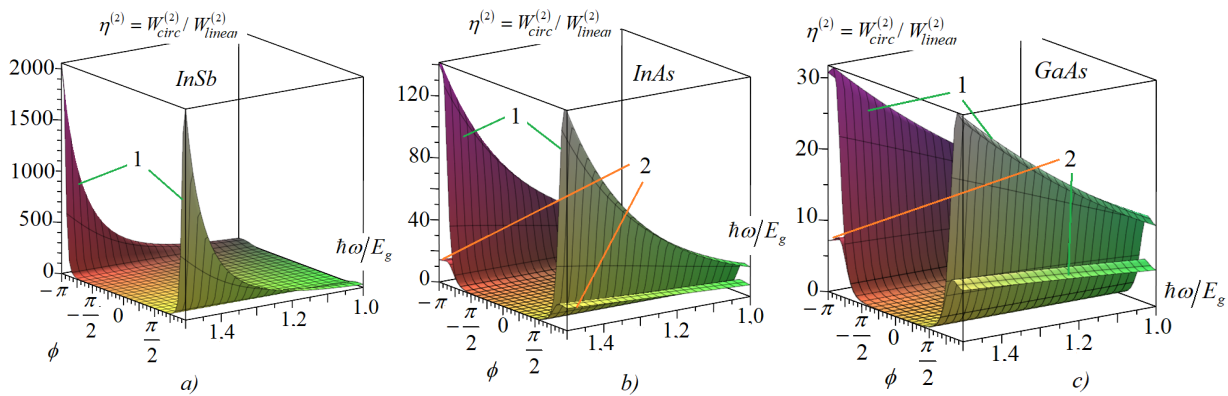


Figure 4. Frequency-angular dependence of the two-quantum coefficient of linear-circular dichroism $\eta^{(2)}$, caused by optical transitions from the branch of light holes to the conduction band of semiconductors InSb (a), InAs (b), GaAs (c), where graphs 1 correspond to $E_g(T = 0\text{ K})$, and graphs 2 - $E_g(T = 30\text{ K})$ (graphs 2). The calculations did not take into account the contribution of the coherent saturation effect in $\eta^{(2)}$.

CONCLUSIONS

In conclusion, we note that in Kane’s three-band approximation:

A quantitative theory of two-quantum interband linear-circular dichroism in InSb, InAs and GaAs semiconductors is constructed, which takes into account the admixture of valence band states to conduction band states and the temperature dependence of the band gap in the multiband Kane model.

It is shown that the probabilities of interband two-quantum optical transitions in both narrow- and wide-bandgap semiconductors with a frequency rostrum at a fixed temperature first increase, then, passing through a maximum, decreases, regardless of the degree of polarization of the light.

Frequency and temperature dependence of the probability of two-quantum optical transitions $W_{circ}^{(2)}$ from the light hole branch to the conduction band of semiconductors InSb (a), InAs (b), GaAs (c) under the influence of circularly polarized light.

ORCID

✉Rustam Y. Rasulov, <https://orcid.org/0000-0002-5512-0654>; ✉Voxob R. Rasulov, <https://orcid.org/0000-0001-5255-5612>

REFERENCES

- [1] K.S. Novoselov, A.K. Geim, S.V. Morozov, D. Jiang, Y. Zhang, S.V. Dubonos, I.V. Grigorieva, and A.A. Firsov, “Electric field effect in atomically thin carbon films,” *Science*, **306**(5696), 666–669 (2004). <https://doi.org/10.1126/science.1102896>
- [2] L.A. Chernozatonskii, and A.A. Artyukh, “Quasi-two-dimensional transition metal dichalcogenides: structure, synthesis, properties and applications,” *UFN*, **188**(1), 3–30 (2018). <https://doi.org/10.3367/UFNr.2017.02.038065> (in Russian)

- [3] W.S. Yun, S.W. Han, S.C. Hong, I.G. Kim, and J.D. Lee, "Thickness and strain effects on electronic structures of transition metal dichalcogenides: 2H-MX₂ semiconductors (M = Mo, W; X = S, Se, Te)," *Phys. Rev. B*, **85**(3), 033305 (2012). <https://doi.org/10.1103/PhysRevB.85.033305>
- [4] N. Huo, Y. Yang, Y.-N. Wu, X.-G. Zhang, S.T. Pantelides, and G. Konstantatos, "High carrier mobility in monolayer CVD-grown MoS₂ through phonon suppression," *Nanoscale*, **10**(31), 15071-15077 (2018). <https://doi.org/10.1039/C8NR04416C>
- [5] A. Taffelli, S. Dirè, A. Quaranta, and L. Pancheri, "MoS₂ based photodetectors: a review," *Sensors*, **21**(8), 2758 (2021). <https://doi.org/10.3390/s21082758>
- [6] G.H. Shin, C. Park, H.J. Lee, H.J. Jin, and S.-Y. Choi, "Ultrasensitive phototransistor based on WSe₂-MoS₂ van der Waals heterojunction," *Nano Lett.* **20**(8), 5741-5748 (2020). <https://doi.org/10.1021/acs.nanolett.0c01460>
- [7] T. Wang, F. Zheng, G. Tang, J. Cao, P. You, J. Zhao, and F. Yan, "2D WSe₂ Flakes for Synergistic Modulation of Grain Growth and Charge Transfer in Tin-Based Perovskite Solar Cells," *Adv. Sci.* **8**(11), 2004315 (2021). <https://doi.org/10.1002/advs.202004315>
- [8] W. Choi, N. Choudhary, G.H. Han, J. Park, D. Akinwande, and Y.H. Lee, "Recent development of two-dimensional transition metal dichalcogenides and their applications," *Mater. Today*, **20**(3), 116-130 (2017). <https://doi.org/10.1016/j.mattod.2016.10.002>
- [9] S.-H. Su, W.-T. Hsu, C.-L. Hsu, C.-H. Chen, M.-H. Chiu, Y.-C. Lin, W.-H. Chang, et al., "Controllable synthesis of band-gap-unable and monolayer transition-metal dichalcogenide alloys," *Front. Energy Res.* **2**, 27 (2014). <https://doi.org/10.3389/fenrg.2014.00027>
- [10] C. Ermandes, L. Khalil, H. Almabrouk, D. Pierucci, B. Zheng, J. Avila, P. Dudin, et al., "Indirect to direct band gap crossover in two-dimensional WS₂(1-x)Se_{2x} alloys," *Nano. Mater. Appl.* **5**(1), 7 (2021). <https://doi.org/10.1038/s41699-020-00187-9>
- [11] E.L. Ivchenko, *Optical Spectroscopy of Semiconductor Nanostructures*, (Alpha Science International Ltd., Harrow, UK, 2005).
- [12] M.M. Glazov, "Elektron and Nuclear Spin Dynamics in Semiconductor Nanostructures," in: *Series on Semiconductor Science and Technology*, (OUP, Oxford, 2018). <https://doi.org/10.13140/RG.2.2.18718.56640>
- [13] R.Ya. Rasulov, Kh. Sidikova, and Yu. Ganiev, "Theory of photovoltaic phenomena with n-GaP," *FTP*, **27**(3), 374-385 (1993). (In Russian)
- [14] V.R. Rasulov, R.Ya. Rasulov, and I. Eshboltaev, "Linearly and circular dichroism in a semiconductor with a complex valence band with allowance for four-photon absorption of light," *Physics of the Solid State*, **59**(3), 463-468 (2017). <https://doi.org/10.1134/S1063783417030283>
- [15] V.R. Rasulov, R.Ya. Rasulov, and I. Eshboltaev, "Linear-Circular Dichroism of Four-Photon Absorption of Light in Semiconductors with a Complex Valence Band," *Russian Physics Journal*, **58**(12), 1681-1686 (2015). <https://doi.org/10.1007/s11182-016-0702-2>
- [16] V.R. Rasulov, R.Ya. Rasulov, and I. Eshboltaev, "On the Theory of the Shift Linear Photovoltaic Effect in Semiconductors of Tetrahedral Symmetry Under Two-Photon Absorption," *Russian Physics Journal*, **59**(1), 92-98 (2016). <https://doi.org/10.1007/s11182-016-0742-7>

**ВПЛИВ ЗМІШУВАННЯ СТАНІВ ВАЛЕНТНОЇ ЗОНИ ДО СТАНІВ ЗОНИ ПРОВІДНОСТІ НА
ДВОКВАНТОВИЙ ЛІНІЙНО-КОЛОВИЙ ДІХРОЇЗМ У НАПІВПРОВІДНИКАХ**
Рустам Ю. Расулов^a, Воксоб Р. Расулов^a, Нурілло У. Кодіров^a, Мардон Х. Насіров^a, Ікбол М. Ешболтаєв^b

^aФерганський державний університет, Фергана, Узбекистан

^bКокандський державний педагогічний інститут, Коканд, Узбекистан

Побудовано кількісну теорію двофотонного лінійно-кругового дихроїзму між підзонами легких і важких дірок валентної зони та зони провідності, яка враховує домішку станів валентної зони до станів зони провідності та температурну залежність ширина забороненої зони ($E_g(T)$) у напівпровідниках тетраедричної симетрії в багатозонній моделі Кейна. Показано, що вид коливальної кутової залежності або амплітудні значення ймовірностей двофотонних оптичних переходів залежать від стану поляризації світла. Це пояснюється тим, що під дією лінійно поляризованого світла відбувається вирівнювання вздовж імпульсу, а під дією циркулярно поляризованого світла відбувається орієнтація моментів носіїв струму. Визначено, що ймовірність двофотонних оптичних переходів із підзони важких дірок у зону провідності напівпровідників при фіксованій температурі зростає зі збільшенням частоти і проходить через максимум і різко зменшується незалежно від ступеня поляризації світла, оскільки а також ширина забороненої зони.

Ключові слова: ймовірність двофотонного поглинання світла; частота; температура; коливальна залежність; ступінь поляризації світла; лінійно-круговий дихроїзм; напівпровідник; багатозонна модель Кейна

THEORY OF ELECTRON TRANSPORT IN TWO-BARRIER FIVE-LAYER SEMICONDUCTOR STRUCTURES

✉ **Rustam Y. Rasulov**^a, ✉ **Voxob R. Rasulov**^{a*}, ✉ **Makhliyo A. Mamatova**^a, ✉ **Mardonbek X. Nasirov**^a,
Umida M. Isomaddinova^b

^a Fergana State University, Fergana, Uzbekistan

^b Kokand State pedagogical Institute, Kokand, Uzbekistan

*Corresponding Author e-mail: vrrasulov83@gmail.com

Received April 20, 2024; revised June 14, 2024; accepted June 18, 2024

The dependence of the transparency coefficient of a five-layer two-barrier structure on the electron energy and the ratio of the widths of two neighboring potential barriers is calculated. It is shown that the extremum of the transparency coefficient significantly depends on the geometric dimensions of the structure layers. In a symmetric five-layer two-barrier semiconductor structure, the condition for the occurrence of "resonant" electron transitions is defined. It is demonstrated that the mechanism of such (resonant) transitions is explained by the interference of de Broglie waves of electrons in the potential well, where the phases of de Broglie waves are determined by the geometric dimensions of the structure, and their amplitudes - by the ratio of the carrier energy to the height of the potential barrier. It has been established that with an increase in the effective mass of charge carriers, the number of intersections of the quantities $f_R(\xi)$ and $\frac{(1-2\xi)}{\sqrt{\xi-\xi^2}}$ increases. These intersections determine the dimensionally-quantized levels where electrons are localized.

Keywords: Potential Barrier; Potential Well; Two-Barrier Five-Layer Structure; Transmission coefficient; Size Quantization

PACS: 71.20. - b, 71.28. + d

INTRODUCTION

The investigation of charge carrier transport through multilayer semiconductors considering the symmetry of the structure is a relevant task due to its applications in the field of solid-state physics, particularly in nanoelectronics [1-5]. In works [6-9], the dynamic conductivity $\sigma(\omega)$ or the current $j(\omega)$ response of the system to external stimuli in a semiconductor multilayer structure has been calculated. The theory has been developed using various models and mathematical methods to solve the full Schrödinger equation [10] for a system of electrons interacting with the electromagnetic field in a structure with delta-shaped potential barriers. In works [1-10], electronic transport through multilayer structures has been investigated without considering the Bastard condition [11], i.e., the difference in the effective masses of electrons in the layers of the structure has not been taken into account.

In the studies we have examined, computations are primarily conducted on computers, where it is difficult to analyze intermediate calculations [7-9], while analytical calculations have been performed [13-18], where changes in the effective masses of electrons when transitioning from one layer to another are not considered.

Based on the results of works [1, 2, 14-20], it can be concluded that the transmission coefficient of electrons through an isolated potential barrier is less than unity and does not depend on whether the electron passes through the potential barrier from the left or the right. Based on this conclusion, it follows that in systems consisting of a periodically arranged sequence of "potential well + potential barrier," the resulting transmission coefficient of electrons through the potential barrier may be less than unity. However, it is not always possible to consider the resulting transmission coefficient through such structures as the sum of the transmission coefficients of electrons through individually isolated potential barriers. This is because the de Broglie waves belonging to electrons in a fixed well consist of components approaching the barrier, scattered from the barrier, and passing through the barrier, the first and second components of which interfere since they differ in amplitude and phase. As a result, not only the nature of the physical analysis of the problem changes but also the theoretical calculations applied to electron transport in multilayer semiconductor structures.

QUANTUM-MECHANICAL ANALYSIS OF ELECTRON TRANSPORT

Therefore, let us consider the two-barrier five-layer structure below, where each barrier is located between two adjacent potential wells (Fig. 1). In solving this problem, unlike simple quantum mechanical approximation [10], we take into account the change in the effective mass of the electron when transitioning from one layer to another, that is, we consider the carrier masses to be different in all layers [16-18].

It is worth noting that from Fig. 1, heterostructures with different energy structures can be obtained by choosing the magnitude and sign of the potential barrier heights.

In particular, it provides the energy structure of ladder-cascade and other heterostructures, in which the height of the potential barriers increases, i.e., $U_1 > U_2 > U_3 > U_4$, or decreases, i.e., $U_1 < U_2 < U_3 < U_4$. For all the cases mentioned

above, by solving the Schrödinger equation with the Bastard condition [11-12, 16-18], one can determine characteristic parameters such as the transmission coefficient of the structure. However, depending on whether the electron's energy is significantly higher or lower than the height of the considered potential barrier, the electron's wave vector can be either a real or an imaginary quantity. Therefore, in intermediate calculations, especially when separating the wave function into real and imaginary parts in the initial stages of the calculation, one must be extremely careful to avoid confusion in the analysis of the final results.

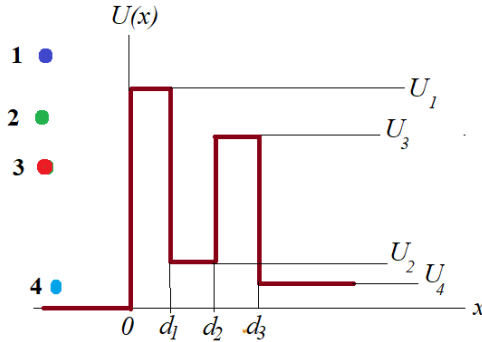


Figure 1. Carrier transport through a five-layer semiconductor structure. 1 corresponds to carrier transport above the potential, 4 - below the potential, 2, 3 - transport below the first and above the second potential. In case 1, the energy of the carriers exceeds all potential barrier heights, in case 4, the energy of the carriers is less than all potential barrier heights, and in the remaining cases, the energy is higher than some potential barrier height and lower than the height of another.

Thus, let us denote the solution of the Schrödinger equation for case 1 in the potential depicted in Fig. 1, i.e., the electron transition above the potential, as follows:

$$\psi_1(x) = A_i \exp(ik_i x) + B_i \exp(-ik_i x), \tag{1}$$

where $k_1 = \sqrt{\frac{2m_1}{\hbar^2} E}$, $k_i = \sqrt{\frac{2m_i}{\hbar^2} (E - U_i)}$, $i = 2,3,4$ are quantities determined by the boundary conditions of the problem, such as continuity and finiteness conditions of the wave functions at the interface of two adjacent layers.

If the energy of the electron is lower than the heights of the potential barriers in all layers, then the solution of the Schrödinger equation can be written in the form (1), where one needs to make the substitution $k_i = i\kappa_i$, which for an electron with energy $E < U_i$ takes the form:

$$\psi_i(x) = A_i \exp(\kappa_i x) + B_i \exp(-\kappa_i x) D_i. \tag{2}$$

Then, following the work [17], it is not difficult to obtain the expression for the electron transmission coefficient for case 1 as:

$$t_{\text{overbarrier}} = 4 \frac{\tilde{k}_5}{\tilde{k}_1} \left\{ \Re_1^2 + \Re_3^2 + (\Re_2^2 + \Re_4^2 - \Re_1^2 - \Re_3^2) \sin^2(\tilde{k}_3(d_2 - d_1)) + 2(\Re_1 \Re_2 + \Re_3 \Re_4) \cos(k_3(d_2 - d_1)) \sin(\tilde{k}_3(d_2 - d_1)) \right\}, \tag{3}$$

Here:

$$\begin{aligned} \Re_1 &= \frac{1}{\tilde{k}_1} \left[\tilde{k}_1 + \tilde{k}_5 + \frac{\tilde{k}_4^2 \tilde{k}_1 + \tilde{k}_5 \tilde{k}_2^2}{\tilde{k}_2 \tilde{k}_4} \operatorname{tg}(k_2(d_2 - d_1)) \operatorname{tan}(k_4(d_4 - d_1 - d_2)) \right] \times \\ &\times \cos(k_2(d_2 - d_1)) \cos(k_4(d_4 - d_1 - d_2)), \\ \Re_2 &= \frac{1}{\tilde{k}_1 \tilde{k}_3} \left[\frac{\tilde{k}_5 \tilde{k}_2^2 - \tilde{k}_1 \tilde{k}_3^2}{\tilde{k}_2} + \frac{\tilde{k}_4^2 \tilde{k}_1 - \tilde{k}_3^2 \tilde{k}_5}{\tilde{k}_4} \operatorname{cot}(k_2(d_2 - d_1)) \operatorname{tan}(k_4(d_4 - d_1 - d_2)) \right] \times \\ &\times \sin(k_2(d_2 - d_1)) \cos(k_4(d_4 - d_1 - d_2)), \\ \Re_3 &= \frac{1}{\tilde{k}_1} \left[\frac{\tilde{k}_2^2 - \tilde{k}_1 \tilde{k}_5}{\tilde{k}_2} + \frac{\tilde{k}_4^2 - \tilde{k}_1 \tilde{k}_5}{\tilde{k}_4} \operatorname{cot}(k_2(d_2 - d_1)) \operatorname{tan}(k_4(d_4 - d_1 - d_2)) \right] \times \\ &\times \sin(k_2(d_2 - d_1)) \cos(k_4(d_4 - d_1 - d_2)), \\ \Re_4 &= -\frac{1}{\tilde{k}_1 \tilde{k}_3} \left[\tilde{k}_3^2 + \tilde{k}_1 \tilde{k}_5 - \frac{\tilde{k}_2^2 \tilde{k}_4^2 + \tilde{k}_1 \tilde{k}_3^2 \tilde{k}_5}{\tilde{k}_2 \tilde{k}_4} \operatorname{tanh}(k_2(d_2 - d_1)) \operatorname{tan}(k_4(d_4 - d_1 - d_2)) \right] \times \\ &\times \cos(k_2(d_2 - d_1)) \operatorname{cosh}(k_4(d_4 - d_1 - d_2)). \end{aligned} \tag{4}$$

Fig.2 shows the graph of the oscillatory dependence of the above-barrier transmission coefficient on the electron energy (in electron-volts) and the ratio of the widths of the two potential barriers $ns = \frac{d_2}{d_4}$, where d_2 is the thickness of the second layer (first potential barrier), d_4 is the thickness of the fourth layer (second potential barrier). In the calculations, it was assumed that the effective masses of electrons in the 1st, 2nd, 3rd, and 4th layers are respectively equal to $m_1 = 0.15 \cdot m_0$, $m_2 = 0.0623 \cdot m_0$, $m_3 = 0.0122 \cdot m_0$, $m_4 = 0.12 \cdot m_0$, and the width of the potential wells is 25 nm. In this case, a) $0.47 \text{ eV} < E < 0.59 \text{ eV}$; b) $0.80 \text{ eV} < E < 0.95 \text{ eV}$ corresponds to the energy range. From this figure, it can be seen that the amplitude values of $t_{\text{overbarrier}}(E, ns)$ significantly depend on the ratio of the thicknesses of the potential barriers and the electron energy, and the oscillatory dependence is described by the interference of de Broglie waves approaching the barrier and scattered from it. Since the interfering waves differ in amplitude and phase, the oscillation in $t_{\text{overbarrier}}(E, ns)$ as a function of both E and ns is asymmetric.

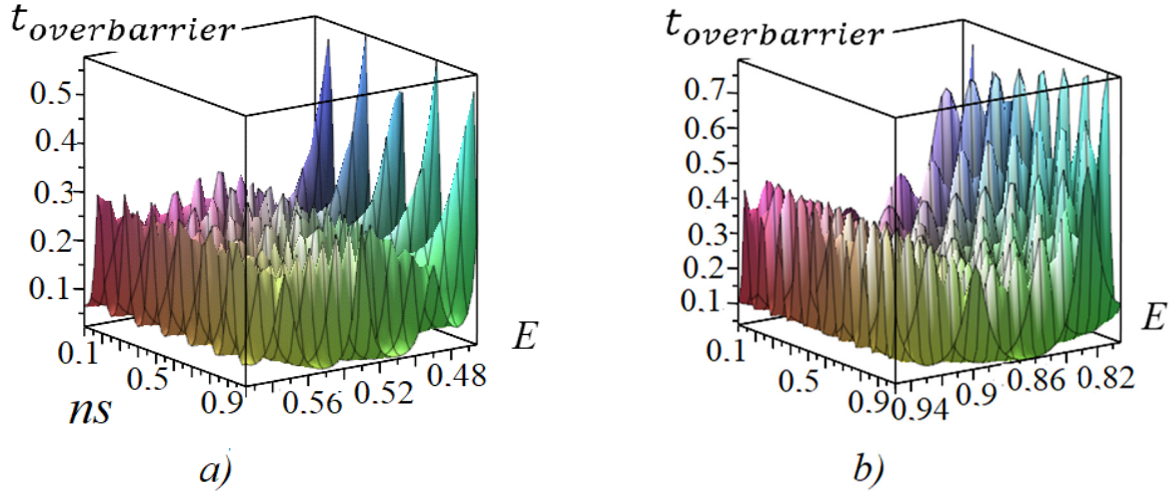


Figure 2. Graph of the dependence of the transparency coefficient of the potential barrier on the electron energy (in electron-volts) and the ratio of the widths of the two potential barriers ($ns = \frac{d_2}{d_4}$) when electrons pass through the potential barrier:
a) $0.47 \text{ eV} < E < 0.59 \text{ eV}$; b) $0.80 \text{ eV} < E < 0.95 \text{ eV}$.

In case 2, i.e., when the energy of the electrons is lower than the height of the first barrier and higher than the height of the second barrier, the transition coefficient can be determined using (3), where the quantities $\mathfrak{R}_j (j = 1, 2, 3, 4)$ should be replaced by $\mathfrak{R}'_j (j = 1, 2, 3, 4)$:

$$\begin{aligned} \mathfrak{R}'_1 &= \frac{1}{\tilde{k}_1} \left[\tilde{k}_1 + \tilde{k}_5 - \frac{\tilde{k}_1 \tilde{k}_4 \tilde{k}_4 + \tilde{k}_5 \tilde{k}_2^2}{\tilde{k}_2 \tilde{k}_4} \tanh(\kappa_2(d_2 - d_1)) \tan(\kappa_4(d_4 - d_1 - d_2)) \right] \times \\ &\times \text{ch}(\kappa_2(d_2 - d_1)) \cos(\kappa_4(d_4 - d_1 - d_2)), \\ \mathfrak{R}'_2 &= \frac{1}{\tilde{k}_1 \tilde{k}_3} \left[\frac{\tilde{k}_5 \tilde{k}_2^2 - \tilde{k}_1 \tilde{k}_3^2}{\tilde{k}_2} - \frac{\tilde{k}_4^2 \tilde{k}_1 + \tilde{k}_3^2 \tilde{k}_5}{\tilde{k}_4} \left(\frac{K_4}{K_3} + \frac{K_3 K_5}{K_1 K_4} \right) \coth(\kappa_2(d_2 - d_1)) \text{tg}(\kappa_4(d_4 - d_1 - d_2)) \right] \times \\ &\times \sinh(\kappa_2(d_2 - d_1)) \cos(\kappa_4(d_4 - d_1 - d_2)), \\ \mathfrak{R}'_3 &= \frac{1}{\tilde{k}_1} \left[\frac{\tilde{k}_2^2 - \tilde{k}_1 \tilde{k}_5}{\tilde{k}_2} - \frac{\tilde{k}_4^2 + \tilde{k}_1 \tilde{k}_5}{\tilde{k}_4} \coth(\kappa_2(d_2 - d_1)) \text{tg}(\kappa_4(d_4 - d_1 - d_2)) \right] \times \\ &\times \sinh(\kappa_2(d_2 - d_1)) \cos(\kappa_4(d_4 - d_1 - d_2)), \\ \mathfrak{R}'_4 &= -\frac{1}{\tilde{k}_1 \tilde{k}_3} \left[\tilde{k}_3^2 + \tilde{k}_1 \tilde{k}_5 - \frac{\tilde{k}_2^2 \tilde{k}_4 \tilde{k}_4 - \tilde{k}_1 \tilde{k}_3^2 \tilde{k}_5}{\kappa_2 \tilde{k}_4} \tanh(\kappa_2(d_2 - d_1)) \text{tg}(\kappa_4(d_4 - d_1 - d_2)) \right] \times \\ &\times \cosh(\kappa_2(d_2 - d_1)) \cos(\kappa_4(d_4 - d_1 - d_2)), \end{aligned}$$

Here: $k_i = \sqrt{2m_i E_i \hbar^{-2}}$.

In case 4, i.e., if the energy of the electrons is lower than the heights of both potential barriers, the transition coefficient is also determined using (3), but in this case, the expressions $\mathfrak{R}_j (j = 1, 2, 3, 4)$ should be replaced by the quantities $\mathfrak{R}''_j (j = 1, 2, 3, 4)$, given below:

$$\begin{aligned} \Re_1'' &= \frac{1}{\tilde{k}_1} \left[\tilde{k}_1 + \tilde{k}_5 + \frac{\tilde{\kappa}_4^2 \tilde{k}_1 + \tilde{k}_5 \tilde{\kappa}_2^2}{\tilde{\kappa}_2 \tilde{\kappa}_4} \tanh(\kappa_2(d_2 - d_1)) \tanh(\tilde{\kappa}_4(d_4 - d_1 - d_2)) \right] \times \\ &\times \cosh(\kappa_2(d_2 - d_1)) \cosh(\kappa_4(d_4 - d_1 - d_2)), \\ \Re_2'' &= \frac{1}{\tilde{k}_1 \tilde{k}_3} \left[\frac{\tilde{k}_5 \tilde{\kappa}_2^2 - \tilde{k}_1 \tilde{\kappa}_3^2}{\tilde{\kappa}_2} + \frac{\tilde{\kappa}_4^2 \tilde{k}_1 - \tilde{k}_3^2 \tilde{k}_5}{\tilde{\kappa}_4} \cath(\kappa_2(d_2 - d_1)) \th(\kappa_4(d_4 - d_1 - d_2)) \right] \times \\ &\times \sinh(\kappa_2(d_2 - d_1)) \cosh(\kappa_4(d_4 - d_1 - d_2)), \\ \Re_3'' &= \frac{1}{\tilde{k}_1} \left[\frac{\tilde{\kappa}_2^2 - \tilde{k}_1 \tilde{k}_5}{\tilde{\kappa}_2} + \frac{\tilde{\kappa}_4^2 - \tilde{k}_1 \tilde{k}_5}{\tilde{\kappa}_4} \cath(\kappa_2(d_2 - d_1)) \tanh(\kappa_4(d_4 - d_1 - d_2)) \right] \times \\ &\times \sinh(\kappa_2(d_2 - d_1)) \cosh(\kappa_4(d_4 - d_1 - d_2)), \\ \Re_4'' &= -\frac{1}{\tilde{k}_1 \tilde{k}_3} \left[\tilde{k}_3^2 + \tilde{k}_1 \tilde{k}_5 - \frac{\tilde{\kappa}_2^2 \tilde{\kappa}_4^2 + \tilde{k}_1 \tilde{k}_3^2 \tilde{k}_5}{\kappa_2 \tilde{\kappa}_4} \tanh(\kappa_2(d_2 - d_1)) \tanh(\kappa_4(d_4 - d_1 - d_2)) \right] \times \\ &\times \cosh(\kappa_2(d_2 - d_1)) \cosh(\kappa_4(d_4 - d_1 - d_2)). \end{aligned}$$

Fig. 3 presents the graphs of the dependence of the transparency coefficient of the potential barriers on the electron energy (in electron-volts) and the ratio of the widths of the two potential barriers when electrons pass below the potential barrier in a five-layer structure considering the Bastard condition, where: in Fig. a) the range of electron energy values is 0.47 eV < E < 0.59 eV, and in Fig. b) it is 0.80 eV < E < 0.95 eV. The following values are used in the calculations: $m_1 = 0.15 \cdot m_0$, $m_2 = 0.0623 \cdot m_0$, $m_3 = 0.0122 \cdot m_0$, $m_4 = 0.12 \cdot m_0$, where is the effective mass of electrons in the 1st, 2nd, 3rd, and 4th layers, respectively, and the widths of the potential wells are 25 nm.

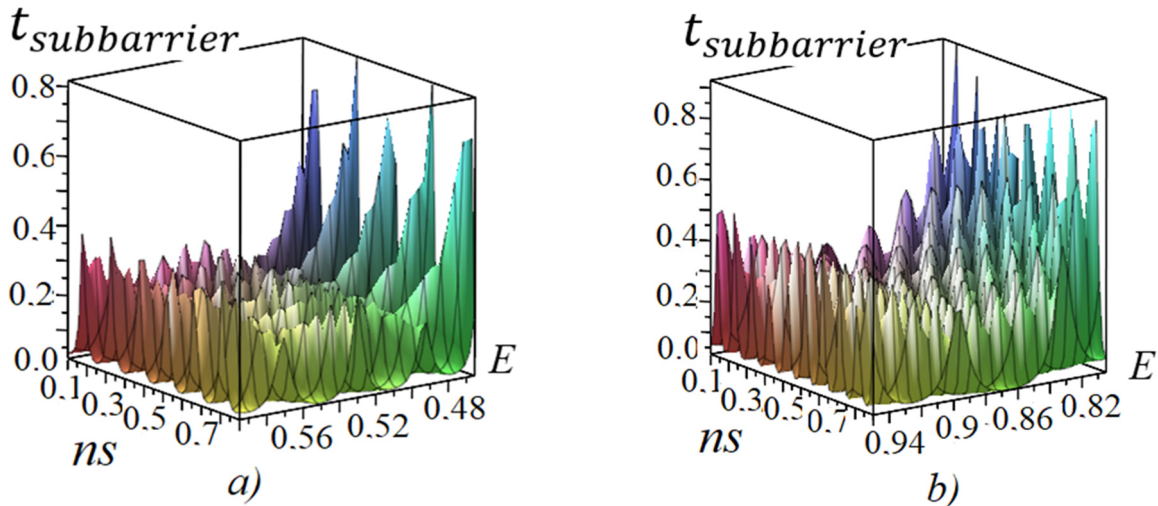


Figure 3. Graph of the dependence of the transparency coefficient of the potential barrier on the electron energy and $ns = \frac{d_2}{d_4}$ when electrons pass below the potential barrier: a) 0.47 eV < E < 0.59 eV; b) 0.80 eV < E < 0.95 eV. In the calculations, the effective masses of electrons in the 1st, 2nd, 3rd, and 4th layers are respectively $m_1 = 0.15 \cdot m_0$, $m_2 = 0.0623 \cdot m_0$, $m_3 = 0.0122 \cdot m_0$, $m_4 = 0.12 \cdot m_0$, and the widths of the potential wells are 25 nm.

ANALYSIS OF THE RESULTS

Now let's consider a five-layer structure with symmetric double potential barriers, i.e., $U_3 = U_5 = 0$, $U_2 = U_4 = U_0$, as shown in Fig. 1, where we assume that the effective masses of charge carriers in all layers are the same. Then the electron transmission coefficient for case 2 is expressed as follows:

$$t_2 = \left\{ 1 + \frac{(k^2 + \kappa^2)^2 \operatorname{sh}^2(\kappa(d_2 - d_1)) [2k\kappa - (k^2 - \kappa^2) \operatorname{th}(\kappa(d_2 - d_1)) \operatorname{tg}(kd_1)]^2}{4k^4 \kappa^4 \operatorname{ch}^{-2}(\kappa(d_2 - d_1)) \cos^{-2}(kd_1)} \right\}^{-1}, \tag{5}$$

where d_1 – is the thickness of the first layer, $\tilde{d}_2 = d_2 - d_1$ is the thickness of the second layer, $k = \sqrt{2m\hbar^{-2}E}$ and $\kappa = \sqrt{2m\hbar^{-2}(U_0 - E)}$

Calculations show that in the aforementioned symmetric five-layer double-barrier semiconductor structure, the transmission coefficient equals unity under the condition.

$$\frac{1-2\xi}{\sqrt{\xi-\xi^2}} = f_R(\xi), \tag{6}$$

where resonant transitions occur, where $f_R(\xi) = 2ctg(\kappa_0\sqrt{1-\xi}(d_2-d_1))ctg(\kappa_0\sqrt{\xi}d_1)$, $\xi = \frac{E}{U_0}$, $\kappa_0 = \sqrt{\frac{2m}{\hbar^2}}U_0$. The latter condition is the condition for observing "resonant" transitions through a symmetric five-layer structure, where the phases and amplitudes of de Broglie waves obey this condition, where the phases of de Broglie waves are determined by the geometric dimensions of the structure, and their amplitudes are determined by the ratio of the carrier energy to the height of the potential barrier.

In Fig. 4, graphs of the dependence of the function $f_R(\xi)$ on $\xi = E/U_0$ are shown for $n_S = \tilde{d}_2/d_1 = 1.01$ (Figure 4a) and $n_S = \tilde{d}_2/d_1 = 1.5$ (Figure 4b) for various values of the effective masses of charge carriers. Here, $d_1 = 50nm$ is the thickness of the first layer, \tilde{d}_2 is the thickness of the second layer, $U_0 = 0.1eV$ is the height of the first potential barrier, m_0 is the mass of a free electron.

In Fig. 4a, it is shown that with an increase in the effective mass of charge carriers, the number of intersections of the values of $f_R(\xi)$ and $\frac{1-2\xi}{\sqrt{\xi-\xi^2}}$ increases, leading to an increase in the value of the transmission coefficient. Thus, in crystals with large effective masses of charge carriers, the transparency coefficient approaches unity. A comparison of the results in Figures 4a and 4b shows that the number of intersections of $f_R(\xi)$ and $\frac{(1-2\xi)}{\sqrt{\xi-\xi^2}}$ in the low-energy region does not change with the increase in the parameter $n_S = \tilde{d}_2/d_1$ in the range of its values from 1.0 to 1.5.

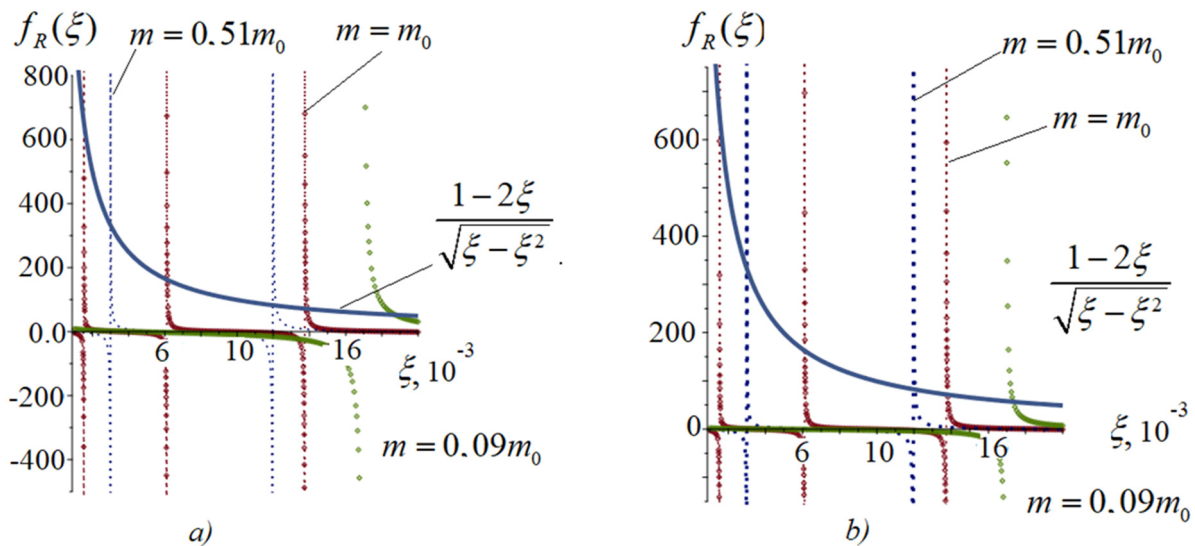


Figure 4. Graphs of the dependence of the function $f_R(\xi)$ on the ratio $\xi = E/U_0$ for $n_S = \tilde{d}_2/d_1 = 1.01$ (a), and $n_S = \tilde{d}_2/d_1 = 1.5$ (b) for various values of the effective masses of electrons. Here, $d_1 = 50nm$ is the thickness of the first layer, \tilde{d}_2 is the thickness of the second layer, $U_0 = 0.1eV$ is the height of the first potential barrier, m_0 is the mass of a free electron.

CONCLUSIONS

In this way, the dependence of the transparency coefficient of the five-layer double-barrier structure on the electron energy and the ratio of the widths of two adjacent potential barriers has been calculated. It has been demonstrated that the extremum of the transparency coefficient significantly depends on the geometric dimensions of the structure layers. In the symmetric five-layer double-barrier semiconductor structure, a condition has been defined under which the numerical value of the transmission coefficient through the potential barriers is approximately unity, indicating a "resonant" electron transition.

It has been shown that the mechanism of such a "resonant" transition is explained by the interference of de Broglie waves of electrons in the potential well. It has been established that the phases of de Broglie waves are determined by the geometric dimensions of the structure, while their amplitudes are determined by the ratio of the carrier energy to the height of the potential barrier.

It has been determined that with an increase in the effective mass of charge carriers, the number of intersections of $f_R(\xi)$ and $\frac{(1-2\xi)}{\sqrt{\xi-\xi^2}}$, increases, which determine the dimensionally-quantized levels where electrons are localized. It has also been shown that the number of intersections of $f_R(\xi)$ and $\frac{(1-2\xi)}{\sqrt{\xi-\xi^2}}$ in the low-energy region remains unchanged for values of $n_S = \tilde{d}_2/d_1$ ranging from 1.0 to 1.5 in crystals with a large effective mass of electrons.

ORCID

- Rustam Y. Rasulov, <https://orcid.org/0000-0002-5512-0654>; ● Voxob R. Rasulov, <https://orcid.org/0000-0001-5255-5612>
- Makhliyo A. Mamatova, <https://orcid.org/0000-0001-6980-9877>; ● Mardonbek X. Nasirov, <https://orcid.org/0000-0002-6811-072X>

REFERENCES

- [1] E.L. Ivchenko, and G.E. Pikus, *Superlattices and other heterostructures. Symmetry and optical phenomena.* (Springer, Berlin, 1995).
- [2] E.L. Ivchenko, *Optical spectroscopy of semiconductor nanostructures.* (Alpha Science, Harrow (UK), 2005), pp. 350. ISBN: 1-84265-150-1.
- [3] V.E. Borisenko, and A.I. Vorobieva, *Nanoelectronics. Part 2. Tutorial.* (BSUIR, Minsk, 2003). (in Russian)
- [4] A.Ya. Shik, L.G. Bakueva, S.F. Musikhin, and S.A. Rykov, *Physics of low-dimensional systems*, edited by A.I. Shik, (Nauka, SPb., 2001). (in Russian)
- [5] V. Timofeev, "Electron correlation phenomena in semiconductor low-dimension structures and nanostructures," *UFN*, **174**, 1109 (2004). <https://doi.org/10.3367/UFNr.0174.200410f.1109>. (in Russian)
- [6] J.N. Davies, *The Physics of low-dimensional semiconductors.* (Cambridge University, 1998).
- [7] V.F. Elesin, and I.Y. Kateev, "High-frequency properties of double-well nanostructures," *Semiconductors*, **42**(5), 571–575 (2008). <https://doi.org/10.1134/S106378260805014X>
- [8] V.F. Elesin, "Resonant tunneling of interacting electrons in an alternating electric field," *JETP*, **144**(11), 1086-1098 (2013). <https://doi.org/10.7868/S0044451013110199>
- [9] V.F. Elesin, "Transient processes in double-barrier nanostructures," *JETP*, **145**(6), 1078-1086 (2014). <https://doi.org/10.7868/S004445101406>
- [10] L.D. Landau, and E.M. Lifshitz, *Quantum Mechanics: Non-Relativistic Theory*, 3rd ed. (Butterworth-Heinemann, 2004).
- [11] G. Bastard, "Theoretical investigations of superlattice band structure in the envelope-function approximation," *Physical Review B*, **25**(12), 7584-7594 (1982). <https://doi.org/10.1103/PhysRevB.25.7584>
- [12] R. Ferreira, and G. Bastard, "Unbound states in quantum heterostructures," *Nanoscale Research Letters*, **1**, 120-136 (2006). <https://doi.org/10.1007/s11671-006-9000-1>
- [13] L.E. Golub, E.L. Ivchenko, and R.Ya. Rasulov, "Intersubband absorption of light in the quantum well of a semiconductor with a complex band structure," *FTP*, **29**(6), 1093-1100 (1995). (in Russian)
- [14] R.Ya. Rasulov, V.R. Rasulov, I.M. Eshboltayev, M. Kuchkarov, and K.K. Urinova, "To the theory of dimensional quantization in crystals in the Kane approximation," *Journal of Physics: Conference Series*, **2697**(1), 012003 (2024). <https://doi.org/10.1088/1742-6596/2697/1/012003>
- [15] R.Ya. Rasulov, V.R. Rasulov, B.B. Akhmedov, I.A. Muminov, and K.K. Urinova, "Dimensional quantization in InSb and GaAs in three-zone model," *Journal of Physics: Conference Series*, **2697**(1), 012005 (2024). <https://doi.org/10.1088/1742-6596/2697/1/012005>
- [16] V.R. Rasulov, "To the theory of electron passage in a semiconductor structure consisting of alternating asymmetric rectangular potential wells and barriers," *Russian Physics Journal*, **59**(10), 1699-1702 (2017). <https://doi.org/10.1007/s11182-017-0963-4>
- [17] R.Ya. Rasulov, V.R. Rasulov, I.M. Eshboltayev, M. Kuchkarov, and K.K. Urinova, "To the theory of dimensional quantization in crystals in the Kane approximation," *Journal of Physics: Conference Series*, **2697**(1), 012003 (2024). <https://doi.org/10.1088/1742-6596/2697/1/012003>
- [18] V.R. Rasulov, R.Y. Rasulov, M.A. Mamatova, and F. Qosimov, "Semiclassical theory of electronic states in multilayer semiconductors. Part 2," *Journal of Physics: Conference Series*, **2388**(1), 012158 (2022). <https://doi.org/10.1088/1742-6596/2388/1/012158>
- [19] Rasulov, R. Y., Rasulov, V. R., Urinova, K. K., Mamatova, M. A., & Akhmedov, B. B. (2024). Single and Multiphoton Optical Transitions in Atomically Thin Layers of Transition Metal Dichalcogenides. *East European Journal of Physics*, (1), 393-397. <https://doi.org/10.26565/2312-4334-2024-1-40>
- [20] S.B. Utamuradova, R.Y. Rasulov, V.R. Rasulov, K.K. Urinova, and K.M. Fayzullaev, "To the Theory of Dimensional Quantization in Narrow-Gap Crystals," *East European Journal of Physics*, (4), 307-310(2023). <https://doi.org/10.26565/2312-4334-2023-4-40>

**ТЕОРІЯ ТРАНСПОРТУ ЕЛЕКТРОНІВ У ДВОБАР'ЄРНИХ П'ЯТИШАРОВИХ
НАПІВПРОВІДНИКОВИХ СТРУКТУРАХ**

Рустам Ю. Расулов^а, Воксоб Р. Расулов^а, Махліїо А. Маматова^а, Мардонбек Х. Насіров^а, Уміда М. Ізомаддінова^б

^а*Ферганський державний університет, Фергана, Узбекистан*



^б*Кокандський державний педагогічний інститут, Коканд, Узбекистан*

Розраховано залежність коефіцієнта прозорості п'ятишарової двобар'єрної структури від енергії електронів та відношення ширин двох сусідніх потенційних бар'єрів. Показано, що екстремум коефіцієнта прозорості істотно залежить від геометричних розмірів шарів структури. У симетричній п'ятишаровій двобар'єрній напівпровідниковій структурі визначено умову виникнення «резонансних» електронних переходів. Показано, що механізм таких (резонансних) переходів пояснюється інтерференцією хвиль де Бройля електронів у потенційній ямі, де фази хвиль де Бройля визначаються геометричними розмірами структури, а їх амплітуди – відношення енергії носія до висоти потенційного бар'єру. Встановлено, що зі збільшенням ефективної маси носіїв заряду кількість перетинів величин $f_R(\xi)$ і $(1-2\xi)/\sqrt{(\xi-\xi^2)}$ зростає. Ці перетини визначають розмірно-квантовані рівні, на яких локалізовані електрони.

Ключові слова: потенційний бар'єр; потенційна яма; двобар'єрна п'ятишарова структура; коефіцієнт пропускання; квантування розміру

THEORY OF LINEAR-CIRCULAR DICHROISM IN MONOATOMIC LAYERS OF TRANSITION METAL DICHALCOGENIDES TAKING INTO ACCOUNT THE RABI EFFECT

 **Rustam Y. Rasulov**,  **Voxob R. Rasulov***,  **Mardon K. Nasirov**,

 **Makhliyo A. Mamatova**,  **Islomjon A. Muminov**

Fergana State University, Fergana, Uzbekistan

**Corresponding Author e-mail: vrrasulov83@gmail.com*

Received April 20, 2024; revised June 18, 2024; accepted June 25, 2024

We have developed a theory of dimensional quantization for nanostructures, both one-dimensional and zero-dimensional, constructed from monoatomic layers of transition metal dichalcogenides (TMDCs). This theory has enabled us to derive expressions for the energy spectra of charge carriers in both even and odd states (relative to coordinate inversion), as these states occur within quantum-confined lines and points of the TMDC monoatomic layers, dependent on their geometric dimensions. Our numerical analysis provides a detailed exploration of the quantum-confined energy states of electrons within these nanostructures, offering insights into their potential applications in advanced nanoelectronic devices. This work not only advances our understanding of the energy characteristics of TMDC monoatomic layers but also contributes to the broader field of material science by exploring the effects of dimensional quantization on electronic properties.

Keywords: *Dimensional quantization; One- and zero-dimensional nanostructure; Monatomic layer of transition metal dichalcogenides; Energy dispersion; Valence band; Conduction band*

PACS: 72.80.Vp, 78.67.Wj, 68.65.Pq, 42.65.Ky

INTRODUCTION

A vital component of modern solid-state physics, both in experimental and theoretical aspects, is the rapidly developing field of low-dimensional systems of charge carriers. In particular, such low-dimensional systems include various nano-sized structures: superlattices, structures with quantum-confined wells, wires, and dots [1-3], the practical development of which is continually growing with the advancement of modern technologies for their fabrication [4]. Alongside, these low-dimensional structures serve as the elemental base of contemporary nanoelectronics and are the subjects of forward-looking research aimed at creating fundamentally new devices for spintronics, opto- and nanoelectronics with unique physical properties [5-8]. The main properties of these quantum-confined structures are determined by the spatial restriction of charge carriers' movement in one or several directions, which leads to the restructuring of the sample's band structure, i.e., the energy dispersion of carriers and other quasiparticles, such as phonons, excitons, and polaritons [9-11].

The unique properties of quantum-confined structures, which distinguish them from bulk samples on which they are based, allow for addressing the following tasks: a) new effects often arise in such structures related to dimensional quantization, and studying them is of undeniable interest from the physical point of view for analyzing the fundamental properties of low-dimensional objects. Secondly, nanostructures can be used to create solid-state devices of a new generation [12].

It should be noted that while many studies have been dedicated to dimensional quantization in crystals with tetrahedral symmetry and their multilayer structures [13-16], the question of quantizing the energy dispersion of charge carriers in monoatomic layers of transition metal dichalcogenides (TMDCs) remains open, which is the focus of this work.

ENERGY DISPERSION IN A QUANTUM WIRE GROWN FROM MONOATOMIC LAYERS OF TRANSITION METAL DICHALCOGENIDES

Fig. 1a, b schematically shows the crystal structure and arrangement of atoms in TMD monolayers. The monomolecular layer D_{3h} is characterized by a point group in which the horizontal plane of specular reflection passes through the layer of metal atoms. The elementary lattice contains a metal atom and two chalcogen atoms located in planes above and below the metal plane. The Brillouin zone is described as a regular hexagon (Fig. 1c). The correct exclusion zone is determined at the points K_{\pm} , which are determined by the time inversion operator with each other. K_{\pm} electron dispersion in the valence band and conduction band near the points has a parabolic form (Fig. 1d). Note that the K_{\pm} inclination of the bands relative to the spin at the points completely disappears. In this case, symmetry with respect to the time reversal operator makes it possible to associate states with opposite spins in different valleys.

The effective Hamiltonian of electrons in bulk transition metal dichalcogenides is represented as [17]

$$H = \begin{pmatrix} E_g/2 & \gamma k_- \\ \gamma k_+ & -E_g/2 \end{pmatrix}, \quad (1)$$

where $k_{\pm} = k_x \pm ik_y$, $\vec{k}_{\perp} = k_{\perp}(\sin\varphi, \cos\varphi)$ - is a two-dimensional wave vector directed along the interface, $\gamma = \hbar(\tilde{E}_g/m^*)^{1/2}$ is the bandgap width, m^* is the effective mass of the charge carriers. For simplicity, in subsequent calculations of wave functions and energy spectra of charge carriers in quantum-confined structures grown based on TMDCs, assume that the effective mass of the charge carriers does not depend on the quantum number of dimensional quantization.

First, consider dimensional quantization in a potential well with infinitely high walls, made from monatomic layers of TMDCs, where it is assumed that the direction of dimensional quantization corresponds to the Ox axis. Then, the Schrödinger equation with Hamiltonian (1) is written as

$$(H - E)\psi = \begin{bmatrix} (E_g/2) - E & \gamma(k_x - ik_y) \\ \gamma(k_x + ik_y) & (-E_g/2) - E \end{bmatrix} \psi = 0, \quad (2)$$

The solution of which is a column matrix with dimensions of 1×2 .

Then, from the equality $\det(H - E) = 0$, it is easy to obtain the Schrödinger equation, with which one can determine the wave function and energy dispersion of charge carriers

$$\frac{\partial^2 \psi}{\partial x^2} + \kappa_y^2 \psi = 0, \quad (3)$$

where $\kappa_y^2 = \frac{1}{\gamma^2}(E^2 - E_y^2)$, $E_y^2 = (E_g/2)^2 + \gamma^2 k_y^2$ and we assume $k_x = -i \frac{\partial}{\partial x}$, k_y - is the wave vector of the charge carriers directed along the Oy axis. Then, by representing solution (3) as a superposition of exponential functions describing de Broglie waves with the wave vector κ_y propagating both along and against the Ox axis, and considering the continuity and uniqueness of the wave function, it is easy to obtain that:

a) The energy dispersion of dimensional quantization in even (with respect to coordinate inversion) states is determined from the condition $e^{i2\kappa_y a} = 1$ ($e^{i\kappa_y a} = \pm 1$). Then, the condition $\cos(\kappa_y a) = +1$ yields the expression for the quantum-confined energy dispersion as

$$E_a^{(\pm)} = \pm \left[(E_g/2)^2 + \gamma^2 k_y^2 + \gamma^2 \frac{\pi^2}{4a^2} n^2 \right]^{1/2}, \quad (4)$$

From the condition $\cos(\kappa_y a) = -1$, we obtain

$$E_b^{(\pm)} = \pm \left[(E_g/2)^2 + \gamma^2 k_y^2 + \gamma^2 \frac{\pi^2}{4a^2} (2n + 1)^2 \right]^{1/2}, \quad (5)$$

where n - is the number of quantum-confined states;

b) The quantum-confined energy dispersion in odd (with respect to coordinate inversion) states is determined from the condition $\sin(\kappa_y a) = 0$, from which we obtain the expression determined by equation (4).

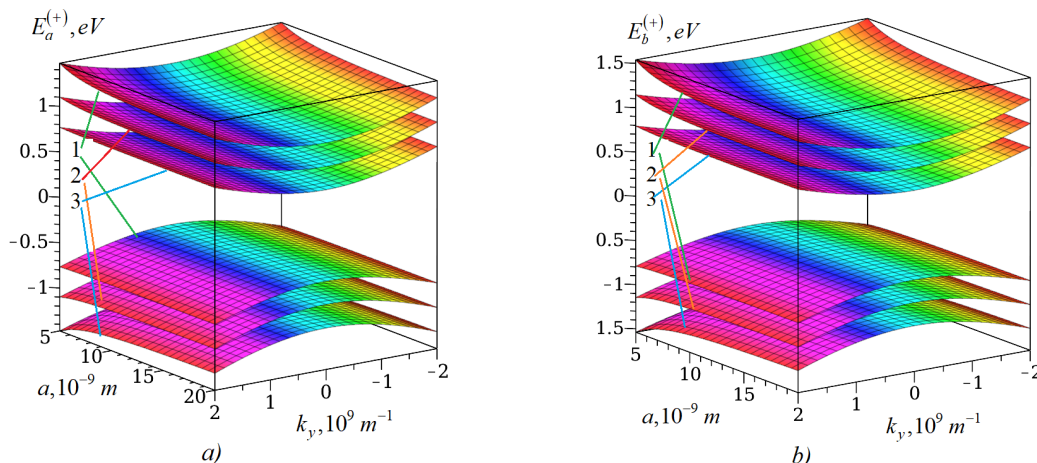


Figure 1. Graphs of the first quantum-confined energy dispersion of charge carriers as a function of well thickness and wave vector of charge carriers in a one-dimensional quantum well in a monatomic layer of various TMDCs, with bandgap widths $E_g = 1$ eV (graph 3), $E_g = 1.5$ eV (graph 2), and $E_g = 2$ eV (graph 3): a) energy dispersion of even states; b) energy dispersion of odd states.

On Fig. 1, the graphs of the first quantum-confined energy dispersion of charge carriers are presented as a function of well thickness and wave vector of charge carriers in a one-dimensional quantum well in a monatomic layer of TMDCs for bandgap widths $E_g = 1$ eV (graph 3), $E_g = 1.5$ eV (graph 2), and $E_g = 2$ eV (graph 3): a) energy dispersion of even states; b) energy dispersion of odd states, where the wave vector of the charge carriers is in units of 10^9 m^{-1} . Calculations were carried out according to formulas (5) and (6) with $m = 0.5 m_0$. It can be seen from Fig. 1 that the energy dispersion

of charge carriers, both for even and odd states, consists of a set of quantum-confined subbands, the shape of which (in momentum space $\hbar k_y$) remains almost unchanged.

In Fig. 2, graphs of the quantum-confined energy dispersion of charge carriers in a one-dimensional quantum well in a monatomic layer of TMDCs are presented for a bandgap width of $E_g = 1\text{ eV}$ (Figures a and b) and $E_g = 1.5\text{ eV}$ (Figures c and d): a) and c) energy dispersion of even states; b) and d) energy dispersion of odd states, where the wave vector of the charge carriers is in units of 10^9 m^{-1} . Calculations were carried out according to formulas (5) and (6) with $m = 0.5 m_0$. It can be seen from Fig. 2 that for both even and odd states, the shape (steepness in momentum space k_y) of the quantum-confined subbands depends on both the subband number and the geometric size (a). In particular, the bandgap width in this quantum-confined structure increases with decreasing a, which is associated with the fact that the energy dispersion of charge carriers is inversely proportional to the magnitude of a.

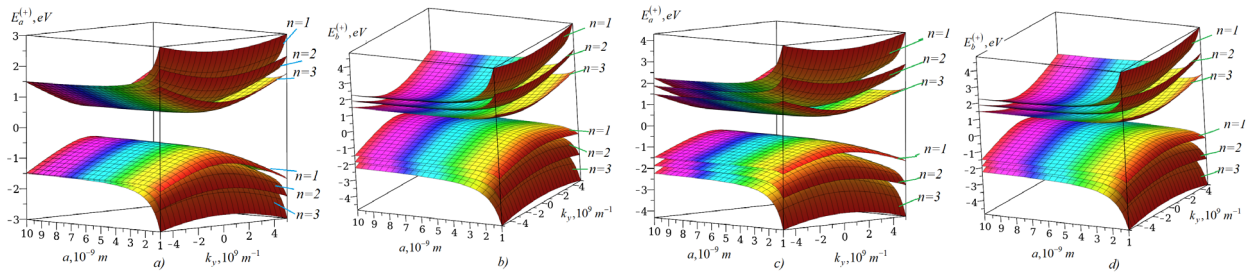


Figure 2. Graphs of the quantum-confined energy dispersion of charge carriers as a function of well thickness and wave vector of charge carriers in a one-dimensional quantum well in a monatomic layer of two TMDCs, with bandgap widths $E_g = 1\text{ eV}$ (Figures a and b) and $E_g = 1.5\text{ eV}$ (Figures c and d): a) and c) energy dispersion of even states; b) and d) energy dispersion of odd states.

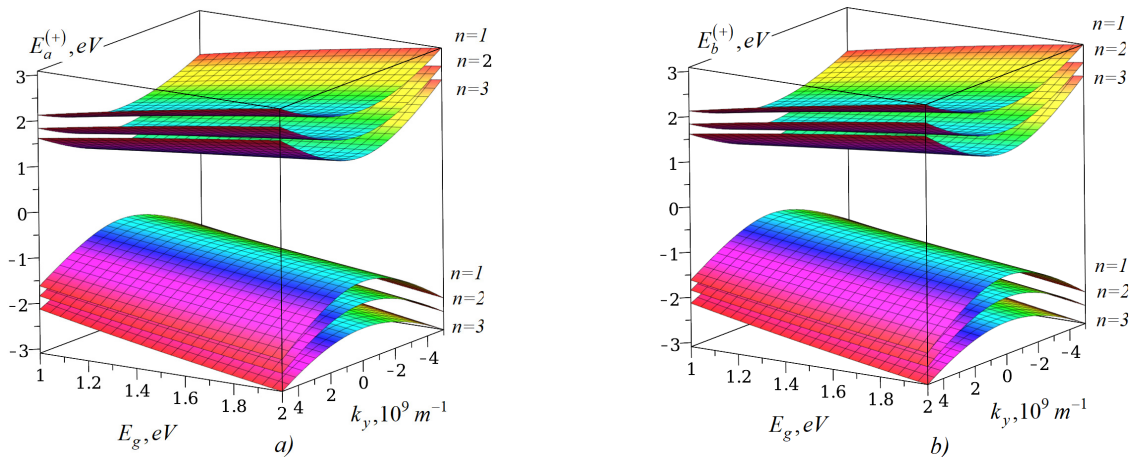


Figure 3. Graphs of the quantum-confined energy dispersion of charge carriers as a function of bandgap width and wave vector of charge carriers in a one-dimensional quantum wire of a monatomic layer of TMDCs, depending on the bandgap width E_g : a) energy dispersion of even states; b) energy dispersion of odd states.

$$E_b^{(\pm)} = \pm \left[(E_g/2)^2 + \gamma^2 k_y^2 + \gamma^2 \frac{\pi^2}{4a^2} (2n + 1)^2 \right]^{1/2}. \quad (6)$$

On Fig. 3, graphs of the quantum-confined energy dispersion of charge carriers in a one-dimensional structure - a quantum wire grown from a monatomic layer of TMDCs are presented as a function of the bandgap width E_g : a) energy dispersion of even states; b) energy dispersion of odd states, where the well thickness is in units of $20 \cdot 10^{-10}\text{ m}$, and the wave vector of the charge carriers is in units of 10^9 m^{-1} . Calculations were carried out according to formulas (5) and (6) with $m = 0.5 m_0$. It can be seen from Fig. 3 that for both even and odd states of the quantum-confined energy dispersion of charge carriers, the narrower the bandgap width of the two-dimensional TMDC layer, the more noticeably the bandgap width of the one-dimensional structure decreases. This is associated with the dimensional quantization of the energy dispersions of the valence band and conduction band separately.

THE ENERGY DISPERSION IN A QUANTUM DOT GROWN FROM A MONATOMIC LAYER OF TMDCS

To calculate the energy spectrum in a quantum dot grown from a monatomic layer of TMDCs, let's choose the potential to be zero.

Where a and b are the thicknesses of the potential well along the Ox and Oy axes, respectively.

Then the Schrödinger equation takes the form:

$$\begin{bmatrix} (E_g/2) - E & \gamma(k_x - ik_y) \\ \gamma(k_x + ik_y) & (-E_g/2) - E \end{bmatrix} \begin{bmatrix} \psi_1 \\ \psi_2 \end{bmatrix} = 0, \quad (7)$$

where $k_x = \frac{1}{i} \frac{\partial}{\partial x}$, $k_y = \frac{1}{i} \frac{\partial}{\partial y}$. Considering the operators of wave vectors, it is easy to

$$\begin{cases} [(E_g/2) - E]\psi_1 + \gamma \left(\frac{1}{i} \frac{\partial \psi_2}{\partial x} - i \frac{1}{i} \frac{\partial \psi_2}{\partial x} \right) = 0, \\ \gamma \left(\frac{1}{i} \frac{\partial \psi_1}{\partial x} + i \frac{1}{i} \frac{\partial \psi_1}{\partial x} \right) + [(-E_g/2) - E]\psi_2 = 0, \end{cases} \quad (8)$$

where ψ_1 and ψ_2 . Considering the operators of wave vectors, it is easy to

$$\psi_1 = -\frac{\gamma}{(E_g/2)-E} \left(\frac{1}{i} \frac{\partial \psi_2}{\partial x} - \frac{\partial \psi_2}{\partial y} \right), \quad \psi_2 = -\frac{\gamma}{(-E_g/2)-E} \left(\frac{1}{i} \frac{\partial \psi_1}{\partial x} + \frac{\partial \psi_1}{\partial y} \right).$$

Then it is easy to obtain the Schrödinger equation for ψ_1

$$\frac{\partial^2 \psi_1}{\partial x^2} + \frac{\partial^2 \psi_1}{\partial y^2} + \frac{E^2 - (E_g/2)^2}{\gamma^2} \psi_1 = 0, \quad (9)$$

assuming $\psi_1(x, y) = X(x) \times Y(y)$, we obtain equations for the functions $X(x)$ and $Y(y)$

$$\frac{\partial^2 X(x)}{\partial x^2} + \kappa^2 X(x) = 0, \quad \frac{\partial^2 Y(y)}{\partial y^2} + \chi^2 Y(y) = 0, \quad (10)$$

where

$$\chi^2 = \frac{E^2 - (E_g/2)^2}{\gamma^2} - \kappa^2, \quad (11)$$

where κ^2 is an unknown quantity determined depending on the boundary conditions of the problem. We seek solutions to the latter equations in the form of

$$X(x) = C_+ e^{i\kappa x} + C_- e^{-i\kappa x}, \quad Y(y) = D_+ e^{i\chi y} + D_- e^{-i\chi y}. \quad (12)$$

From the continuity condition of wave functions for even states with respect to coordinate inversion, we obtain the following relationships:

$$X_+(x) = (2\kappa)^{1/2} e^{-i\kappa a} \frac{\cos(\kappa(x-a))}{[\cos(\kappa a) \cdot \sin(\kappa a) + \kappa a]^{1/2}}, \quad (13)$$

$$Y_+(y) = (2\chi)^{1/2} e^{-i\chi b} \frac{\cos(\chi(x-b))}{[\cos(\chi b) \cdot \sin(\chi b) + \chi \cdot b]^{1/2}}, \quad (14)$$

and for odd states

$$X_-(x) = (2\kappa)^{1/2} e^{-i\kappa a} \frac{\sin(\kappa(x-a))}{[-\cos(\kappa a) \cdot \sin(\kappa a) + \kappa a]^{1/2}}, \quad (15)$$

$$Y_-(y) = (2\chi)^{1/2} e^{-i\chi b} \frac{\sin(\chi(y-b))}{[-\cos(\chi b) \cdot \sin(\chi b) + \chi b]^{1/2}}, \quad (16)$$

From the condition of uniqueness of the wave functions $X(x)$ and $Y(y)$, we obtain expressions for the unknown quantity κ^2 as follows:

a) for even states: $\kappa = \frac{\pi}{2a} (2n_x + 1)$, and for odd states: $\kappa^2 = \frac{\pi^2}{a^2} n_x^2$;

b) for the quantity χ , we have the following relationships: for even states: $\chi = \frac{\pi}{2a} (2n_y + 1)$, and for odd states: $\chi = \frac{\pi}{b} n_y$, where n_x and n_y are integers numbering the quantum-confined states of charge carriers moving in the directions of Ox and Oy .

Taking into account the previous results, we obtain expressions for the quantum-confined energy dispersion of charge carriers in the quantum dot grown from a monoatomic layer of TMDCs as follows:

a) for even states

$$E_{sim}^{(\pm)}(n_x, n_y) = \pm \left\{ (E_g/2)^2 + \gamma^2 \left[\frac{\pi^2}{4a^2} (2n_x + 1)^2 + \frac{\pi^2}{4a^2} (2n_y + 1)^2 \right] \right\}^{1/2}; \quad (17)$$

b) for odd states

$$E_{asim}^{(\pm)}(n_x, n_y) = \pm \left\{ (E_g/2)^2 + \gamma^2 \left[\frac{\pi^2}{a^2} n_x^2 + \frac{\pi^2}{b^2} n_y^2 \right] \right\}^{1/2}. \quad (18)$$

From the last relationships, it is evident that if the quantum dot has symmetric shape (cube), i.e., equal dimensions $a = b$, then both $E_{sim}^{(\pm)}(n_x, n_y)$ and $E_{asim}^{(\pm)}(n_x, n_y)$ are degenerate for certain values of the quantum number. This means

that the energy dispersion of charge carriers is doubly degenerate. Specifically, we have $E_{asymm(sim)}^{(\pm)}(1,2) = E_{asymm(sim)}^{(\pm)}(2,1)$, $E_{asymm(sim)}^{(\pm)}(3,2) = E_{asymm(sim)}^{(\pm)}(2,3)$, and so on. A similar situation occurs in an asymmetric quantum dot (when $a \neq b$) (see Fig. 4).

On Fig. 4, graphs of the quantum-confined energy dispersion of charge carriers in the quantum dot grown from a monatomic layer of TMDCs are presented for band gap widths $E_g = 1 \text{ eV}$ (Figs. a and b) and $E_g = 1.5 \text{ eV}$ (Figs. 4 c and d) as a function of geometric dimensions: a) and c) energy dispersion of even states; b) and d) energy dispersion of odd states. Here, the well thickness is in units of 10^{-9} m , and the wave vector of the charge carriers is in units of 10^9 m^{-1} . The calculations are performed according to formulas (18) and (19) with $m = 0.5 m_0$. The quantum numbers are chosen as (n_x, n_y) . From Fig. 4, it can be observed that: a) the energy dispersion of charge carriers consists of a set of quantum-confined subbands, the values of which depend on both the band parameters and the geometric dimensions of the sample, as well as on the quantum number of the subbands; b) the energy difference between closely spaced quantum-confined subbands increases as the geometric dimensions of the structure decrease, which is related to the fact that the energy dispersion is inversely proportional to the size of the structure; c) some quantum-confined subbands intersect, resulting in a twofold degeneracy, and the regions of intersection depend on both the quantum numbers of the quantum-confined subbands and the aspect ratio (a/b).

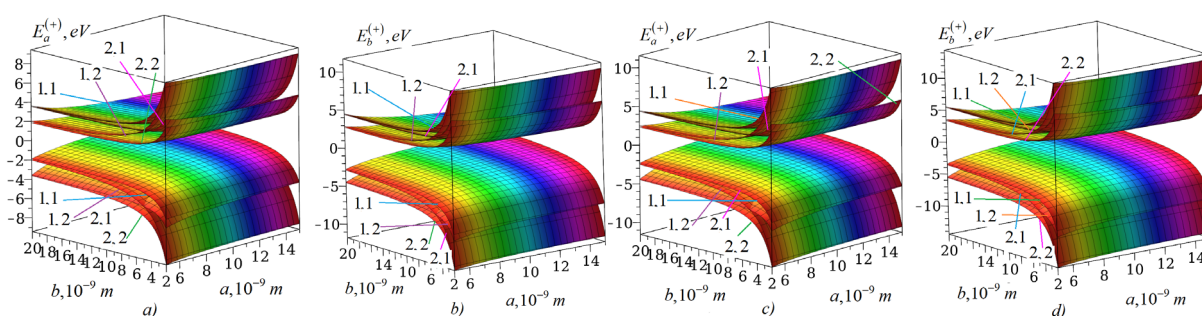


Figure 4. Graphs of the quantum-confined energy dispersion of charge carriers in the quantum dot of a monatomic layer of TMDCs for band gap widths $E_g = 1 \text{ eV}$ (Figs. a and b) and $E_g = 1.5 \text{ eV}$ (Figs. c and d): a) and c) energy dispersion of even states; b) and d) energy dispersion of odd states. The quantum numbers are represented on the figure as (n_x, n_y) .

CONCLUSIONS

A theory of dimensional quantization of energy dispersions of charge carriers has been developed both in the valence band and in the conduction band in zero and one-dimensional nanostructures grown from monolayers of transition metal dichalcogenides (TMDs). Expressions for the energy spectra of charge carriers in one- and zero-dimensional structures have been obtained for both even and odd (with respect to spatial inversion) states, showing that the energy dispersion of charge carriers consists of dimensionally quantized subbands. The energy gap between them increases with decreasing geometric dimensions of the structure, both in quantum wires and quantum dots made from monolayers of TMDs

It should be noted here that the energy dispersion of charge carriers in dimensionally quantized structures grown based on monolayers of transition metal dichalcogenides (TMDs) should depend on temperature and mechanical deformation due to changes in the width of the bandgap, both in bulk [18, 19, 20] and in low-dimensional [21] semiconductors. However, this case requires separate consideration.

ORCID

- Rustam Y. Rasulov, <https://orcid.org/0000-0002-5512-0654>;
 Voxob R. Rasulov, <https://orcid.org/0000-0001-5255-5612>
 Mardon K. Nasirov, <https://orcid.org/0000-0002-6811-072X>;
 Makhliyo A. Mamatova, <https://orcid.org/0000-0001-6980-9877>
 Islomjon A. Muminov, <https://orcid.org/0000-0001-5892-9937>

REFERENCES

- [1] V.V. Mitin, V.A. Kochelap, and M.A. Stroscio, *Introduction to Nanoelectronics Science, Nanotechnology, Engineering, and Applications*, (Cambridge University Press, New York, 2008).
- [2] V.V. Mitin, V.A. Kochelap, and M.A. Stroscio, *Introduction to Optical and Optoelectronic Properties of Nanostructures*, (Cambridge University Press, 2019), pp. 414.
- [3] V.E. Gasumyants, S.N. Lykov, D.A. Pshenai-Severin, S.A. Rykov, and D.A. Firsov, *Dimensional quantization. Part 1. Energy spectrum of nanostructures*, (Publishing House of the Polytechnic University, St. Petersburg, 2008). (in Russian).
- [4] M. Baldo, *Introduction to Nanoelectronics*, (MIT Open Course Ware Publication, Cambridge, MA, 2011).
- [5] Sarma, Sankar Das, "Spintronics: A new class of device based on the quantum of electron spin, rather than on charge, may yield the next generation of microelectronics," *American Scientist*, **89**, 516-523 (2001).
- [6] S.A. Wolf, D.D. Awschalom, R.A. Buhrman, J.M. Daughton, S. Von Molnár, M.L. Roukes, A.Y. Chtchelkanova, et al., "Spintronics: a spin-based electronics vision for the future," *Science*, **294**(5546), 1488-1495 (2001). <https://doi.org/10.1126/science.1065389>

- [7] S.D. Bader, and S.P. Parkin, "Spintronics," *Annual Review of Condensed Matter Physics*, **1**, 71-88 (2010). <https://doi.org/10.1146/annurev-conmatphys-070909-104123>
- [8] W. Han, R.K. Kawakami, and M. Gmitra, "Graphene spintronics," *Nature Nanotechnology*, **9**(10), 794-807 (2014). <https://doi.org/10.1038/nnano.2014.214>
- [9] V.E. Gasumyants, S.N. Lykov, D.A. Pshenai-Severin, and D.A. Firsov, *Dimensional quantization. Part 2. Optical and kinetic properties of semiconductor nanostructures*, (Publishing House of the Polytechnic University, St. Petersburg, 2010). (in Russian).
- [10] V.R. Rasulov, R.Ya. Rasulov, B.B. Akhmedov, I.A. Muminov, and K.K. Urinova, "Dimensional quantization in InSb and GaAs in three-zone model," *Journal of Physics: Conference Series*, **2697**(1), 012005 (2024). <https://doi.org/10.1088/1742-6596/2697/1/012005>
- [11] V.R. Rasulov, R.Ya. Rasulov, I.M. Eshboltayev, M. Kuchkarov, and K.K. Urinova, "To the theory of dimensional quantization in crystals in the Kane approximation," *Journal of Physics: Conference Series*, **2697**(1), 012003 (2024). <https://doi.org/10.1088/1742-6596/2697/1/012003>
- [12] J. Knoch, *Nanoelectronics: From Device Physics and Fabrication Technology to Advanced Transistor Concepts*, 2nd edition, (De Gruyter, 2024).
- [13] R.Y. Rasulov, V.R. Rasulov, and I. Eshboltaev, "Linear-Circular Dichroism of Four-Photon Absorption of Light in Semiconductors with a Complex Valence Band," *Russian Physics Journal*, **58**(12), 1681-1686 (2016). <https://doi.org/10.1007/s11182-016-0702-2>
- [14] V.R. Rasulov, R.Ya. Rasulov, I.M. Eshboltaev, and R.R. Sultonov, "Size Quantization in n-GaP," *Semiconductors*, **54**(4), 429-432 (2020). <https://doi.org/10.1134/S1063782620040132>
- [15] V.R. Rasulov, "To the theory of electron passage in a semiconductor structure consisting of alternating asymmetric rectangular potential wells and barriers," *Russian Physics Journal*, **59**(10), 1699-1702 (2017). <https://doi.org/10.1007/s11182-017-0963-4>
- [16] R.Ya. Rasulov, V.R. Rasulov, N.Z. Mamadaliyeva, and R.R. Sultanov, "Subbarrier and overbarrier electron transfer through multilayer semiconductor structures," *Russian Physics Journal*, **63**(4), 537-546 (2020). <https://doi.org/10.1007/s11182-020-02067-7>
- [17] M.M. Glazov, and E.L. Ivchenko, "Valley Orientation of Electrons and Excitons in Atomically Thin Transition Metal Dichalcogenide Monolayers (Brief Review)," *Journal of Experimental and Theoretical Physics Letters*, **113**(1), 7-17 (2021). <https://doi.org/10.1134/S0021364021010033>
- [18] R. Y. Rasulov, V.R. Rasulov, K.K. Urinova, M.A. Mamatova, and B.B. Akhmedov, "Single and Multiphoton Optical Transitions in Atomically Thin Layers of Transition Metal Dichalcogenides," *East European Journal of Physics*, (1), 393-397. <https://doi.org/10.26565/2312-4334-2024-1-40>
- [19] G.L. Bir, and G.E. Pikus, *Symmetry and Strain-induced Effects in Semiconductors*, (Wiley, New York, 1972). <https://www.scirp.org/reference/ReferencesPapers?ReferenceID=13474>
- [20] Ivchenko, E.L., Rasulov, R.Ya. *Symmetry and real band structure of semiconductors*. (Fan, Tashkent, 1989), pp. 126. <https://koha.lib.tsu.ru/cgi-bin/koha/opac-detail.pl?biblionumber=125752>.
- [21] E.L. Ivchenko, and G.E. Pikus, in: *Superlattices and Other Heterostructures: Symmetry and Optical Phenomena*, 2nd ed. (Springer-Verlag Berlin Heidelberg, 1997), pp. 38-70. <https://doi.org/10.1007/978-3-642-97589-9>

ТЕОРІЯ ЛІНІЙНО-КРУГОВОГО ДИХРОЇЗМУ В ОДНОАТОМНИХ ШАРАХ ДИХАЛЬКОГЕНІДІВ ПЕРЕХІДНИХ МЕТАЛІВ З УРАХУВАННЯМ ЕФЕКТУ РАБІ

Рустам Я. Расулов, Воксоб Р. Расулов, Мардон К. Насіров, Махліїо А. Маматова, Ісломжон А. Мумінов

Ферганський державний університет, Фергана, Узбекистан

Ми розробили теорію розмірного квантування для наноструктур, як одновимірних, так і нульвимірних, побудованих з одноатомних шарів дихалькогенідів перехідних металів (ДПМ). Ця теорія дозволила нам отримати вирази для енергетичних спектрів носіїв заряду як у парних, так і в непарних станах (щодо інверсії координат), оскільки ці стани відбуваються в межах квантово обмежених ліній і точок моноатомних шарів ДПМ, залежно від їхніх геометричних розмірів. Наш чисельний аналіз забезпечує детальне дослідження квантово-обмежених енергетичних станів електронів у цих наноструктурах, пропонуючи розуміння їхнього потенційного застосування в передових наноелектронних пристроях. Ця робота не тільки покращує наше розуміння енергетичних характеристик моноатомних шарів ДПМ, але й робить внесок у ширшу сферу матеріалознавства, досліджуючи вплив розмірного квантування на електронні властивості.

Ключові слова: розмірне квантування; одно- та нульвимірні наноструктура; одноатомний шар дихалькогенідів перехідних металів; енергетична дисперсія; валентна зона; зона провідності

CHARGE TRANSPORT MECHANISM IN IMPLANTED p-GaSe:H⁺ SINGLE CRYSTAL

R.S. Madatov^{a,b}, A.S. Alekperov^{c,d}, S.A. Hacıyeva^a, N.M. Muradov^e,  R.E. Huseynov^{f,*}

^a*Institute of Radiation Problems, Ministry of Science and Education Republic of Azerbaijan, Baku, AZ-1143, Azerbaijan*

^b*National Aviation Academy, Baku, AZ-1045, Azerbaijan*

^c*Azerbaijan State Pedagogical University, Baku, AZ-1000, Azerbaijan*

^d*Western Caspian University, Baku AZ-1001, Azerbaijan*

^e*Military Aerospace Agency Space, Instrumentation Special Design Bureau, Baku, AZ-1141, Azerbaijan*

^f*Institute of Physics, Ministry of Science and Education Republic of Azerbaijan, Baku, AZ-1143, Azerbaijan*

*Corresponding Author e-mail: r.e.huseynov@gmail.com

Received March 19, 2024; revised June 6, 2024; accepted June 16, 2024

The study analysed the impact of radiation defects on p-GaSe single crystal implanted with H⁺ ions (70 keV) on its charge transport mechanism. The research was conducted at 100 K and 300 K in an electric field of 10²-10⁴ V/cm. The study found that the activation energy of charge carriers injected at low temperatures and electric fields $E < 10^3$ V/cm ranged from 0.23-0.39 eV. This was observed due to the trapping of charge carriers in concentration traps of approximately $9 \cdot 10^{13}$ cm⁻³, leading to monopolar injection. In the fields, $E > 10^3$ V/cm, a sharp increase in current was observed, which was explained by the thermal ionisation of local levels following the Frenkel mechanism. The study determined that the charge transport mechanism in GaSe:H⁺ crystals at low temperatures has a non-activated character.

Keywords: *Implantation; GaSe; Single crystal; Frenkel mechanism*

PACS: 72.20.-i; 61.72.Vv

1. INTRODUCTION

Studying the effects of materials under external influences helps us determine their potential applications. Recently, there has been a significant interest in studying functional materials under external influences like pressure, temperature, and radiation. With the development of computing technologies, some processes can now be studied by modelling them. As a result, complex studies are being conducted in this direction [1-5].

Among functional materials, chalcogenide conductors hold a special place. Recently, there has been a wide exploration of these materials' structure, thermal, and electrical properties. Researchers are studying the effects of ionising radiation to expand their application possibilities [6-10]. Radiation defects formed in the crystal lattice under the influence of radiation rays cause changes in the status of the Fermi level in the forbidden zone. Thus, the electrophysical properties of the crystal are modified [11,12].

The nature and properties of radiation defects formed in the crystal, especially in complex semiconductors, depend on the structure of the material and the distribution of primary defects [13,14]. Complex defects formed due to the interaction of radiation defects with structural and additive atoms lead to changes in the electronic characteristics of the crystal. Studying these mechanisms for the first time in layered crystals may allow us to propose a mechanism for purposeful control of the radiation resistance and properties of crystals.

The defects that arise from the impact of charged particles, such as H⁺ and Sb⁺, in complex semiconductors are complex and dynamic. Various factors, including the structure of the crystal lattice, radiation, temperature, and more can cause these defects. To understand these factors and determine the mechanism of charge transport, researchers have chosen to study a GaSe single crystal with a layered structure. To control the distribution of defects in the crystal lattice, they have used H⁺ implantation and thermal infusion methods.

The GaSe single crystal D₆H₄ crystallizes in a hexagonal lattice with spatial plane symmetry. The elementary lattice has two layers, with each layer consisting of two molecules. Weak Van der Waals forces connect the atoms of neighbouring layers. As a result, many physical properties of these crystals are two-dimensional. These crystals' concentration of structural defects is estimated to be around 10¹⁷ cm⁻³.

The effect of γ -quanta on the electrical and photoelectric properties of GaSe single crystals has been partially studied. It has been shown that resulting defects can be located within the layer and in the interlayer region. As a result of their influence, the conductivity increases due to the decrease of the specific reluctance of the crystals. However, information about the nature of radiation defects and the mechanism of their formation was not provided.

To clarify the mechanism of formation of these defects and the effect of external factors on them, researchers studied the effect of H⁺ ions (70 keV) and subsequent thermal infusion on the mechanism of current passage in GaSe single crystal.

2. EXPERIMENTS

The GaSe single crystal was studied, which was obtained using the Bridgman-Stockbarger method. The crystal had p-type conductivity, and its specific resistance was $2 \cdot 10^9$ Ohm·cm and $1 \cdot 10^8$ Ohm·cm in the directions parallel and perpendicular to the layers, respectively, at room temperature.

To investigate the effect of H⁺ ions on the physical properties of the GaSe single crystal, samples were studied before implantation, and after being implanted with $2 \cdot 10^{15}$ ions/cm² of H⁺ ions with an energy of 70 keV, followed by thermal annealing at 100-200°C for 1 hour. A sample thickness of ~ 50 μm was selected for the study. The average penetration depth of a proton with an energy of 70 keV in a GaSe crystal is $R_p \sim 1.40$ μm [12]. The GaSe crystal was implanted with H⁺ ions using an ESU-2 accelerator, with the entire surface of the sample being implanted with H⁺ ions in the indicated doses. The energy of H⁺ ions was 70 keV, and the current density was 0.15 μA/cm².

The samples' volt-ampere characteristics and specific conductance were studied before and after irradiation in the ranges of electric field 10 - 10^4 V/cm and temperature 100-300 K. The distance between the contacts was ~ 50 μm. After the study, the characteristics of the implanted samples were studied again after being annealed (1 hour) in the temperature range of 100-200°C. The obtained results were analysed based on relevant theories.

3. RESULTS AND DISCUSSIONS

Figure 1 displays the volt-ampere characteristics of a GaSe single crystal before implantation (1), after implantation (2) and after thermal annealing (3) at different temperatures. The I-u curves consist of three regions: ohmic, quadratic and sharp growth. It can be observed that after implantation, the transition voltage from the ohmic region to the quadratic region decreases, as shown by curve 2. After thermal annealing of the implanted samples, the transition voltage value increases, as shown by curve 3. These results indicate that the defects caused by H⁺ ion implantation are mainly of an acceptor nature and that the specific resistance of the samples decreases as a result of implantation. This suggests that the injected charge carriers from the electrode cannot fill the traps, and conduction occurs due to thermal ionization of shallow levels. As the voltage applied to the samples increases, the concentration of the injected charge carriers also increases, partially filling the traps. After the traps are filled, there is a sharp increase in the current, up to the quadratic region, as shown by curve 2.

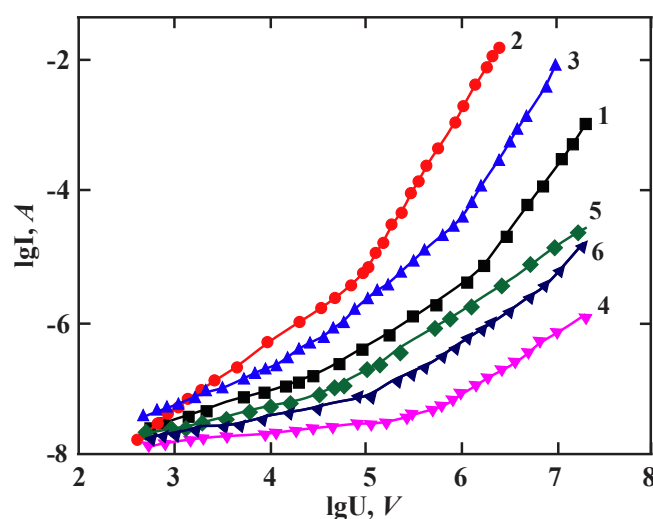


Figure 1. Volt-ampere characteristic of GaSe single crystal at room and nitrogen temperatures. 1. GaSe-initial, 2. GaSe(H⁺), 3. GaSe(H⁺) T = 300 K, 4. GaSe-initial, 5. GaSe(H⁺), 6. GaSe(H⁺) T = 100 K.

Based on [15], the concentrations of charge carriers in equilibrium in GaSe crystals were calculated using Figure 1. The concentration values were determined based on the transition voltage from the ohmic region to the quadratic region for the crystals. The values were found to be $n_0 \sim 2.8 \cdot 10^{10}$ cm⁻³, $6.8 \cdot 10^{11}$ cm⁻³ and $8.2 \cdot 10^{11}$ cm⁻³, respectively. The concentration of traps was also calculated based on the electric capacitance of the sample at an input voltage of $U = 0$ ($C = 5 \cdot 10^{-10}$ F) and the transition voltage of the traps to a fully charged state (U_{tr}). For GaSe crystals from curves 1-3, $N_{t01} = CU_{\text{tr}}/qv = 5 \cdot 10^{14}$ cm⁻³, $N_{t02} = 9 \cdot 10^{13}$ and $N_{t03} = 4 \cdot 10^{13}$ cm⁻³.

The comparison of the calculated parameters shows that the transition voltage decreases from the ohmic region to the quadratic region due to the formation of acceptor-type defects after H⁺ ion implantation. After thermal annealing, the transition voltage at both temperatures increases again (curves 3 and 6). The results of the $I \sim U^n$ dependences show that the defects (Frenkel pair) formed during H⁺ implantation in GaSe crystals interact with structural defects to form acceptor-donor complexes and affect the charge transport mechanism.

A comparison of curves 1-3 in Figure 1 shows that the increase in the current value at the temperature $T = 300$ K after implantation with H⁺ ions is due to the rise in the concentration of acceptor-type levels. The decrease in current after thermal annealing occurs due to the recombination of defects created during implantation. The obtained results correspond to the theory of the current limited by the area of charges, and the parameters of the energy levels are presented in Table 1.

Table 1. Physical parameters of implanted and non-implanted GaSe samples.

Sample	ΔE_t (eV)	$\Delta E_{1/2}$ (eV)	λ (cm)	r_m (cm)	N_t (cm ⁻³)	p_0 (cm ⁻³)
GaSe (pure)	0.23	0.35	$8.9 \cdot 10^{-6}$	$5 \cdot 10^{-6}$	$5 \cdot 10^{14}$	$1.4 \cdot 10^{13}$
GaSe ($5 \cdot 10^5$ ion impl)	0.26	0.32	$7 \cdot 10^{-6}$	$14 \cdot 10^{-6}$	$9 \cdot 10^{13}$	$3.44 \cdot 10^{13}$
GaSe (H ⁺) + TT = 100°	0.28	0.39	$7.9 \cdot 10^{-6}$	$4.5 \cdot 10^{-6}$	$4 \cdot 10^{13}$	$3.55 \cdot 10^{13}$

Figure 2 depicts the temperature dependence of the electrical conductivity of a GaSe crystal before and after implantation at varying electric field intensities. Comparing curves 1-3 reveals that two energy levels (0.19 and 0.34 eV) were present in the forbidden zone before implantation (curve 1). After implantation, the conductivity of the crystal increased partially (curve 2), and new energy levels with ionization energy of 0.18 eV and 0.45 eV were added. However, after thermal infusion at 370 K, the conductivity of the sample decreased, returning to its previous character. By comparing the electrical conductivity values in curves 1-3, it can be concluded that the defects created in the Ga and Se lattices during implantation are dominated by acceptor-type defects and V_{Ga} - vacancy.

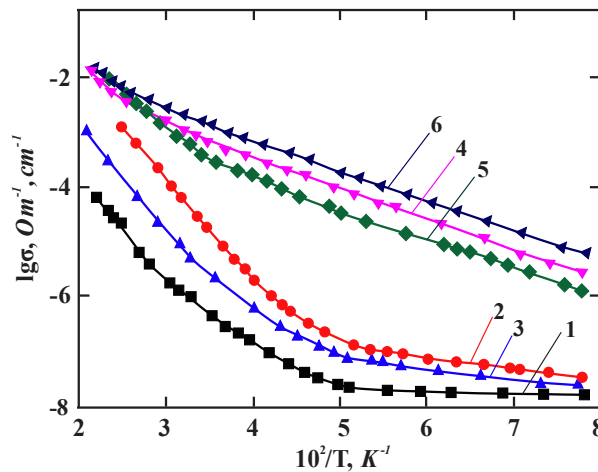


Figure 2. Temperature dependence of the conductivity of GaSe single crystal in the dark at a voltage of 10 V:
 1. GaSe-initial, 2. GaSe(H⁺), 3. GaSe(H⁺)+T; 4. GaSe-primary, 5. GaSe(H⁺), 6. GaSe(H⁺)+T, U = 10 V under the influence of light

Thermal annealing shows that the defects created during implantation undergo partial recombination at low temperatures due to their excitation, and hence the conductivity of the crystal (curve 2) decreases. The nature of the levels formed during implantation is determined by curves 4-6. It has been revealed that since the trapping-filling process takes place at local levels during illumination, the conductivity in the temperature range of 110-300 K increases linearly with increasing temperature. The ionisation energy of the level was calculated for all three cases and is approximately 0.32 eV from the slope of the curves. By comparing curves 1-3, it can be inferred that the defects created in layered crystals during implantation are of the same nature as primary structural defects. After thermal annealing, only the concentration of defects changes, and this fact is compensated during illumination (curves 4-6).

In Figure 3, we can see the temperature dependence of the specific electrical conductivity ($\lg \sigma_F/\sigma_0$) in a GaSe crystal at different voltages (10-40 V). Curves 1-6 in Figure 3 show that the curves' inclination and the current value increase with the electric field intensity. The dependence of $\ln \sigma \sim f(E^{1/2})$ in a GaSe crystal follows Frenkel's theory.

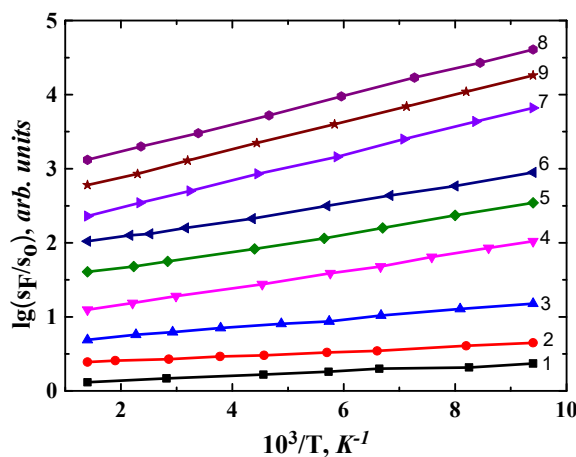


Figure 3. Temperature dependence of the conductivity of GaSe single crystal at different (10-40 V) voltage:
 1. GaSe-initial, 2. GaSe(H⁺), 3. GaSe(H⁺)+T, 4. GaSe-initial, 5. GaSe(H⁺), 6. GaSe(H⁺).

Based on the experimental results, it can be said that conductivity $\sigma_0 = A \exp(-\Delta E_0/2kT)$ in weak electric fields (ohmic region), and in high fields $\sigma_0 = A \exp(-\Delta E_t - 2e(eE/\epsilon)^{1/2}/2ekT)$ follows. The slope of the curve increases as the temperature increases in the dependence of $\ln \sigma \sim f(E^{1/2})$. This result is confirmed in Figure 4, which shows that the dependence $\ln \sigma \sim f(E^{1/2})$ consists of two parts. At weak values of the field intensity ($E < 10^2$ V/cm), the conductivity does not change, and at high values, a linear exponential dependence is observed.

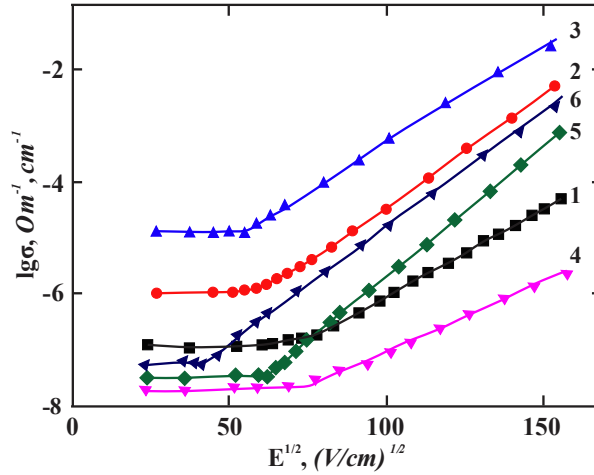


Figure 4. Dependence of conductivity on electric field intensity at different temperatures:
 1. GaSe-initial, 2. GaSe(H⁺), 3. GaSe(H⁺)+T T = 100 K; 4. GaSe-initial, 5. GaSe(H⁺), 6. GaSe(H⁺)+T T = 300 K

When temperature decreases, the transition voltage value increases (curves 4-6). By comparing curves 1-6 at different temperatures, we observe that samples implanted with high field intensities exhibit a less steep curve in low and high-temperature ranges (curve 5). This implies that the activation energy associated with the defect level depends on the field intensity. This effect is more noticeable in implanted samples, and the concentration of electroactive centres influences the activation energy at the local level (Et). The increase in curve steepness due to the electric field indicates a change in the energy of the local levels. Considering the Paul-Frenkel effect, the reduction of Et under the field's influence is determined by the following expression:

$$\Delta E_t(E) = E_t(0) - (e^3 E / \pi \epsilon \epsilon_0)$$

where $\Delta E_t(0)$ is the activation energy of the level corresponding to the ohmic region ($E = 0$), $\Delta E_t(E)$ is the activation energy of the energy level in high fields.

The dependence of $\Delta E_t(E) \sim f(E^{1/2})$ is shown in Fig. 5 for thermally brewed GaSe crystals before and after implantation and after implantation. It can be seen from the figure that the energy of local levels decreases linearly with the increase of $\Delta E_t \sim E^{1/2}$. The activation energy of the trap was determined from the extrapolation of the linear dependence of $\Delta E \sim f(E^{1/2})$ under the condition $E = 0$ and was 0.23, 0.26 and 0.28 eV for low temperatures and 0.35, 0.32 and 0.31 eV for high temperatures, respectively.

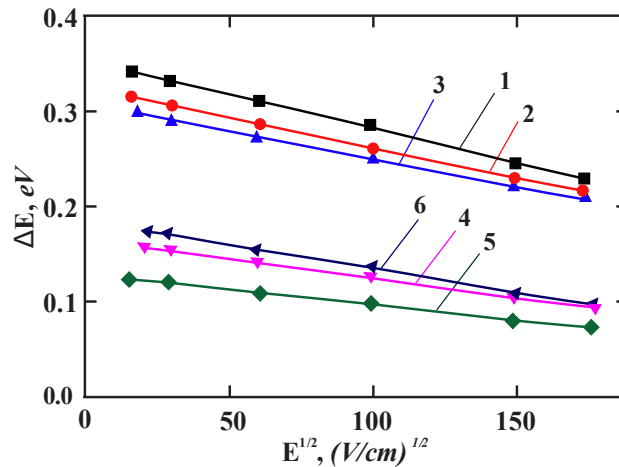


Figure 5. Dependence of trap activation energy ($\Delta E_t(E)$) on $E^{1/2}$ at different temperatures

At values of critical field intensity $E_k > 10^2$ V/cm, the field dependence of electrical conductivity obeys Frenkel's law. It can be seen from Figure 5 that the range of 5-40 V/cm of the field corresponds to the ohmic part, and the dependence of the conductivity on the field intensity is not observed in the dependence of $\ln \sigma \sim E^{1/2}$. After the E_k value of the field intensity,

the conductivity line increases according to the law, and with increasing temperature, the value of E_k and the slope of the dependence decrease. This indicates the thermal ionization of local levels of conductivity and corresponds to Frenkel's theory. Based on the experimental results, the value of the β -Frenkel coefficient was calculated according to the following expression: $\beta = 1/kT (e^3/\pi\epsilon\epsilon_0)^{1/2}$ and the dependence of $\beta \sim 1/T$ is given in Figure 6. It can be seen from the figure that the regularity $\beta \sim 1/T$ is fulfilled in GaSe crystals before implantation and thermally affected. It is proven that the conductivity depends on the intensity of the electric field and the temperature. From the comparison of curves 1-3 in Figure 6, it can be seen that the variation of the Frenkel coefficient β at the same temperature may be related to the possibility of the dielectric permittivity ϵ to accumulate radiation defects in the intralayer and interlayer regions.

The ionization of the local level depends on the field intensity, the height of the potential barrier, and the free escape path of the charge carrier. For this process to occur, the condition $\lambda > r_m$ must be met. To determine the length of the escape path of free carriers (λ) and the distance from the potential barrier to the bottom of the conduction zone (r_m) before and after implantation in a p-GaSe single crystal, as well as after thermal annealing, various conditions were taken into account such as $T = 300$ K, $E_k > 10^3$ V/cm, $\beta = 2.7 \cdot 10^{-2}$ V^{-1/2} cm^{1/2}. The results were obtained and presented in a Table 1.

After comparing the values of λ and r_m given in the table, it can be concluded that the condition $\lambda > r_m$ is fulfilled for pure and thermally brewed GaSe crystals after implantation. This means that the electro-thermal ionization of local levels occurs, leading to an increase in current at values of $E_k > 10^3$ V/cm. In the case of samples implanted with H⁺ ion, the condition $\lambda < r_m$ is met. This indicates that GaSe: H⁺ local levels are filled with injected charge carriers at high field values, and the conductivity is determined by monopolar injection.

Based on these experimental results, the parameters of local energetic levels in GaSe: H⁺ crystals were calculated and presented in Table 1.

A model using proton stimulation was used to explain how H⁺ ion defects are formed in layered crystals. When a proton interacts with an atom, the electrons break away and the atom becomes excited. This causes the electron layer to become ionized, and the nucleus interacts with the crystal lattice, resulting in defects. These defects are known as Frenkel pairs. In semiconductors, the defects caused by protons in the forbidden zone are energy levels that act as recombination centres for charge carriers of acceptor and donor type or non-equilibrium. During irradiation, Ga-vacancies increase the rate of stimulated diffusion of defects. Because these levels are unstable, their mobility and nature depend on temperature, making them important in modifying physical properties. Based on experimental results analyzed in [16-18], a mechanism for defect formation in layered p-GaSe crystals under low-energy H⁺ (70 keV) ions was determined. According to this mechanism, defects are primarily formed at the end of the escape path (radiation loss $\sim 1-2$ keV, escape path ~ 1.4 μ m). The generation of defects (Frenkel pairs) along the trajectory is unequal in terms of volume, and the resulting vacancies and interstitial atoms migrate. The acceptor nature of the defects created during initial irradiation ($2 \cdot 10^{15}$ ions/cm²) leads to an increase in conductivity in the GaSe crystal. As a result of thermal annihilation, the migration rate of interstitial atoms increases, and defects are annihilated in the runaway distance (radiation annihilation), resulting in a decrease in the conductivity of the crystal.

CONCLUSIONS

It investigated how electric field and temperature affect the mechanism of charge transport in GaSe crystal implantation with H⁺ ions and thermally soaked crystals. The study was conducted in the temperature range of 100-200 K, and the following results were determined:

1. During the implantation of 70 keV H⁺ ions into p-GaSe layered crystal, dynamic local point defects are formed at a running distance of ~ 1.5 μ m. When the surface layer undergoes thermal annihilation (100-200 °C) of defects formed, partial annihilation of defects occurs in the lattice due to ion-stimulated diffusion of metastable defects, and defects become stable. This increases the crystal's resistance to radiation.

2. The study determined that local point defects (0.23-0.39) eV and $\sim 9 \cdot 10^{13}$ cm⁻³) formed in the p-GaSe crystal as a result of implantation of H⁺ ions determine the charge transport mechanism in the temperature range of 100-300 K. At electric field values $E_k < 10^3$ V/cm, primary and implanted crystals exhibit monopolar injection. At values of $E > 10^3$ V/cm, an increase in current due to the Frenkel mechanism is observed as a result of thermal ionization of local levels in all crystals. At low temperatures in thermally annealed GaSe:H⁺ crystals, the charge transport mechanism has a non-activated character.

ORCID

© R.E. Huseynov, <https://orcid.org/0000-0003-0636-3948>

REFERENCES

- [1] R.S. Madatov, Sh.G. Gasimov, S.S. Babayev, A.S. Alekperov, I.M. Movsumova, and S.H. Jabarov, "Features of the electrical-conductivity mechanism in γ -Irradiated TlInSe₂ single Crystals under hydrostatic pressure," *Semiconductors*, **54**, 1180-1184 (2020). <https://doi.org/10.1134/S1063782620100206>
- [2] N.T. Dang, D.P. Kozlenko, S.E. Kichanov, S.G. Jabarov, A.I. Mammadov, R.Z. Mekhtieva, and T.L. Phan, et al., "Revealing the formation mechanism and effect of pressure on the magnetic order of multiferroic BiMn₂O₅ through neutron powder diffraction," *Journal of Electronic Materials*, **46**, 3373-3380 (2017). <https://doi.org/10.1007/s11664-017-5351-x>
- [3] H.N. Nazarov, T.O. Rakhimov, and B.B. Yusupov, "Mathematical models of multi-coordinate electromechatronic systems of intellectual robots," *Journal of Modern Technology and Engineering*, **4**(1), 47-51 (2019). <http://jomardpublishing.com/UploadFiles/Files/journals/JTME/V4N1/Nazarov.pdf>

- [4] A.S. Alekperov, A.O. Dashdemirov, A.E. Shumskaya, and S.H. Jabarov, "High-temperature exciton photoconductivity of Ge_{1-x}Nd_xS crystals," *Crystallography Reports*, **66**, 1322-1327 (2021). <https://doi.org/10.1134/S1063774521070026>
- [5] S.H. Jabarov, "High pressure effect on the crystal structure of the BaTiO₃," *International Journal of Modern Physics B*, **33**(30), 1950357 (2019). <https://doi.org/10.1142/S0217979219503570>
- [6] R.S. Madatov, A.S. Alekperov, F.N. Nurmammadova, N.A. Ismayilova, and S.H. Jabarov, "Preparation of n-Si-p-GaSe heterojunctions based on an amorphous GaSe layer without impurities and study of their electrical properties," *East European Journal of Physics*, (1), 322-326 (2024). <https://doi.org/10.26565/2312-4334-2024-1-29>
- [7] Kh.S. Daliev, Sh.B. Utamuradova, J.J. Khamdamov, and Z.E. Bahronkulov, "Electrophysical properties of silicon doped with lutetium," *Advanced Physical Research*, **6**(1), 42-49 (2024). <https://doi.org/10.62476/apr61.49>
- [8] A.S. Alekperov, S.H. Jabarov, M.N. Mirzayev, E.B. Asgerov, N.A. Ismayilova, Y.I. Aliyev, T.T. Thabethe, and N.T. Dang, "Effect of gamma irradiation on microstructure of the layered Ge_{0.995}Nd_{0.005}S," *Modern Physics Letters B*, **33**(09), 1950104 (2019). <https://doi.org/10.1142/S0217984919501045>
- [9] S.R. Azimova, N.M. Abdullayev, Y.I. Aliyev, M.N. Mirzayev, V.A. Skuratov, A.K. Mutali, and S.H. Jabarov, "Study on the thermodynamic behavior of Sb-Te binary systems with swift heavy-ions irradiation at the high temperatures," *Journal of the Korean Physical Society*, **77**, 240-246 (2020). <https://doi.org/10.3938/jkps.77.240>
- [10] G.M. Agamirzayeva, G.G. Huseynov, Y.I. Aliyev, T.T. Abdullayeva, and R.F. Novruzov, "Crystal structure and magnetic properties of the compound Cu₃Fe_{0.5}Se₂," *Advanced Physical Research*, **5**(1), 19-25 (2023). http://jomardpublishing.com/UploadFiles/Files/journals/APR/V5N1/Agamirzayeva_et_al.pdf
- [11] Z.D. Kovalyuk, O.A. Politanska, O.N. Sydor, and V.T. Maslyuk, "Electrical and photoelectric characteristics of structures based on InSe and GaSe layered semiconductors irradiated with 12.5-MeV electrons," *Semiconductors*, **42**, 1292-1297 (2008). <https://doi.org/10.1134/S1063782608110092>
- [12] A.Z. Abasova, R.S. Madatov, and V.I. Stafeyev, *Radiation-stimulated processes in chalcogenide structures*, (Elm, Baku, 2010).
- [13] A.A. Garibov, R.S. Madatov, F.F. Komarov, V.V. Pilko, Yu.M. Mustafayev, F.I. Akhmedov, and M.M. Jakhangirov, "Spectrometry of the Rutherford backscattering of ions and the Raman scattering of light in GaS single crystals irradiated with 140-keV H²⁺ ions," *Semiconductors*, **49**, 586-589 (2015). <https://doi.org/10.1134/S1063782615050073>
- [14] F.F. Komarov, O.V. Mil'chanin, V.V. Pil'ko, and Yu.G. Fokov, "Formation of extended defects in silicon by high-dose implantation of hydrogen ions," *Journal of Surface Investigation. X-ray, Synchrotron and Neutron Techniques*, **4**, 27-30 (2008).
- [15] A.G. Milnes, *Deep impurities in semiconductors*, (N.Y.-London, 1973).
- [16] O.B. Tagiev, and G.A. Kasimova, "Charge transfer in (Ga₂S₃)_{1-x}(Eu₂O₃)_x single crystals in strong electric fields," *Physica Status Solidi (a)*, **128**, 167-174 (1991). <https://doi.org/10.1002/pssa.2211280119>
- [17] R.S. Madatov, G.B. Baylarov, R.M. Mamishova, and U.F. Faradjova, "Effect of γ -radiation defects on the electrophysical properties in the p-CuTlS monocrystal," *Journal of Radiation Researches*, **8**(1), 24-29 (2021). <https://jradres.az/storage/473/4-Journal-of-Radiation-Researches,-vol.8,-No.1,-2021,-pp.24-29.pdf>
- [18] G.J. Dienes, and A.C. Damask, "Radiation enhanced diffusion in solids," *Journal of Applied Physics*, **29**(12), 1713 (1958). <https://doi.org/10.1063/1.1723032>

МЕХАНІЗМ ТРАНСПОРТУ ЗАРЯДУ В ІМПЛАНТОВАНОМУ МОНОКРИСТАЛІ p-GaSe:H⁺

R.C. Madatov^{a,b}, A.S. Alekperov^{c,d}, S.A. Gaczeva^a, H.M. Muradov^e, P.E. Guseynov^f

^aІнститут радіаційних проблем Міністерства науки і освіти Азербайджанської Республіки, Баку, AZ-1143, Азербайджан

^bНаціональна авіаційна академія, Баку, AZ-1045, Азербайджан

^cАзербайджанський державний педагогічний університет, Баку, AZ-1000, Азербайджан

^dЗахіднокаспійський університет, Баку AZ-1001, Азербайджан

^eВійськове аерокосмічне агентство, спеціальне конструкторське бюро приладобудування, Баку, AZ-1141, Азербайджан

^fІнститут фізики Міністерства науки і освіти Азербайджанської Республіки, Баку, AZ-1143, Азербайджан

У дослідженні проаналізовано вплив радіаційних дефектів монокристала p-GaSe, імплантованого іонами H⁺ (70 кеВ), на механізм переносу заряду. Дослідження проводили при 100К і 300К в електричному полі 10²-10⁴ В/см. Дослідження показало, що енергія активації носіїв заряду, інжекттованих при низьких температурах і електричних полях E < 10³ В/см, коливалася в межах 0,23-0,39 еВ. Це спостерігалось через захоплення носіїв заряду в концентраційні пастки приблизно 9·10¹³ см⁻³, що призвело до монополярної інжекції. У полях E > 10³ В/см спостерігалось різке зростання струму, що пояснювалось термоіонізацією локальних рівнів за механізмом Френкеля. Дослідженням встановлено, що механізм переносу заряду в кристалах GaSe:H⁺ при низьких температурах має неактивований характер.

Ключові слова: імплантація; GaSe; монокристал; механізм Френкеля

ANALYSIS OF THE INFLUENCE OF FORMATION OF Pd SILICIDES ON SURFACE LAYERS OF Si ON THE DIFFUSION OF ATOMS OF CONTACTING METAL

D.A. Tashmukhamedova^a, X.E. Abdiev^{a*}, S.T. Gulyamova^a, E.A. Rabbimov^b, B.E. Umirzakov^a

^aTashkent State Technical University named after Islam Karimov, Tashkent, 100095 Republic of Uzbekistan

^bJizzakh Polytechnical Institute, Jizzakh, 130100 Republic of Uzbekistan

*Corresponding Author e-mail: abdiev.xasan.92@bk.ru

Received April 30, 2024; revised June 14, 2024; accepted June 17, 2024

4-probe measurements of surface resistivity, measurements of dark and light current-voltage characteristics, the possibilities of using a thin PdSi film to obtain perfect nano-sized ohmic contacts on the Si(111) surface have been investigated using Auger electron spectroscopy methods in combination with ion etching of the surface. It has been shown that the depth of Ni diffusion in the Ni-Si (111) system is 400 - 500 Å at indoor temperature, and 70 - 80 Å in the Ni-PdSi-Si (111) system. The quality of the ohmic contact in the latter case does not change up to $T = 800$ K and withstands luminous flux illumination up to $F = 1100$ lux. It is shown that the resistivity of the PdSi film passes through a minimum at $T = 900 - 1000$ K. An analysis of the results obtained will be given in the article.

Keywords: Atomic diffusion; Ohmic contact; Luminous flux illumination; Auger spectrum; Resistivity; Sputtering; Luminous flux; Current-voltage characteristic

PACS: 61.72.uj, 68.55.Ln

INTRODUCTION

Physics of multilayer film structures of nanoscale thickness on various substrates has been intensively developing recent years. Such structures can be obtained by molecular beam and gas-phase epitaxy [1, 2], sputtering [3 - 5], ion beam deposition [6] and ion implantation [7 - 9]. Using reflection electron diffraction in combination with layer-by-layer chemical etching, the structure of the Pd-Si interface subjected to heat treatment in the temperature range 330-870 K was studied in [10]. It was revealed that a transition layer (TL) consisting of an amorphous region is formed at the phase interface and the adjacent region of elastically deformed silicon of nanometer thicknesses. The total thickness of the TL is determined by the heat treatment temperature. Three-phase amorphization model was proposed.

The most used type of ethanol vapor sensors are semiconductor-based resistive gas sensors at present time. The use of porous silicon, for example por-Si/Pd, formed by metal-stimulated etching, as a sensitive structure allows the formation of a sensitive element and electronic wiring in a single technological process. The possibility of forming resistive gas sensors using the method of metal-stimulated chemical etching of silicon is presented in [11, 12]. Experimental samples based on porous silicon of p- and n-type conductivity were prepared. An empirical explanation of ethanol sensitivity mechanism of the investigated structures is presented. The possibility of forming a sensitive structure and electronic wiring in a single technological process is shown.

When creating various multilayer and thin-film systems, it is very important to obtain nano-sized contacts with small transition layers [13-15]. Contact systems based on silicides have been used in the development of semiconductor devices, along with traditional ones (nickel, titanium, palladium, platinum, etc.) recent years [16, 17].

It was created an active Pd-Si interface with tunable electronic metal-substrate interaction (EMSI) by growing a thin permeable silica layer on the surface of a non-reducible oxide ZSM-5 (named Pd@SiO₂/ZSM-5) in [18]. The active Pd-Si interface is shown to enhance charge transfer from deposited Si to Pd, creating an electron-rich Pd surface that significantly reduces the activation barriers to O₂ and H₂O.

The authors of [19, 20] showed that low-energy ion implantation is an effective means of creating barrier layers on the Si surface, which allows reducing the penetration depth of the contacting metal into Si.

Development and assessment of the catalytic activity of electrode nanocomposites platinum-porous silicon and palladium-porous silicon, obtained by chemical reduction in microemulsions with a nonionic surface active substances (SAS, or surfactants) - Triton X-100 were carried out in [21]. The thermal stability of thin PdSi films was studied in the temperature range from 300 to 700 °C in [22]. PdSi, in contact with crystalline Si, transforms into Pd₂Si and Si at a temperature of 500-700 °C, which contradicts the equilibrium phase diagram. It has been established that the transformation rate depends on the structure and orientation of Si. When heated above 750 °C, Pd₂Si again transforms into PdSi. However, PdSi is resistant to annealing when in contact with Pd₂Si or an inert SiO₂ substrate. The authors suggest that the transformation of PdSi to Pd₂Si and Si in the presence of crystalline Si occurs due to the lower energy of the Pd₂Si interface compared to the PdSi-Si interface.

During the solid-phase reaction of the Ni(Pd) alloy with Si(100), phase separation of binary silicides Ni and Pd occurs [23]. PdSi monosilicide nucleates at temperatures well below the widely accepted temperature of nucleation of the

binary system. The decrease in nucleation temperature is due to the presence of isomorphous NiSi, which reduces the nucleation interface energy of PdSi. Despite the mutual solubility of NiSi and PdSi, these two binary compounds coexist in the temperature range of 100 °C. Solid solution form of $\text{Ni}_{1-x}\text{Pd}_x\text{Si}$ can be formed only above 700°C, which, in turn, delays the NiSi₂ formation process to a higher temperature due to the entropy of mixing. The authors highlight the general importance of interface energy for nucleation in ternary systems.

The possibility of using a PdSi nanofilm (≤ 250 Å) to create a barrier layer between the contacting metal (Ni) and single-crystalline silicon has been investigated for the first time in this research.

EXPERIMENTAL TECHNIQUE

Single-crystal samples of Si (111) KEF (K – Silicon, E – Electronic conductivity, F – Phosphorus)-4.5 with dimensions of $10 \times 10 \times 1$ mm³, polished and treated in hydrofluoric acid, were used as a substrate. Before the studies, the Si (111) surface was degassed at $T = 1200$ K for 4–5 hours in combination with short-term heating to $T = 1500$ K in a vacuum of no worse than 10^{-7} Pa. Then Pd atoms were deposited onto the Si (111) surface using the SPE method with a thickness of $d \approx 100$ Å. The film deposition rate was preliminarily determined using the AES method in combination with ion etching and was ~ 0.5 Å/min.

Deposition of Pd atoms, heating samples, studies of their composition and parameters of energy bands using the methods of Auger electron and ultraviolet photoelectron spectroscopy (AES and UVES) and measurement of the coefficient of light passing through the sample K have been carried out in the same device, created by the authors of this research at based on the UUVI (Universal ultra-high vacuum installation), under ultra-high vacuum conditions ($P = 10^{-7}$ Pa).

The depth distribution profiles of atoms were determined by the AES method in combination with surface sputtering with Ar^+ ions with $E_0 = 1$ keV at an angle of $10 - 15^\circ$ relative to the surface.

EXPERIMENTAL RESULTS AND DISCUSSION

Polycrystalline Pd₂Si films were obtained in a vacuum of $\sim 10^{-6}$ Pa by deposition of Pd on a Si(111) surface, followed by heating at $T = 1050$ K for 40 minutes. The PdSi film thickness was ~ 200 Å. Then, Ni atoms with a thickness of $d = 600$ Å were deposited onto the surface of pure Si(111) and PdSi/Si(111). Figure 1 shows the dependence of the concentration of nickel atoms C_{Ni} over depth h for the Ni/Si(111) system, obtained after heating the system at different T . Heating of each T is ~ 40 min. It can be seen from Fig. 1 that noticeable interdiffusion of atoms occurs at the Ni/Si(111) interface at indoor temperature. The penetration depth of h Ni into Si is $\sim 400 - 500$ Å. After heating the system to $T = 900$ K, h increased by 3–4 times.

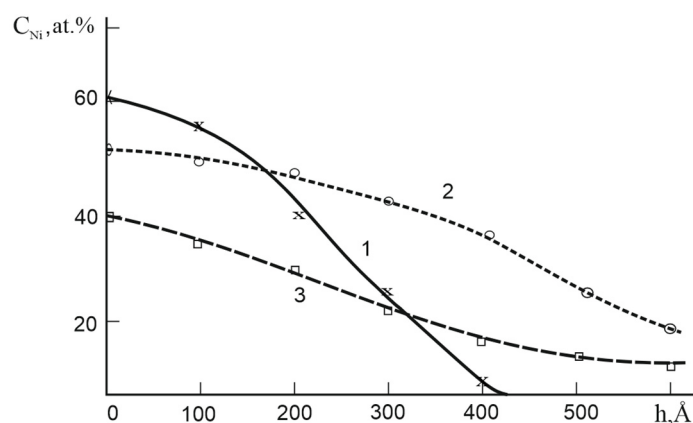


Figure 1. Dependence of C_{Ni} on h for the Ni/Si(111) system, obtained after heating at temperatures T , K: 1-300, 2-600, 3-900

The penetration depth of Ni into the PdSi/Si system is only $70 - 80$ Å in the case of the Ni – PdSi – Si system at indoor temperature (Fig. 2). In this case, no noticeable diffusion of Pd into Ni occurs, and Si atoms penetrate into Ni up to $20 - 30$ Å. The penetration depth of Ni into Si increases to $130 - 150$ Å after heating at $T = 800$ K. Here, the concentration of Si in the Ni film increases noticeably, and Pd atoms are also detected. It should be noted that PdSi films were obtained at $T = 1050$ K. Therefore, the appearance of Pd atoms in the Ni film can be explained as follows. During heating, a significant amount of Ni penetrates into PdSi, which apparently leads to a weakening of the Pd + Si bond and the appearance of a certain number of unbound Pd and Si atoms, consequently their diffusion to Ni. However, this does not lead to a noticeable change in the quality of contact. A significant change in composition and thickness occurs at the Ni/PdSi/Si(111) contact region at $T = 1000$ K. In this case, Ni atoms partially penetrate (Fig. 2, curve 3) into Si.

The dependence $\rho_{\text{PdSi}}(T)$ in the region T from 400 to 1200 K on the resistivity of the contacting layer was studied to clarify the effect of changes in composition at the PdSi/Si interface during heating (Fig. 3). The heating time was ~ 40 min. at each T . It can be seen that the value of ρ up to $T = 1000$ K practically does not change, and then decreases, passing

through a minimum ($\rho = 20 - 30 \mu\Omega \cdot \text{cm}$) it increases sharply at $T = 1000 \text{ K}$. Results of Fig. 3 can be explained as follows. The composition of the film does not change noticeably up to $T = 900 \text{ K}$, therefore ρ_k does not change significantly until this temperature.

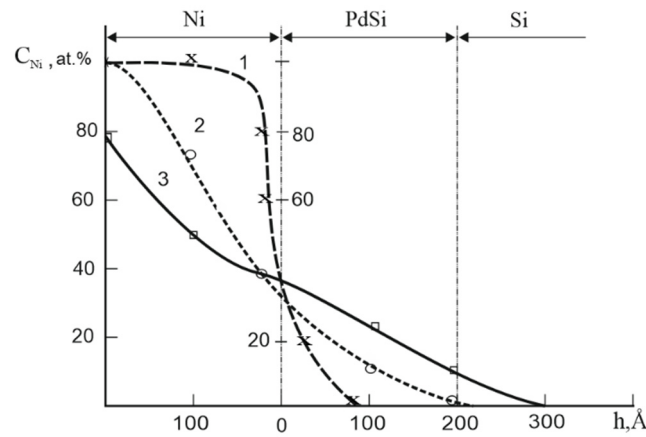


Figure 2. Dependence of C_{Ni} on h for the Ni/PdSi/Si system, obtained after heating at $T, \text{ K}$: 1-300, 2-800, 3-1000.

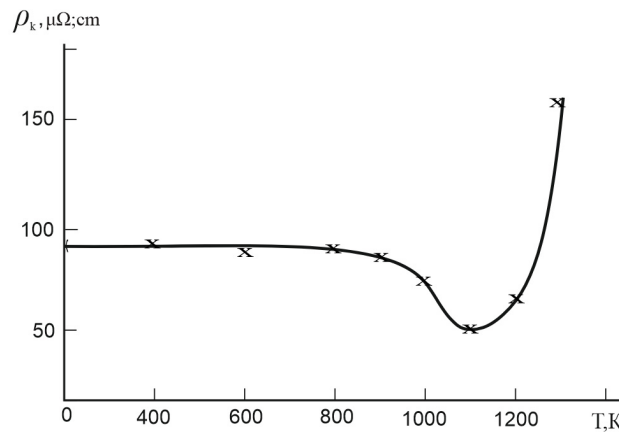


Figure 3. Dependence of the resistivity of the surface of layers of the PdSi/Si(111) system on the heating temperature. Heating time at each T is 40 minutes.

The decrease of ρ in the range $900 - 1000 \text{ K}$ can be associated with some ordering of the structure of the PdSi film and its enrichment with Ni atoms. The sharp increase in ρ of the film at $T \geq 1000 \text{ K}$ is explained first by the formation of PdSi islands, and then by the decomposition of PdSi into components and their evaporation.

Figure 4 shows the dark and light (curves 2 – 4) current-voltage characteristics of the Ni/PdSi/Si(111) system. The measurements were carried out at indoor temperature. It can be seen that at zero illumination ($E_L = 0$), the forward and reverse branches of the current dependence on voltage overlap each other, i.e. there is an ohmic contact.

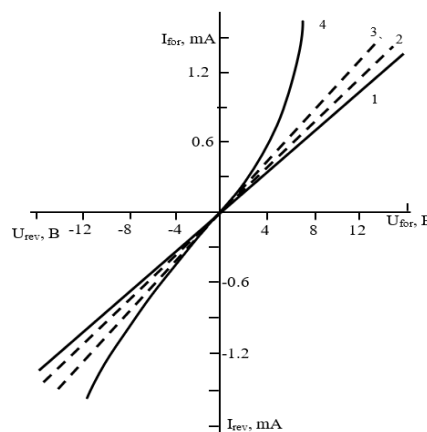


Figure 4. Dependence of p_k on the illumination density, dark and light current-voltage characteristics for the Ni/PdSi/Si system

A slight decrease in contact resistance R_k is observed as E_L increases, which was estimated using the equation:

$$R_k = \left(\frac{\partial I}{\partial U} \right)^{-1} = \frac{\Delta U}{\Delta I} \quad (1)$$

The value of $R = 6 \text{ k}\Omega$ at $E_L = 0$. Illumination of the surface with a luminous flux of up to 1100 lux does not affect the appearance of the curves. Starting from $E_L = 1300 \text{ lux}$, a sharp change in the current-voltage characteristic (CVC) occurs, i.e. the ohmic contact is destroyed.

CONCLUSIONS

It has been discovered for the first time that the presence of a thin layer ($\leq 200 \text{ \AA}$) of palladium silicide on the Si surface sharply reduces (up to 5–6 times) the penetration depth of atoms of the contacting metal (Ni) into Si.

It has been shown that up to $T = 850 - 900 \text{ K}$ the properties of the ohmic contact do not change noticeably.

The dependence of the resistivity ρ of the PdSi film on the heating temperature of the PdSi/Si (111) system has been studied. It has been shown that ρ of the film decreases to a minimum at $T = 950 - 1000 \text{ K}$ and then increases sharply. The latter is explained first (at $T = 1000 - 1100 \text{ K}$) by the transition of a continuous film to an island film, and then (at $T \geq 1100 \text{ K}$) by the decomposition of PdSi into components and their evaporation.

The dark and light current-voltage characteristics of the Ni/PdSi/Si(111) system have been studied. It is shown that the perfection of the ohmic contact practically does not change when illuminating the surface with a luminous flux up to $E_L = 1100 \text{ lux}$.

ORCID

✉ D.A. Tashmukhamedova, <https://orcid.org/0000-0001-5813-7518>; ✉ X.E. Abdiev, <https://orcid.org/0000-0003-3843-1503>

✉ S.T. Gulyamova, <https://orcid.org/0009-0005-4074-2310>; ✉ E.A. Rabbimov, <https://orcid.org/0000-0002-3046-2025>

✉ B.E. Umirzakov, <https://orcid.org/0000-0002-9815-2111>

REFERENCES

- [1] L.L. Chang, and K. Ploog, *Molecular beam epitaxy and heterostructures*, Part of the book series: NSSE, vol. 87 (1985). <https://doi.org/10.1007/978-94-009-5073-3>
- [2] D.A. Tashmukhamedova, *Izvestiya Akademii Nauk. Ser. Fizicheskaya*, **70**(8), 1230 (2006). <https://elibrary.ru/item.asp?id=9296378>. (in Russian)
- [3] Z.Yu. Gotra, *Technology of microelectronic devices: Handbook*, (Radio and communication, Moscow, 1986). <https://rutracker.org/forum/viewtopic.php?t=6090709> (in Russian)
- [4] B.E. Umirzakov, Zh.Sh. Sodikjanov, D.A. Tashmukhamedova, A.A. Abduvayitov, and E. Rabbimov, *Technical Physics Letters*, **47**(8), 620-623 (2021). <https://doi.org/10.1134/S1063785021060262>
- [5] D.A. Tashmukhamedova, and M.B. Yusupjanova, *Journal of Surface Investigation: X-ray, Synchrotron and Neutron Techniques*, **10**(6), 1338-1340 (2016). <https://doi.org/10.1134/S1027451016050438>
- [6] L.B. Gulina, and V.P. Tolstoy, *Synthesis by ion layering*, in: Intl. conf. Glass and solid electrolytes, (St. Petersburg, 1999), pp. 149.
- [7] B.E. Umirzakov, D.A. Tashmukhamedova, and Kh.Kh. Kurbanov, *Tech. Phys.* **58**, 841 (2013). <https://doi.org/10.1134/S1063784213060261>
- [8] Kh.Kh. Boltaev, D.A. Tashmukhamedova, and B.E. Umirzakov, *Journal of Surface Investigation. Xray, Synchrotron and Neutron Techniques*, **8**(2), 326 (2014). <https://doi.org/10.1134/S1027451014010108>
- [9] Y.S. Ergashov, D.A. Tashmukhamedova, and B. E. Umirzakov, *J. Surf. Invest.: X-ray, Synchrotron Neutron Tech.* **11**, 480 (2017). <https://doi.org/10.1134/S1027451017020252>
- [10] P.N. Krilov, A.B. Fedotov, and I.V. Fedotova, "The formation of Pd-Si multilayer interface during heat treatment", *Journal Chemical Physics and Mesoscopics*, **17**(2), 282–286 (2015). https://www.mathnet.ru/php/archive.phtml?wshow=paper&jrnmid=chphm&paperid=35&option_lang=eng&ysclid=lxbrsftlxbx495807277. (in Russian)
- [11] G. Li, X. Zhang, H. Lu, Yanchao, *et al.*, Ethanol sensing properties and reduced sensor resistance using porous Nb₂O₅-TiO₂ n-n junction nanofibers," *Sensors and Actuators B: Chemical*, **283**, 602-612 (2019). <https://doi.org/10.1016/j.snb.2018.12.074>
- [12] G.O. Silakov, E.N. Lazorkina, S.A. Gavrilov, O.V. Volovlikova, A.V. Zheleznyakova, and A.A. Dudin, *Russian Microelectronics*, **52**, 572–576 (2023). <https://doi.org/10.1134/S1063739723070259>
- [13] S.V. Tomilin, and A.S. Yanovsky, *Journal of Nano- and Electronic Physics*, **4**(1), 01013 (2012). <https://core.ac.uk/reader/14056570>
- [14] N.S. Boltovets, V.V. Basanets, V.N. Ivanov, V.A. Krivutsa, V.A. Fesunenکو, and A.V. Tsvir, *Technology and design in electronic equipment*, (4), 35 (1999).
- [15] L.P. Anufriev, V.V. Baranov, Ya.A. Soloviev, and M.V. Tarasikov, *Technology and design in electronic equipment*, (4), 55-56, (2005). <http://dspace.nbu.gov.ua/handle/123456789/53610>. (in Russian)
- [16] A.I. Blesman, and R.B. Burlakov, *Omsk Scientific Bulletin*, 1(163), (2019). <https://doi.org/10.25206/1813-8225-2019-163-50-54>
- [17] V.A. Saladukha, V.A. Pilipenko, V.A. Gorushko, and V.A. Philippenya, "The impact of formation modes of platinum silicide by the quick heat treatment on Schottky diodes parameters," **119**(1), 62-66 (2019). https://libelodoc.bsuir.by/bitstream/123456789/34383/1/Solodukha_Vliyaniye.PDF (in Russian)
- [18] T. Dong, *et al.*, *JACS Au*, **3**(4), 1230-1240 (2023). [10.1021/jacsau.3c00093](https://doi.org/10.1021/jacsau.3c00093)
- [19] D.M. Muradkabilov, D.A. Tashmukhamedova, and B.E. Umirzakov, *J. Surf. Invest.: X-Ray, Synchrotron Neutron Tech.* **7**(5), 967 (2013). <https://doi.org/v10.1134/S1027451013050376>
- [20] B.E. Umirzakov, *Poverkhni.: Fiz., Khim., Mekh.* **9**(2), 119 (1992) (in Russian)

- [21] N.A. Yashtulov, L.N. Patrikeev, V.O. Zenchenko, S.E. Smirnov, M.V. Lebedeva, V.R. Flid, Nanotechnol Russia, **10**, 910–916 (2015). <https://doi.org/10.1134/S1995078015060142>
- [22] B.Y. Tsaur, Appl. Phys. Lett. **37**, 708–711 (1980). <https://doi.org/10.1063/1.92054>
- [23] A. Schrauwen, J. Demeulemeester, A. Kumar, W. Vandervorst, C.M. Comrie, C. Detavernier, K. Temst, et al., Journal of applied physics, **114**, 063518 (2013). <https://doi.org/10.1063/1.4818333>

**АНАЛІЗ ВПЛИВУ УТВОРЕННЯ СИЛІЦИДІВ Pd НА ПОВЕРХНЕВИХ ШАРАХ Si НА ДИФУЗІЮ АТОМІВ
КОНТАКУЮЧОГО МЕТАЛУ**

Д.А. Ташмухамедова^а, Х.Е. Абдієв^а, С.Т. Гулямова^а, Є.А. Рабімов^б, Б.Є. Умірзаков^а

^аТашкентський державний технічний університет імені Іслама Карімова, Ташкент, 100095 Республіка Узбекистан

^бДжизакський політехнічний інститут, Джизак, 130100 Республіка Узбекистан

Методами Оже-електронної спектроскопії досліджено 4-зондові вимірювання питомого поверхневого опору, вимірювання темнових і світлих вольт-амперних характеристик, можливості використання тонкої плівки PdSi для отримання ідеальних нанорозмірних омичних контактів на поверхні Si(111). поєднання з іонним травленням поверхні. Показано, що глибина дифузії Ni в системі Ni-Si (111) становить 400 500 Å при кімнатній температурі та 70 – 80 Å в системі Ni-PdSi-Si (111). Якість омичного контакту в останньому випадку не змінюється до T = 800 K і витримує освітленість світлового потоку до F = 1100 лк. Показано, що питомий опір плівки PdSi проходить через мінімум при T = 900 – 1000 K. Аналіз отриманих результатів наведено в статті.

Ключові слова: атомна дифузія; омичний контакт; освітлення світловим потоком; Оже-спектр; питомий опір; наплення; світловий потік; вольт-амперна характеристика

ANTICIPATING PRESSURE CHANGES IN HALIDES UNDER COMPRESSION

Abhay Prakash Srivastava^{a*},  Brijesh Kumar Pandey^b, Mukesh Upadhyaya^c

^aDepartment of Physics, R. R. Institute of Modern Technology, Lucknow, India

^bDepartment of Physics & Material Science, MMM University of Technology, Gorakhpur (UP), India

^cDepartment of Physics, North Eastern Regional Institute of Science and Technology (NERIST),

Nirjuli (Itanagar) Arunachal Pradesh, India

*Corresponding Author e-mail: abhay.srivastava831@gmail.com

Received April 30, 2024; revised June 8, 2024; accepted June 18, 2024

A new equation of state (NEOS) for Halides has been developed using the theory of lattice potential and the concept of volume dependence of the short-range force constant. The derivation of this equation of state involved the use of the third-order approximation of the lattice potential. A comparative analysis was conducted between the isothermal equations of state, including Vinet EOS, Murnaghan EOS, Holzapfel EOS, Born-Mie EOS, Birch-Murnaghan EOS, and the newly derived NEOS. The NEOS was used to analyze the compression behavior of Halides, and it was found that Vinet EOS and NEOS agreed with the experimental data for Halides up to high compression. However, Murnaghan EOS, Born-Mie EOS, Holzapfel EOS, and Birch-Murnaghan EOS are usually less sensitive to calculating pressure at high compression. It was also observed that for some Halides, such as NaBr and NaI, Vinet EOS could not produce results consistent with experimental findings. In contrast, NEOS consistently produced results that matched the experimental findings for all Halides samples, unequivocally demonstrating its reliability and accuracy.

Keywords: Equation of state (EOS); Vinet EOS; Murnaghan EOS; Holzapfel EOS; Born-Mie EOS; Birch-Murnaghan EOS; New EOS (NEOS); Halides

PACS: 64.10.+h, 62.20.de.

1. INTRODUCTION

Studying ionic and mixed crystals under non-ambient conditions is a crucial aspect of materials science. Owing to their unique properties, ionic crystals and halides, in particular, are scientifically and technologically significant. Researchers have focused on these materials to better understand their behavior under different conditions [1-3].

Understanding the compression behavior of materials is essential to their application in various fields. The equation of state (EOS) is crucial to understanding this. Several potentials and equations of state have been developed to estimate the compression behavior of solids and their thermoelastic properties. These properties are essential in condensed matter physics, geophysics, and ceramic sciences [4-7].

The EOS formulations are based on three thermodynamic parameters: pressure (P), volume (V), and temperature (T). In this research, we have tested the validity of different equations of state, including Vinet EOS, Murnaghan EOS, Holzapfel EOS, Born-Mie EOS, Birch-Murnaghan EOS, and a newly developed isothermal equation of state (NEOS), to calculate the pressure at different compressions [7-10].

Our research aims to provide a comprehensive understanding of the compression behavior of materials under different conditions. We hope our findings will contribute to developing more accurate equations of state and potentials for predicting the behavior of materials under non-ambient conditions [11, 12].

2. METHOD OF ANALYSIS

According to the essential thermodynamics relation [13], the compression-dependent pressure and bulk modulus B_T are expressed as

$$P = -\frac{dW}{dV} \quad (1)$$

And

$$B_T = -V \frac{dP}{dV} = V \frac{d^2W}{dV^2} \quad (2)$$

where B_T is the bulk modulus at constant temperature and W is the crystal lattice potential energy, which can be expressed as a function of the unit cell volume V . The volume of the unit cell in terms of interatomic separation r is given by

$$V = kr^3 \quad (3)$$

where k is the geometrical factor depending on the structure of the solid. Using equation (3) in the equation (1) and second, we get

$$\frac{dW}{dV} = \frac{dW}{dr} \times \frac{dr}{dV} = \frac{1}{3kr^2} \frac{dW}{dr} \tag{4}$$

and

$$V \frac{d^2W}{dV^2} = \frac{1}{9kr} \left[\frac{d^2W}{dr^2} - \frac{2}{r} \frac{dW}{dr} \right] \tag{5}$$

Using equation (1) and (4) in equation (5) then we get

$$V \frac{d^2W}{dV^2} = \frac{1}{9kr} \left(\frac{d^2W}{dr^2} + \frac{2}{r} \frac{dW}{dr} \right) + \frac{4P}{3} \tag{6}$$

Using the standard definition of the short-range force constant A in terms of the Laplacian operator can be given by Born and Huang [14],

$$A = \frac{1}{3} \left[\frac{d^2W}{dr^2} + \frac{2}{r} \frac{dW}{dr} \right] \tag{7}$$

Then equation (6) can be written as

$$V \frac{d^2W}{dV^2} = \frac{A}{3kr} + \frac{4P}{3} \tag{8}$$

The short-range force constant can be expressed as a function of the interatomic separation and lattice volume, and the volume derivative of A have been used in studies on the pressure dependence of the dielectric properties [15]. Using equation (3) and (8), equation (2) can be written as

$$B_T = \frac{A}{3k^{2/3}V^{1/3}} + \frac{4P}{3} \tag{9}$$

Where B_T is the bulk modulus at temperature T .

The pressure derivative of B_T represented by $B'_T = \frac{dB_T}{dP}$ obtained from equation (9) given below

$$B'_T = \left(\frac{4}{3} \frac{P}{B_T} - 1 \right) \left(\frac{V}{A} \frac{dA}{dV} - \frac{5}{3} \right) + \frac{16P}{9B_T} \tag{10}$$

To find the volume dependence of A we consider

$$A = A_0 f \tag{11}$$

Where A_0 is volume independent constant and f is a function of V/V_0 . Now at $P = 0, V = V_0$ we have from equations (9) and (11)

$$\frac{A_0}{3k^{2/3}} = \frac{B_0 V_0^{1/3}}{f_0} \tag{12}$$

Where B_0 is the value of the isothermal bulk modulus at $P = 0$ and f_0 is the value of f at $V = V_0$. Using the definition of B_T and using equation (12) in equation (9), we get

$$-V \left(\frac{dP}{dV} \right)_T = \frac{B_0}{f_0} \left(\frac{V}{V_0} \right)^{-1/3} \times f + \frac{4}{3} P \tag{13}$$

On integrating equation (13), we get

$$P \left(\frac{V}{V_0} \right)^{4/3} = - \frac{B_0}{f_0 V_0} \int_{V_0}^V f dV \tag{14}$$

Equation (14) is the basic equation that leads to the derivation of an EOS. [16]Shanker et al. have shown that the above formulation is valid for all EOS for different types of solid material [17] that equation (14) yields the Born-Mie EOS [18, 19-26] and the Brenan-Stacey EOS [27].

The equation of state can be derived by taking the short-range potential function as inverse or exponential form. In the case of the exponential function, the range force remains finite to the limit of substantial compression (i.e. $V/V_0 \rightarrow 0$) but inverse power function gives infinitely large force. Here, we consider the exponential function $f(V/V_0)$ as

$$f = \frac{V}{V_0} \exp \alpha \left(1 - \frac{V}{V_0} \right) \quad (15)$$

Let $y = 1 - \frac{V}{V_0}$ then

$$f = (1 - y)^{-1} \exp(\alpha y)$$

$$f = (1 + y + y^2 + y^3 + \dots) \exp(\alpha y)$$

The integration of f is so complicated then by the approximation f can be written as

$$f = (1 + y + y^2 + y^3) \exp(\alpha y) \quad (16)$$

At $V = V_0$, $f = f_0 = 1$ and $\alpha = 0$. Using equation (15) in the (14) then we get

$$P = B_0 \left(\frac{V}{V_0} \right)^{-4/3} \int_0^y (1 + y + y^2 + y^3) e^{\alpha y} dy \quad (17)$$

Where B_0 bulk modulus at zero pressure.

Integrating equation (17), we get a new EOS as

$$P = B_0 \left(\frac{V}{V_0} \right)^{-4/3} \left[\frac{(\alpha^3(1 + y + y^2 + y^3) + \alpha^2(-3y^2 - 2y - 1) + \alpha(6y + 2) - 6)e^{\alpha y} - (\alpha^3 - \alpha^2 + 2\alpha - 6)}{\alpha^4} \right] \quad (18)$$

Using the boundary condition $B_T' = B_0'$ at $P = 0$ and $V = V_0$ in equations (11) and (15), then we obtain

$$\alpha = \frac{3B_0' - 8}{3}$$

The Vinet EOS, Murnaghan EOS, Holzapfel EOS, Born-Mie EOS and Birch-Murnaghan third order EOS [25-34] are as follows

$$P = 3B_0 x^{-2} (1 - x) \exp\{\eta(1 - x)\} \quad (19)$$

Where, $x = (V/V_0)^{1/3}$ and $\eta = \frac{3}{2}(B_0' - 1)$

$$P = \frac{B_0}{B_0'} \left[\left(\frac{V}{V_0} \right)^{-B_0'} - 1 \right] \quad (20)$$

$$P = 3B_0 x^{-5} (1 - x) \exp[f(1 - x)] \quad (21)$$

Where $x = (V/V_0)^{1/3}$ and $f = \frac{3}{2}(B_0' - 3)$

$$P = \frac{3B_0}{3B_0' - 8} \left[\left(\frac{V}{V_0} \right)^{\frac{4}{3} - B_0'} - \left(\frac{V}{V_0} \right)^{\frac{4}{3}} \right] \quad (22)$$

$$P = \frac{3B_0}{2} \left[\left(\frac{V}{V_0} \right)^{-7/3} - \left(\frac{V}{V_0} \right)^{-5/3} \right] \left[1 + \frac{3}{4}(B_0' - 4) \left\{ \left(\frac{V}{V_0} \right)^{-2/3} - 1 \right\} \right] \quad (23)$$

The expression given above for P based on different EOS has been used in the present study to obtain the results discussed in the following section.

3. RESULT AND DISCUSSION

The present work has derived a new equation of state using the concept of third-order approximation of lattice potential energy, which is given in equation (18). We extended the calculations to the high compression value to validate our result.

Equations (19), (20), (21), (22), and (23) give the equations of state for Vinet, Murnaghan, Hozapfel, Born-Mie, and Birch-Murnaghan, respectively.

To estimate the compression behavior of Halides and test the validity of said EOS, we have taken NaF, NaCl, NaBr, and NaI samples whose experimental results are available. For computing the compression behavior of different halide samples, we need the input values of isothermal bulk modulus at zero pressure (B_0) and its pressure derivatives (B'_0), which are given in Table 1 [32, 33].

Table1. Values of input data B_0 (GPa), B'_0 (GPa) all at P=0 [32,33].

Solids	B_0	B'_0
NaF	46.5	5.28
NaCl	24	5.39
NaBr	19.9	5.49
NaI	15.1	5.59

The computed results using different EOS for the selected samples of halides are tabulated in Table 2. For further clarity, we have also calculated the deviation of results obtained from different EOS with respect to the available experimental results [34, 35]. The variations of compression corresponding to different pressure P (GPa) for other samples, such as NaF, NaCl, NaBr, and NaI, are shown in Fig. 1, Fig. 2, Fig. 3, and Fig. 4, respectively.

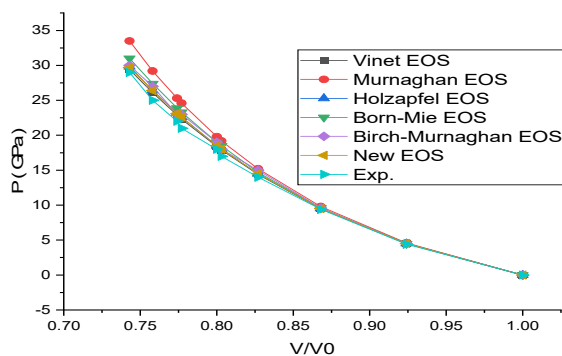


Figure 1. Compression behavior of NaF with pressure

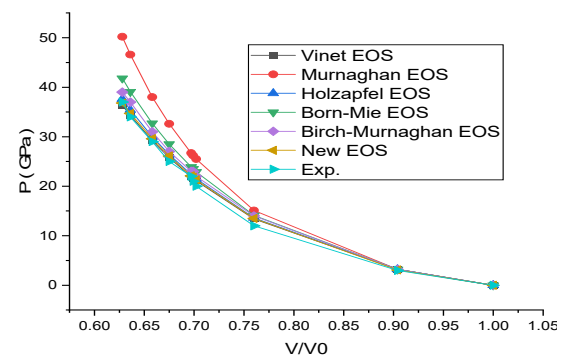


Figure 2. Compression behavior of NaCl with pressure

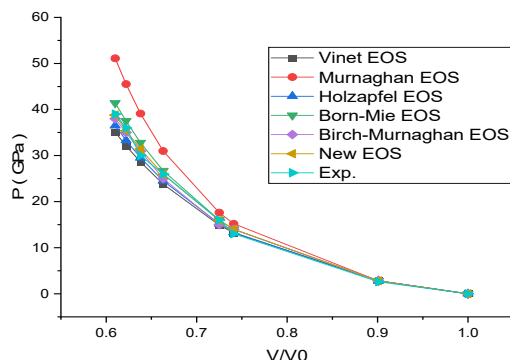


Figure 3. Compression behavior of NaBr with pressure

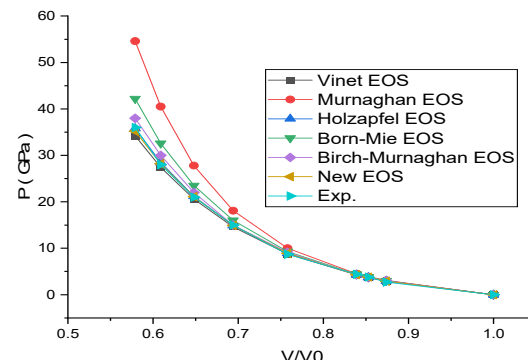


Figure 4. Compression behavior of NaI with pressure

It has also been compared with the experimental results in the respective figures. Deviation plots for different EOS for corresponding samples are shown in Fig. (5-8), respectively. Based on a comparative analysis of various equations of state (EOS), it has been observed that the Vinet EOS and New EOS produce pressure values that are closer to the experimental results than the Murnaghan EOS, Holzapfel EOS, Born-Mie EOS, and Birch-Murnaghan EOS. The analysis also revealed that the Vinet EOS is only suitable for some samples, while the new EOS consistently works for all the samples compared to other EOS. In conclusion, the new EOS is recommended for accurate pressure calculations.

From the close observation of results obtained from different equations of state for NaF, it is evident that all the results are almost the same as experimental values below 14 GPa. Still, above this pressure, the results obtained using all equations of state deviate from experimental values except Vinet EOS and NEOS. The same situation is observed for NaCl. However, when observed in the case of NaBr and NaI at higher pressure, the Vinet EOS also deviates from the experimental results. At the same time, the NEOS is still consistent and very close to the experimental results. The consistent validity of NEOS is based on the fundamental concept considered during its derivation. The NEOS has been derived by considering the third-order approximation of lattice potential energy, while in the other EOSs, only up to second-order approximation has been considered. The choice of third-order approximation not only includes the vibrational behavior of lattice parameters but also gives it the choice of odd and even numbers of higher degree approximations to include the change in the material's behavior at their atomic and molecular level at higher compression. Thus, the consistent NEOS can also be applied to predict the compression behavior of those halides for which the experimental results are still awaited.

Table 2. Values of P (GPa) calculated from Vinet EOS P(V), Murnaghan EOS P(M), Holzappel EOS P(H), Born-Mie EOS (B) and new EOS P(N)

Element	V/V0	P(V)	P(M)	P(H)	P(B)	P(BM)	P(N)	P(Exp.)	% Dev. (V)	% Dev. (M)	% Dev. (H)	% Dev. (B)	% Dev. (BM)	% Dev. (N)
NaF	1	0	0	0	0	0	0	0	0	0	0	0	0	0
	0.924	4.5	4.6	4.5	4.5	4.5	4.5	4.4	2.7	4	2.7	2.3	2.3	2.3
	0.868	9.5	9.8	9.5	9.6	9.6	9.5	9.4	1.1	4	1.4	2.1	2.1	1.1
	0.827	14.4	15.2	14.5	14.7	15	14.5	14	2.9	9	3.6	5	7.1	3.6
	0.803	17.9	19.2	18	18.5	18	18	17	5.3	13	5.9	8.8	5.9	5.9
	0.8	18.4	19.8	18.5	19	19	18.5	18	2.2	10	2.8	5.6	5.6	2.8
	0.777	22.3	24.6	22.6	23.3	23	22.6	21	6.2	17	7.6	11	9.5	7.6
	0.774	22.9	25.3	23.2	23.9	23	23.1	22	4.1	15	5.5	8.6	4.5	5
	0.758	26.1	29.2	26.4	27.4	27	26.4	25	4.4	17	5.6	9.6	8	5.6
	0.743	29.4	33.5	29.8	31	30	29.7	29	1.4	16	2.8	6.9	3.4	2.4
NaCl	1	0	0	0	0	0	0	0	0	0	0	0	0	0
	0.904	3.2	3.2	3.2	3.2	3.2	3.1	3	6.7	7	6.7	6.7	6.7	3.3
	0.76	13.4	15.1	13.6	14.1	14	13.5	12	12	26	13	18	17	13
	0.702	21.1	25.5	21.5	22.9	22	21.3	20	5.5	28	7.5	15	10	6.5
	0.699	21.6	26.2	22	23.5	23	21.8	21	2.9	25	4.8	12	9.5	3.8
	0.697	21.9	26.7	22.4	23.9	23	22.1	22	0	21	1.8	8.6	4.5	0.5
	0.675	25.8	32.6	26.4	28.5	27	26.1	25	3.2	30	5.6	14	8	4.4
	0.658	29.2	38	30	32.7	31	29.6	29	0.7	31	3.4	13	6.9	2.1
	0.636	34.3	46.6	35.4	39.1	37	34.7	34	0.9	37	4.1	15	8.8	2.1
	0.628	36.3	50.2	37.6	41.8	39	36.8	37	2	36	1.6	13	5.4	1
NaBr	1	0	0	0	0	0	0	0	0	0	0	0	0	0
	0.901	2.8	2.8	2.8	2.8	2.8	2.8	2.6	7.7	7.7	7.7	7.7	7.7	7.7
	0.741	13.2	15.2	13.3	14	14	14	13	1.5	17	2.3	7.7	7.7	7.7
	0.725	14.9	17.6	15.2	16	15	15.9	16	7	10	5	0	6.3	1
	0.663	23.8	31	24.5	26.7	25	25.9	26	8	19	5.8	2.7	3.8	0
	0.638	28.6	39.1	29.5	32.8	31	31.4	30	5	30	1.7	9.3	3.3	4.7
	0.622	32.1	45.5	33.3	37.5	35	35.4	36	11	26	7.5	4.2	2.8	2
	0.61	35.1	51.1	36.5	41.4	38	38.8	39	10	31	6.4	6.2	2.6	1
	1	0	0	0	0	0	0	0	0	0	0	0	0	0
	0.874	2.9	3.1	3	3	3	2.9	2.7	7.4	15	11	11	11	7.4
NaI	0.853	3.7	3.9	3.7	3.8	3.7	3.8	3.8	3	3	2.6	0	2.6	0
	0.839	4.3	4.5	4.3	4.4	4.3	4.3	4.4	2	2	2.3	0	2.3	2
	0.758	8.8	10	8.9	9.3	9.1	8.9	8.7	1.1	15	2.3	6.9	4.6	2.3
	0.694	14.6	18.1	14.9	16	15	14.9	15	3	21	0.7	6.7	0	1
	0.648	20.6	27.8	21.2	23.5	22	21.1	21	2	32	1	12	4.8	0.5
	0.609	27.4	40.5	28.5	32.6	30	28.2	28	2	45	1.8	16	7.1	0.7
	0.579	34.2	54.6	35.8	42.2	38	35.2	36	5	52	0.6	17	5.6	2

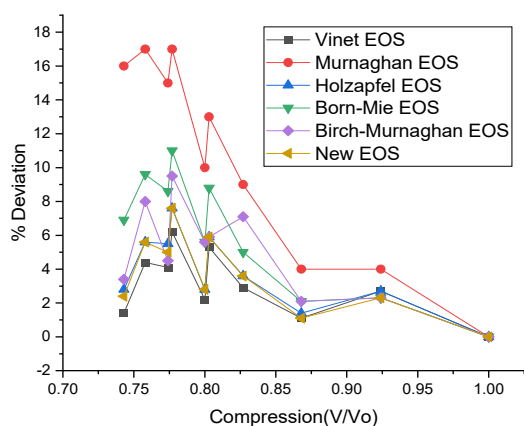


Figure 5. Percentage deviation of calculated value using different EOS with experimental value NaF

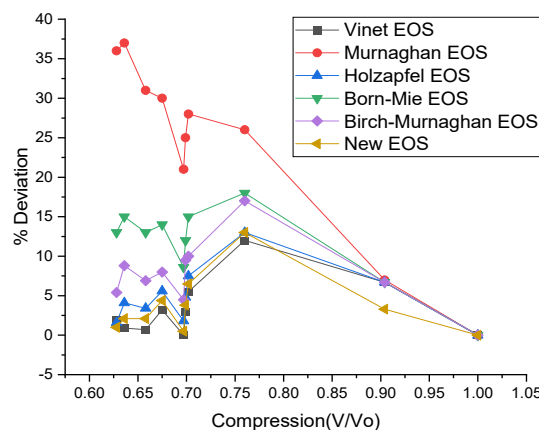


Figure 6. Percentage deviation of calculated value using different EOS with experimental value NaCl

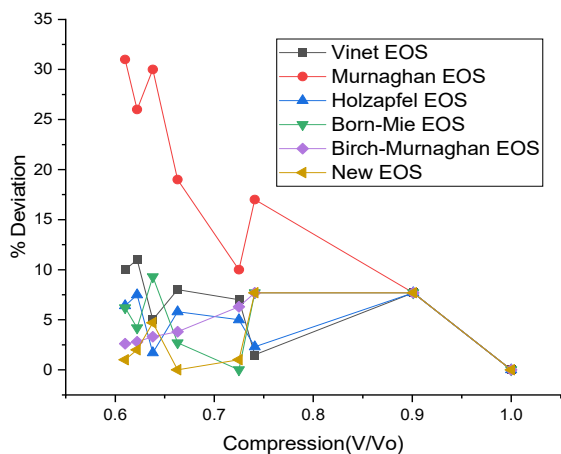


Figure 7. Percentage deviation of calculated value using different EOS with experimental value NaBr

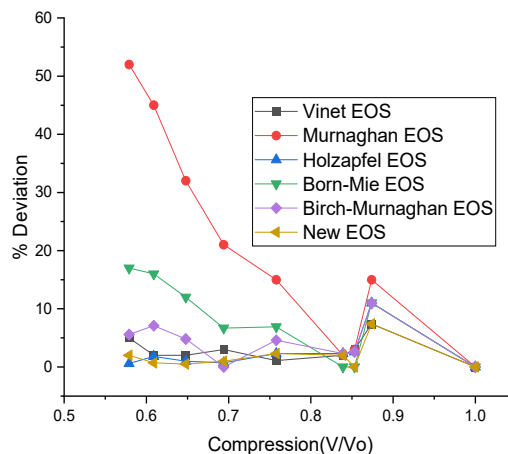


Figure 8. Percentage deviation of calculated value using different EOS with experimental value NaI

4. CONCLUSIONS

The Present study concludes that Vinet EOS and NEOS help calculate the pressure at different compressions. They agree with experimental results at the low-pressure range (≤ 14 GPa) at the higher compression, the Vinet EOS deviates from experimental results. Still, the pressure calculated by NEOS is very close to the experimental values at high compressions. Thus, NEOS is the best EOS for the theoretical prediction of pressure at high compression for Halides.

Ethical Approval. The authors confirm that the manuscript is original and unpublished.

Competing interests. The authors of this paper declare no known financial interests or personal relationships that could have affected the presented work.

Author's Contribution. All the authors collaborated to create the research outline. Abhay P Srivastava performed all the necessary calculations and made the initial manuscript draft. Professor B. K. Pandey provided resources and guidance throughout the project. Finally, Dr. Mukesh Upadhyaya reviewed and edited the final draft.

Funding. The authors have clarified that they do not have any funding agency available for their work.

ORCID

©Brijesh Kumar Pandey, <https://orcid.org/0000-0002-7999-4743>

REFERENCES

- [1] C.K. Dixit, S. Srivastava, P. Singh, and A.K. Pandey, *Nano-Structures & Nano-Objects*, **38**, 101121, (2024). <https://doi.org/10.1016/j.nanoso.2024.101121>
- [2] A.K. Pandey, C.K. Dixit, S. Srivastava, P. Singh, and S. Tripathi, *National Academy Science Letters*, (2023). <https://doi.org/10.1007/s40009-023-01358-0>
- [3] A.G. Davydov, and N.K. Tkachev, *J. Phys. Chem. A*, **126**(23), 3774, (2022). <https://doi.org/10.1021/acs.jpca.2c01614>
- [4] J. Hu, J. Sun, X. Meng, and L.C. Cai, *Acta. Physica Sinica*, **59**(5), 3384 (2010). <https://ir.lzu.edu.cn/handle/262010/116974>
- [5] A. Pandey, S. Srivastava, and C.K. Dixit, *Iranian journal of Science*, **47**, 1877 (2023). <https://doi.org/10.1007/s40995-023-01535-2>
- [6] R.L. Jaiswal, B.K. Pandey, D. Mishra, and H. Fatma, *Int. J. Thermodyn.* **24**, 1 (2021). <https://doi.org/10.5541/ijot.869865>

- [7] P. Singh, B.K. Pandey, S. Mishra, and A.P. Srivastava, *Computational Condensed Matter*, **35**, e00807 (2023). <https://doi.org/10.1016/j.cocom.2023.e00807>
- [8] B.K. Pandey, C.K. Singh, and A.K. Pandey, in: *New Ideas Concerning Science and Technology*, vol. **13**, (2021). pp. 126-131. <https://doi.org/10.9734/bpi/nicst/v13/8362D>
- [9] P.K. Singh, *Computational Condensed Matter*, **31**, e00678 (2022). <https://doi.org/10.1016/j.cocom.2022.e00678>
- [10] R. Gupta, and M. Gupta, *Bulletin of Materials Science*, **44**, 218 (2021). <https://doi.org/10.1007/s12034-021-02503-5>
- [11] S. Srivastava, A.K. Pandey, and C.K. Dixit, *Solid State Communication*, **377**, 115387 (2023). <https://doi.org/10.1016/j.ssc.2023.115387>
- [12] P. Dulari, *International Journal of Mathematics and Physics*, **10**(2), 57 (2019). <https://doi.org/10.26577/ijmph-2019-i2-9>
- [13] F.D. Stacey, and P.M. Davis, *Phys. Earth Planet. Inter.* **142**, 137 (2004). <https://doi.org/10.1016/j.pepi.2004.02.003>
- [14] M. Born, and K. Huang, *Dynamical Theory of Crystal Lattices*, (Oxford University Press, New York, 1954).
- [15] J. Shanker, and S. Dixit, *Phys. Status Solidi (a)*, **123**, 17 (1991). <https://doi.org/10.1002/pssa.2211230102>
- [16] J. Shanker, S.S. Kushwah, and P. Kumar, *Physica B: Condensed Matter*, **239**, 337 (1997). [https://doi.org/10.1016/S0921-4526\(97\)00349-9](https://doi.org/10.1016/S0921-4526(97)00349-9)
- [17] O.L. Anderson, *J. Geophys. Res.* **75**, 2719 (1970). <https://doi.org/10.1029/JB075i014p02719>
- [18] B. J. Brennan, F.D. Stacey, *J. Geophys. Res.* **84**, 5535 (1979). <https://doi.org/10.1029/JB084iB10p05535>
- [19] A. O. L., *Equation of State of Solids for Geophysics and Ceramic Science*, (Oxford Univ. Press, New York, 1995).
- [20] B.W. Dodson, *Phys. Rev. B.* **35**(6), 2619 (1987). <https://doi.org/10.1103/PhysRevB.35.2619>
- [21] F. Birch, *J. Geophys. Res.* **57**(2), 227 (1952). <https://doi.org/10.1029/JZ057i002p00227>
- [22] J. Hama, K. Suito, and N. Kawakami, *Phys. Rev. B.* **39**(5), 3351 (1989). <https://doi.org/10.1103/PhysRevB.39.3351>
- [23] M. Kumar, and S.S. Bedi, *Journal of Physics and Chemistry of Solids*, **57**(1), 133 (1996). [https://doi.org/10.1016/0022-3697\(95\)00150-6](https://doi.org/10.1016/0022-3697(95)00150-6)
- [24] J.H. Rose, J.R. Smith, and J. Ferrante, *Phys. Rev. B.* **28**(4), 1835 (1983). <https://doi.org/10.1103/PhysRevB.28.1835>
- [25] O.L. Anderson, *J. Phys. Chem. Solids*, **58**(2), 335 (1997). [https://doi.org/10.1016/S0022-3697\(96\)00115-1](https://doi.org/10.1016/S0022-3697(96)00115-1)
- [26] A.V. Singh, J.C. Sharma, and J. Shanker, *Phys. B.* **94**(3), 331 (1978). [https://doi.org/10.1016/0378-4363\(78\)90039-6](https://doi.org/10.1016/0378-4363(78)90039-6)
- [27] Y. Sato-Sorensen, *J. Geophys. Res.* **88**(B4), 3543 (1983). <https://doi.org/10.1029/JB088iB04p03543>
- [28] Q. Liu, and Z.M. Niu, *Int. J. Thermophys.* **33**, 2267 (2012). <https://doi.org/10.1007/s10765-012-1288-8>
- [29] K. Kholiya, J. Chandra, and S. Verma, *The Scientific World Journal*, **2014**, 289353 (2014). <http://dx.doi.org/10.1155/2014/289353>
- [30] P.K. Singh, *Indian Journal of Pure and Applied Physics*, **48**, 403 (2010).
- [31] M.A. Mohammed, and H.B. Mohammed, *Advances in Condensed Matter Physics*, **2023**, 9518475 (2023). <https://doi.org/10.1155/2023/9518475>
- [32] R.W. Roberts, and C.S. Smith, *J. Phys. Chem. Solids*, **31**, 619 (1970). [https://doi.org/10.1016/0022-3697\(70\)90196-4](https://doi.org/10.1016/0022-3697(70)90196-4)
- [33] C.S. Smith, and L.S. Cain, *J. Phys. Chem. Solids*, **36**, 205 (1975). [https://doi.org/10.1016/0022-3697\(75\)90010-4](https://doi.org/10.1016/0022-3697(75)90010-4)
- [34] S.N. Vaidya, and G.C. Kennedy, *J. Phys. Chem. Solids*, **32**, 951 (1971). [https://doi.org/10.1016/S0022-3697\(71\)80340-2](https://doi.org/10.1016/S0022-3697(71)80340-2)
- [35] Y.Sato-Sorensen, *J. Geophys. Res.* **88**, 3543 (1983). <https://doi.org/10.1029/JB088iB04p03543>

ПРОГНОЗУВАННЯ ЗМІНИ ТИСКУ В ГАЛОЇДАХ ПІД СТИСНЕННЯМ

Абхай Пракаш Шривастава^a, Брієш Кумар Пандей^b, Мукеш Упадх'я^c

^aКафедра фізики, Інститут сучасних технологій P. P., Лакхнау, Індія

^bКафедра фізики та матеріалознавства, Технологічний університет МММ, Горакхпур (UP), Індія


^cКафедра фізики, Північно-Східний регіональний інститут науки і технологій (NERIST),

Нірджулі (Ітанагар) Аруначал-Прадеш, Індія

Нове рівняння стану (NEOS) для галогенідів було розроблено з використанням теорії потенціалу ґратки та концепції об'ємної залежності короткодіючої силової постійної. Виведення цього рівняння стану передбачало використання третього порядку наближення потенціалу ґратки. Було проведено порівняльний аналіз між ізотермічними рівняннями стану, включаючи EOS Віне, EOS Мурнагана, EOS Хольцапфеля, EOS Борна-Мі, EOS Берча-Мурнагана та нещодавно отриману NEOS. NEOS використовувався для аналізу поведінки стиснення галогенідів, і було виявлено, що Vinet EOS і NEOS узгоджуються з експериментальними даними для галогенідів до високого стиснення. Однак EOS Мурнагана, EOS Борна-Мі, EOS Хольцапфеля та EOS Берча-Мурнагана зазвичай менш чутливі до обчислення тиску при високому стисненні. Було також помічено, що для деяких галогенідів, таких як NaBr і NaI, Vinet EOS не може дати результати, які відповідають експериментальним висновкам. Навпаки, NEOS послідовно давав результати, які збігалися з експериментальними результатами для всіх зразків галогенідів, недвозначно демонструючи свою надійність і точність.

Ключові слова: рівняння стану (EOS); Vinet EOS; Murnaghan EOS; Holzappel EOS; Born-Mie EOS; Бірч-Мурнаган EOS; новий EOS (NEOS); галогіди

STUDY OF PHOTOCONDUCTIVITY OF THIN FILMS OF CADMIUM SELENIDE OBTAINED BY CHEMICAL DEPOSITION

L.N. Ibrahimova^a, N.M. Abdullayev^b, N.A. Gardashbeyova^a, A.S. Alekperov^{c,d},
S.R. Azimova^b,  Y.I. Aliyev^{c,d*}

^a Nakhchivan State University, Nakhchivan, AZ-7012, Azerbaijan

^b Institute of Physics, Ministry of Science and Education of Azerbaijan, Baku, AZ-1143, Azerbaijan

^c Azerbaijan State Pedagogical University, Baku, AZ-1000, Azerbaijan

^d Western Caspian University, Baku, AZ-1001, Azerbaijan

*Corresponding Author e-mail: yusifafshar@gmail.com

Received May 1, 2024; revised June 13, 2024; accepted June 18, 2024

In this work, the photoconductivity (PC) spectrum of thin CdSe films was studied. In the course of studies on glass substrates, thin films of cadmium and selenium with a thickness of $h = 200$ nm and $h = 400$ nm were selected. The thickness of the samples obtained by chemical deposition was determined by the gravimetric method. Since CdSe crystal is a light-sensitive semiconductor material, the photoconductivity of thin films has been studied. The spectra obtained during studies carried out at a wavelength $\lambda = 600$ -1100 nm were analyzed. It has been established that the spectrum is chaotic, since in the $h = 200$ nm layers the phase is not completely formed. In the layers $h = 400$ nm, a maximum centered at the wavelength $\lambda = 710$ nm was recorded.

Keywords: Chemical deposition; CdSe; Thin film; Photoelectricity spectrum; Band gap

PACS: 73.50.Pz, 73.61.-r

INTRODUCTION

Chalcogenide semiconductors occupy a special place among functional materials. Their interesting electrical and optical properties have been widely studied. It is established that changing the atoms in this crystal structure causes a change in the electronic configuration. Therefore, both the crystal structure and the electronic structure of chalcogenides are studied theoretically and experimentally [1-5]. The study of crystal structure, phase transitions and electronic processes determines the possibilities of using these materials. It is very important to study these processes in binary semiconductors, obtain new systems with cation-cation and anion-anion substitutions in these compositions, and predict and control in advance the processes occurring in these systems [6-9].

Cadmium selenide is one of the most studied chalcogenide semiconductors. This compound crystallizes in various modifications. It has been established that CdSe is an n-type semiconductor substance; in the sphalerite phase, this compound has a cubic crystal structure with space group F43m and $E_g = 1.74$ eV [10]. In the wurtzite phase, it has a hexagonal crystal structure with space group P63mc and $E_g = 1.80$ eV [11]. Therefore, this material is used when purchasing various converters and solar panels in modern electronics.

Recently, electronic processes in thin layers of semiconductor materials have been studied. It has been established that materials retain their structural properties when producing thin layers [12,13]. The discovery of functional properties at small sizes makes it possible to obtain smaller converters based on them, which leads to the miniaturization of instruments and devices. Therefore, both the structural properties and various physical properties of thin layers of CdSe compounds are studied using modern research methods [14-17]. The processes of phase formation in thin layers of this compound were studied in the course of structural studies carried out by X-ray diffraction. It has been established that with increasing thickness, the process of phase formation begins in thin layers of cadmium selenide, and the phase corresponding to the CdSe compound is completely formed in the resulting layers with a thickness of $h = 400$ nm [14]. Although both the structural properties and a number of optical properties of these thin films have been studied, the photoelectric properties have not been studied. Interesting optical properties have also been discovered for thin CdS films with similar chemical shape and physical properties [17, 18]. Thus, CdSe thin films are expected to exhibit interesting photovoltaic properties with potential for practical applications.

It is known that the process of phase formation in thin CdSe films occurs at $h \geq 400$ nm. Therefore, to study the photoelectric properties, one sample from each phase was selected. The photoelectric properties of thin films with a thickness of $h = 200$ nm and $h = 400$ nm, obtained by chemical deposition on glass substrates, have been studied. In the course of research, the influence of phase formation processes in thin CdSe films on photoelectric properties was established.

EXPERIMENTAL PART

During the research, thin CdSe films obtained by chemical deposition were studied. The starting materials are designed to produce thin layers with a thickness of $h < 400$ nm and $h \geq 400$ nm. The solution used for chemical

deposition of the CdSe thin film was prepared by taking equal amounts of each of the components (13 ml volume): 0.5 M cadmium chloride ($\text{CdCl}_2 \times 2.5\text{H}_2\text{O}$), 13.4 M (25%) sodium hydroxide (NH_3OH), 7.4 M triethanolamine ($\text{C}_6\text{H}_{15}\text{NO}_3$) and 0.2 M sodium selenosulfate (Na_2SSeO_3). The chemical precipitation process was carried out in a 60 ml beaker at room temperature. The technology for producing thin layers was carried out according to work [14]. Thin films of CdSe were obtained on glass substrates. The thickness of the resulting layers was determined by the gravimetric method. It was found that the thickness of the resulting thin CdSe films was $h = 200$ nm and $h = 400$ nm.

Thin CdSe films were examined by X-ray diffraction to determine structure formation. The studies were carried out on a D8 Advance diffractometer (Bruker, Germany) with $\text{CuK}\alpha$ radiation, 40 kV, 40 mA ($\lambda = 1.5406$ Å). The resulting spectra were analyzed in the Origin program and the Miller indices corresponding to the diffraction maxima obtained in the X-ray diffraction spectra were determined.

The photoconductivity spectrum of thin CdSe films obtained by chemical deposition was studied in an optical device based on an MDR-2 monochromator. The studies were carried out at room temperature, in the wavelength range $\lambda = 600$ – 1100 nm. A PZh-27 lamp with a vertical wire was used as a light source, and the photosignal generated when the thin layer was exposed to light was amplified by an E6-13 teraohmmeter and entered into a computer system. Silver paste was used to create thin layers of ohmic contacts. Based on the spectrum obtained during the research, the photoconductivity of thin CdSe layers with thicknesses $h = 200$ nm and $h = 400$ nm was recorded, and the band gap for CdSe was determined.

RESULTS AND DISCUSSIONS

A structural-phase analysis of thin CdSe films with a thickness of $h = 200$ nm and $h = 400$ nm, obtained by chemical deposition, was carried out. The spectra obtained by X-ray diffraction in the range of diffraction angles $5^\circ \leq 2\theta \leq 80^\circ$ are shown in Fig. 1. As can be seen from the spectra, two different diffraction maxima were observed in a thin CdSe layer with a thickness of $h = 200$ nm, and three different diffraction maxima were observed in a thin CdSe layer with a thickness of $h = 400$ nm.

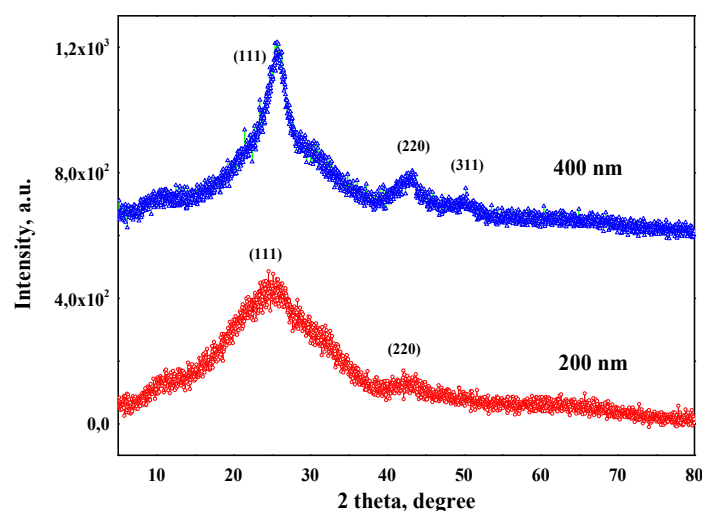


Figure 1. X-ray diffraction spectra of CdSe thin films at room temperature

When comparing the X-ray diffraction spectra shown in Figure 1 with the results obtained in previous studies, it was found that the center of the peak in the spectrum of a thin film with a thickness of $h = 200$ nm, located at a diffraction angle of $2\theta = 25^\circ$, corresponds to the atomic planes belonging to the indices Miller in the crystal structure of hexagonal symmetry (111) of the CdSe compound. The central peak, located at the diffraction angle $2\theta = 43^\circ$, corresponds to the atomic planes belonging to the Miller indices in the crystal structure of the CdSe compound with hexagonal symmetry (220) [19]. In thin CdSe films, in the spectrum of a thin film with a thickness of $h = 400$ nm, another diffraction maximum was observed at a central diffraction angle of $2\theta = 50^\circ$, which corresponds to the atomic plane of the Miller index (311). It is known that in thin layers the structural properties are weaker than in bulk crystals. As can be seen from the analysis of the spectra presented in Fig. 1, in each of the thin layers a phase corresponding to a CdSe crystal was formed. However, better structural properties were found in a thin film with a thickness of $h = 400$ nm than in a thin film with a thickness of $h = 200$ nm.

The photoconductivity spectrum of thin CdSe films obtained on a glass substrate by chemical deposition was also studied. Photoconductivity spectra of thin CdSe films with thicknesses $h = 200$ nm and $h = 400$ nm, obtained at a wavelength $\lambda = 600$ – 1100 nm, are presented in Figures 2 and 3. A two-component photoconductivity model was used to interpret photoconductivity spectra and determine the properties of thin films [20]. According to this model, the photocurrent generated in a thin CdSe film consists of a positive component generated in the bulk of the film and a negative component generated on the surface of the film and heavily occupied by surface traps. During these processes,

at certain wavelengths of light incident on the surface of a thin layer, a decrease in photoconductivity is detected due to the capture of charge carriers by traps.

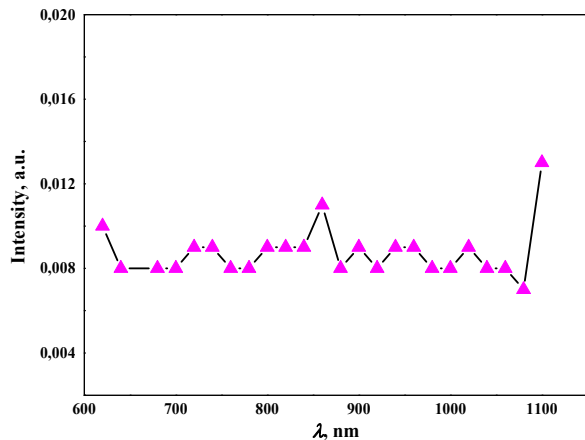


Figure 2. Photoconductivity spectrum of a thin CdSe film obtained with a thickness $h = 200$ nm

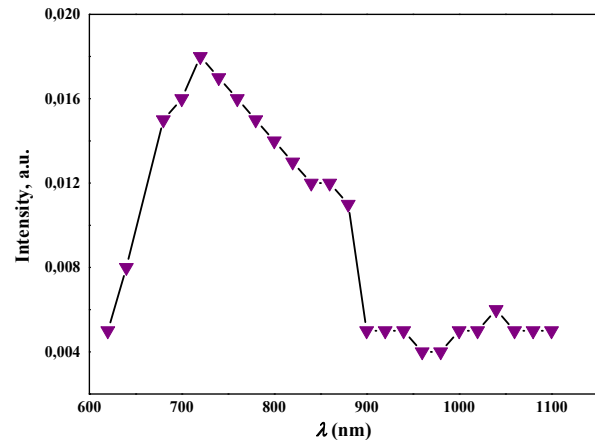


Figure 3. Photoconductivity spectrum of a thin CdSe film obtained with a thickness $h = 400$ nm

At small values of the thickness of thin layers ($h = 200$ nm), a sharp decrease in photoconductivity due to self-damping was recorded. As can be seen from the graph in Figure 2, chaos was observed over a wide range of wavelengths of the incident beam. This process can be explained by the incomplete formation of the CdSe phase in the thin film. As a result of defects in the structure of the thin layer and the capture of charge carriers by these defects, the special properties of the CdSe compound are not fully formed. A different picture was observed in the PE spectrum of a thin CdSe layer with a thickness of $h = 400$ nm. From the graph shown in Fig. 3, it is clear that this sample is photosensitive in the wavelength range $\lambda = 700$ - 900 nm and a photoconverter can be manufactured on its basis. The spectrum recorded a maximum with wavelength $\lambda = 0.71$ μm . Based on this maximum, the band gap of a thin CdSe film with a thickness $h = 400$ nm was calculated:

$$E_g = 1,24 / \lambda_{max} \text{ (eV)}$$

It was found that the band gap of this sample is $E_g = 1.746$ eV.

In the course of a comparative study of the structure and photoconductivity of thin films of cadmium selenide obtained by chemical deposition, it was found that the CdSe phase cannot be completely formed in these systems up to a thickness $h \leq 400$ nm. Therefore, it is impossible to obtain a photosensitive system of this size. At greater thickness, a cadmium-selenium phase may form and the photoelectric properties of cadmium-selenium may appear. Such systems provide a wide range of applications for CdSe thin films.

CONCLUSIONS

In parallel, the structure and photoconductivity of thin films of cadmium selenide obtained by chemical deposition were studied, and the structural aspects of photoconductivity were studied in a comparative manner. During the research, thin films with a thickness of $h = 200$ nm and $h = 400$ nm, obtained on glass substrates, were studied. The results obtained were analyzed and it was found that a thin layer of CdSe with $h = 400$ nm is a photosensitive substance in the spectral region of $\lambda = 700$ - 900 nm. The band gap was $E_g = 1.746$ eV. As the thickness of the thin layer decreases, photosensitivity sharply decreases due to the capture of charge carriers by traps on its surface.

ORCID

© Y.I. Aliyev, <https://orcid.org/0000-0001-8896-2180>

REFERENCES

- [1] Y.I. Aliyev, N.A. Ismayilova, R.F. Novruzov, A.O. Dashdamirov, H.J. Huseynov, S.H. Jabarov, and A.A. Ayubov, "Electron structure and density of states' calculations of Ag_2S and Ag_2Se crystals from first-principle," *Modern Physics Letters B*, **33**(21), 1950242 (2019). <https://doi.org/10.1142/S0217984919502427>
- [2] S.H. Jabarov, S.I. Ibrahimova, F.V. Hajiyeva, E.M. Huseynov, and Y.I. Aliyev, "Structural, vibrational, and dielectric properties of CuInZnSe_3 chalcogenide compound," *Arabian Journal for Science and Engineering*, **47**(6), 7817-7823 (2022). <https://doi.org/10.1007/s13369-022-06745-1>
- [3] N.A. Ismayilova, and S.H. Jabarov, "First-principles study of the electronic structure and DOS spectrum of TlGaSe_2 ," *Optoelectronics and Advanced Materials-Rapid Communications*, **11**, 353-356 (2017). <https://oam-rc.inoe.ro/articles/first-principles-study-of-the-electronic-structure-and-dos-spectrum-of-tlgase2/fulltext>
- [4] B.G. Tagiyev, O.B. Tagiyev, A.I. Mammadov, V.X. Quang, T.G. Naghiyev, S.H. Jabarov, M.S. Leonenya, et al., "Structural and luminescence properties of $\text{Ca}_x\text{Ba}_{1-x}\text{Ga}_2\text{S}_4$: Eu^{2+} chalcogenide semiconductor solid solutions," *Physica B: Condensed Matter*, **478**, 58-62 (2015). <https://doi.org/10.1016/j.physb.2015.08.061>

- [5] G.M. Agamirzayeva, G.G. Huseynov, Y.I. Aliyev, T.T. Abdullayeva, and R.F. Novruzov, "Crystal structure and magnetic properties of the compound $\text{Cu}_3\text{Fe}_{0.5}\text{Se}_2$," *Advanced Physical Research*, **5**(1), 19-25 (2023). http://jomardpublishing.com/UploadFiles/Files/journals/APR/V5N1/Agamirzayeva_et_al.pdf
- [6] N.N. Mursakulov, N.N. Abdulzade, S.H. Jabarov, and Ch.E. Sabzalieva, "Investigation of $\text{CuIn}_{1-x}\text{Ga}_x\text{Se}_2$ thin films for solar cells obtained by the magnetron sputtering method from two magnetrons shifted to each other, *New Materials*," *Compounds and Applications*, **6**(2), 140-147 (2022). http://jomardpublishing.com/UploadFiles/Files/journals/NMCA/v6n2/Mursakulov_et_al.pdf
- [7] R.S. Madatov, A.S. Alekperov, F.N. Nurmammadova, N.A. Ismayilova, and S.H. Jabarov, "Preparation of N-Si-P-GaSe heterojunctions based on an amorphous GaSe layer without impurities and study of their electrical properties," *East European Journal of Physics*, **1**(1), 322-326 (2024). <https://doi.org/10.26565/2312-4334-2024-1-29>
- [8] Y.I. Aliyev, Y.G. Asadov, R.D. Aliyeva, T.G. Naghiyev, and S.H. Jabarov, "Influence of partial substitution of Cu atoms by Zn and Cd atoms on polymorphic transformation in the $\text{Cu}_{1.75}\text{Te}$ crystal," *Modern Physics Letters B*, **33**(11), 1850128 (2019). <https://doi.org/10.1142/S0217984919501288>
- [9] A.S. Alekperov, S.H. Jabarov, M.N. Mirzayev, E.B. Asgerov, N.A. Ismayilova, Y.I. Aliyev, T.T. Thabethe, *et al.*, "Effect of gamma irradiation on microstructure of the layered $\text{Ge}_{0.995}\text{Nd}_{0.005}\text{S}$," *Modern Physics Letters B*, **33**(09), 1950104 (2019). <https://doi.org/10.1142/S0217984919501045>
- [10] D.M. Freik, L.I. Nykyruy, T.O. Parashchuk, and B.P. Volochanska, "Thermodynamic properties of CdSe crystals using first principles calculations and experiment," *International Journal of Engineering and Innovative Technology (IJEIT)*, **4**(2), 99-104, (2014). https://www.ijeit.com/Vol%204/Issue%202/IJEIT1412201408_19.pdf
- [11] Y.N. Xu, and W.Y. Ching, "Electronic, optical, and structural properties of some wurtzite crystals," *Physical Review B*, **48**, 4335-4351 (1993). <https://doi.org/10.1103/PhysRevB.48.4335>
- [12] Kh.N. Ahmadova, and S.H. Jabarov, "Obtaining of Al nanosized thin Layers and their structural properties," *Arabian Journal for Science and Engineering*, **48**, 8083-8088 (2023). <https://doi.org/10.1007/s13369-022-07449-2>
- [13] A.S. Alekperov, S.H. Jabarov, T.A. Darzieva, G.B. Ibragimov, A.M. Nazarov, and S.S. Farzaliev, "Effect of an electric field on the crystallization behavior of amorphous $\text{TlIn}_{1-x}\text{Sn}_x\text{Se}_2$ films," *Inorganic Materials*, **59**(1), 8-11 (2023). <https://doi.org/10.1134/S0020168523010028>
- [14] L.N. Ibrahimova, N.M. Abdullayev, M.E. Aliyev, G.A. Garashova, and Y.I. Aliyev, "Phase formation process in CdSe thin films," *East European Journal of Physics*, **1**(1), 493-496 (2024). <https://doi.org/10.26565/2312-4334-2024-1-54>
- [15] H.N. Rosly, C. Doroody, M.N. Harif, I.S. Mohamad, M. Isah, and N. Amin, "Optoelectrical properties of treated CdSe thin films with variations in indium chloride concentration," *Materials*, **16**, 4108 (2023). <https://doi.org/10.3390/ma16114108>
- [16] R.P. Dutta, and N. Neog, "An investigation of CdSe thin film for photovoltaic properties under different annealing temperature," *Materials Today: Proceedings*, **42**(2), 893-896 (2021). <https://doi.org/10.1016/j.matpr.2020.11.739>
- [17] A.A. Abduvaitov, G.T. Imanova, Kh.Kh. Boltsev, B.E. Umirzakov, D.A. Tashmukhamedova, and G. Abdurakhmanov, "Analysis of the change in the composition of the CdTe surface upon implantation of O^{2+} ions and subsequent annealing," *Advanced Physical Research*, **6**(1), 36-41 (2024). <https://doi.org/10.62476/apr61.41>
- [18] R. Asaba, K. Wakita, A. Kitano, Y.G. Shim, N. Mamedov, A. Bayramov, E. Huseynov, and I. Hasanov, "Structure and optical properties of CdS:O thin films," *Physica Status Solidi C*, **10**(7-8), 1098-1101 (2013). <https://doi.org/10.1016/j.jaubas.2011.10.001>
- [19] A. Kitano, Y.G. Shim, K. Wakita, Kh. Khalilova, N. Mamedov, A. Bayramov, E. Huseynov, and I. Hasanov, "Optical characterization of non-annealed CdS: O films for window layers in solar cells," *Physica Status Solidi C*, **10**(7-8), 1107-1110 (2013). <https://doi.org/10.1002/pssc.201200834>
- [20] A. Singh, A. Kunwar, and M.C. Rath, "L-cysteine capped CdSe quantum dots synthesized by photochemical route," *Journal of Nanoscience and Nanotechnology*, **17**, 1-8 (2017). <https://doi.org/10.1166/jnn.2018.14687>
- [21] L.S. Palatnik, *Fundamentals of film semiconductor materials science*, (Energy, Moscow, 1973). (in Russian)

ДОСЛІДЖЕННЯ ФОТОПРОВІДНОСТІ ТОНКИХ ПЛІВОК СЕЛЕНІДУ КАДМІЮ, ОТРИМАНИХ ХІМІЧНИМ ОСАДЖЕННЯМ

Л.Н. Ібрагімова^a, Н.М. Абдуллаєв^b, Н.А. Гардашбейова^a, А.С. Алекперов^{c,d}, С.Р. Азімова^b, Ю.І. Алієв^d

^aНахічеванський державний університет, Нахічевань, AZ-7012, Азербайджан

^bІнститут фізики Міністерства науки і освіти Азербайджану, Баку, AZ-1143, Азербайджан



^cАзербайджанський державний педагогічний університет, Баку, AZ-1000, Азербайджан

^dЗахіднокаспійський університет, Баку, AZ-1001, Азербайджан

У даній роботі досліджено спектр фотопровідності (ФП) тонких плівок CdSe. У ході досліджень на скляних підкладках були відібрані тонкі плівки кадмію та селену товщиною $h = 200$ нм та $h = 400$ нм. Товщину зразків, отриманих хімічним осадженням, визначали гравіметричним методом. Оскільки кристал CdSe є світлочутливим напівпровідниковим матеріалом, досліджували фотопровідність тонких плівок. Проаналізовано спектри, отримані під час досліджень, проведених на довжині хвилі $\lambda = 600$ -1100 нм. Встановлено, що спектр є хаотичним, оскільки в шарах $h = 200$ нм фаза сформована не повністю. У шарах $h = 400$ нм зафіксовано максимум з центром на довжині хвилі $\lambda = 710$ нм.

Ключові слова: хімічне осадження; CdSe; тонка плівка; фотоелектричний спектр; зазор

OPTIMIZATION OF THE INFLUENCE OF TEMPERATURE ON THE ELECTRICAL DISTRIBUTION OF STRUCTURES WITH RADIAL p-n JUNCTION STRUCTURES

 Jo'shqin Sh. Abdullayev^{a*},  Ibrokhim B. Sapaev^{a,b}

^aNational Research University TIIAME, Department of Physics and Chemistry, Tashkent, Uzbekistan

^bWestern Caspian University, Scientific researcher, Baku, Azerbaijan

*Corresponding Author e-mail: j.sh.abdullayev6@gmail.com

Received May 5, 2024; revised June 30, 2024; accepted July 7, 2024

In recent years, advances in optoelectronics and electronics have prioritized optimizing semiconductor device performance and reducing power consumption by modeling new semiconductor device geometries. One such innovative structure is the radial p-n junction structure. In this work, we present a concept that submicron three-dimensional simulations were conducted on radial p-n junction structures based on GaAs material to investigate the influence of temperature ranging from 250K to 500K with a step of 50K on the electrophysical distribution, such as space charge, electro-potential, and electric field, in radial p-n junction structures, as well as various forward voltages. In particular, we focus on the shell radius within the structure: 0.5 μm and 1 μm for the shell. The modeling results were compared with the results obtained from solving the theoretical Poisson equation in the cylindrical coordinate system.

Keywords: Core-shell; Radial p-n junction; Cylindrical coordinates; Space charge density; Gallium Arsenide (GaAs)

PACS: 73.40.Lq, 73.61.Cw, 73.61.Ey, 72.20.Jv

INTRODUCTION

Until now, modern scientific publications on semiconductor electronic devices have mainly focused on planar structures of p-n and p-i-n junction structures. On the other side, in recent years, theoretical [1-3] and practical [4,5] studies and modeling semiconductor devices, have made it possible to explore new geometric configurations, revealing intriguing and unexplored electrical properties. One such configuration is the radial structures of p-n and p-i-n junction structures and so on.

Although planar p-n and p-i-n junction structures offer numerous advantages, such as ease of fabrication, they also have limitations, such as limited active surface area [6]. This limitation can impact performance in applications where intense charge carrier interactions are critical such as detectors [7]. Additionally, in optoelectronic devices, planar p-n and p-i-n junction structures may exhibit limited light-matter interactions compared to their 3D counterparts [8].

Hence, studying the electrical and optical characteristics of novel geometric structures becomes essential. Radial designs of p-n and p-i-n junctions offer several advantages compared to their flat counterparts. First, radial p-n and p-i-n junction structures offer increased surface area, which improves the interaction between charge carriers and potentially improves device performance [9]. Moreover, in some photonic applications, radial structures exhibit superior light absorption characteristics compared to planar structures. Additionally, radial configurations can reduce series resistance, thereby increasing the overall efficiency of the device [10]. Indeed, depending on the intended application of the semiconductor electronic devices, the implementation of various modifications can lead to new effects and further advances. Hence, the study of the electrophysical and optoelectrical features of radial p-n and p-i-n junction structures is becoming a critical area of research. Experimental methods for growing radial p-n and p-i-n junction structures using GaAs material have been studied for several research purposes [11-14].

Various methods for fabricating radial pn junction structures have emerged, including vapor-liquid-solid (VLS) [15], chemical vapor deposition (CVD) [16], and plasma-enhanced chemical vapor deposition (PECVD), [17] and metal chemical etching (MACE) [18]. Using these techniques, researchers have successfully created structures such as nanowire arrays [19], nanocones [20], and micropillars [21] designed for enhanced light absorption in radial p-n and p-i-n junction configurations.

This arrangement provides many advantages. For example, the design of a radial p-n junction aligns the direction of light absorption perpendicular to the direction of minority carrier transport. This configuration allows the cell to maintain sufficient thickness to effectively absorb light while simultaneously providing a short path for carrier collection. This design is suitable for highly integrated optoelectronic devices such as solar cells [22], biosensors, memories [23], light emitting diodes (LEDs) [24], radial photodiodes, high electron mobility transistors [25] and field effect transistors [26].

Despite significant advances in the theory and application of radial p-n junctions and p-i-n junctions, unresolved problems remain, especially regarding the electrophysical distributions, such as space charge density, electric potential, and electric field, in radial p-n junction structures as well as various forward voltages at different radii and over a wide temperature range. In addition, the injection of minority charge carriers has practically not been studied in scientific works. The electrophysical distributions in planar p-n and p-i-n junction structures intended for sensor devices have been extensively studied [27]. However, the electrophysical distributions in radial p-n and p-i-n junction structures have not

been fully explored. Hence, it is imperative to investigate the dependence of electrophysical distributions in radial p-n and p-i-n junction structures on various external parameters.

Thus, our research efforts in this work are focused on the in-depth study and modeling of the electrical properties of radial p-n junction structures using GaAs material, known for its bandgap suitability for optoelectronic devices. Given the wide bandgap of GaAs ($E_g = 1.42\text{eV}$), it is widely used in semiconductor optoelectronics. The simulation results are compared with the solutions obtained by solving the Poisson equation in a cylindrical coordinate system at different temperatures [28]. Section METHODS AND MATERIAL provides an overview of the sample geometry, and material characteristics, as well as methodological studies of the distribution of space charge density, electric potential, and electric field. Section RESULTS AND DISCUSSION details the results of our new model and discusses its implications.

METHODS AND MATERIAL

In this study, submicron three-dimensional simulations were conducted on radial p-n junction structures based on GaAs material to investigate the influence of temperature ranging from 250K to 500K with a step of 50K on the electrophysical distribution, such as space charge, electro-potential, and electric field, in radial p-n junction structures, as well as from 0 to 1 Volt forward voltages. In particular, we focus on the shell radius within the structure: $0.5\ \mu\text{m}$ and $1\ \mu\text{m}$ for the shell.

METHODS AND THEORETICAL BACKGROUND

At the same time, it is required to solve the Poisson equation to determine the appearance of electrophysical distributions in the Planar and Radial p-n and p-i-n transition structures and to study the influence of external factors on the electrophysical distributions. Taking into account that electrophysical distributions in radial p-n and p-i-n junction structures and the mechanism of current flow in them are hardly studied, we solve Poisson's equation in the cylindrical coordinate system. The three-dimensional Poisson's equation in cylindrical coordinates is given by Eq. (1):

$$\frac{\partial^2 \varphi(r)}{\partial r^2} + \frac{1}{r} \frac{\partial \varphi(r)}{\partial r} + \frac{1}{r^2} \frac{\partial^2 \varphi(r)}{\partial \theta^2} + \frac{\partial^2 \varphi(r)}{\partial z^2} = -\frac{\rho(r, \theta, z)}{\epsilon \epsilon_0} \quad (1)$$

Here, r represents the radial dimension, z denotes an axial dimension, θ signifies an azimuthal angle, $\rho(r)$ represents charge density, and $\varphi(r)$ stands for electrostatic potential. If Poisson's equation is expressed solely for one radial dimension, it appears as follows Eq. (2a) and (2b):

$$\frac{\partial^2 \varphi(r)}{\partial r^2} + \frac{1}{r} \frac{\partial \varphi(r)}{\partial r} = -\frac{\rho(r)}{\epsilon \epsilon_0} \quad (2a)$$

$$\frac{dE(r)}{dr} + \frac{dE(r)}{r} = \frac{\rho(r)}{\epsilon \epsilon_0} \quad (2b)$$

Where $E(r)$ represents the electric field, ϵ denotes the permittivity of the semiconductor material, for GaAs ϵ is 12.9, $\epsilon_0 = 8.85 \cdot 10^{-12}\ \text{F} \cdot \text{m}^{-1}$ vacuum permittivity. By solving the second-order differential equation, we can determine the following distributions in the radial dimension from Eq. (3a) and (3b): $\rho(r)$ represents the charge density, $\varphi(r)$ denotes the electrostatic potential, and $E(r)$ signifies the electric field. Through this process, distributions in radial p-n and p-i-n junction structures can be determined.

$$\varphi(r) = -\frac{\rho(r) \cdot r^2}{4\epsilon \epsilon_0} + C_1 \cdot \ln(r) + C_2 \quad (3a)$$

$$E(r) = -\frac{d\varphi(r)}{dr} = \frac{\rho(r) \cdot r}{2\epsilon \epsilon_0} - \frac{C_1}{r} \quad (3b)$$

To achieve this, it is necessary to establish the initial and boundary conditions for solving the second-order differential equation, identify C_1 and C_2 , and find the solutions individually of electrostatic potential and electric field. We introduce the conditions as follows: $E(R/2 + r_n) = 0$, $E(R/2 - r_p) = 0$, $\varphi(R/2 - r_p) = 0$, $\varphi(R/2 + r_n) = \varphi_k$. Here φ_k is built potential, for $\varphi_k = 1.28\ \text{Volt}$ GaAs, r_n and r_p are border radial dimensions of depletion region respectively core (p-type) and shell (n-type) side. See Figure 1 to understand the radial distance here.

$$E(-R \leq r < -r_n) = 0 \quad \text{and} \quad E(0 \leq r < r_p) = 0 \quad (5a)$$

$$E(r_p < r < r_n) = \frac{qN_A}{2\epsilon \epsilon_0} (r + r_p) \quad (5b)$$

$$E(-r_p < r < -r_n) = -\frac{qN_D}{2\epsilon\epsilon_0}(r - r_n) \tag{5c}$$

$$E(-r_p < r \leq 0) = 0 \text{ and } E(r_n < r \leq R) = 0 \tag{5d}$$

Expressions (5a), (5b), (5c), and (5d) are obtained by solving expression (3b) using integrals with the initial conditions stated above. The solutions to these derived equations are presented graphically in Figure 4. The graphs in the next section were obtained from the solutions of these equations. Here, Majority carrier concentration $p_p = n_n = N_A = N_D = 2 \cdot 10^{16} \text{ cm}^{-3}$, minority carrier concentration $p_n = \frac{n_i^2}{N_D}$, $n_p = \frac{n_i^2}{N_A}$. Here n_i is intrinsic concentration, $n_i = 1.7 \cdot 10^6 \text{ cm}^{-3}$ for GaAs. Electrons and holes mobility $\mu_n = 8500 \left[\frac{\text{cm}^2}{\text{V} \cdot \text{s}} \right]$ and $\mu_p = 400 \left[\frac{\text{cm}^2}{\text{V} \cdot \text{s}} \right]$ for GaAs align closely with their respective literature values and the functional parameters of GaAs material are sourced from the following literature [29].

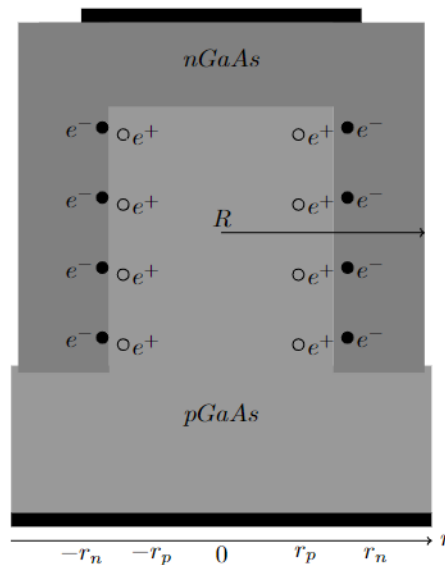


Figure 1. 2D cross-section of the radial p-n junction. The light grey area signifies the p-type GaAs, while the dark grey area represents the n-type GaAs. The black field indicates the Ohmic contact prepared with Al. Here e^- and e^+ denote electrons and holes respectively, while r denotes the radial dimension. R is the radius of the shell.

We aim to explore the electrophysical characteristics of an individual radial p-n junction structure at a submicron scale, considering both the periodic recurrence of radial structures within submicron dimensions and the cyclical nature of electrophysical processes occurring within them. In this paper, we assume that donor and acceptor ions are completely ionized within the chosen temperature range. Additionally, we have selected the symmetric p-n junction with complete ionization, where $p = n = N_A = N_D = 2 \cdot 10^{16} \text{ cm}^{-3}$. In particular, we focus on the core and shell radii within the structure: $R = 0.5 \mu\text{m}$ and $R = 1 \mu\text{m}$ for the shell. In both cases, the core radius, denoted by $R/2$ is chosen to be equal to half the shell radius. This choice enables us to consider the symmetric electrical distribution. Semiconductor electronic devices heavily depend on the operational efficiency of the p-n junction. Therefore, this study is dedicated to examining the electrical distribution occurring within the radial p-n junction. We did not include the electrical distribution within the substrate in this analysis. The results obtained from the models and samples employed in this section are thoroughly presented and scrutinized in Section RESULTS AND DISCUSSION.

RESULTS AND DISCUSSION

This section presents graphs illustrating the variations of current I with voltage U and their analysis as the temperature changes from 250K to 500K in 50K increments. Additionally, it includes distributions of electrophysical properties such as space charge density, electrostatic potential, and electric field.

Distributions of Electrophysical Parameters

The maximum value of charge density is dependent on doping concentration and is not influenced by geometric parameters by Equation (2). Hence, So, regardless of whether the radius is $0.5 \mu\text{m}$ or $1 \mu\text{m}$, the maximum value of charge density remains the same. Indeed, the change in radius alters the charge distribution in radial p-n junction structures, as illustrated in Figure 2. The change in charge distribution within the core-shell terminal is observed from $-0.8 \mu\text{m}$ to $-0.4 \mu\text{m}$ and from $0.4 \mu\text{m}$ to $0.8 \mu\text{m}$ $d \sim 0.4 \mu\text{m}$ within the depletion region thickness, d is representing the depth of the depletion region. With the increase in temperature, the charge density of carriers also increases.

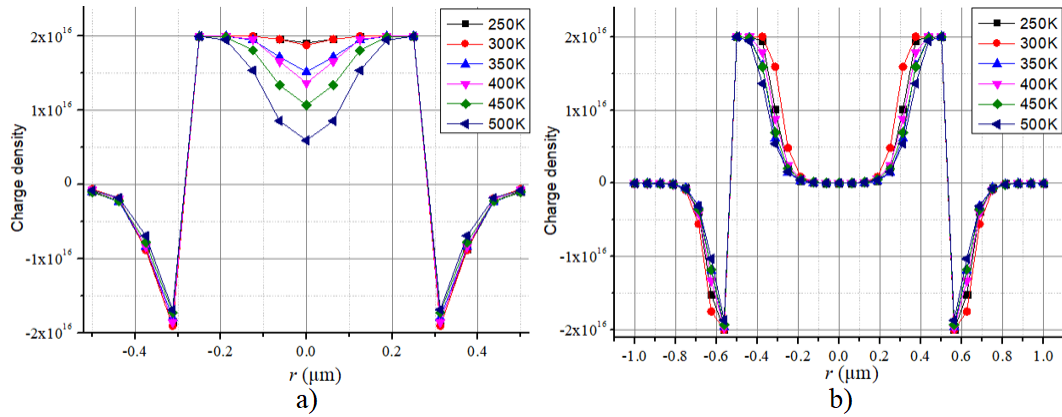


Figure 2. Distribution of space charge density $\rho(r)$ [cm^{-3}] across radial p-n junction structure by radial dimension a) corresponding to $R=0.5 \mu\text{m}$ and b) corresponding to $R=1 \mu\text{m}$ based on GaAs.

In Figure 2, it's evident that the charge distribution within the thickness of the shell remains uniform for both $R=0.5 \mu\text{m}$ and $1 \mu\text{m}$, whereas it varies within the thickness of the core. This observation can be attributed to the difference in charge distribution within the core, which ultimately constrains the charge density [30-33]. The distribution of electrostatic potential under the influence of forward voltage shows that potential changes are predominantly observed in the depleted regions of both the core and shell. Other areas show minimal changes.

From the expression for $E(r) = -d\phi(r)/dr$ it's evident that the electrostatic field reaches its maximum value at locations where changes in charge density and electrostatic potential occur, as depicted in Figures 2 and 3. Additionally, the electrostatic field increases with rising temperature and the radius of the shell.

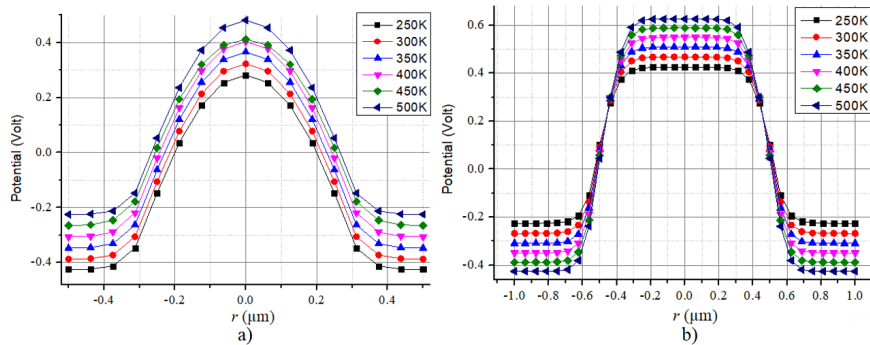


Figure 3. Distribution of Electrostatic potential $\phi(r)$ across radial p-n junction structures by radial dimension a) corresponding to $R=0.5 \mu\text{m}$ and b) corresponding to $R=1 \mu\text{m}$ based on GaAs.

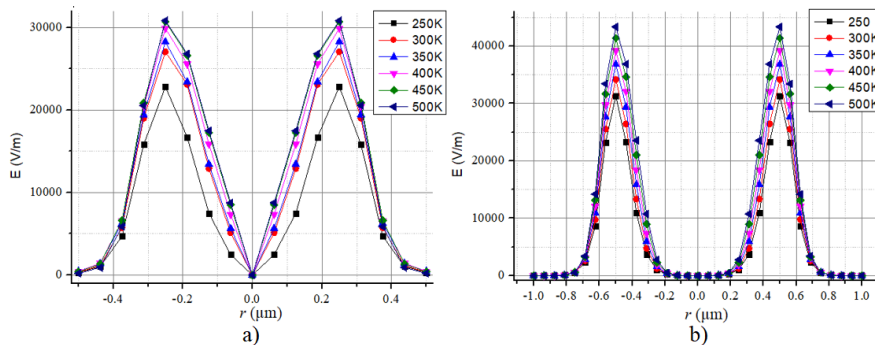


Figure 4. Distribution of Electric field $E(r)$ across radial p-n junction structures by radial dimension in 1D system a) corresponding to $R=0.5 \mu\text{m}$ and b) corresponding to $R=1 \mu\text{m}$ based on GaAs.

It represents the dependence of the electric field distribution on the 1D radial dimension, showing that the electric field has a high value at the p-n junction. In case a) corresponding to $R=0.5 \mu\text{m}$, the electric field value is 30 kV/m , while in case b) at $R=1 \mu\text{m}$, the electric field reaches a maximum value of 45 kV/m . To explain this situation, we approach it as follows: the change in electrostatic potential and the value of the space charge density are considered by taking a large value.

Analyze I-U-T Curves

The current transport mechanism in p-n junction structures can often be discerned by analyzing the representation of the I-U curve on a semi-logarithmic graph. Therefore, we illustrated a semi-logarithmic I-U curve in Figure 3. Upon

observing the volt-ampere characteristics, it becomes evident that the current transport mechanism remains consistent despite variations in radius. However, the current values vary, a phenomenon attributed to changes in geometric size. In semiconductor electronic devices, the analysis of the I-U curve is critical for assessing the quality of the selected sample for a model. This curve provides valuable insights into the device's performance, aiding in the identification of any irregularities or inefficiencies that may affect its functionality. The semi-logarithmic scale of the I-U curve can fully elucidate the current flow mechanism, hence its utilization in our representation. However, a noteworthy observation reveals that the current transport mechanism does change with temperature variations. Figure 5 demonstrates this phenomenon: At low voltages up to 0.4 V, the recombination-generation mechanism predominates. In the voltage range from 0.4 to 0.8 V, the drift-diffusion mechanism prevails. Beyond these ranges, the phenomenon of high injection is observed, extending up to 1 volt.

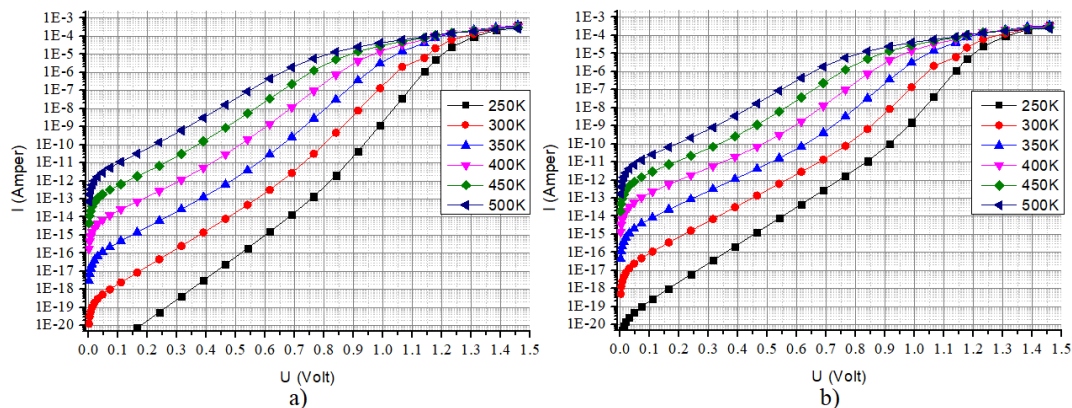


Figure 5. depicts the semi-logarithmic current-voltage characteristics for a GaAs-based p-n junction, with a) $R=0.5 \mu\text{m}$ and b) $R=1 \mu\text{m}$ respectively.

At homogeneous values of temperature and forward voltage, at different values of radius $R=0.5 \mu\text{m}$ and $R=1 \mu\text{m}$, the current transport mechanism remained unchanged, and the value of the current increased. This situation can be explained by the increase of the current passing active surface with the change of geometric size.

CONCLUSIONS

In summary, the maximum value of the charge density depends on the doping concentration and is independent of geometric parameters. This finding suggests that both nano- and micro-scale pn junctions exhibit the same maximum charge density at equivalent concentrations. Under uniform temperature and forward voltage conditions, different radii ($R=0.5 \mu\text{m}$ and $R=1 \mu\text{m}$) do not alter the current transfer mechanism, but they do increase the current value. This can be attributed to the increase in the current-carrying active surface area with changes in geometric size. Analysis of the I-U curve in the model reveals that the current transport mechanism remains consistent across different radii in radial p-n junction structures. However, an interesting observation indicates that the current transport mechanism does change with temperature variations. In Figure 5, I-U curve 5 illustrates that at low voltages (up to 0.4 V), the recombination-generation mechanism predominates, while in the range of 0.4 to 0.8 V, the drift-diffusion mechanism prevails. In other cases, the phenomenon of high injection is observed up to 1 volt. In future studies, we will explore the C-U characteristic using this model.

ORCID

©Jo'shqin Sh. Abdullayev, <https://orcid.org/0000-0001-6110-6616>; ©Ibrokhim B. Sapaev, <https://orcid.org/0000-0003-2365-1554>

REFERENCES

- [1] Sh. Qian, S. Misra, J. Lu, Z. Yu, L. Yu, J. Xu, J. Wang, *et al.*, *Appl. Phys. Lett.* **107**, 043902 (2015). <https://doi.org/10.1063/1.4926991>
- [2] E. Gnani, A. Gnudi, S. Reggiani, and G. Baccarani, *IEEE Trans. Electron Devices*, **58**(9), 2903 (2011). <https://doi.org/10.1109/TED.2011.2159608>
- [3] Z. Arefinia, A. Asgari, *Solar Energy Materials and Solar Cells*, **137**, 146 (2015). <https://doi.org/10.1016/j.solmat.2015.01.032>
- [4] O.V. Pylypova, A.A. Evtukh, P.V. Parfenyuk, I.I. Ivanov, I.M. Korobchuk, O.O. Havryliuk, and O.Yu. Semchuk, *Opto-Electronics Review*, **27**(2), 143 (2019). <https://doi.org/10.1016/j.opelre.2019.05.003>
- [5] R. Ragi, R.V.T. da Nobrega, U.R. Duarte, and M.A. Romero, *IEEE Trans. Nanotechnol.* **15**(4), 627 (2016). <https://doi.org/10.1109/TNANO.2016.2567323>
- [6] R.D. Trevisoli, R.T. Doria, M. de Souza, S. Das, I. Ferain, and M.A. Pavanello, *IEEE Trans. Electron Devices*, **59**(12), 3510 (2012). <https://doi.org/10.1109/TED.2012.2219055>
- [7] N.D. Akhavan, I. Ferain, P. Razavi, R. Yu, and J.-P. Colinge, *Appl. Phys. Lett.* **98**(10), 103510 (2011). <https://doi.org/10.1063/1.3559625>
- [8] A. V. Babichev, H. Zhang, P. Lavenus, F.H. Julien, A. Y. Egorov, Y.T. Lin, and M. Tchernycheva, *Applied Physics Letters*, **103**(20), 201103 (2013). <https://doi.org/10.1063/1.4829756>

- [9] D.H.K. Murthy, T. Xu, W.H. Chen, A.J. Houtepen, T.J. Savenije, L.D.A. Siebbeles, *et al.*, *Nanotechnology*, **22**(31), 315710 (2011). <https://doi.org/10.1088/0957-4484/22/31/315710>
- [10] B. Pal, K.J. Sarkar, and P. Banerji, *Solar Energy Materials and Solar Cells*, **204**, 110217 (2020). <https://doi.org/10.1016/j.solmat.2019.110217>
- [11] I. Aberg, G. Vescovi, D. Asoli, U. Naseem, J.P. Gilboy, C. Sundvall, and L. Samuelson, *IEEE Journal of Photovoltaics*, **6**(1), 185 (2016). <https://doi.org/10.1109/JPHOTOV.2015.2484967>
- [12] P. Dubey, B. Kaushik, and E. Simoen, *IET Circuits, Devices & Systems*, (2019). <https://doi.org/10.1049/iet-cds.2018.5169>
- [13] M.-D. Ko, T. Rim, K. Kim, M. Meyyappan, and C.-K. Baek, *Scientific Reports*, **5**(1), 11646 (2015). <https://doi.org/10.1038/srep11646>
- [14] A.M. de Souza, D.R. Celino, R. Ragi, and M.A. Romero, *Microelectronics J.* **119**, 105324 (2021). <https://doi.org/10.1016/j.mejo.2021.105324>
- [15] M.C. Putnam, S.W. Boettcher, M.D. Kelzenberg, D.B. Turner-Evans, J.M. Spurgeon, E.L. Warren, *et al.*, *Energy & Environmental Science*, **3**(8), 1037 (2010). <https://doi.org/10.1039/C0EE00014K>
- [16] S. Osono, Y. Uchiyama, M. Kitazoe, K. Saito, M. Hayama, A. Masuda, A. Izumi, *et al.*, *Thin Solid Films*, **430**, 165 (2003). [https://doi.org/10.1016/S0040-6090\(03\)00100-7](https://doi.org/10.1016/S0040-6090(03)00100-7)
- [17] R. Elbersen, R.M. Tiggelaar, A. Milbrat, G. Mul, H. Gardeniers, and J. Huskens, *Advanced Energy Materials*, **5**(6), 1401745 (2014). <https://doi.org/10.1002/aenm.201401745>
- [18] A.A. Leonardi, M.J.L. Faro, and A. Irrera, *A Review. Nanomaterials*, **11**(2), 383 (2021). <https://doi.org/10.3390/nano11020383>
- [19] A. Yesayan, F. Jazaeri, and J.-M. Sallese, *IEEE Trans. Electron Devices*, **63**(3), 1368 (2016). <https://doi.org/10.1109/TED.2016.2521359>
- [20] Y. Li, M. Li, P. Fu, R. Li, D. Song, C. Shen, and Y. Zhao, *Scientific Reports*, **5**(1), 11532 (2015). <https://doi.org/10.1038/srep11532>
- [21] J.C. Shin, D. Chanda, W. Chern, K.J. Yu, J.A. Rogers, and X. Li, *IEEE Journal of Photovoltaics*, **2**(2), 129 (2012). <https://doi.org/10.1109/JPHOTOV.2011.2180894>
- [22] D. Choi, and K. Seo, *Advanced Energy Materials*, **11**(5), 2003707 (2021). <https://doi.org/10.1002/aenm.202003707>
- [23] M. Shahram, T. Iman, and N.R. Mahdiyar, *Optical and Quantum Electronics*, **54**(2), 115 (2022). <https://doi.org/10.1007/s11082-021-03499-2>
- [24] Bryan Melanson, M. Hartensveld, C. Liu, and J. Zhang, *AIP Advances*, **11**(9), 095005 (2021). <https://doi.org/10.1063/5.0061381>
- [25] Y. Xiao, B. Zhang, H. Lou, L. Zhang, and X. Lin, *IEEE Trans. Electron Devices*, **63**(5), 2176 (2016). <https://doi.org/10.1109/TED.2016.2535247>
- [26] B. Liu, J. Wang, Z. Li, Z. Sun, C. Li, J.-M. Seo, J. Li, *et al.*, *Nano Energy*, **126**, 109611 (2024). <https://doi.org/10.1016/j.nanoen.2024.109611>
- [27] R.K. Patnaik, and D.P. Patnaik, in: *2016 International Conference on Signal Processing, Communication, Power and Embedded Systems (SCOPEs)*, (Paralakhemundi, India, 2016). <https://doi.org/10.1109/SCOPEs.2016.7955628>
- [28] A.C.E. Chia, and R.R. LaPierre, *J. Appl. Phys.* **112**, 063705 (2012). <https://doi.org/10.1063/1.4752873>
- [29] S.M. Sze, and K.K. Ng, *Physics of Semiconductor Devices*, Third Edition, (John Wiley & Sons, Inc., 2007).
- [30] G.E. Cirlin, V.G. Dubrovskii, I.P. Soshnikov, N.V. Sibirev, Y.B. Samsonenko, A.D. Bouravleuv, J.C. Harmand, *et al.*, *Phys. Status Solidi (RRL)*, **3**, 112 (2009). <https://doi.org/10.1002/pssr.200903057>
- [31] T.J. Kempa, R.W. Day, S.-K. Kim, H.-G. Park, and C.M. Lieber, *Energy Environ. Sci.* **6**(3), 719 (2013). <https://doi.org/10.1039/c3ee24182c>
- [32] M.I. Khan, I.K.M.R. Rahman, and Q.D.M. Khosru, *IEEE Trans. Electron Devices*, **67**(9), 3568 (2020). <https://doi.org/10.1109/TED.2020.3011645>
- [33] D.R. Bachman, S.E. Park, S. Thaveepunsan, J.S. Fitzsimmons, K.-N. An, and S.W. O'Driscoll, *Journal of Orthopaedic Trauma*, **1** (2018). <https://doi.org/10.1097/BOT.0000000000001278>

ОПТИМІЗАЦІЯ ВПЛИВУ ТЕМПЕРАТУРИ НА ЕЛЕКТРИЧНИЙ РОЗПОДІЛ КОНСТРУКЦІЙ ІЗ РАДІАЛЬНИМИ СТРУКТУРАМИ P-N ПЕРЕХОДУ

Джошкін Ш. Абдуллаєв^a, Іброхім Б. Сапаєв^{a,b}

^aНаціональний дослідницький університет ТІАМЕ, фізико-хімічний факультет, Ташкент, Узбекистан
^bЗахідно-Каспійський університет, науковий співробітник, Баку, Азербайджан

Останніми роками досягнення в оптоелектроніці та електроніці віддають перевагу оптимізації продуктивності напівпровідникових пристроїв і зниженню енергоспоживання шляхом моделювання нових геометрій напівпровідникових пристроїв. Однією з таких інноваційних структур є структура радіального p-n переходу. У цій роботі ми представляємо концепцію, згідно з якою субмікронне тривимірне моделювання було проведено на структурах радіального p-n-переходу на основі матеріалу GaAs для дослідження впливу температури в діапазоні від 250 К до 500 К з кроком 50 К на електрофізичний розподіл, такий як просторовий заряд, електропотенціал і електричне поле в структурах радіального p-n переходу, а також різні прями напруги. Зокрема, ми зосереджуємося на радіусі оболонки всередині конструкції: 0,5 μm і 1 μm для оболонки. Результати моделювання порівнювали з результатами, отриманими при розв'язуванні теоретичного рівняння Пуассона в циліндричній системі координат.

Ключові слова: ядро-оболонка, радіальний p-n-перехід; циліндричні координати; просторова густина заряду; арсенід галію (GaAs)

PREPARATION OF CALCIUM TITANATE PEROVSKITE COMPOUND, OPTICAL AND STRUCTURAL PROPERTIES

✉ **Khujamkul T. Davranov**^a, ✉ **Muradulla T. Normuradov**^a, ✉ **Muzaffar A. Davlatov**^b,
✉ **Kuvondiq T. Dovranov**^{a*}, **T.U. Toshev**^b, **N.A. Kurbonov**^b

^aKarshi State University, Karshi, 180100, Uzbekistan

^bKarshi Engineering and Economic Institute, Karshi, 180100, Uzbekistan

*Corresponding Author e-mail: quvondiqdavronm@gmail.com

Received May 6, 2024; revised July 14, 2024; accepted July 19, 2024

In this work, we have successfully fabricated a calcium titanate perovskite compound. The resulting CaTiO₃ compound was studied by preparing samples by compacting it in a powder state and using a Pousson device. The distance between the planes d_{hkl} , Miller indices (hkl), degree of crystallinity and amorphism, structure and lattice parameters of the calcium titanate perovskite compound were determined using an X-ray diffractometer. Also, according to the results of FT-IR analysis, the formation of CaTiO₃ perovskite is confirmed as a result of the study of molecular vibrations. The main broad peaks are observed in the range of 680–400 cm⁻¹, the absorption band at the wave number of 543,93 cm⁻¹ corresponds to the specific stretching vibrations of Ti-O bonds and indicates the formation of the CaTiO₃ perovskite type structure implies. Based on the results of these measurements, it will be possible to use semiconductor compounds in the future to create nanofilms by magnetron sputtering.

Keywords: X-ray phase analysis; Miller indices; Interplanar distance; Calcium titanate; Crystalline and amorphous phases; FT-IR
PACS: 61.05.C, 61.80.Ba, 61.43.Dq, 42.72.Ai

INTRODUCTION

Along with the rapid development of science and technology, the demand for energy is increasing day by day. The world is rapidly depleting non-renewable energy sources such as hydrocarbon fuels. Therefore, humanity needs to find alternative ways to solve these pressing problems. One of the most effective ways to combat global climate change is concrete measures such as replacing fossil fuels with new energy-efficient materials and renewable energy sources [1]. Based on this, the developed countries of the world are increasing their investments in this field every year in order to achieve sustainable development of new technologies and green energy [2]. Among renewable energy sources, photovoltaic generators are the most promising way to replace fossil fuels. Photovoltaic generators are based on the properties and characteristics of semiconductor materials, and in recent years have been derived from polycrystalline and monocrystalline silicon compounds. Obtaining high-quality thin coatings of metals, alloys, and semiconductors is one of the most important tasks in the production technology of integrated circuit elements, various temperature and pressure sensors, and micro and nanoelectronics in general. In particular, semiconductor nanofilms with a narrow area are needed to create thermal sensors. Metal silicides are one such semiconductor. Therefore, obtaining thin-layered and thin-sized films from these semiconductors is an urgent task [3].

Many different methods are used to obtain thin film coatings. The most popular methods of vacuum deposition of coatings on various types of surfaces are thermal evaporation, electron beam evaporation and various types of ion-plasma spraying. In this case, only the methods of applying thin films are based on the sputtering of the material with ions of heavy gases. These include ion-beam and magnetron methods of deposition of thin-film structures, which have been intensively developed recently [4]. They have a number of advantages: new materials, the ability to obtain oxides, good film adhesion and physicochemical properties. Especially important in the production of microelectronics and solar energy elements, it is necessary to use multi-structured coatings such as metal-semiconductor-dielectric, etc., which requires the use of various vacuum plasma equipment [5].

In recent times, it is known to everyone that it is almost impossible to imagine electronics without semiconductor heterostructures. Such structures are widely used to create light-emitting diodes, short-wave photodetectors, semiconductor lasers, solar cells, and other products of modern optoelectronics. An important factor in the widespread use of such devices is low cost and resistance to high temperature conditions. Calcium titanate is a promising material for creating various optoelectronic devices based on it. Calcium titanate is a combination of barium and titanium oxides. Crystal modification of calcium titanate with perovskite structure is ferroelectric with photorefractive and piezoelectric effect. Calcium titanate is characterized by high values of dielectric conductivity, on the basis of which several types of ferroelectric ceramics have been developed, which are used to create capacitors, piezoelectric sensors and posistors [6].

In this work, we study the structural properties and optical spectra of CaTiO₃ through the absorption properties of X-rays and infrared spectrum of light, physicochemical properties.

PREPARATION OF SAMPLES

The starting material used for synthesizing CaTiO_3 was analytical reagent grade, initially mixing calcium (96%) powder to titanium oxide (TiO_2) powder in a 1:1 ratio at room temperature using a digital mechanical stirrer for two hours. This mixture was stepwise calcined by heating in a muffle furnace at a rate of $20\text{ }^\circ\text{C}/\text{min}$ increasing the temperature to the next higher temperature until the terminal temperature of the reaction mixture was reached. The resulting powder was thermally heated in a muffle furnace at 800°C for 1 hour, then heated to 1100°C for another 1 hour, and then naturally cooled to room temperature by heating to 1300°C for half an hour. The resulting CaTiO_3 compound was studied by preparing samples by compacting it in a powder state and using a Pousson device.

METHODS

X-ray diffractometers and infrared spectrophotometers were used to determine the qualitative composition of the sample, the crystal structure of the substance, as well as the unit cell parameters (full profile analysis - Rietveld method), the crystal size of the polycrystalline sample (coherent scattering region). X-ray diffraction patterns were obtained using a XDR-6100 (Shumadzu) diffractometer with a Cu-K α (β - filter, Ni, current and voltage mode 30 mA, 40 kV) as a radiation source. Measurements were made with a step of 0.05 degrees, a constant detector rotation speed of 4 deg/min ($\omega/2\theta$ -link) and the scanning angle varied from 10° to 100° at 2θ . The X-ray power was 2 kW. The results were analyzed using the database [7]. The penetration depth of Cu-K α radiation is about 1 mm (980 μm) for light elements (carbon), several microns for heavy elements (Ag, W). For most inorganic substances, Cu-K α - is tens of microns (μm) for simple compounds.

Elemental analysis was performed using Fourier-transform infrared (FTIR) spectroscopy. Absorption and transmission spectra of the samples were obtained using the "Happ-Hanzel" method on an IRTracer-100 spectrophotometer. In order to reduce the effect of water vapor (H_2O) and carbon dioxide (CO_2) molecules in the sample in the range of $400\div 4000\text{ cm}^{-1}$, several of the following corrections were performed: addition, smoothing, main zero correction, normalization and ATR correction.

RESULTS AND THEIR DISCUSSION

X-ray diffraction analysis

Figure 1 shows the spectral relationships of the CaTiO_3 compound obtained by the powder diffractometer method. In addition, the Miller indices are given, as well as the distance between planes d_{hkl} for these samples. We used the Rietveld method to refine the structure from X-ray powder data [7]. The principle of the method is to use independent intensity measurements at each point of the diffraction pattern, to describe the line profile using analytical functions, instead of using the integral reflection intensity. Feature parameters, including structural, device, and other characteristics, are refined using a nonlinear least-squares method. Using this refinement method, we determined the distance between the planes d_{hkl} and the Miller index (hkl). As mentioned above, powder X-ray diffraction allows for quantitative elemental analysis.

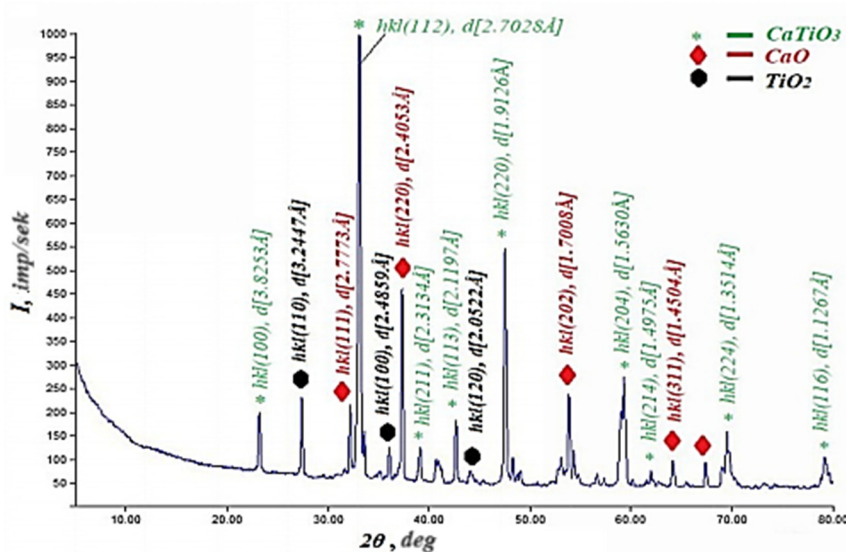


Figure 1. Spectral dependence CaTiO_3 , is obtained by the method of powder diffractometer. Miller indices are given

The degree of crystallinity and amorphism was evaluated for the samples measured by X-ray diffraction analysis using Search and Match software [8]. For calcium titanate, the amorphous phase is 71.35% and the crystalline phase is 28.65%, respectively. In addition, the phase composition (Weight %) and elemental composition of the CaTiO_3 sample was determined using the "Profex" program. The phase composition of the sample prepared for magnetron spraying corresponds to 90.7% perovskite (CaTiO_3), 3.8% titanium, 5.5% calcium. Our elemental analysis of the samples using

Search and Match software shows that the samples have the following composition (in weight percent): 35.7% Ti, 32.2% Ca, and 32.0% O.

As is known from the literature data [9], Miller indices are applicable in all synagogues. As the Miller index increases, the interplanar spacing decreases [3].

Table 1. X-ray analysis of CaTiO₃ perovskite: Miller index, 2theta, intensities, distance between planes, FWHM

No.	hkl	2theta [°]	d [Å]	I/I ₀ (peak height)	Counts (peak area)	FWHM
1	100	23.22	3.8253	120.92	396.92	0.2000
2	110	27.42	3.2447	159.16	417.97	0.1600
3	111	32.20	2.7773	147.20	386.55	0.1600
4	112	33.12	2.7028	1000.00	3939.12	0.2400
5	220	37.36	2.4053	401.92	1055.47	0.1600
6	220	47.54	1.9126	512.76	2019.83	0.2400
7	202	53.86	1.7008	162.85	320.75	0.1200
8	204	59.04	1.5630	157.46	1033.76	0.4000
9	214	62.12	1.4975	181.27	952.06	0.3200
10	224	69.50	1.3514	110.16	361.61	0.2000

Figure 2 shows an X-ray image of a CaTiO₃ compound measured at room temperature. X-ray phase analysis at room temperature shows that peaks at different degrees 23.22, 27.42, 32.20, 33.12, 37.36, 47.54, 53.86, 59.04, 59.32, 69.50 are visible at several angles.

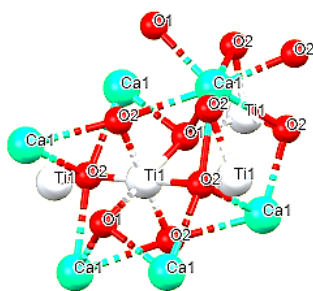


Figure 2. Crystal structure (orthorhombic structure sp. gr. Pbnm)

Processing by the full-profile method of X-ray diffraction data showed that the sample has an orthorhombic structure (sp. gr. Pbnm) with the following lattice parameters: a = 5.3064 Å, b = 5.3531 Å, c = 7.1760 Å and positions, coordinates of atoms in the unit cell (Table 2).

Table 2. Comparative analysis of lattice parameters with the literature

Lattice parameters	a/ Å	b/ Å	c/ Å
This work	5.3064	5.3531	7.1760
Literature [12]	5.380	5.443	7.640

Figure 2 shows the crystal structure CaTiO₃ of calcium titanate, the unit cell of the crystal lattice CaTiO₃ corresponds to the orthorhombic space group and consists of three chemical formulas: Ca, Ti, O.

Infrared spectroscopy analysis

Powder absorption and transmission infrared (IR) spectra of perovskite CaTiO₃ annealed several times at different temperatures were investigated in the range of 400÷4000 cm⁻¹ at room temperature. The spectra vary depending on the composition, annealing temperature and structural state. Autocorrelation analysis was used to determine the variation of the average line width of groups of peaks in primary IR spectra [13-15]. Fourier transform infrared spectroscopy (FTIR) analysis of CaTiO₃ synthesized at high temperature (1300°C) was carried out and its spectrum is shown in Fig. 3. It can be seen from the transmission spectrum that there is a band at the wave number 3600 ÷ 3800 cm⁻¹. It corresponds to the symmetric and asymmetric stretching vibration of weakly bound water interacting with the environment through hydrogen bonding and the O - H stretching modes corresponding to the stretching vibrations of hydrogen-bonded OH groups. As the molar ratio increased to 1:4, no peak was found indicating the absence of moisture and water molecules in this system [16]. Therefore, a molar ratio of 1:4 is the best condition for the anhydrous formation of CaTiO₃ perovskite powders.

The main broad peaks are observed in the range of 680÷400 cm⁻¹, the absorption band at the wave number of 543.93 cm⁻¹ corresponds to the specific stretching vibrations of Ti-O bonds, which indicates the presence of TiO₆ octahedra and CaTiO₃ implies the formation of a perovskite-type structure [17]. The band at wave number 435.91 cm⁻¹ is characteristic of Ca-Ti-O bending vibrations of calcium titanate. It is due to a weaker, symmetric stretching band (C-O) in the range of 1480÷1380 cm⁻¹ [18]. The strongest peaks correspond to the wave number of 543.93 cm⁻¹, 435.91 cm⁻¹, 420.48 cm⁻¹, 405.05 cm⁻¹, characteristic vibrations of calcium titanate in the range of 910÷3600 cm⁻¹ at 1100 °C. its

absence indicates the formation of pure CaTiO_3 [19]. This clearly shows that thermal annealing can be one of the well-established synthetic routes to prepare calcium titanate perovskite materials. Table 3 presents several correlations and wavenumber intensities in the absorption spectrum of a sample prepared using a stoichiometric mixture.

Table 3. Multiple correlations and intensity in the absorption spectrum of CaTiO_3

no	Peak Intensity	Corr. Intensity	Base (H)	Base (L)	Area Corr.	Area	Area color
1	405.05	24.00	5.71	410.84	401.19	699.526	29.405
2	420.43	28.43	5.06	422.41	420.84	802.448	32.825
3	543.93	31.05	3.90	553.27	532.05	1395.688	50.320
4	858.32	23.13	23.68	857.93	857.63	6531.839	1185.06
5	1473.62	83.92	6.46	1455.11	1422.32	398.420	82.770

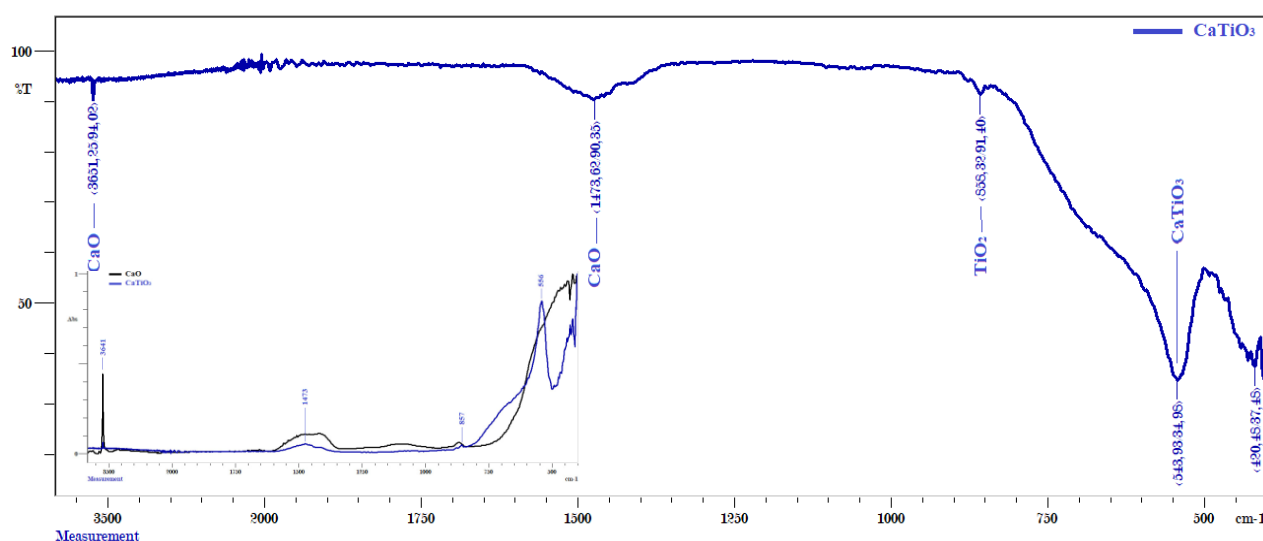


Figure 3. FTIR transmission and absorption spectrums of CaTiO_3 prepared at 1300°C

The results of X-ray and IR absorption measurements of the CaTiO_3 perovskite compound show that it is one of the most versatile oxides of the perovskite family for applications in fields such as electronics and photovoltaics due to its structural structure and optical properties. Therefore, it is important to study the ways of forming semiconductor material.

CONCLUSION

The qualitative composition of CaTiO_3 perovskite compound formed by mechanical mixing and thermal heating, the amorphous and crystalline phase of the substance, and its structure were studied with the help of XDR-6100 type diffractometer. Using "Fullprof", "Profex" processing programs, unit cell parameters, Miller indices and interplanar distance of the sample were determined. It was observed that as the Miller index increased, the distance between the planes decreased. For calcium titanate, the amorphous phase is 71.35% and the crystalline phase is 28.65%, respectively. The phase composition of the sample corresponds to 90.7% perovskite (CaTiO_3), 3.8% titanium, 5.5% calcium. Elemental analysis shows that the samples have the following composition (in weight percent): 35.7% – Ti, 32.2% – Ca and 32.0% – O. FT-IR analyzes of the CaTiO_3 compound were conducted. The main broad peaks are observed in the range of $680\div 400\text{ cm}^{-1}$, the absorption band at the wave number of 538.14 cm^{-1} corresponds to the specific stretching vibrations of Ti-O bonds and indicates the formation of the CaTiO_3 perovskite type structure implies. The band at wave number 435.91 cm^{-1} is characteristic of Ca-Ti-O bending vibrations of calcium titanate. The strongest peaks correspond to the wave numbers of 543.93 cm^{-1} , 435.91 cm^{-1} , 420.48 cm^{-1} , 405.05 cm^{-1} . Absence of characteristic vibrations of calcium titanate in the range of $910\div 3600\text{ cm}^{-1}$ at 1100°C indicates the formation of calcium titanate perovskite. Based on the results of these measurements, it will be possible to use semiconductor compounds in the future to create nanofilms by magnetron sputtering.

ORCID

© Khujamkul Davranov, <https://orcid.org/0000-0002-2373-3026>; © Muradulla Normuradov, <https://orcid.org/0000-0003-1771-0853>
 © Muzaffar Davlatov, <https://orcid.org/0000-0002-1160-7831>; © Kuvondiq Dovranov, <https://orcid.org/0000-0003-1476-6552>

REFERENCES

- [1] S. Dahlke, J. Sterling, and C. Meehan, "Policy and market drivers for advancing clean energy," *Advances in Clean Energy Technologies*, 451-485 (2021). <https://doi.org/10.31219/osf.io/hsbry>
- [2] J. Grove, "Triple miracle' sees huge rise in EU funds for frontier research," *Times Higher Education*, **28**, (2011).

- [3] M.T. Normuradov, Sh.T. Khozhiev, K.T. Dovranov, Kh.T. Davranov, M.A. Davlatov, and F.K. Khollokov, "Development of a technology for the production of nano-sized heterostructured films by ion-plasma deposition. Structure of materials," Ukr. J. Phys. **68**(3), (2023). <https://doi.org/10.15407/ujpe68.3.210>
- [4] F. Giustino, and H.J. Snaith, "Toward lead-free perovskite solar cells," ACS Energy Letters, **1**(6), 1233-1240 (2016). <https://doi.org/10.1021/acseenergylett.6b00499>
- [5] D.D. Nematov, A.S. Burhonzoda, and F. Shokir, "Analysis of the structural characteristics and optoelectronic properties of CaTiO₃ as a non-toxic raw material for solar cells: a DFT study," (2020). <https://doi.org/10.48550/arXiv.2210.14835>
- [6] S.S. Gaikwad, A.V. Borhade, and V.B. Gaikwad, "A green chemistry approach for synthesis of CaTiO₃ Photocatalyst: its effects on degradation of methylene blue, phytotoxicity and microbial Study," Der Pharma Chemica, **4**(1), 184-193 (2012). <https://www.derpharmachemica.com/pharma-chemica/a-green-chemistry-approach-for-synthesis-of-catio3-photocatalyst-its-effects-on-degradation-of-methylene-blue-phytotoxic.pdf>
- [7] M.Yu. Tashmetov, F.K. Khallokov, N.B. Ismatov, I.I. Yuldashova, I. Nuritdinov, and S.Kh. Umarov, "Study of the influence of electronic radiation on the surface, structure and Raman spectrum of a TlInS₂ single crystal," Phys. B, **613**, 412879 (2021). <https://doi.org/10.1016/j.physb.2021.412879>
- [8] M.Yu. Tashmetov, F.K. Khallokov, N.B. Ismatov, I.I. Yuldashova, and S.Kh. Umarov, "Electronic irradiation of TlInS_xSe_{2-x} (x-1): Morphology, structure and raman scattering," Intern. J. Modern Phys. B, **35**(28), 2150289 (2021). <https://doi.org/10.1142/S0217979221502891>
- [9] L. Smrčok, V. Langer, M. Halvarsson, and S. Rupp, "A new Rietveld refinement of k-Al₂O₃," Zeitschrift fuer Kristallographie **216**, 409 (2001). <https://doi.org/10.1524/zkri.216.7.409.20361>
- [10] W. Dong, Q. Bao, X. Gu, and G. Zhao, "Controlled synthesis of flower-like CaTiO₃ and effects of morphology on its photocatalytic activities," Journal of the Ceramic Society of Japan, **123**(8), 643-648 (2015). <https://doi.org/10.2109/jcersj2.123.643>
- [11] M.T. Normuradov, Sh.T. Khozhiev, L.B. Akhmedova, I.O. Kosimov, M.A. Davlatov, and K.T. Dovranov, "Peculiarities of BaTiO₃ in electronic and X-Ray analysis," E3S Web Conf. **383**, 04068 (2023). <https://doi.org/10.1051/e3sconf/202338304068>
- [12] Q. Fan, J. Yang, C. Deng, J. Zhang, and J. Cao, "Electronic structure and optical properties of CaTiO₃: An ab initio study," in: Proc. SPIE 9794, Sixth International Conference on Electronics and Information Engineering, 97942I (2015). <https://doi.org/10.1117/12.2203278>
- [13] D. Parajuli, N. Murali, K. Samatha, N.L. Shah, and B.R. Sharma, "Structural, Morphological, and Textural Properties of Coprecipitated CaTiO₃ for Anion Exchange in the Electrolyzer," Journal of Nepal Physical Society, **9**(1), 137-142 (2023). <https://doi.org/10.3126/jnphysoc.v9i1.57751>
- [14] I.R. Bekpulatov, G.T. Imanova, B.E. Umirzakov, K.T. Dovranov, V.V. Loboda, S.H. Jabarov, I.X. Turapov, et al., "Formation of thin CrSi₂ films by the solid-phase ion-plasma method and their thermoelectric properties," Materials Research Innovations, (2024). <https://doi.org/10.1080/14328917.2024.2339001>
- [15] K.T. Dovranov, M. Normurodov, Kh.T. Davranov, and I.R. Bekpulatov, "Formation of Mn₄Si₇/Si(111), CrSi₂/Si(111), and CoSi₂/Si(111) Thin Film and Evaluation of Their Optically Direct and Indirect Band Gap," Ukrainian Journal of Physics, **20**(69), (2024). <https://doi.org/10.15407/ujpe69.1.20>
- [16] M. Mostafa, Z.A. Alrowaili, M.M. Al Shehri, M. Mobarak, and A.M. Abbas, "Structural and Optical Properties of Calcium Titanate Prepared from Gypsum," Journal of Nanotechnology, **2022**, 6020378 (2022). <https://doi.org/10.1155/2022/6020378>
- [17] A. Kumar, C. Schuerings, S. Kumar, A. Kumar, and V. Krishnan, "Perovskite-structured CaTiO₃ coupled with g-C₃N₄ as a heterojunction photocatalyst for organic pollutant degradation," Beilstein J. Nanotechnol. **9**, 671-685 (2018). <https://doi.org/10.3762/bjnano.9.62>
- [18] A.A.A. Torimtubun, A.C. Augusty, E. Maulana, and L. Ernawati, "Affordable and sustainable new generation of solar cells: calcium titanate (CaTiO₃)-based perovskite solar cells," E3S Web of Conferences, **67**, 01010 (2018). <https://doi.org/10.1051/e3sconf/20186701010>
- [19] M. Rizwan, Z. Usman, M. Shakil, S.S.A. Gillani, S. Azeem, H.B. Jin, C.B. Cao, et al., "Electronic and optical behaviour of lanthanum doped CaTiO₃ perovskite," Materials Research Express, **7**(1), 015920 (2020). <https://doi.org/10.1088/2053-1591/ab6802>

ОТРИМАННЯ ПЕРОВСКІТНОЇ СПОЛУКИ ТИТАНАТУ КАЛЬЦІЮ, ОПТИЧНІ ТА СТРУКТУРНІ ВЛАСТИВОСТІ

Худжамкул Т. Давранов^а, Мураддулла Т. Нормурадov^а, Музаффар А. Давлатов^б, Куводдик Т. Довранов^а,
Т.У. Тошев^б, Н.А. Курбонов^б

^аКаршинський державний університет, Карші, 180100, Узбекистан

^бКаршинський інженерно-економічний інститут, Карші, 180100, Узбекистан

У цій роботі ми успішно виготовили перовскітну сполуку титанату кальцію. Отриману сполуку CaTiO₃ досліджували шляхом приготування зразків пресуванням у порошкоподібному стані та використанням приладу Пуссона. За допомогою рентгенівського дифрактометра визначали відстань між площинами dhkl, індекси Міллера (hkl), ступінь кристалічності та аморфізму, структуру та параметри решітки перовскітної сполуки титанату кальцію. Також за результатами FT-IR аналізу підтверджено утворення перовскіту CaTiO₃ в результаті дослідження молекулярних коливань. Основні широкі піки спостерігаються в діапазоні 680÷400 см⁻¹, смуга поглинання на хвильовому числі 543,93 см⁻¹ відповідає питомим валентним коливанням зв'язків Ti-O і свідчить про утворення передбаченої перовскітної структури CaTiO₃. За результатами цих вимірювань у майбутньому можна буде використовувати напівпровідникові сполуки для створення наноплівки методом магнетронного розпилення.

Ключові слова: рентгенофазовий аналіз; індекси Міллера; міжплощинна відстань; титанат кальцію; кристалічна та аморфна фази; FT-IR

LOW-TEMPERATURE GROWTH OF CARBON NANOTUBES USING NICKEL CATALYST

Ilyos J. Abdisaidov*, **Sevara G. Gulomjanova**, **Ilyos Kh. Khudaykulov**, **Khatam B. Ashurov**
*Institute of Ion-Plasma and Laser Technologies named after U.A. Arifov, Academy of Sciences of the Republic of Uzbekistan,
100125, Durmon yuli st. 33, Tashkent, Uzbekistan*

**Corresponding Author e-mail: ilyos.abdisaidov@mail.ru*

Received May 7, 2024; revised July 8, 2024; accepted July 17, 2024

This study presents the results of a comprehensive investigation into the fabrication of single-walled carbon nanotubes (SWCNTs) employing chemical vapor deposition (CVD) technique, with nickel nanoparticles serving as crucial catalysts. These nanoparticles are synthesized via the reduction of oxide precursors using hydrogen and are strategically incorporated with ethanol vapor as the primary carbon source. The effectiveness and reproducibility of this synthesis method are thoroughly validated using advanced analytical techniques. Particularly noteworthy is the demonstrated ability to conduct the process at relatively low temperatures, not exceeding 500°C, which is of significant importance. Such precise control over synthesis conditions not only augurs well for the scalability of SWCNT production but also carries substantial implications for the advancement of nanomaterial synthesis methodologies.

Keywords: *Catalysts, Single-walled carbon nanotubes, Multi-walled carbon nanotubes, X-ray phase analysis, Light scattering spectroscopy, Scanning electron microscopy*

PACS: 61.46-w, 61.46.+w, 61.46.Np

INTRODUCTION

Carbon nanotubes (CNTs) possess exceptional electrical and thermal conductivity alongside remarkable strength and durability [1]. These properties render them valuable across various fields such as energy storage [2-3], construction materials [4], chip technology [5], biomedical applications [6], and increasingly, electronic microcircuits due to their high electrical conductivity [7]. CNTs, essentially seamless cylinders comprised of rolled-up graphene sheets, exist in two primary forms: single-walled and multi-walled. Single-walled CNTs have diameters ranging from 0.4 to 4 nm, while multi-walled CNTs consist of several concentric shells of single-walled tubes with diameters ranging from 1.4 to 100 nm and a wall-to-wall distance of 0.34 nm [8].

Since their discovery, methods for synthesizing CNTs have garnered increasing interest [9], including arc discharge, laser ablation, chemical vapor deposition (CVD), and plasma-enhanced chemical vapor deposition (PECVD). Among these methods, CVD stands out for its cost-effectiveness, scalability, and widespread adoption. The quality of CNTs synthesized via CVD depends on various parameters such as catalyst type, substrate, carbon source, reaction conditions (time and temperature), gas flow rate, and specific surface area of the resulting powder [10]. Additionally, the diameter of CNTs obtained via CVD is influenced by the catalyst type, with commonly used catalysts including Fe, Ni, Co, and their alloys. Studies have shown that pure nickel and cobalt exhibit higher catalytic activity compared to iron [11].

For instance, in [12], CNTs were synthesized from ethanol at 1150°C using catalysts from the VIII group (Fe, Co, Ni) based on corresponding metallocenes. Employment of trimetallic catalysts notably enhanced CNT yield, although mixtures of two or three metallocenes as catalysts led to increased structural defects in CNTs. In another study [13], multi-walled CNTs were synthesized on a silicon substrate via CVD using ethanol at 800°C with three different metallic catalysts (iron, copper, and nickel). Moreover, [14] observed improved CNT quality with a gradual temperature increase from 500°C to 650°C, but further temperature elevation hindered CNT formation, attributed to nickel particle enlargement at higher temperatures.

In summary, relatively few studies have investigated CVD synthesis of CNTs using nickel as a catalyst at low temperatures. Our work addresses this gap, presenting results from CVD synthesis of single-walled CNTs utilizing a nickel catalyst at relatively low process temperatures.

The CVD method is widely employed for synthesizing CNTs. In this process, a gas mixture containing carbon source materials (such as methane, ethylene, or acetylene) is introduced into a reactor, where it reacts with a heated substrate coated with a catalyst. Carbon atoms then condense on the substrate's surface, sequentially adding to the growing nanotube, thereby controlling its structure and properties, including length, diameter, orientation, and efficiency.

EXPERIMENTAL PROCEDURE

In our experiments, pairs of ethanol vapor with a purity of 96.5% served as the hydrocarbon source. Nickel nanoparticles, obtained through the hydrogen reduction of nickel oxide synthesized via the sol-gel method, were utilized as the catalyst. Upon obtaining nickel nanoparticles, hydrogen supply to the reactor was halted, and the temperature was elevated to 500°C to initiate the synthesis of carbon nanotubes (CNTs). Ethanol vapor was introduced into the reactor

using Ar as the carrier gas at a flow rate of 5 l/min. The CNT synthesis process lasted approximately 30 minutes, during which side products resulting from pyrolysis were eliminated through combustion. The characteristics of the synthesized CNTs were examined utilizing scanning electron microscopy (SEM), X-ray structural analysis (XRD), and energy-dispersive X-ray spectroscopy (EDX) techniques employing state-of-the-art, metrologically certified equipment.

RESULTS AND DISCUSSION

Figure 1 displays an image acquired through scanning electron microscopy, illustrating a cluster of single-walled carbon nanotubes synthesized under the described conditions. The resultant product manifested as spiderweb-like fibers, predominantly aggregating at the bottom of the reactor. Analysis of the product revealed its composition to comprise fibrous carbon with traces of nickel and oxygen, devoid of any other impurities.

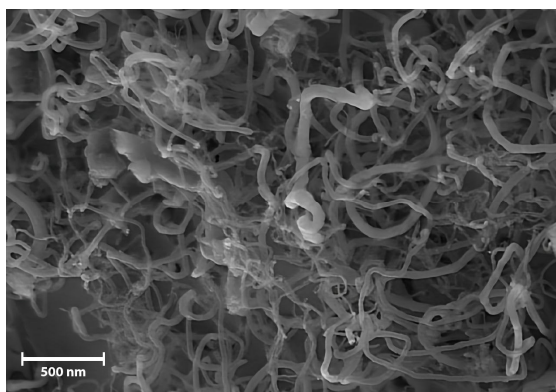


Figure 1. SEM image of a group of carbon nanotubes.

Additionally, a portion of the product deposited as wall-like formations exhibiting similar morphology and purity. The elemental composition of the nanotubes was determined through EDX analysis, with the results depicted in Figure 2. The analysis revealed that over 94% of the carbon nanotubes are composed of carbon.

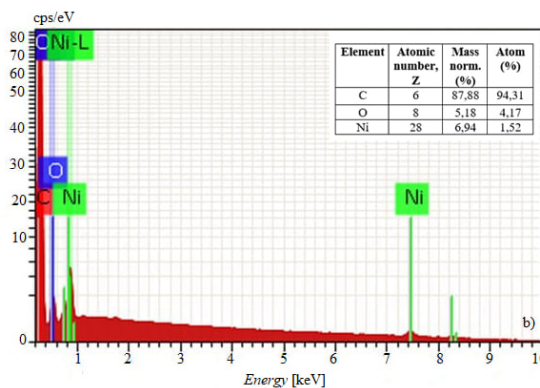


Figure 2. Results of energy-dispersive X-ray (EDX) analysis illustrating the composition of carbon nanotubes synthesized via the chemical vapor deposition (CVD) method

The elemental composition of the nanotubes was determined by EDX analysis (Bruker, SDD, XFlash 6/60, Berlin, Germany), the results of which are presented. It can be seen that more than 94% of the CNTs consist of carbon.

Raman spectroscopy studies were performed using equipment produced by "Renishaw", United Kingdom. A "green" laser with a wavelength of 532 nm and a nominal power of 100 mW was selected for measurement. Measurements were carried out in the wavenumber range from 100 to 3200 cm⁻¹. The signal acquisition time was 10 seconds. The results are shown in Figure 3.

The radial breathing mode (RBM) peak exclusively manifests in single-walled carbon nanotubes (SWCNTs), within the frequency spectrum ranging from 100 to 500 cm⁻¹. This peak's position is inversely correlated with the diameter of the nanotube and can be determined by the following Equation (1).

$$\omega_{RBM} = A/(dt) + B, \tag{1}$$

where, ω_{RBM} represents the oscillation frequency, while A and B are constants, and dt denotes the diameter of the carbon nanotube (CNT).

The observation of the characteristic peak, namely the radial breathing mode (RBM) peak, at a frequency of 121 cm⁻¹ indicates the successful synthesis of single-walled CNTs using nickel as a catalyst via the chemical vapor deposition

(CVD) method. Based on this result, it can be inferred that the diameter of the single-walled CNTs synthesized, as determined by Equation (1), is approximately ~ 2 nm.

Furthermore, the D peak, indicative of defects in the CNTs, as shown in Figure 3, is measured at 1341 cm^{-1} . Additionally, the G peak, primarily describing the C-C bond and deformation in CNTs, registers at 1568 cm^{-1} . The G' peak, which characterizes doping and isotopic features in CNTs, corresponds to 2683 cm^{-1} . The quality assessment of synthesized CNTs is commonly evaluated by the ratio of the intensity of the D peak (I_D) to the intensity of the G peak (I_G), denoted as (I_D/I_G). In this case, the calculated ratio is 0.5, indicating qualitative adherence to the definition of this parameter.

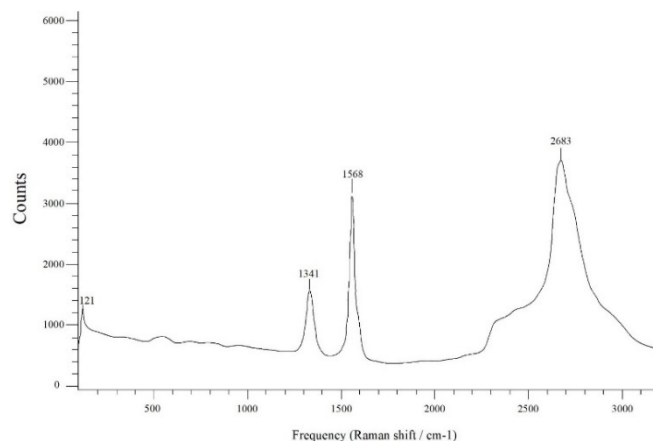


Figure 3. Raman spectra of carbon nanotubes synthesized by the CVD method

Figure 4 presents X-ray diffraction (XRD) patterns of carbon nanotubes. XRD, a rapid analysis technique, is utilized for material identification, notable for its capacity to evaluate both local and overall material characteristics, encompassing lattice structure with phase morphology [15], interlayer distances, among others.

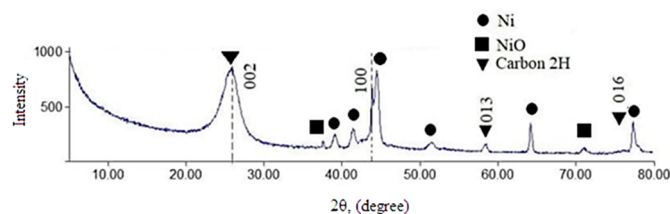


Figure 4. X-ray diffraction (XRD) patterns of carbon nanotubes synthesized by the CVD method

Figure 4 presents X-ray diffraction (XRD) patterns of carbon nanotubes. XRD, a rapid analysis technique, is utilized for material identification, notable for its capacity to evaluate both local and overall material characteristics, encompassing lattice structure with phase morphology [15], interlayer distances, among others.

The X-ray diffraction (XRD) analysis was conducted using the XRD-6100 Shimadzu X-ray diffractometer, employing Cu-K α radiation with a wavelength (λ) of 1.541874 \AA . The angular range of 2θ spanned from 5° to 80° , with a step size of 0.05° .

It is well-established that the intensity of diffraction peaks in carbon nanotubes (CNTs) is contingent upon the morphological orientation of the nanotubes. Specifically, when X-rays interact with a single wall of the CNT, they generate peaks (002) along with some parallel (h k l) reflections. As the X-rays traverse through the hollow central core of the CNT, supplementary arrays of hexagonal peaks (h k o) are produced.

The CNTs synthesized in our experiment exhibited two characteristic peaks at $2\theta = 25.5^\circ$ and 43.3° , corresponding to the diffraction from the C(002) and C(100) planes of carbon nanotubes, respectively [16]. Furthermore, literature [17] suggests that in addition to C(100) and C(002), peaks such as C(004) and C(110) may be observable at $2\theta = 54.8^\circ$ and 79.2° . In Figure 3, it is evident that the CNTs possess four characteristic peaks at $2\theta = 25.8^\circ$, 43.3° , 58.4° , and 78.1° , attributable to the diffraction from the planes C(100), C(002), C(013), and C(016) of the synthesized carbon nanotubes.

Moreover, the XRD pattern suggests the formation of hybrid CNTs in our case. This inference is supported by the most intense diffraction peak observed at $2\theta = 24.31^\circ$, corresponding to the (002) reflection, indicative of a crystalline and cylindrical structure [18]. Additionally, traces of nickel oxide are discernible only in two peaks, specifically at angles 37.9° and 71.8° , with low intensity.

CONCLUSIONS

Utilizing the chemical vapor deposition (CVD) technique at relatively moderate temperatures, employing ethanol vapor as the precursor and hydrogen-reduced nickel oxide nanoparticles as catalysts, a successful synthesis of carbon nanotubes (CNTs) was achieved under controlled environmental conditions. Scanning electron microscopy (SEM)

analysis revealed the formation of fibrous carbon structures, suggestive of hybrid CNTs, indicative of a complex and intertwined nanotube network. Elemental analysis via energy-dispersive X-ray (EDX) spectroscopy exhibited a substantial carbon content, constituting 88% by mass and 94% by atomic number, affirming the predominantly carbonaceous nature of the synthesized material. Furthermore, X-ray diffraction (XRD) investigations demonstrated the presence of four discernible peaks characteristic of carbon nanotubes, emanating from diffraction events associated with the lattice planes C(100), C(002), C(013), and C(016).

The amalgamated findings from these analytical methodologies collectively underscore the successful production of single-walled carbon nanotubes (SWCNTs) under controlled and mild temperature conditions, not surpassing 500°C. This synthesis approach, facilitated by the judicious selection of precursor and catalyst materials, underscores the feasibility of achieving high-quality SWCNTs while mitigating the energy demands associated with traditional high-temperature synthesis methods. The observed structural, elemental, and crystalline characteristics align closely with the anticipated attributes of SWCNTs, further corroborating the efficacy of the employed synthesis strategy. These findings not only contribute to advancing our understanding of CNT synthesis methodologies but also hold promise for various applications in nanotechnology, materials science, and beyond.

Acknowledgments

The authors gratefully acknowledge the financial and technical support provided by the Ministry of Higher Education, Science, and Innovation under project number IL-5421101842.

ORCID

© Ilyos J. Abdusaidov, <https://orcid.org/0000-0001-7473-1074>; © Ilyos Kh. Khudaykulov, <https://orcid.org/0000-0002-2335-4456>
© Khatam B. Ashurov, <https://orcid.org/0000-0002-7604-2333>

REFERENCES

- [1] N. Gupta, S. M. Gupta, and S. K. Sharma, Carbon Letters, **29**, 419 (2019). <https://doi.org/10.1007/s42823-019-00068-2>.
- [2] I. Ashurov, S. Iskandarov, U. Khalilov, and Kh. Ashurov, Applied Solar Energy, **58**(3), 334 (2022). <https://doi.org/10.3103/S0003701X22030033>
- [3] V.M. Rotshteyn, T.K. Turdaliev, and Kh.B. Ashurov, Applied Solar Energy, **57**(6), 480 (2021). <https://doi.org/10.3103/S0003701X21060153>
- [4] K. Cui, J. Chang, L. Feo, C. L. Chow, and D. Lau, Frontiers in Materials, **9**, 861646, (2022). <https://doi.org/10.3389/fmats.2022.861646>
- [5] L. Sun, X. Wang, Y. Wang, and Q. Zhang, Carbon, **122**, 462-474, (2017). <https://doi.org/10.1016/j.carbon.2017.07.006>
- [6] B.O. Murjani, P.S. Kadu, M. Bansod, S.S. Vaidya, and M.D. Yadav, Carbon Letters, **32**(5), 1207 (2022). <https://doi.org/10.1007/s42823-022-00364-4>
- [7] S. Vollebregt, S. Banerjee, F.D. Tichelaar, and R. Ishihara, Microelectronic Engineering, **156**, 126 (2016). <https://doi.org/10.1016/j.mee.2016.01.034>
- [8] M. Tehrani, and P. Khanbolouki, Advances in Nanomaterials, 3-35, (2018). https://doi.org/10.1007/978-3-319-64717-3_1
- [9] S. Iijima, Nature, **354**, 56 (1991). <https://doi.org/10.1038/354056a0>
- [10] V. Sivamaran, V. Balasubramanian, M. Gopalakrishnan, V. Viswabaskaran, A. Gourav Rao, and S. Selvamani, Nanomaterials and Nanotechnology, **12**, 1 (2022). <https://doi.org/10.1177/18479804221079495>
- [11] J. Gao, J. Zhong, L. Bai, J. Liu, G. Zhao, and X. Sun, Scientific reports, **4**(1), 3606 (2014). <https://doi.org/10.1038/srep03606>
- [12] A.R. Karaeva, S.A. Urvanov, N.V. Kazennov, E.B. Mitberg, and V.Z. Mordkovich, Nanomaterials, **10**(11), 2279 (2020). <https://doi.org/10.3390/nano10112279>
- [13] T. Thurakitseree, and C. Pakpum, Applied Mechanics and Materials, **891**, 195 (2019). <https://doi.org/10.4028/www.scientific.net/AMM.891.19>
- [14] L. He, G. Liao, S. Hu, L. Jiang, H. Han, H. Li, and J. Xiang, Fuel, **264**, 116749 (2020). <https://doi.org/10.1016/j.fuel.2019.116749>
- [15] R. Das, S. Bee Abd Hamid, M. Eaqub Ali, S. Ramakrishna, and W. Yongzhi, Current Nanoscience, **11**(1), 23 (2015). <https://doi.org/10.2174/1573413710666140818210043>
- [16] M.S. Dresselhaus, A. Jorio and R. Saito, Annu. Rev. Condens. Matter Phys. **1**(1), 89- (2010). <https://doi.org/10.1146/annurev-conmatphys-070909-103919>
- [17] A.F. Ismail, P.S. Goh, J.C. Tee, S.M. Sanip, and M. Aziz, Nano, **3**(03), 127 (2008). <https://doi.org/10.1142/S1793292008000927>
- [18] D.P. Roe, R. Xu, and C.B. Roberts, Applied Catalysis A: General, **543**, 141 (2017). <https://doi.org/10.1016/j.apcata.2017.06.020>

НИЗЬКОТЕМПЕРАТУРНЕ ВИРОЩУВАННЯ ВУГЛЕЦЕВИХ НАНОТРУБОК З ВИКОРИСТАННЯМ НІКЕЛЕВОГО КАТАЛІЗАТОРА

Ільос Дж. Абдісаїдов, Севара Г. Гуломжанова, Ільос Х. Худайкулов, Хатам Б. Ашуров
Інститут іонно-плазмових і лазерних технологій імені У.А. Аріфова, Академія наук Республіки Узбекистан,
100125, Дурмон йулі вул. 33, Ташкент, Узбекистан

Це дослідження представляє результати всебічного дослідження виготовлення одностінних вуглецевих нанотрубок (SWCNT) із застосуванням техніки хімічного осадження з парової фази (CVD), причому наночастинки нікелю виступають в якості ключових каталізаторів. Ці наночастинки синтезуються шляхом відновлення прекурсорів оксидів за допомогою водню та стратегічно об'єднуються з парами етанолу як основним джерелом вуглецю. Ефективність і відтворюваність цього методу синтезу ретельно перевірені за допомогою передових аналітичних методів. Особливо слід відзначити продемонстровану здатність проводити процес при відносно низьких температурах, не вище 500°C, що має важливе значення. Такий точний контроль над умовами синтезу не тільки сприяє масштабованості виробництва SWCNT, але також має суттєві наслідки для вдосконалення методологій синтезу наноматеріалів.

Ключові слова: каталізатори; одностінні вуглецеві нанотрубки; багаточарові вуглецеві нанотрубки; рентгенофазовий аналіз; спектроскопія розсіювання світла; скануюча електронна мікроскопія

EFFECT OF HEATING OF CHARGE CARRIERS AND PHONONS ON THE CONTACT RESISTANCE OF RECTIFYING METAL-SEMICONDUCTOR STRUCTURES

✉ **Gafur Gulyamov**, ✉ **K.B. Umarov**, ✉ **Alisher Z. Soliyev***

Namangan Engineering-Construction Institute, I. Karimov St. Namangan 160103, Uzbekistan

**Corresponding Author e-mail: szalisher2002@gmail.com*

Received May 27, 2024; revised July 27, 2024; accepted August 7, 2024

The dependence of the temperature of charge carriers and phonons on the contact resistance of the Schottky diode is calculated. It is shown that the increase in contact resistance depends on the current passing through the diode, the surface and volume heat transfer coefficients of electrons and phonons, barrier height, the dimensions of the diode, as well as scattering mechanisms, relaxation time of energy and momentum.

Keywords: *Potential barrier; Contact resistance; Temperature distributions of electrons and phonons; Electronic and phonon thermal conductivities; Nonideality coefficient; Peltier effect; Thermal size effects (TSE)*

PACS: 73.40.Cg

INTRODUCTION

A semiconductor compound with a Schottky potential barrier is one of the key elements of semiconductor electronics. The development of modern semiconductor electronics is largely determined by fundamental research in the field of semiconductor physics. In semiconductor structures, one of the main characteristics is specific contact resistance, which significantly affects their current-voltage characteristics (I-V characteristics) [1-3].

A semiconductor composition with a Schottky potential barrier is a basic element of semiconductor electronics. The development of modern semiconductor electronics is largely determined by fundamental research in the field of semiconductor physics. Among such studies, an important place is occupied by the study of the properties of semiconductors in electric fields, when the average energy of charge carriers significantly exceeds the equilibrium energy determined by the temperature of the crystal lattice [4].

In [5-10], the influence of heating of current carriers (assuming that the temperature of the phonon gas is equal to the ambient temperature) on the current-voltage characteristics of rectifying structures was studied. In [10], contact resistance was studied and it was found that contact resistance strongly depends on the temperature of charge carriers and on the magnitude of the current flowing through the barrier.

In many works [11-15], it has been experimentally established that in the high-temperature region the resistivity of the contact increases with increasing temperature, but this has not been studied theoretically.

The main goal of this work is to study the dependence of the temperature of charge carriers and phonons on the resistance of the Schottky barrier metal-semiconductor contact.

THE INFLUENCE OF HEATING ELECTRONS AND PHONONS ON CURRENT RECTIFYING METAL-SEMICONDUCTOR STRUCTURES

Theoretically calculated the current in rectifying metal-semiconductor diodes as a result of heating of charge carriers and phonons, it is necessary to calculate the carrier and phonon temperature distribution around the diode contact. To do this, we assume that the Schottky contact is located at point $x = 0$, metal-semiconductor boundary, barrier height φ_0 , the thickness of the contact charge region δ . We assume that the conditions of the diode theory are met. We assume that the conditions of the diode theory studied earlier are correct [16]. If the current passes through the barrier, the electrons or holes are considered to be heated by the barrier field and the externally applied field. The energy received by electrons from the field is transferred to phonons. The phonon and electronic subsystems transfer energy to the contacts due to thermal conductivity. We will assume that the scattering of electrons by phonons in a semiconductor is quasi-elastic, and the electron-electron interaction is quite effective. Then the thickness of the region near the contact, where $T_e \neq T_p$, is approximately $l_e \gg l_i$ (l_e , l_i are the relaxation lengths of electron energy and momentum) and in this region the temperature approximation is valid [17]. In the temperature approximation, kinetic coefficients (conductivity, thermal conductivity, and others) depend on T_e and T_p . In the calculations, we will assume that T_e and T_p differ slightly from the equilibrium temperature ($|T_{e,p} - T_0| \ll T_0$) [17].

In [8], the temperature distributions of electrons and phonons in thin ($k_a \ll 1$) and massive ($k_a \gg 1$) diodes are given. The temperature distributions of carriers and phonons in the diode contact region are determined from solving the system equation and taking into account the boundary conditions and give the following expressions:

$$T_{e,p}(x) = T - \Phi_{e,p}(x)I\varphi \tag{1}$$

where $\Phi_{e,p}(x)$ are the parameters depending on the coefficients of surface and volume thermal conductivity of electrons and phonons, barrier height, the size of the diode, as well as the mechanisms of pulse scattering, relaxation time of energy and momentum.

In the volume of the sample, the temperatures of electrons and phonons coincide due to the cooling length k^{-1} and depend linearly on the x coordinate.

To approximate the diode theory, we present the I-V characteristics of a Schottky diode in dimensionless form [16]:

$$I = \exp\left(\frac{Y}{\theta_p} - \frac{Y-U}{\theta_e}\right) - 1 \tag{2}$$

$$\theta_e = 1 - B_e I(Y - U)$$

$$\theta_p = 1 - B_p I(Y - U)$$

$I = \frac{j}{j_s}$ is a current without dimension, $Y = \frac{e\varphi_0}{kT}$ - potential barrier dimensionless height, $U = \frac{eV}{kT}$ dimensionless voltage, $\theta_e = \frac{T_e}{T}$ and $\theta_p = \frac{T_p}{T}$ the dimensionless temperatures of electrons and phonons respectively.

$$B_{e,p} = \frac{j_s^k}{\chi_{ek}} \Phi_{e,p}(\delta) \text{ or } B_{e,p} = \Phi_{e,p} \sqrt{\frac{1}{3\pi(r+5/2)}} \sqrt{\frac{\tau_e}{\tau_p}} e^{-Y} \tag{3}$$

where τ_e is the energy relaxation time, τ_p is the pulse relaxation time, and r is the number that determines the mechanisms of pulse dissipation. It contains as a parameter the surface and volume thermal conductivity of electrons and phonons ($\chi_{e,p}$ and $\eta_{e,p}$).

Transforming (2) the system of equations we obtain the following quadratic equation for ψ :

$$B_p I(1 - B_e I \ln(I + 1))\psi^2 + ((1 + B_e I(Y_0 - \ln(I + 1)) + B_p I \ln(I + 1))\psi - (Y_0 - \ln(I + 1))) = 0, \tag{4}$$

where $\psi = Y_0 - U$. (4) to the quadratic equation is given by the I-V characteristics of the Schottky diode.

If $B_p = 0$, then the diode's current-voltage characteristics has the following form:

$$U = \frac{Y_0 - (Y_0 - \ln(I + 1))(1 - Y_0 I B_e)}{1 + B_e I(Y_0 - \ln(I + 1))}. \tag{5}$$

When $B_p = B_e$, then the I-V characteristics of the diode:

$$U = \frac{(1 - Y_0 B_e) \ln(I + 1)}{1 + B_e I \ln(I + 1)}. \tag{6}$$

From (3) it is clear that the values of the parameters B_e and B_p change the appearance of the diode's current-voltage characteristic. The parameters B_e and B_p are determined through the parameters of the diode: the coefficients of surface and volume thermal conductivity of electrons and phonons, barrier height, the size of the diode, the mechanisms of pulse scattering, energy and momentum relaxation time.

CONTACT RESISTANCE OF A SCHOTTKY DIODE DURING HEATING OF ELECTRONS AND PHONONS

Experimental studies of the electrical properties of metal-semiconductor contacts have shown that the direct branch of the current-voltage characteristic often differs somewhat from the theoretical one and is usually approximated in dimensionless form by the following expression [16]:

$$I = \exp\frac{U}{m} - 1, \tag{7}$$

m is the nonideality coefficient, characterizing the difference between the properties of a real contact and an ideal.

We put expression (5) into (7) and obtain for the nonideality coefficient m at [15]:

$$m = \frac{1 + \frac{B_e I(Y - \ln(I + 1))}{\ln(I + 1)} Y}{1 + B_e I(Y - \ln(I + 1))}. \tag{8}$$

This formula is valid for currents when the Joule heating of the diode base is less than the heating of the barrier region [16].

Contact resistance is the value of the derivative of voltage with respect to current. According to [16], the contact resistance is equal to:

$$R_c = \left(\frac{dI}{dU}\right)^{-1}. \tag{9}$$

Then from expression (7) we can depict the contact resistance in the following dimensionless form:

$$R_c = \left(\frac{dI}{dU}\right)^{-1} = \frac{m}{I+1}. \tag{10}$$

where $R_c = \frac{R_c(U)}{R_c(U_0)}$ is the dimensionless contact resistance.

From expressions (8) and (10) we obtain the contact resistance of the Schottky diode

$$R_c = \frac{1 + \frac{B_e I (Y - \ln(I+1)) Y}{\ln(I+1)}}{(I+1)(1 + B_e I (Y - \ln(I+1)))}. \tag{11}$$

From there it can be seen that the contact resistance determines the parameters of the coefficients of surface and volume thermal conductivity of electrons and phonons, barrier height, the size of the diode, as well as the mechanisms of pulse scattering, relaxation time of energy and momentum.

For each value of B_e and Y , the dependence of contact resistance on current is shown in Fig. 1.

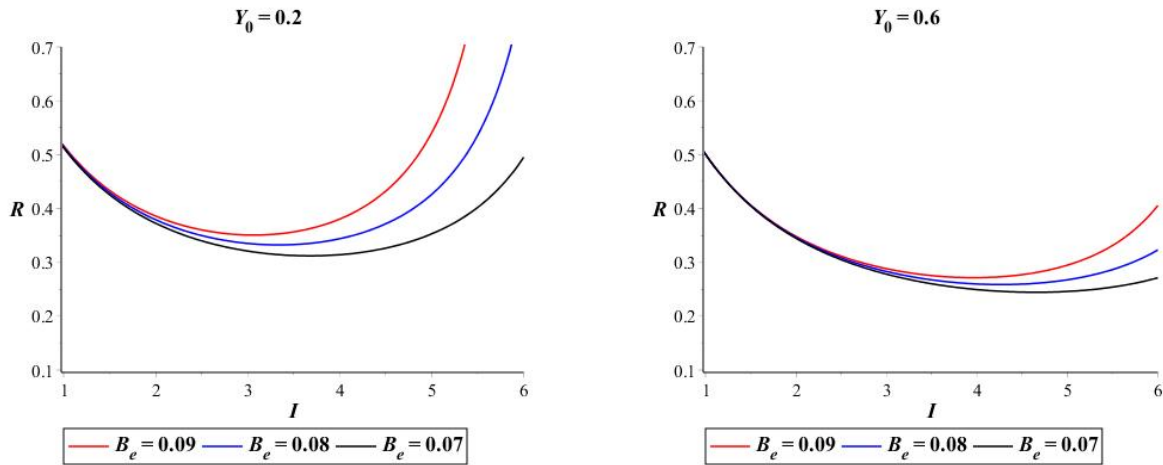


Figure 1. Dependences of $R_c(I)$ for different values of B_e and Y at $B_p=0$.

We put expression (6) into (7) and put the resulting expression for the nonideality coefficient m into (10) expressions for contact resistance at $B_e=B_p$.

$$R_c = \frac{1 - B_e Y I}{(I+1)(1 + B_e I \ln(I+1))}. \tag{12}$$

Figure 2 shows the dependences of $R_c(I)$ for different values of B_e and Y .

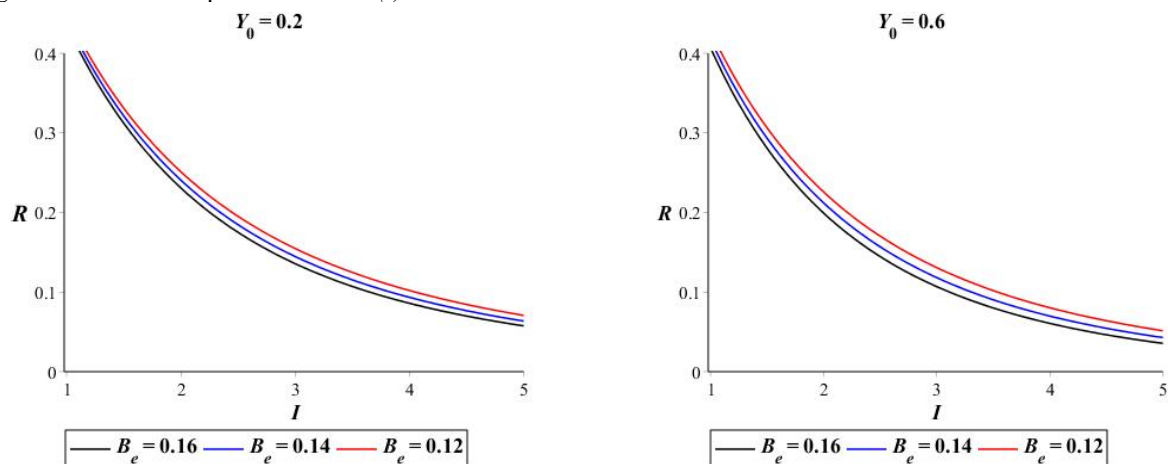


Figure 2. Dependences of $R_c(I)$ for different values of B_e and Y at $B_p = B_e$.

The dependence $\rho_c(T)$ at sufficiently high temperatures can be increasing. In the region of sufficiently low temperatures, the dependences $\rho_c(T)$ are either decreasing or independent of temperature [8].

In [17-20, 22], the temperature dependences of specific contact resistance were studied and a linearly increasing dependence was obtained.

In Figure 3 shows the experimental dependence $\rho_c(T)$, taken from [17], as well as the theoretical dependence. This dependence was explained in [21] within the framework of the mechanism of electron scattering by optical phonons, which leads, in particular, to different values of the coefficient of temperature dependence of resistance than in metals [8].

The results we obtained show that the contact resistance is determined by the parameters of the diode, as well as the electron scattering mechanism. As can be seen from Figures 2 and 3, it agrees quite well.

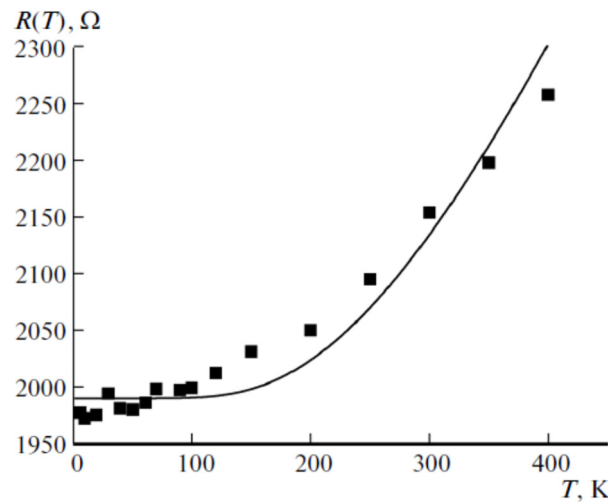


Figure 3. Temperature dependence of resistance $R(T)$: experimental data [21]

CONCLUSIONS

In barrier structures, the contact resistance depends on the parameters: surface and volume thermal conductivity coefficients of electrons and phonons, barrier height, the size of the diode, as well as the mechanisms of pulse scattering, relaxation time of energy and momentum. It is clear from this that stronger thermal dimensional effects are observed in barrier structures than in homogeneous semiconductors. Thermal size effects are due to the Peltier effect. In the volume, electronic and phonon thermal conductivities are infinitely greater, then heating can be neglected.

It is shown that the increase in contact resistance depends on the current passing through the diode, the surface and volume heat transfer coefficients of electrons and phonons, barrier height, the dimensions of the diode, as well as scattering mechanisms, relaxation time of energy and momentum.

Acknowledgments

The work was performed on the basis of the Fundamental Research Grant Programs FZ-20200929243 “The Effect of Hot Electrons and Phonon’s in a Strong Electromagnetic Field on the Characteristics of Semiconductor Solar Photovoltaic Elements and Nanostructures”.

Author Contributions. All the authors contributed equally to the manuscript.

ORCID

✉ Gafur Gulyamov, <https://orcid.org/0000-0001-9879-3165>; ✉ K.B. Umarov, <https://orcid.org/0000-0003-2424-7828>
✉ Alisher Z. Soliyev, <https://orcid.org/0000-0002-4526-2878>

REFERENCES

- [1] A. Ferrario, S. Battiston, S. Boldrini, T. Sakamoto, E. Miorin, A. Famengo, A. Miozzo, *et al.*, *Materials Today: Proceedings*, **2**(2), 573 (2015). <https://doi.org/10.1016/j.matpr.2015.05.078>
- [2] M. Shtern, M. Rogachev, Y. Shtern, D. Gromov, A. Kozlov, and I. Karavaev, *J. Alloys Compd.*, **852**, 156889 (2021). <https://doi.org/10.1016/j.jallcom.2020.156889>
- [3] G. Joshi, D. Mitchell, J. Ruedin, K. Hoover, R. Guzman, M. McAleer, L. Wood, *et al.*, *J. Mater. Chem. C*, **7**(3), 479 (2019). <https://doi.org/10.1039/C8TC03147A>
- [4] N.S. Boltovets, V.V. Kholevchuk, R.V. Konakova, V.F. Mitin, and E.F. Venger. *Sensors Actuators A: Physical*, **92**(1–3), 191 (2001). [https://doi.org/10.1016/S0924-4247\(01\)00562-3](https://doi.org/10.1016/S0924-4247(01)00562-3)
- [5] G. Gulyamov, Q. Umarov, A. Soliyev, and B. Shahobiddinov, *AIP Conference Proceedings*, **2924**(1), 050006 (2024). <https://doi.org/10.1063/5.0181554>
- [6] A.V. Sachenko, A.E. Belyaev, N.S. Boltovets, A.O. Vinogradov, V.P. Kladko, R.V. Konakova, Ya.Ya. Kudryk, *et al.*, *J. Appl. Phys.* **112**(6), 063703 (2012). <https://doi.org/10.1063/1.4752715>

- [7] A.V. Sachenko, A.E. Belyaev, N.S. Boltovets, R.V. Konakova, S.A. Vitusevich, S.V. Novitskii, V.N. Sheremet, *et al.*, *Techn. Phys. Lett.* **42**(6), 649 (2016). <https://doi.org/10.1134/S1063785016060286>
- [8] A.V. Sachenko, A.E. Belyaev, N.S. Boltovets, P.N. Brunkov, V.N. Jmerik, S.V. Ivanov, L.M. Kapitanchuk, *et al.*, *Semiconductors*, **49**(4), 461 (2015). <https://doi.org/10.1134/S1063782615040193>
- [9] A.V. Sachenko, A.E. Belyaev, N.S. Boltovets, R.V. Konakova, L.M. Kapitanchuk, V.N. Sheremet, Yu.N. Sveshnikov, *et al.*, *Semiconductors*, **48**(10), 1308 (2014). <https://doi.org/10.1134/S106378261410025X>
- [10] A.V. Sachenko, A.E. Belyaev, N.S. Boltovets, A.O. Vinogradov, V.A. Pilipenko, T.V. Petlitskaya, V.M. Anischik, *et al.*, *SPQEO*, **17**(1), 1 (2014). http://journal-spqeo.org.ua/n1_2014/v17n1-2014-p001-006.pdf
- [11] A.V. Sachenko, A.E. Belyaev, and R.V. Konakova, *Semiconductors*, **50**(6), 761 (2016). <https://doi.org/10.1134/S106378261606021X>
- [12] A.V. Sachenko, A.E. Belyaev, and R.V. Konakova, *Semiconductors*, **52**(1), 131 (2018). <https://doi.org/10.1134/S1063782618010190>
- [13] D.K. Schroder, *Semiconductor material and device characterization*, 3ed. (IEEE Press, John Wiley & Sons, Inc. 2006).
- [14] G. Gulyamov, A. Gulyamov, A. Ergashev, and B. Abdulazizov, *Journal of Modern Physics*, **6**, 1921 (2015). <http://dx.doi.org/10.4236/jmp.2015.613197>
- [15] G. Gulyamov, B. Shahobiddinov; A. Soliyev; Sh. Nazarov; and B. Misliadinov, *AIP Conference Proceedings*, **2700**(1), 020016 (2023). <https://doi.org/10.1063/5.0124940>
- [16] G. Gulyamov, K.B. Umarov, and A.Z. Soliyev. *Romanian Journal of Physics*, **68**, 613 (2023). https://rjp.nipne.ro/2023_68_5-6/RomJPhys.68.613.pdf
- [17] S.M. Sze, and K.Ng. Kwok, *Physics of Semiconductor Devices*, (John Wiley & Sons. Inc., New York, London, 2007).
- [18] G. Joshi, D. Mitchell, J. Ruedin, K. Hoover, R. Guzman, M. McAleer, L. Wood, *et al.*, *J. Mater. Chem. C*, **7**(3), 479 (2019). <https://doi.org/10.1039/C8TC03147A>
- [19] T. Sakamoto, Y. Taguchi, T. Kutsuwa, K. Ichimi, S. Kasatani, and M. Inada, *J. Electron. Mater.* **45**(3), 1321 (2016). <https://doi.org/10.1007/s11664-015-4022-z>
- [20] Y. Thimont, Q. Lognone, C. Goupil, F. Gascoin, and E. Guilmeau, *J. Electron. Mater.* **43**(6), 2023 (2014). <https://doi.org/10.1007/s11664-013-2940-1>
- [21] A.V. Sachenko, A.E. Belyaev, N.S. Boltovets, P.N. Brunkov, V.N. Jmerik, S.V. Ivanov, L.M. Kapitanchuk, *et al.*, "Temperature dependences of the contact resistivity in ohmic contacts to n⁺-InN," *Semiconductors*, **49**, 461-471 (2015). <https://doi.org/10.1134/S1063782615040193>
- [22] G. Gulyamov, and K.B. Umarov, *Semiconductors*, **28**(4), 409-411 (1994).

ВПЛИВ НАГРІВУ НОСІВ ЗАРЯДУ ТА ФОНОНІВ НА КОНТАКТНИЙ ОПІР ВИПРЯМЛЯЮЧИХ МЕТАЛ-НАПІВПРОВІДНИКОВИХ СТРУКТУР

Гафур Гулямов, К.Б. Умаров, Алішер З. Солієв

Наманганський інженерно-будівельний інститут, вул. І. Карімова, Наманган 160103, Узбекистан

Розраховано залежність температури носіїв заряду та фононів від контактного опору діода Шотткі. Показано, що збільшення контактного опору залежить від струму, що проходить через діод, поверхневого та об'ємного коефіцієнтів тепловіддачі електронів і фононів, висоти бар'єру, розмірів діода, а також механізмів розсіювання, часу релаксації енергії та імпульсу.

Ключові слова: потенційний бар'єр; контактний опір; температурний розподіл електронів і фононів; електронна та фононна теплопровідність; коефіцієнт неідеальності; ефект Пельтьє; тепловий ефект розміру (TSE)

STUDY OF STRUCTURAL AND VIBRATIONAL PROPERTIES OF $\text{Cu}_2\text{In}_4\text{Se}_7$ BY ANALYTICAL METHODS

S.I. Ibrahimova^a,  Sakin H. Jabarov^{a*}, G.M. Agamirzayeva^a,  Afsun S. Abiyev^b,  Yusif I. Aliyev^{c,d}

^aInstitute of Physics of Ministry of Science and Education of the Republic of Azerbaijan, Baku, AZ-1143, Azerbaijan

^bInnovation and Digital Development Agency, Baku, AZ-1073, Azerbaijan

^cAzerbaijan State Pedagogical University, Baku, AZ-1000, Azerbaijan

^dWestern Caspian University, Baku, AZ-1001, Azerbaijan

*Corresponding Author e-mail: sakin@jinr.ru

Received June 14, 2024; revised July 30, 2024; accepted August 8, 2024

The compound $\text{Cu}_2\text{In}_4\text{Se}_7$ was synthesized, the crystal structure and atomic dynamics were studied. The studies were carried out at room temperature and under normal conditions using XRD, Raman spectroscopy and FTIR spectroscopy. The obtained X-ray structural spectra were analyzed by the Rietveld method and various crystallographic parameters were determined. It was established that the crystal structure of this compound corresponds to tetragonal symmetry with the space group P-42c (112). As a result of the analysis of the Raman spectrum with the Gaussian function, it was established that in the $\text{Cu}_2\text{In}_4\text{Se}_7$ crystal in the frequency range $\nu = 0-800 \text{ cm}^{-1}$ 3 main vibrational modes are observed: $\nu_1 = 146 \text{ cm}^{-1}$, $\nu_2 = 171 \text{ cm}^{-1}$ and $\nu_3 = 229 \text{ cm}^{-1}$. It was found that these modes correspond to vibrations of InSe_4 tetrahedra formed by In-Se bonds. As a result of analysis of the FTIR spectrum, it was established that 3 main vibration modes are observed in the $\text{Cu}_2\text{In}_4\text{Se}_7$ crystal in the wavenumbers range $\nu = 400-4000 \text{ cm}^{-1}$. These modes are associated with water and carbon dioxide molecules in the sample.

Key words: *Crystal structure; Chalcogen; Atomic dynamics; Crystallographic parameters*

PACS: 74.62.bf, 61.10.nz, 36.20.ng

1. INTRODUCTION.

The crystal structure and various physical properties of copper and silver chalcogenide semiconductors have long been studied by various methods. However, there are still a number of questions in this direction that require study. Compounds and solid solutions of the ABX_2 type (A – Cu, Ag; B – Fe, In, Ga; X – S, Se, Te) have been in the field of research for many years as promising electrically and optically sensitive materials. Studying the structure of these compounds, structural phase transitions and atomic dynamics is important for explaining their other physical properties. Therefore, extensive research has been carried out in this direction recently [1-5].

Copper chalcogenides have some advantages and disadvantages compared to other chalcogenides. The main advantage is that copper atoms, due to their variable valency, can form crystals of various configurations. These crystals differ in both electronic structure and crystal structure. The missing point is that two- and three-phase systems are often observed in these compositions. At high temperatures, the process of phase formation occurs and a single-phase system is formed [6-10].

In chalcogenide semiconductors, the effect of cation-cation substitutions is big. Because with substitutions, important changes occur in both the electronic structure and the crystal structure. At this time, chalcogenides exhibited interesting optical, electrical, and thermal properties. Therefore, extensive research is being carried out in this direction [11-13]. It has been established that the acquisition and study of single-phase systems with cation-cation substitution leads to the production of semiconductors with stable properties. In this work, a new compound $\text{Cu}_2\text{In}_4\text{Se}_7$ with $\text{Cu} \rightarrow \text{In}$ substitutions was synthesized. The structure and atomic dynamics of the resulting compound were studied by analytical methods.

2. EXPERIMENTAL PART

2.1. Synthesis. Polycrystalline sample of the $\text{Cu}_2\text{In}_4\text{Se}_7$ compound was synthesized by a standard method typical of chalcogenide semiconductors [14,15]. In the synthesis process, metal chalcogen elements Cu, In and Se with a purity of at least 99.98% were used. Based on the stoichiometry of the intended sample, the elements were weighed on a high-precision electronic balance, then a mixed mass weighing 5 g was poured into a synthesis ampoule and air ($\sim 10^{-2} \text{ Pa}$) was sucked into the ampoule). The oven temperature was previously raised to 700 K. For the synthesis process, the finished ampoule is placed in an inclined oven. After holding in this mode (700 K) for an hour, the furnace temperature was increased to 1200 K at a rate of 50 degrees/hour. The ampoule was shaken periodically and kept at this temperature for 1.5 hours. At the next stage, the oven temperature was again reduced to 750 K. To achieve sample homogeneity, long-term tabulation was carried out. During the heating process, the sample was kept at a temperature of 750 K for fifteen days. Upon opening the ampoule, it was noticed that the synthesized mass mainly consists of small single-crystalline tetrahedral grains.

2.2. XRD analysis. The crystal structure of the chalcogenide compound $\text{Cu}_2\text{In}_4\text{Se}_7$ was studied by X-ray diffraction. X-ray diffraction experiments of the synthesized sample were carried out on a modern D8 ADVANCE diffractometer. Diffractometer parameters: with $\text{CuK}\alpha$ irradiation, $\lambda = 1.5406 \text{ \AA}$, 40 kV, 40 mA. The synthesized polycrystal was ground in a mortar, and then structural studies were carried out. The X-ray phase spectrum obtained at room temperature and under normal conditions for the $\text{Cu}_2\text{In}_4\text{Se}_7$ compound was analyzed by the Rietveld method in the Mag2Pol program and the crystallographic parameters were determined.

2.3. Raman spectroscopy. Vibrational properties of the samples were studied by Raman spectroscopy method. The experiments were carried out on the Nanofinder 30 Raman spectrometer at room-temperature. Nd:YAG laser with a wavelength $\lambda = 532 \text{ nm}$ and a maximum power of 10 mW was used as an excitation source. The obtained spectra were analyzed by the Gaussian function.

2.4. FTIR spectroscopy. The sample for the FTIR (Fourier transforms infrared spectroscopy) experiment was prepared from cylindrical $\text{Cu}_2\text{In}_4\text{Se}_7$ compounds. The infrared spectrum was obtained at room temperature in the wavenumber range $\nu = 400\text{--}4000 \text{ cm}^{-1}$ using a Varian 640 FT-IR instrument.

3. RESULTS AND DISCUSSIONS

The X-ray diffraction spectrum of the chalcogenide compound $\text{Cu}_2\text{In}_4\text{Se}_7$ obtained at room temperature is shown in Figure 1.

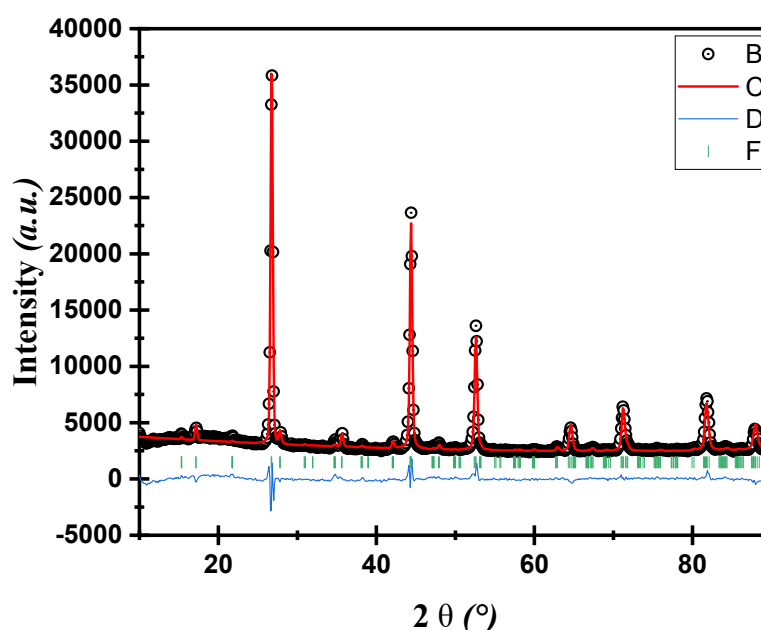


Figure 1. X-ray diffraction spectrum of $\text{Cu}_2\text{In}_4\text{Se}_7$ compound

B – experimental points, C – calculated curve, D – difference between experimental and calculated curves, F – atomic planes.

The diffraction spectrum obtained for the $\text{Cu}_2\text{In}_4\text{Se}_7$ compound in the diffraction angle range $10^\circ \leq 2\theta \leq 90^\circ$ was analyzed by the Rietveld method in the Mag2Pol program. As a result of the analysis, it was established that the crystal structure of this compound corresponds to a tetragonal system with space group P-42c(112). Values of lattice parameters: $a = b = 5.7624 \text{ \AA}$, $c = 11.5432 \text{ \AA}$, $V = 383.295 \text{ \AA}^3$, $\rho = 4.9697 \text{ g/cm}^3$, $Z = 2$. As a result of spectrum analysis, the coordinates of Cu, In and Se located in different crystallographic positions (Table 1).

Table 1. Atomic coordinates of the $\text{Cu}_2\text{In}_4\text{Se}_7$ compound.

Atom	<i>x</i>	<i>y</i>	<i>z</i>	Occ
In1	0.00000	0.50000	0.25000	0.930
In2	0.50000	0.50000	0.00000	0.600
In3	0.50000	0.00000	0.25000	0.400
Se	0.25345	0.22727	0.12586	0.875
Cu	0.00000	0.00000	0.00000	1.000

It has been established that the crystal structure of the $\text{Cu}_2\text{In}_4\text{Se}_7$ compound consists of Cu atoms located at lattice sites, In atoms distributed throughout the lattice volume, and Se atoms forming tetrahedra by combining with In atoms. The three-dimensional crystal structure obtained in the Diamond 3.2 program, corresponding to tetragonal symmetry, is presented in Figure 2.

From the structure presented in Figure 2, it is clear that indium atoms combine with selenium atoms, forming InSe_4 tetrahedra. Although the indium atoms occupy three different positions, they are all monovalent, and all the polyhedra they form with the chalcogen atoms are tetrahedra. It is known that copper atoms form monovalent and divalent covalent

bonds in crystals. In the $\text{Cu}_2\text{In}_4\text{Se}_7$ compound, the copper atoms are located in the same crystallographic position and are in the monovalent state. Therefore, the crystal structure has a fairly simple form. It is known that copper atoms form monovalent and divalent covalent bonds in crystals. Interatomic distances were determined depending on the atomic coordinates and ionic radii. The obtained values are shown in Table 2.

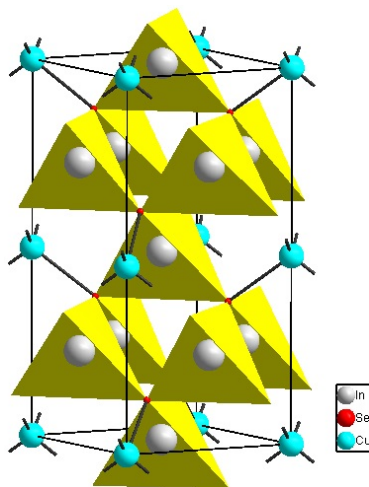


Figure 2. Crystal structure of the $\text{Cu}_2\text{In}_4\text{Se}_7$ compound

Table 2. Interatomic distances in the $\text{Cu}_2\text{In}_4\text{Se}_7$ compound

Atoms	Interatomic distances
In1 - Se	2.5800
In2 - Se	2.5689
In3 - Se	2.4056
Cu - Se	2.4411

Crystals with a polyhedral structure exhibit interesting atomic dynamic. Vibrations corresponding to both metal-chalcogen-metal bonds and vibrations of polyhedra are observed. From the structure shown in Fig. 2, it is clear that the $\text{Cu}_2\text{In}_4\text{Se}_7$ compound also forms a structure consisting of polyhedra. This predicts the observation of interesting vibrational properties in this compound. Therefore, the atomic dynamics of the $\text{Cu}_2\text{In}_4\text{Se}_7$ compound was studied using Raman spectroscopy. The Raman spectrum obtained in the wavenumbers range $\nu = 0\text{-}800\text{ cm}^{-1}$ at room temperature is shown in Figure 3.

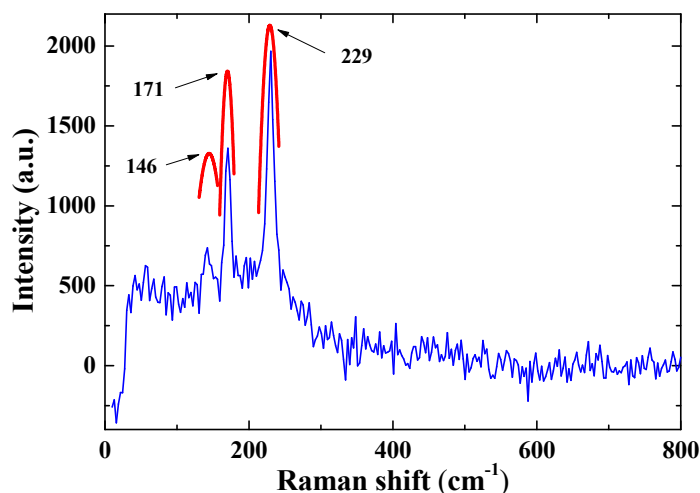


Figure 3. Raman spectrum of the $\text{Cu}_2\text{In}_4\text{Se}_7$ compound

From Figure 3 it can be seen that 3 main vibration modes are observed in the $\text{Cu}_2\text{In}_4\text{Se}_7$ crystal. These vibrational modes were interpreted using a Gaussian function. It has been established that these vibration modes correspond to the following wavenumbers: $\nu_1 = 146\text{ cm}^{-1}$, $\nu_2 = 171\text{ cm}^{-1}$ and $\nu_3 = 229\text{ cm}^{-1}$. It is known that in the wavenumbers range $\nu = 0\text{-}100\text{ cm}^{-1}$ vibrations of bonds formed by heavy elements are observed. At higher wavenumbers, vibrations of bonds formed by atoms of light elements such as H, C and O are observed. The main reason for the absence of such vibrations in the Raman spectrum obtained for the $\text{Cu}_2\text{In}_4\text{Se}_7$ crystal is that the sample was obtained with high purity. Consequently,

the obtained vibration modes correspond only to the frequencies of the bonds formed by the chemical elements included in the composition. It has been established that these modes correspond to In – Se bonds and vibrations of InSe_4 octahedra formed by these bonds. From the Raman spectrum it is clear that vibration modes are not observed at wavenumbers $\nu > 250 \text{ cm}^{-1}$. Vibration modes that occur at higher wavenumbers are observed mainly in bonds formed by atoms of light elements, such as H, C, O. It is known that there are no atoms of light elements in the $\text{Cu}_2\text{In}_4\text{Se}_7$ compound. However, in real crystals, due to contact with molecules of water and carbon dioxide in the air, it becomes possible to form bonds under the influence of atoms of light elements. FTIR spectroscopy studies were carried out to determine such connections. In Figure 4 shows the Fourier transform IR spectrum obtained for a $\text{Cu}_2\text{In}_4\text{Se}_7$ crystal under normal conditions and at room temperature.

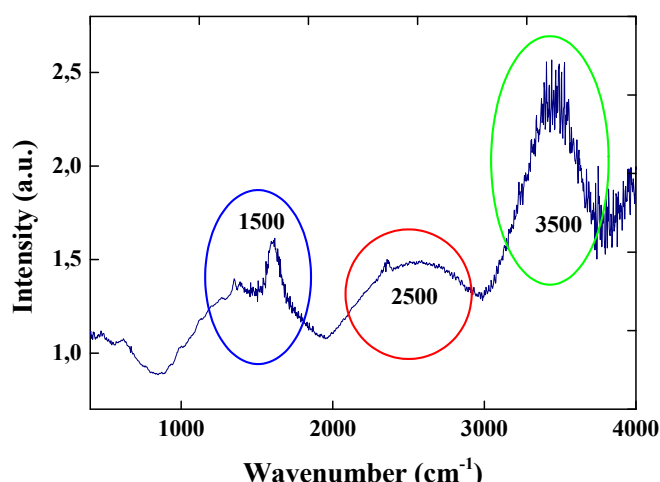


Figure 4. FTIR spectrum of the compound $\text{Cu}_2\text{In}_4\text{Se}_7$

From the spectrum shown in Figure 4, it is clear that in the wavenumbers range $\nu = 400\text{--}4000 \text{ cm}^{-1}$ three main maxima are observed. These maxima correspond to the values $\nu_1 = 1500$, $\nu_2 = 2500$ and $\nu_3 = 3500 \text{ cm}^{-1}$. In previous studies, it was found that vibrations with a wavenumber of $\nu \sim 1500 \text{ cm}^{-1}$ are carbon and oxygen, vibrations with a wavenumber of $\nu \sim 2500 \text{ cm}^{-1}$ are carbon, oxygen and hydrogen, and vibrations with a wavenumber of $\nu \sim 3500 \text{ cm}^{-1}$ are vibrations of bonds formed by oxygen and hydrogen atoms correspond to [16].

It is known that copper atoms are a metal of variable valence. The lengths of the bonds formed by chemical elements with variable valence are also different. Therefore, these systems have a complex structure. In the $\text{Cu}_2\text{In}_4\text{Se}_7$ compound, each of the Cu, In and Se atoms is in a stable divalent state. Therefore, such crystals have a simple structure. Such structures can be used as model objects to explain the structural aspects of certain physical properties. In recent years, crystal structures have begun to be used for theoretical and practical modeling of a number of processes [17,18]. From this point of view, the structural data obtained for the $\text{Cu}_2\text{In}_4\text{Se}_7$ compound may be useful for various purposes in the future. The results obtained can be used to study the electrical, optical, thermal and other physical properties of this crystal.

4. CONCLUSIONS

In the course of studying the crystal structure and atomic dynamics of the $\text{Cu}_2\text{In}_4\text{Se}_7$ compound, the following main results were obtained:

1. It has been established that the compound under study, $\text{Cu}_2\text{In}_4\text{Se}_7$, crystallizes in tetragonal systems and its crystallographic parameters are: $a = b = 5.7624 \text{ \AA}$, $c = 11.5432 \text{ \AA}$, $V = 383.295 \text{ \AA}^3$, $\rho = 4.9697 \text{ g/cm}^3$, $Z = 2$ and $P-42c(112)$, corresponding to their values.
2. When studying the atomic dynamics of the $\text{Cu}_2\text{In}_4\text{Se}_7$ compound, it was found that the vibration modes corresponding to the wavenumbers $\nu_1 = 146 \text{ cm}^{-1}$, $\nu_2 = 171 \text{ cm}^{-1}$ and $\nu_3 = 229 \text{ cm}^{-1}$ belong to In – Se bonds and vibrations of polyhedra formed by these bonds. The vibration modes observed at higher wavenumbers correspond to water and carbon dioxide molecules in the sample.

ORCID

- ©Sakin H. Jabarov, <https://orcid.org/0000-0002-3153-5804>; ©Afsun S. Abiyev, <https://orcid.org/0009-0009-9377-7567>
 ©Yusif I. Aliyev, <https://orcid.org/0000-0001-8896-2180>

REFERENCES

- [1] Y.I. Aliyev, N.A. Ismayilova, R.F. Novruzov, A.O. Dashdamirov, H.J. Huseynov, S.H. Jabarov, and A.A. Ayubov, "Electron structure and density of states' calculations of Ag_2S and Ag_2Se crystals from first-principle," *Modern Physics Letters B*, **33**(21), 1950242 (2019). <https://doi.org/10.1142/S0217984919502427>
- [2] G.M. Agamirzayeva, G.G. Huseynov, Y.I. Aliyev, T.T. Abdullayeva, and R.F. Novruzov, "Crystal structure and magnetic properties of the compound $\text{Cu}_3\text{Fe}_{0.5}\text{Se}_2$," *Advanced Physical Research*, **5**(1), 19-25 (2023). http://jomardpublishing.com/UploadFiles/Files/journals/APR/V5N1/Agamirzayeva_et_al.pdf

- [3] Y.I. Aliyev, P.R. Khalilzade, Y.G. Asadov, T.M. Ilyasli, F.M. Mammadov, N.A. Ismayilova, M.N. Mirzayev, *et al.*, “Behavior of thermal properties of $\text{AgCu}_{1-x}\text{Fe}_x\text{S}$ compounds under non-isothermal conditions,” *International Journal of Modern Physics B*, **33**(28), 1950339 (2019). <https://doi.org/10.1142/S0217979219503399>
- [4] S.H. Jabarov, S.I. Ibrahimova, F.V. Hajiyeva, E.M. Huseynov, and Y.I. Aliyev, “Structural, vibrational, and dielectric properties of CuInZnSe_3 chalcogenide compound,” *Arabian Journal for Science and Engineering*, **47**(6), 7817-7823 (2022). <https://doi.org/10.1007/s13369-022-06745-1>
- [5] N.N. Mursakulov, N.N. Abdulzade, S.H. Jabarov, and Ch.E. Sabzalieva, “Investigation of $\text{CuIn}_{1-x}\text{Ga}_x\text{Se}_2$ thin films for solar cells obtained by the magnetron sputtering method from two magnetrons shifted to each other,” *New Materials, Compounds and Applications*, **6**(2), 140-147 (2022). http://jomardpublishing.com/UploadFiles/Files/journals/NMCA/v6n2/Mursakulov_et_al.pdf
- [6] Y.I. Aliyev, Y.G. Asadov, R.D. Aliyeva, T.G. Naghiyev, and S.H. Jabarov, “Influence of partial substitution of Cu atoms by Zn and Cd atoms on polymorphic transformation in the $\text{Cu}_{1.75}\text{Te}$ crystal,” *Modern Physics Letters B*, **33**(11), 1850128 (2019). <https://doi.org/10.1142/S0217984919501288>
- [7] Y.G. Asadov, Y.I. Aliyev, A.O. Dashdemirov, S.H. Jabarov, and T.G. Naghiyev, “High-temperature X-ray diffraction study of $\text{Ag}_2\text{S-Cu}_2\text{S}$ system,” *Modern Physics Letters B*, **34**, 2150018 (2020). <https://doi.org/10.1142/S0217984921500184>
- [8] Kh.M. Guliyeva, N.N. Mursakulov, N.A. Aliyeva, and Y.I. Aliyev, “Synthesis, structure and thermal properties of the Cu_2NiSeTe ,” *Integrated Ferroelectrics*, **237**, 67-72 (2023). <https://doi.org/10.1080/10584587.2023.2227048>
- [9] N.A. Aliyeva, Y.I. Aliyev, and A.S. Abiyev, “Study of thermal properties of $\text{Cu}_4\text{Se}_{1.5}\text{Te}_{0.5}$ and $\text{Cu}_4\text{Te}_{1.5}\text{Se}_{0.5}$ compounds by differential thermal analysis,” *Advanced Physical Research*, **4**(2), 94-99 (2022). http://jomardpublishing.com/UploadFiles/Files/journals/APR/V4N2/Aliyeva_et_al.pdf
- [10] S.H. Jabarov, Y.I. Aliyev, T.M. Ilyasli, A.A. Baylarova, A.O. Dashdemirov, V.I. Nasirov, N.A. Ismayilova, *et al.*, “AgCuS compound as a thermodynamic system under the influence of gamma rays,” *Integrated Ferroelectrics*, **221**, 180-185 (2021). <https://doi.org/10.1080/10584587.2021.1965843>
- [11] A.O. Dashdemirov, S.G. Asadullayeva, A.S. Alekperov, N.A. Ismayilova, and S.H. Jabarov, “Electronic and optical properties of GeS and GeS: Gd,” *International Journal of Modern Physics B*, **35**(30), 2150305 (2021). <https://doi.org/10.1142/S0217979221503057>
- [12] A.S. Alekperov, A.O. Dashdemirov, N.A. Ismayilova, and S.H. Jabarov, “Fabrication of a Ge-GeS: Nd heterojunction and investigation of the spectral characteristics,” *Semiconductors*, **54**, 1406-1409 (2020). <https://doi.org/10.1134/S1063782620110044>
- [13] N.A. Ismayilova, and S.H. Jabarov, “First principles calculations of the magnetic properties of $\text{PbTi}_{1-x}\text{Mn}_x\text{O}_3$,” *Canadian Journal of Physics*, **100**(9), 398-404 (2022). <https://doi.org/10.1139/cjp-2022-0008>
- [14] A. Ridhova, V. Puspasari, and M.I. Amal, “5-Synthesis methods for chalcogenides and chalcogenides-based nanomaterials for photocatalysis,” *Micro and Nano Technologies*, **2021**, 105-134 (2021). <https://doi.org/10.1016/B978-0-12-820498-6.00005-6>
- [15] S.H. Jabarov, N.A. Ismayilova, D.P. Kozlenko, T.G. Mammadov, N.T. Mamedov, H.S. Orudzhev, S.E. Kichanov, *et al.*, “Structural and elastic properties of TlInSe_2 at high pressure,” *Solid State Sciences*, **111**, 106343 (2021). <https://doi.org/10.1016/j.solidstatesciences.2020.106343>
- [16] E.M. Huseynov, R.R. Hakhiyeva, and N.M. Mehdiyev, “FTIR study of nanocrystalline titanium carbide (TiC) particles exposed to gamma radiation,” *Solid State Communications*, **378**, 115417 (2024). <https://doi.org/10.1016/j.ssc.2023.115417>
- [17] S.H. Jabarov, and Y.I. Aliyev, “Possibilities of using perovskite structure in modern architecture and carpet weaving,” *New Design Ideas*, **7**(3), 607-611 (2023). http://jomardpublishing.com/UploadFiles/Files/journals/NDI/V7N3/Jabarov_Aliyev.pdf
- [18] R.A.J. Driessen, B.O. Loopstra, D.P. de Bruijn, H.P.C.E. Kuipers, and H. Schenk, “Crystallographic modelling,” *Journal of Computer-Aided Molecular Design*, **2**, 225-233 (1988). <https://doi.org/10.1007/BF01531996>

ДОСЛІДЖЕННЯ СТРУКТУРНИХ ТА КОЛИВАЛЬНИХ ВЛАСТИВОСТЕЙ $\text{Cu}_2\text{In}_4\text{Se}_7$ АНАЛІТИЧНИМИ МЕТОДАМИ

С.І. Ібрагімова^а, Сакін Х. Джабаров^а, Г.М. Агамірзаєва^а, Афсун С. Абієв^б, Юсіф І. Алієв^{с,д}

^аІнститут фізики Міністерства науки і освіти Азербайджанської Республіки, Баку, AZ-1143, Азербайджан

^бАгентство інновацій та цифрового розвитку, Баку, AZ-1073, Азербайджан

^сАзербайджанський державний педагогічний університет, Баку, AZ-1000, Азербайджан

^дЗахіднокаспійський університет, Баку, AZ-1001, Азербайджан

Синтезовано сполуку $\text{Cu}_2\text{In}_4\text{Se}_7$, досліджено кристалічну структуру та атомну динаміку. Дослідження проводили при кімнатній температурі та звичайних умовах із застосуванням XRD, рамановської спектроскопії та FTIR-спектроскопії. Отримані рентгенівські структурні спектри аналізували методом Рітвельда та визначали різні кристалографічні параметри. Встановлено, що кристалічна структура цієї сполуки відповідає тетрагональній симетрії з просторовою групою $P-42c$ (112). В результаті аналізу КР спектра з функцією Гауса встановлено, що в кристалі $\text{Cu}_2\text{In}_4\text{Se}_7$ в діапазоні частот $\nu = 0-800 \text{ cm}^{-1}$ спостерігаються 3 основні коливальні моди: $\nu_1 = 146 \text{ cm}^{-1}$, $\nu_2 = 171 \text{ cm}^{-1}$ і $\nu_3 = 229 \text{ cm}^{-1}$. Встановлено, що ці моди відповідають коливанням тетрадрів InSe_4 , утворених зв'язками In-Se . В результаті аналізу спектру FTIR встановлено, що в кристалі $\text{Cu}_2\text{In}_4\text{Se}_7$ спостерігаються 3 основні моди коливань в діапазоні хвильових чисел $\nu = 400-4000 \text{ cm}^{-1}$. Ці режими пов'язані з молекулами води і вуглекислого газу в зразку.

Ключові слова: кристалічна структура; халькоген; атомна динаміка; кристалографічні параметри

A COMPUTATIONAL INVESTIGATION ON THE STRUCTURAL, ELECTRONIC AND MAGNETIC PROPERTIES OF SI-DOPED L1₀-FENI ALLOY FOR CLEAN ENERGY

 Zineb Zine^{a,b},  Nassima Meftah^{b*}

^aLABTHOP Laboratory, Faculty of Exact Sciences, University of El-Oued, 3900 El-Oued, Algeria

^bDepartment of physics, Faculty of Exact Sciences, University of El-Oued, 39000 El-Oued, Algeria

*Corresponding Author e-mail: meftahnassima@yahoo.fr

Received June 22, 2024; revised July 24, 2024; accepted August 8, 2024

For the first time, this study conducts a computational analysis by employing density functional theory (DFT) to investigate the effects of silicon doping as substitutional defects on the structural, electronic, and magnetic characteristics of the L1₀-FeNi alloy. The aim of this study was to explore the potential applications of Si-doped FeNi compounds as alternatives to rare-earth permanent magnets. For this, we have performed full potential calculations of L1₀-FeNi with substitutional Si-doping within a generalized gradient approximation. Two types of substitutional Si-doping (O_{Fe}/O_{Fe}) in the Ni/Fe site of the parent alloy have been investigated. The computed formation energy (E_f) indicates that the incorporation of silicon defects increases the structural stability of tetragonally distorted L1₀-FeNi. Moreover, our findings demonstrate that the FeNi:Si(O_{Ni}) in the L1₀-structure has a stable saturation magnetization (M_s), whereas the FeNi:Si (O_{Fe}) has a small reduction in M_s . Therefore, Si-substituted FeNi alloys can be tuned to become a good candidate for permanent magnets.

Keywords: Ordered L1₀-FeNi; Density functional theory; Rare-earth free magnets; Substitutional defects

PACS: 61.43.Bn, 71.15.Mb

INTRODUCTION

Permanent magnets have a significant role in many modern technologies, including electric motors, generators, sensors, and data storage devices [1,2]. These materials retain their magnetic characteristics even in the absence of an external magnetic field, making them ideal for a variety of applications. Permanent magnet performance is essentially governed by its magnetic characteristics, including coercivity, remanence, and maximal energy product [3, 4].

Rare-earth magnets, such as neodymium-iron-boron (NdFeB) and samarium-cobalt (SmCo), are the most powerful permanent magnets on the market today [5]. NdFeB magnets are well-known for their high magnetic strength and are commonly employed in applications that demand strong magnetic fields in small places, such as hard disk drives, electric vehicle motors, and wind turbines [6]. SmCo magnets, while somewhat less strong than NdFeB magnets, have higher temperature stability and corrosion resistance, making them ideal for high-temperature and harsh environmental applications [7]. However, research on permanent magnet materials is ongoing, with the goal of enhancing performance, lowering prices, and finding alternatives to rare-earth elements due to their scarcity and geopolitical difficulties. New alloy compositions, developments in production processes, and the research of hybrid materials that combine the greatest qualities of many types of magnets are all examples of innovation.

The ordered tetragonal FeNi alloy, commonly referred to as L1₀-FeNi or tetrataenite, is receiving widespread attention in the materials research community because of its promising magnetic characteristics, which are crucial for advanced technological applications [8, 9]. L1₀-FeNi has an arranged tetragonal structure, which contributes to its unusual magnetic characteristics [10]. Tetrataenite is found naturally in meteorites and formed by a highly slow cooling process of around 0.1 K per million years at 600 K [11, 12]. This gradual cooling allows the Fe and Ni atoms to organize themselves in a structured manner, resulting in the L1₀ phase, which consists of alternating layers of Fe and Ni. Maât *et al.* (2020) found that the ordered tetragonal FeNi alloy has strong saturation magnetization ($M_s = 1.5$ T), a high Curie temperature ($T_C \approx 830$ K), and considerable magnetocrystalline anisotropy (MCA ≈ 1 MJ/m³) [13]. These features make L1₀-FeNi an appealing material for high-performance permanent magnets. However, while its MCA value is considerable, it is less than that required for optimal performance in permanent magnet applications [14]. Whereas, researchers have discovered several techniques, such as chemical vapor deposition, mechanical alloying and annealing, and electro-deposition, to synthesize L1₀-FeNi in the laboratory, as duplicating the natural gradual cooling process is impossible [15-17]. Defect engineering is now recognized as an important technique to improve the characteristics of L1₀-FeNi [18]. The introduction of controlled quantities of impurities or defects can have a major impact on the material's magnetic properties. Rani *et al.* (2019) discovered that substitutional platinum (Pt) doping cause tetragonal distortion, which boosts the MCA of L1₀-FeNi [19]. However, Pt doping is not cost-effective in large-scale applications. Furthermore, different techniques involve interstitial nitrogen (N) doping. Computational studies have demonstrated that N-doping can enhance the structural stability and MCA of tetragonally deformed FeNi, although with a minor decrease in saturation magnetization [20]. This method makes use of the strong bonding between nitrogen and the FeNi lattice to maintain the ordered structure and increase magnetic anisotropy.

For the first time, this study investigated the effects of substitutional silicon doping on the structural, electronic, and magnetic properties of L1₀-FeNi alloys in order to improve their performance by using first-principles density functional theory (DFT) computational techniques. The substitutional silicon-doping was done at two separate sites: the Fe site (O_{Fe}) and the Ni site (O_{Ni}). However, the silicon atom was chosen for its size and chemical affinity for FeNi alloys.

COMPUTATIONAL METHODS

The L1₀-FeNi alloy has an AuCu-type tetragonal crystal structure with Fe and Ni layers that alternate along the c-axis. The L1₀-FeNi material has experimental lattice parameters $a = 2.53 \text{ \AA}$ and $c = 3.58 \text{ \AA}$ [21] and a crystal structure classified as P4/mmm. The supercells of FeNi with dimensions of $2 \times 2 \times 2$ and $2 \times 2 \times 3$ were considered to allow substitutional Si-doping at levels of 12.5% and 8.3%, respectively. To calculate the structural, electronic, and magnetic properties of pure FeNi and optimized Si-substituted FeNi, we use the full potential linearized augmented plane wave (FPLAPW) method, which is implemented in WIEN2k software [22], within the framework of density functional theory (DFT) [23]. To determine exchange-correlation energy, this study applied the spin-polarized Generalized Gradient Approximation (GGA) proposed by Perdew, Becke, and Ernzerhof (PBE) [24]. In FPLAPW calculations, the valence levels were considered scalar relativistically, but the core states were treated completely relativistically. Furthermore, the wave functions of valence electrons identified within the Muffin-Tin sphere have been substantially expanded, especially up to $l_{\text{max}} = 10$. The radius of the Muffin-Tin (RMT) spheres for each atom is selected so that they are almost touching, limiting charge leakage. $R_{\text{MT}, \text{max}} = 7$ was used to calculate the plane wave cut-off parameters, whereas G_{max} was set to 12 a.u.^{-1} for the Fourier expansion of potential in the interstitial area. The convergence criterion was set at 10^{-4} Ryd total energy. We employed the Monkhorst-pack technique in the Brillouin zone, with a $6 \times 6 \times 4$ k-mesh.

RESULTS AND DISCUSSION

L1₀-FeNi crystal structure can be characterized by two types of unit cells: (i) face centered tetragonal (fct) and (ii) body centered tetragonal (bct); however, the bct, or primitive unit cell, will typically be chosen as the input structure for calculations due to its smallest basis and minimal computational cost [25]. Figure 1 depicts a $2 \times 2 \times 2$ supercell of FeNi (bct) which simulates 12.5% substitutional doping of Si by substituting one Ni atom with Si. Likewise, 8.3% Si-doping may be obtained in a $2 \times 2 \times 3$ supercell.

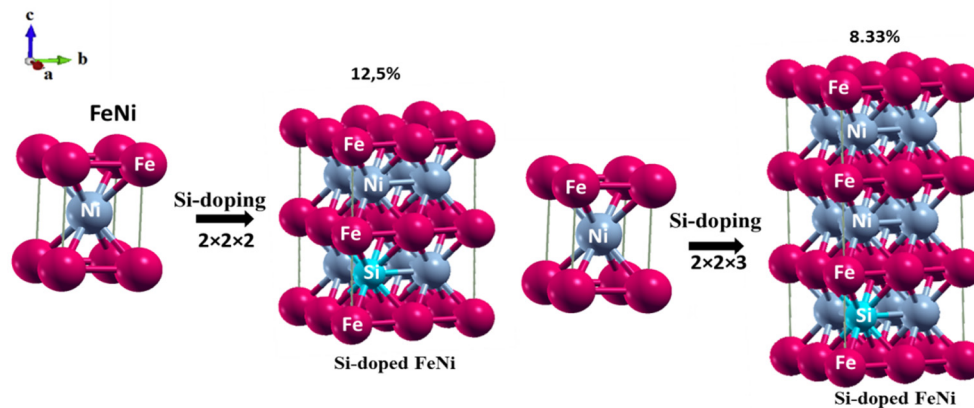


Figure 1. Front view of a $2 \times 2 \times 2$ and $2 \times 2 \times 3$ supercell of FeNi employed to simulate silicon-substitutional doping at 12.5% and 8.33% respectively

In order to get the ground state values of the lattice parameters (a and c) of FeNi and Si-doped FeNi alloys, we optimized the volume using L. D Marks' optimization approach [26].

The equilibrium lattice parameters and bulk modulus value for L1₀-FeNi and Si-doped L1₀-FeNi alloy were determined by fitting the total energy vs. volume data to the nonlinear Murnaghan equation of state [27], as shown in Fig. 2.

To examine the stability of the structure, the formation energy (E_{for}) of FeNi and FeNi:Si alloys was estimated using the prescribed formulae [19]:

$$E_{\text{for}}^{\text{FeNi}} = E_{\text{FeNi}} - E_{\text{Fe}} - E_{\text{Ni}}, \quad (1)$$

$$E_{\text{for}}^{\text{FeNi-Si}} = (E_{\text{FeNi-Si}} - \alpha E_{\text{Fe}} - \beta E_{\text{Ni}} - \gamma E_{\text{Si}}). \quad (2)$$

Where E_{FeNi} , $E_{\text{FeNi-Si}}$, E_{Fe} , E_{Ni} , and E_{Si} designate the ground state energies of pure FeNi, FeNi-Si supercells, and individual Fe, Ni, and Si atoms. However, α , β and γ represent the number of Fe, Ni, and Si atoms in the respective supercell.

The optimized lattice parameters (a and c), c/a ratio, formation energy, $E_{\text{For}}/f.u.$ (eV), the bulk modulus B (GPa) and first order derivative of bulk modulus (B'_0) of FeNi:Si alloys have been computed and are presented in Table 1. Our computed c/a ratio and formation energy for $L1_0\text{-FeNi}$ are consistent with previous findings for tetragonal ordered FeNi reported by Rani et al. (2019) [19]. As seen in Table 1, the c/a ratio increases with Si substitution, reflecting an increase in tetragonal distortion while keeping the area of the a - b plane roughly the same. The increased tetragonal distortion improves the structural stability of $L1_0\text{-FeNi}$, which is in accordance with the experimental findings published by Mizuguchi et al. (2011) [28]. As a result, we proved that substitutional silicon doping at either the Fe or Ni sites increases the stability of the $L1_0\text{-FeNi}$ alloy. However, the negative values of formation energies (E_{For}) that were observed in each case are indicative of structural stability.

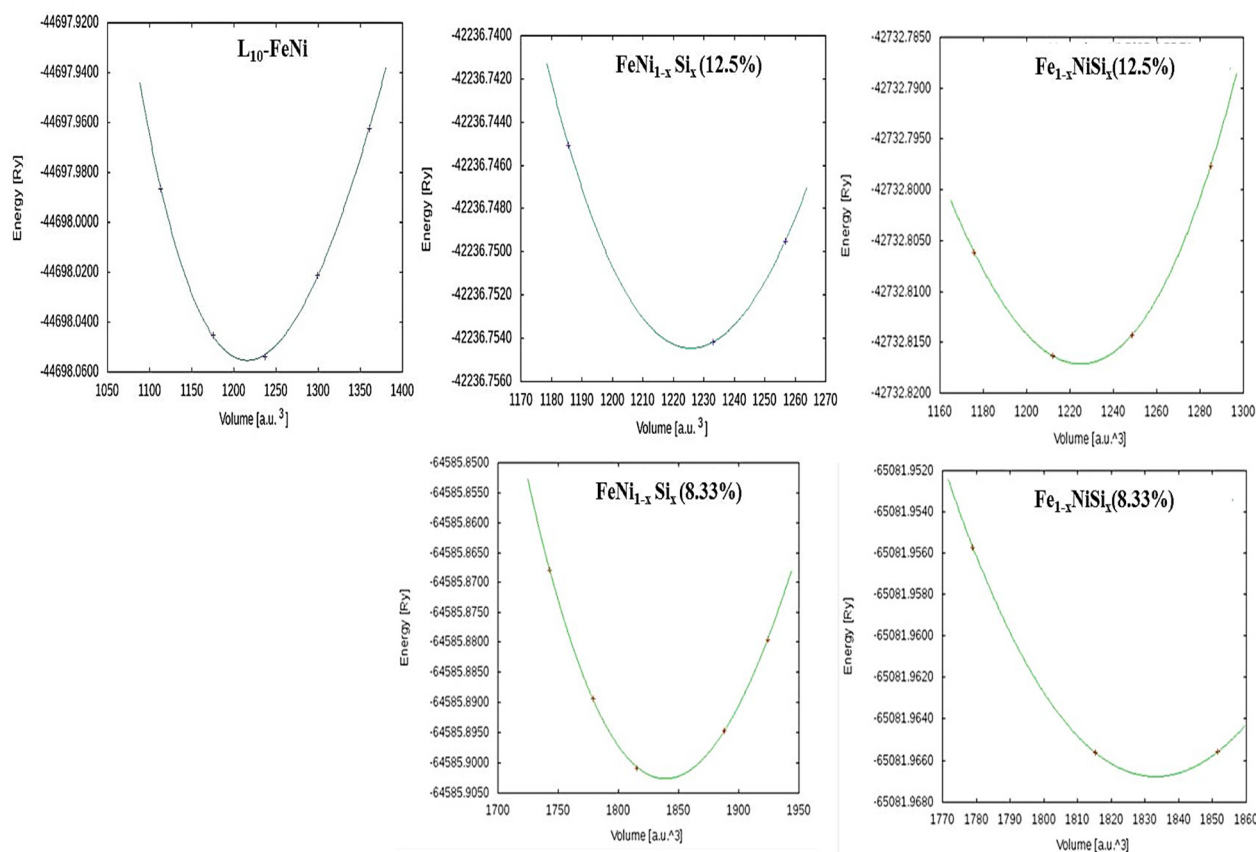


Figure 2: The total energy as a function of the volume of the compounds: $L1_0\text{FeNi}$, $\text{FeNi}_{1-x}\text{Si}_x$ (12.5%), $\text{Fe}_{1-x}\text{NiSi}_x$ (12.5%), $\text{FeNi}_{1-x}\text{Si}_x$ (8.33%) and $\text{Fe}_{1-x}\text{NiSi}_x$ (8.33%)

Table 1. The optimized lattice parameters (a and c), tetragonal distortion (c/a), formation energy, $E_{\text{For}}/f.u.$ (eV), the bulk modulus B (GPa) and first order derivative of bulk modulus (B'_0) of $L1_0\text{-FeNi}$ and Si doped FeNi compounds

Compound	$a(\text{\AA})$	$c(\text{\AA})$	c/a	$V(\text{\AA}^3)$	$B(\text{GPa})$	B'_0	$E_{\text{For}}/f.u$
FeNi (ref. [19])	2.531	3.579	1.414	22.93			- 0.18
FeNi (this work)	2.5140	3.562	1.417	22.51	197.828	4.763	- 0.181
$\text{Fe}_{1-x}\text{NiSi}_x$ (12.5%)	2.5196	3.6059	1.4311	22.89	177.0856	6.01	- 0.027
$\text{Fe}_{1-x}\text{NiSi}_x$ (8.33%)	2.5206	3.5778	1.4195	22.73	184.9932	4.0254	- 0.0283
$\text{FeNi}_{1-x}\text{Si}_x$ (12.5%)	2.5181	3.6038	1.4311	22.85	195.8518	5.000	- 0.034
$\text{FeNi}_{1-x}\text{Si}_x$ (8.33%)	2.5173	3.5815	1.4227	22.69	191.3532	5.000	- 0.0285

To investigate their electronic properties, Figure 3 shows the total and orbital projected density of states (DOS) for $L1_0\text{-FeNi}$, FeNi:Si (O_{Fe}), and FeNi:Si (O_{Ni}). The total DOS of all compounds appears highly spin polarized and metallic in nature. The fundamental electronic configurations of elements constituting pristine and Si-doped FeNi are Fe: $[\text{Ar}] 4s^2 3d^6$, Ni: $[\text{Ar}] 4s^2 3d^8$, and Si: $1s^2 2s^2 2p^6 3s^2 3p^2$, as represented in the projected electronic densities of states of all atoms. In pure FeNi , Fe-3d and Ni-3d hybridize thoroughly thereby contributing equally to total DOS. The fully filled 3d-orbitals of Fe and Ni in majority spin states are easily recorded, but in minority spin states, they are partly

occupied, resulting in high ferromagnetism for all compounds. On Si substitution, we see that hybridization between Fe-3d and Si-3p does not induce any significant shift in either the majority or minority spin states. The DOS in the vicinity of E_F are due to the admixture of Fe-3d/Ni-3d and Si-3p states.

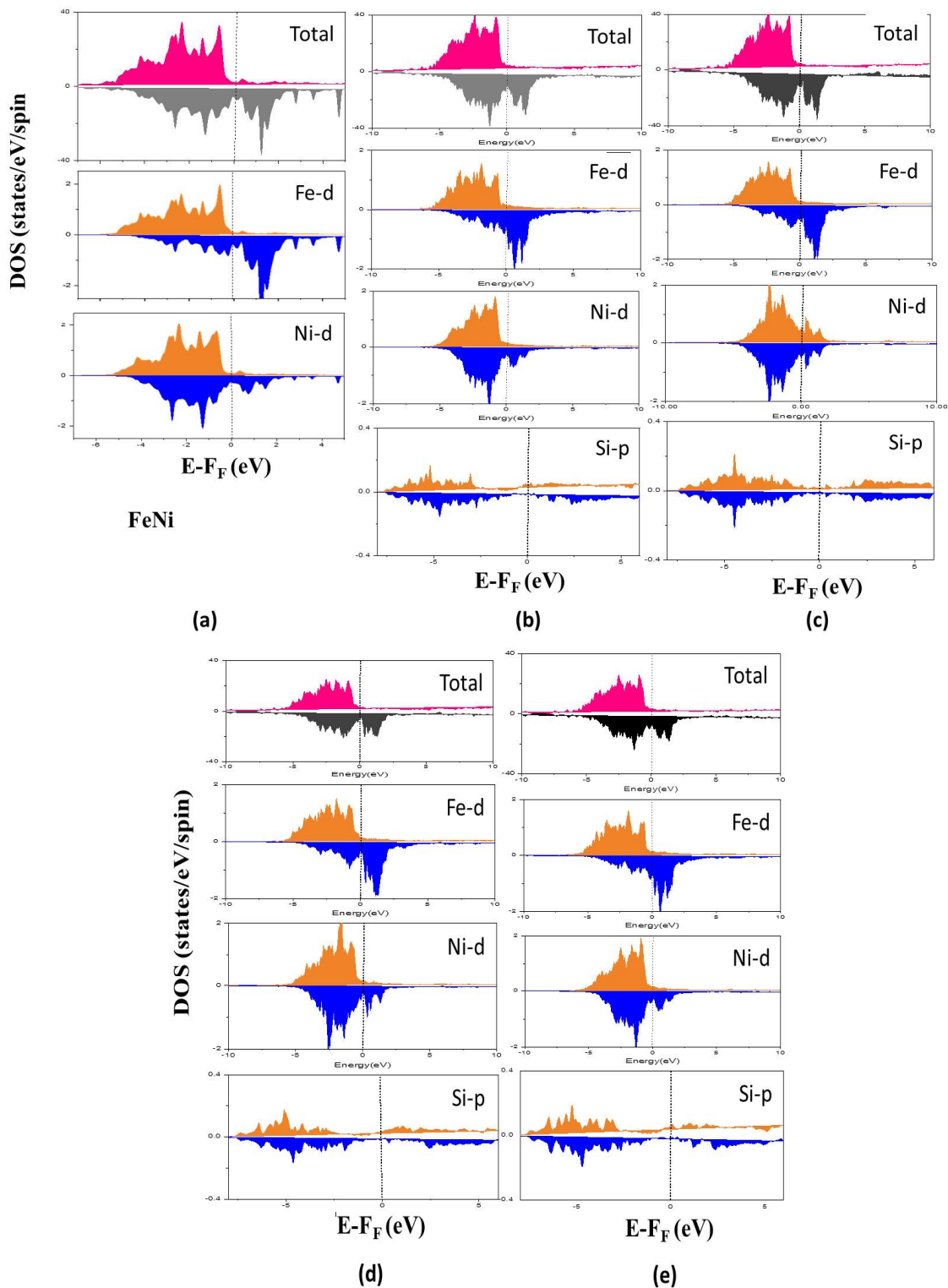


Figure 3. Computed total and projected density of states (DOS): (a) FeNi, (b) $Fe_{1-x}Ni_x$ (8.3%), (c) $FeNi_{1-x}Si_x$ (8.3%), (d) $Fe_{1-x}Ni_x$ (12.5%) and (e) $FeNi_{1-x}Si_x$ (12.5%)

The difference between the majority and minority spin states in the occupied area may be used to determine the net magnetic moment. Table 2 displays the total atom-resolved spin magnetic moments as well as saturation magnetization (M_s) for pure and Si-doped FeNi alloys. According to the results, incorporating silicon affects the magnetic moments of the constituent atoms as well as the overall magnetic moment.

Table 2. Total and atom-resolved spin magnetic moments (μ_B), and saturation magnetization (M_s) of pure and Si-doped FeNi alloy.

Compounds	Magnetic Moments (μ_B)				M_s (T)
	Fe	Ni	Si	total	
FeNi (ref. [29])	2.701	0.645	/	3.272	1.33
FeNi (this work)	2.702	0.651	/	3.265	1.31
Fe _{1-x} NiSi _x (12.5%)	2.6717	0.6113	-0.0385	2.8190	1.14
Fe _{1-x} NiSi _x (8.33%)	2.6528	0.6531	-0.0315	2.9373	1.19
FeNi _{1-x} Si _x (12.5%)	2.6090	0.7086	-0.0673	3.0456	1.28
FeNi _{1-x} Si _x (8.33%)	2.7126	0.75027	-0.0688	3.1704	1.30

The minority spin states in Fe ($3d^6$) are less populated than in Ni ($3d^8$), resulting in a greater spin magnetic moment for Fe ($2.7 \mu_B$) than Ni ($0.65 \mu_B$). The decrease in the total spin magnetic moment of FeNi:Si (O_{Ni}/O_{Fe}) can be attributed to the phenomenon of hybridization between Ni-3d/Fe-3d states, in conjunction with the p-states of a non-magnetic impurity atom (Si-3p). This hybridization process leads to a reduction in the overall spin magnetic moment observed in the system. The decrease is more pronounced in FeNi:Si (O_{Fe}) due to antiparallel alignment of Si-3p with Fe-3d and Ni-3d states. All alloys have isotropic computed spin magnetic moments.

The saturation magnetization (M_s) is calculated as total spin magnetic moment per unit volume. As indicated in Table 2, the saturation magnetization of $L1_0$ -FeNi is 1.31 T, which is almost equal to the previously computed theoretical value of 1.33 T [29, 30]. When Si substitutes into (O_{Fe}) in $L1_0$ -FeNi alloy, the saturation magnetization M_s decreases from 1.31 T to 1.14 (1.19)T for FeNi:Si 12.5% (8.33%), and when Si is substituted into (O_{Ni}), the saturation magnetization M_s relatively decreases from 1.31 T to 1.28 (1.30)T for FeNi:Si 12.5% (8.33%). This reduce becomes more obvious in FeNi:Si(O_{Fe}) due to the decrease in Fe moment in the plane containing non-magnetic Si impurity. In addition, Fe is antiferromagnetically linked with the Si impurity in this case. Thus, the structural stability and magnetic properties clarify that out of two FeNi:Si alloys, FeNi:Si(O_{Ni}) 8.33% is more suitable candidate to act as permanent magnetic material.

CONCLUSIONS

We have studied the effect of doping the $L1_0$ -FeNi binary alloy by introducing silicon (Si) atoms as a substitutional defect in the $L1_0$ -bct structure. We have studied the structural, electronic and magnetic properties using the DFT from the first principle, as described above. Compared to the pristine FeNi alloy, we found that for FeNi:Si, the tetragonal distortion was increased, which yields the structural stability of these alloys. However, the saturation magnetization (M_s) was slightly reduced by the introduction of the Si atom, however, when the Si atom was substituted in the Ni site (8.33%), the saturation magnetization change was very small. Therefore, among those alloys, FeNi:Si (O_{Ni}) can be tuned to become a good candidate for permanent magnets, or the requirement for permanent magnets is achieved by this compound.

ORCID

© Zineb Zine, <https://orcid.org/0000-0001-8961-6220>; © Nassima Meftah, <https://orcid.org/0000-0001-7646-8572>

REFERENCES

- [1] J. Ormerod, *Permanent magnet markets and applications*. In *Modern Permanent Magnets*, (Woodhead Publishing, 2022), pp. 403-434.
- [2] A.H. King, and R.G. Eggert, *Critical materials for permanent magnets*. In *Modern Permanent Magnets*, (Woodhead Publishing, 2022), pp. 343-370.
- [3] J.M.D. Coey, "Perspective and prospects for rare earth permanent magnets," *Engineering*, **6**(2), 119-131 (2020). <https://doi.org/10.1016/j.eng.2018.11.034>
- [4] Z. Shao, and S. Ren, "Rare-earth-free magnetically hard ferrous materials," *Nanoscale Adv.* **2**(10), 4341-4349 (2020). <https://doi.org/10.1039/D0NA00519C>
- [5] A. H. King, and R. G. Eggert, *Critical materials for permanent magnets*. In *Modern Permanent Magnets*, (Woodhead Publishing, 2022), pp. 343-370, <https://doi.org/10.1016/B978-0-323-88658-1.00003-0>
- [6] H. Sepehri-Amin, S. Hirosawa, and K. Hono, "Advances in Nd-Fe-B based permanent magnets," in: *Handbook of magnetic materials*, **27**, 269-372 (2018). <https://doi.org/10.1016/bs.hmm.2018.08.003>
- [7] O. Gutfleisch, M.A. Willard, E. Brück, C.H. Chen, S.G. Sankar, and J.P. Liu, "Magnetic materials and devices for the 21st century: stronger, lighter, and more energy efficient," *Advanced materials*. **23**(7), 821-842 (2011). <https://doi.org/10.1002/adma.201002180>
- [8] S. Mandal, M. Debata, P. Sengupta, and S. Basu, " L_{10} FeNi: a promising material for next generation permanent magnets," *Critical Reviews in Solid State and Materials Sciences*, **48**(6), 703-725 (2023). <https://doi.org/10.1080/10408436.2022.2107484>
- [9] T.Y. Tashiro, M. Mizuguchi, T. Kojima, T. Koganezawa, M. Kotsugi, T. Ohtsuki, and K. Takanashi, "Structural and magnetic properties of FeNi thin films fabricated on amorphous substrates," *Journal of Applied Physics*, **117**(17), 17E309 (2015). <https://doi.org/10.1063/1.4913935>
- [10] S. Mandal, A. Panigrahi, A. Rath, M. Bönisch, P. Sengupta, M. Debata, and S. Basu, "Formation of $L1_0$ Ordering in FeNi by Mechanical Alloying and Field-Assisted Heat Treatment: Synchrotron XRD Studies," *Acs Omega*, **8**(15), 13690-13701 (2023). <https://doi.org/10.1021/acsomega.2c07869>
- [11] E.R. Scott, "Iron meteorites: Composition, age, and origin," in: *Oxford Research Encyclopedia of Planetary Science*, (2020).

- [12] N. Meftah, S. Mostefaoui, A. Jambon, E.H. Guedda, and S. Pont, "Minor and trace element concentrations in adjacent kamacite and taenite in the Krymka chondrite," *Meteorit. Planet. Sci.* **51**(4), 696-717 (2016). <https://doi.org/10.1111/maps.12617>
- [13] N. Maât, I. McDonald, R. Barua, B. Lejeune, X. Zhang, G.M. Stephen, A. Fisher, et al., "Creating, probing and confirming tetragonality in bulk FeNi alloys," *Acta Materialia*, **196**, 776-789 (2020). <https://doi.org/10.1016/j.actamat.2020.07.019>
- [14] Y. Miura, S. Ozaki, Y. Kuwahara, M. Tsujikawa, K. Abe, and M. Shirai, "The origin of perpendicular magneto-crystalline anisotropy in L_{10} -FeNi under tetragonal distortion," *Journal of physics: Condensed matter*, **25**(10), 106005 (2013), <https://doi.org/10.1088/0953-8984/25/10/106005>
- [15] I.Z. Hlova, O. Dolotko, M. Abramchuk, A. Biswas, Y. Mudryk, and V.K. Pecharsky, "Enhancement of hard magnetism and chemical order of synthetic L_{10} -FeNi," *J. Alloys Compd.* **981**, 173619 (2024). <https://doi.org/10.1016/j.jallcom.2024.173619>
- [16] S. Mandal, A. Panigrahi, A. Rath, M. Bönisch, P. Sengupta, M. Debata, and S. Basu, "Formation of L_{10} Ordering in FeNi by Mechanical Alloying and Field-Assisted Heat Treatment: Synchrotron XRD Studies," *Acs Omega*, **8**(15), 13690-13701 (2023). <https://doi.org/10.1021/acsomega.2c07869>
- [17] F. Meneses, A. Pedernera, C. Blanco, N. Bajales, S.E. Urreta, and P.G. Bercoff, " L_{10} -FeNi ordered phase in AC electrodeposited iron-nickel biphasic nanowires," *Journal of Alloys and Compounds*, **766**, 373-381 (2018). <https://doi.org/10.1016/j.jallcom.2018.06.307>
- [18] M. Ali, and F. Ahmad, "A review of processing techniques for Fe-Ni soft magnetic materials," *Materials and Manufacturing Processes*, **34**(14), 1580-1604 (2019). <https://doi.org/10.1080/10426914.2019.1662038>
- [19] P. Rani, J. Thakur, A. Taya, and M.K. Kashyap, "Magnetocrystalline anisotropy of Pt-doped L_{10} -FeNi compound for clean energy applications," *Vacuum*, **159**, 186-190 (2019). <https://doi.org/10.1016/j.vacuum.2018.10.023>
- [20] P. Manchanda, R. Skomski, N. Bordeaux, L.H. Lewis, and A. Kashyap, "Transitionmetal and metalloid substitutions in L_{10} -ordered FeNi," *J. Appl. Phys.* **115**, 17A710 (2014). <https://doi.org/10.1063/1.4862722>
- [21] P. Rani, R. Singla, J. Thakur, A.H. Reshak, and M.K. Kashyap, "Enhancement in magnetic parameters of L_{10} -FeNi on Pd-substitution for permanent magnets," *Indian J. Phys.* **97**, 67-72 (2023). <https://doi.org/10.1007/s12648-021-02221-y>
- [22] P. Blaha, K. Schwarz, G.K.H. Madsen, D. Kvasnicka, J. Luitz, R. Laskowski, F. Tran, and L.D. Marks, *WIEN2k an Augmented Plane Wave h Local Orbitals Program for Calculating Crystal Properties, Revised Edition WIEN2k, 19.1*, (Vienna University of Technology, Vienna, Austria, 2019).
- [23] M. Weinert, E. Wimmer, and A.J. Freeman, "Total-energy all-electron density functional method for bulk solids and surfaces," *Phys. Rev. B*, **26**, 4571 (1982). <https://doi.org/10.1103/PhysRevB.26.4571>
- [24] J.P. Perdew, K. Burke, and M. Ernzerhof, "Generalized gradient approximation made simple," *Phys. Rev. Lett.* **77**, 3865 (1996). <https://doi.org/10.1103/PhysRevLett.77.3865>
- [25] A. Edström, J. Chico, A. Jakobsson, A. Bergman, and J. Rusz, "Electronic structure and magnetic properties of L_{10} binary alloys," *Physical Review B*, **90**(1), 014402 (2014). <https://doi.org/10.1103/PhysRevB.90.014402>
- [26] W. Marks, "Multicriteria optimisation of shape of energy-saving buildings," *Building and environment*, **32**(4), 331-339 (1997). [https://doi.org/10.1016/S0360-1323\(96\)00065-0](https://doi.org/10.1016/S0360-1323(96)00065-0)
- [27] F.D. Murnaghan, "The compressibility of media under extreme pressures," *Proceedings of the National Academy of Sciences*, **30**(9), 244-247 (1944). <https://doi.org/10.1073/pnas.30.9.244>
- [28] M. Mizuguchi, T. Kojima, M. Kotsugi, T. Koganezawa, K. Osaka, and K. Takanashi, "Artificial fabrication and order parameter estimation of L_{10} -ordered FeNi thin film grown on a AuNi buffer layer," *Journal of the Magnetism Society of Japan*, **35**(4), 370-373 (2011). <https://doi.org/10.3379/msjmag.1106R008>
- [29] P. Rani, J. Thakur, A. Taya, and M. K. Kashyap, "Effect of tetragonal distortion induced by interstitial C-doping in L_{10} -FeNi," *AIP Conference Proceedings*, **2115**(1), 030497 (2019). <https://doi.org/10.1063/1.5113336>
- [30] E. Poirier, F.E. Pinkerton, R. Kubic, R.K. Mishra, N. Bordeaux, A. Mubarak, L.H. Lewis, et al., "Intrinsic magnetic properties of L_{10} FeNi obtained from meteorite NWA 6259," *Appl. Phys.* **117**, 17E318 (2015). <https://doi.org/10.1063/1.4916190>

ОБЧИСЛОВАЛЬНЕ ДОСЛІДЖЕННЯ СТРУКТУРНИХ, ЕЛЕКТРОННИХ ТА МАГНІТНИХ ВЛАСТИВОСТЕЙ СПЛАВУ L_{10} -FeNi, ЛЕГОВАНОГО Si ДЛЯ ЧИСТОЇ ЕНЕРГЕТИКИ

Зінеб Зіне^{a,b}, Нассіма Мефтах^b

^aЛабораторія LAVTHOP, Факультет точних наук, Університет Ель-Уед, 3900 Ель-Уед, Алжир

^bКафедра фізики, факультет точних наук, Університет Ель-Уед, 39000 Ель-Уед, Алжир

У цьому дослідженні вперше проведено обчислювальний аналіз із застосуванням теорії функціоналу густини (DFT) для дослідження впливу легування кремнієм як дефектів заміщення на структурні, електронні та магнітні характеристики сплаву L_{10} -FeNi. Мета цього дослідження полягала в тому, щоб вивчити потенційні можливості застосування легованих кремнієм сполук FeNi як альтернативи рідкоземельним постійним магнітам. Для цього ми виконали розрахунки повного потенціалу L_{10} -FeNi із замісним легуванням кремнієм у межах узагальненого градієнтного наближення. Досліджено два типи замісного легування Si (O_{Fe}/O_{Fe}) у Ni/Fe місці вихідного сплаву. Обчислена енергія формування (E_f) вказує на те, що включення дефектів кремнію підвищує структурну стабільність тетрагонально спотвореного L_{10} -FeNi. Крім того, наші результати демонструють, що FeNi:Si(O_{Ni}) у структурі L_{10} має стабільну намагніченість насичення (M_s), тоді як FeNi:Si(O_{Fe}) має невелике зниження M_s . Таким чином, Si-заміщені FeNi сплави можуть бути налаштованими, щоб стати хорошим кандидатом на постійні магніти.

Ключові слова: впорядкований L_{10} -FeNi; теорія функціонала густини; магніти без рідкоземельних елементів; дефекти заміни

INVESTIGATION OF SENSITIVE THERMAL SENSORS BASED ON Si<Pt> and Si<Pd>

 Sharifa B. Utamuradova^a,  Dilmurod A. Rakhmanov^{a*},  Afsun S. Abiyev^b

^a*Institute of Semiconductor Physics and Microelectronics at the National University of Uzbekistan,
20 Yangi Almazar st., Tashkent, 100057, Uzbekistan*

^b*Western Caspian University, Baku, AZ1001, Azerbaijan*

*Corresponding Author e-mail: dilmurod-1991@bk.ru

Received June 10, 2024; revised August 7, 2024; accepted August 16, 2024

In this work, new sensitive thermal sensors based on Si<Pt> and Si<Pd> were developed. Single-crystal n- and p-type silicon samples doped with phosphorus and boron during growth were used for the study. These samples were first doped with platinum and palladium, then subjected to ohmic contact with nickel. To manufacture temperature sensors based on n-Si<Pd> and obtain an ohmic contact, this material was subjected to appropriate mechanical and chemical treatments. Metallic nickel with a thickness $d = 1 \mu\text{m}$ was chemically deposited on its surface, followed by thermal annealing in a vacuum at $T = 400\text{-}450^\circ\text{C}$ for $t = 10 - 15$ minutes. To compare the created temperature sensors, a special measuring device, a thermostat, was developed to ensure uniform heat transfer.

Keywords: *Temperature sensor; Silicon; Platinum; Palladium; Doping; Sensitivity*

PACS: 78.30.Am

INTRODUCTION

Without sensitive and fast-acting thermal sensors, it is difficult to imagine a successful solution to modern technical and environmental problems. In this case, of particular interest is the development of temperature sensors that allow remote control and monitoring of the temperature of an object. Existing temperature sensors based on semiconductor materials have practically exhausted their capabilities in terms of sensitivity and speed [1-4]. Therefore, to create a new generation of sensitive sensors, new materials or new physical phenomena should be used. In this regard, the functionality of a doped semiconductor is of great interest.

Thermal sensors are used in almost all sectors of the national economy, as well as in automated systems. Therefore, the main requirements for a temperature sensor are to increase sensitivity, speed, reduce energy consumption and stability of parameters under various conditions. Existing temperature sensors that use additional amplification circuits have almost reached their maximum efficiency, especially since they do not allow remote monitoring of the temperature of objects [5-7]

In most modern automatic electronic devices, temperature sensors are key elements that convert light and thermal energy into electrical vibrations. Without them, high-speed fiber-optic communication channels, automatic and security systems, and fire alarm devices are unthinkable today. Moreover, every year their implementation in all spheres of human activity becomes more intense. Existing thermal sensors, manufactured on the basis of traditional semiconductor materials, no longer meet modern requirements for thermal sensors. Therefore, new temperature sensors with more improved parameters are relevant [8,9].

In this regard, the main goal of this work is to develop a technology for producing silicon with platinum and palladium impurities, select the optimal impurity, determine the optimal concentrations and nominal resistances of temperature sensors, develop a good and reliable ohmic contact, as well as select a material for sealing that allows the use of a temperature sensor in various aggressive conditions and environments.

EXPERIMENTAL PART

Silicon wafers of n- and p-type conductivity with a resistivity of 40 Ohm cm (KEF-40 brand) and 20 Ohm cm (KDB-20) were used as the objects under study. The wafers were cut from silicon ingots grown by the Czochralski method. Diffusion doping of silicon with platinum and palladium was carried out from a layer of metal Pt and Pd deposited on the silicon surface in evacuated quartz ampoules at temperatures of 1200°C for 2 hours. Subsequent cooling of the samples was carried out using the thermal regimes given in [10, 11].

After doping, the type of conductivity and resistivity of the doped samples were determined using a thermal and quadruple probe (Table 1).

From the table it can be seen that after doping with palladium atoms, the resistivity increases significantly and the type of conductivity changes (from n to p). Doping with platinum atoms leads to a decrease in resistivity in both types of samples.

It was shown in [12,13] that electronically active palladium exists in silicon in the form of two independent particles. The first, designated Pd₁, is amphoteric and has an acceptor level 0.22 ± 0.01 eV below the conduction band edge, as well as a donor level 0.33 ± 0.01 eV above the valence band edge. The second species, designated Pd₂, has an acceptor level

0.32 ± 0.1 eV above the valence band edge. The ratio of Pd₁ to Pd₂ embedded in silicon varies from 40 to 5 for diffusion temperatures from 900 to 1200°C, respectively. Platinum is also considered an amphoteric element with good conductivity and has an acceptor and donor level in the band gap of silicon.

Table 1. conductivity and resistivity of the doped samples

No	Brand	Samples	Doping temperature (°C)	Conductivity type	Resistivity (Ohm cm)
1	KEF-40	n-Si	-	n	39.8
3		n-Si<Pd>	1200	p	1665
5		n-Si<Pt>	1200	n	17
6	KDB-20	p-Si	-	p	20
8		p-Si<Pt>	1200	p	3

From these results, we selected n-Si<Pd> p-Si<Pt> samples for the development of temperature sensors. To manufacture temperature sensors based on n-Si<Pd> and obtain an ohmic contact, this material was subjected to appropriate mechanical and chemical treatments. Metallic nickel with a thickness $d = 1 \mu\text{m}$ was chemically deposited on its surface, followed by thermal annealing in a vacuum at $T = 400\text{-}450^\circ\text{C}$ for $t = 10 - 15$ minutes. For temperature sensors based on p-Si<Pt>, silver liquid was used to increase the resistance of the material. To compare the created temperature sensors, a special measuring device, a thermostat, was developed to ensure uniform heat transfer.

RESULTS AND DISCUSSIONS

We know that the resistance of semiconductor materials decreases with increasing temperature, and we measured its change using a digital multimeter. The results obtained are presented in Table 2. For comparison with our temperature sensors, we also obtained the temperature dependence of the resistance of the Chinese MF52 temperature sensor.

Table 2. Temperature dependence of the resistance of the temperature sensors

T, °C	R _{Si<Pt>} Ohm	R _{Si<Pd>} Ohm	R _{MF52} Ohm
34	228000	307	6320
35	206000	278	5750
36	183000	259	4920
37	177300	244	4370
38	167200	227	4300
39	160400	216	4010
40	153700	210	3740
.....			
50	87200	148	1560
51	87000	145	1560
52	83200	145	1510
53	81600	128	1500
54	79500	130	1380
55	59700	124	1280
.....			
75	22500	99.2	420
76	21700	88	347
77	21300	79	336
78	20400	80.5	326
79	20000	79.1	314
80	20300	77.4	307

During the comparison process, each temperature sensor was measured separately, and measurements were carried out in the range from room temperature to 80°C. To determine the temperature sensitivity of these temperature sensors, their temperature sensitivity coefficients β were analyzed. Table 3 shows the β coefficients of temperature sensors.

Table 3. Sensitivity coefficient (β) of temperature sensors

No	Thermal sensors	Sensitivity factor(β) °K	Temperature °C	Sensitivity factor(β) °K	Temperature °C
1	Si<Pt>	5700	34-80	7500	50-60
2	Si<Pd>	3200	34-80	5210	50-60
3	MF52	7200	34-80	5000	50-60

As can be seen from this table, we see that among temperature sensors in the temperature range 34-80°C, the sensitivity of the MF54 temperature sensor made in China is high. It can be seen that the sensitivity of the temperature sensor developed on the basis of Si<Pt> in the temperature range of 34-80°C is better than that of temperature sensors developed on the basis of Si<Pd>, but worse than that of the MF52 temperature sensors developed in China.

As a rule, temperature sensors developed on the basis of silicon are designed to operate in the temperature range from -50 to +150°C, and depending on the purpose and operating temperature of each sensor, they can also be used in short temperature ranges [14, 15]. For example, we developed temperature sensors based on Si<Pt>, Si<Pd> and set ourselves the task of using them in a microelectronic device that controls the temperature (in the range of 50-60°C) of a water desalination system. If we take into account temperature control in the range of 50-60°C in this system using a microelectronic device, as can be seen from Table 3, then we can see that temperature sensors made on the basis of Si<Pt>, Si<Pd> have much better temperature sensitivity in the range of 50-60 °C compared to MF52 temperature sensors. It has been established that temperature sensors developed on the basis of Si<Pt> have the best temperature sensitivity (7500 K).

The authors [16] developed highly sensitive thermal sensors in their work. For the material they chose highly compensated silicon with manganese atoms. The thermal sensitivity of the presented temperature sensors is very high, it was 25-50 times greater than that of the existing most sensitive ones. As a result of theoretical calculations and analysis of the parameters of temperature sensors made on the basis of uncompensated silicon with intrinsic conductivity, obtained by crucibleless zone melting with $\rho \sim 2 \cdot 10^4$ Ohm-cm, it was found that the sensitivity of these temperature sensors is also 50-70% lower than that of the developed us thermal sensors.

Other authors [17] have developed temperature sensors based on silicon doped with nickel. The article says that temperature sensors with a maximum nominal resistance have a very high thermal sensitivity value β in which reaches 7400-7500 K; such temperature sensors are capable of controlling the temperature of an object with an accuracy of 0.005 K.

Based on [16,17], it can be assumed that it is possible to develop highly sensitive silicon-based thermal sensors with transition elements.

CONCLUSION

The resistivity and conductivity of silicon samples doped with platinum and palladium atoms were determined by four-probe and thermal probe methods. To develop high-sensitivity thermal sensors, the necessary samples were selected and nickel atoms were deposited on the surface of silicon samples to obtain ohmic contacts.

As a result of research, it has been established that the temperature sensitivity of the MF52 thermometer made in China is higher in the temperature range of 34-80°C, and in the temperature range of 50-60°C the temperature sensitivity of temperature sensors based on Si<Pt> is higher. In the future, we plan to use these thermometers in a microelectronic device that controls the temperature of a water desalination system.

Acknowledgment

The authors express their gratitude to the J.J. Khamdamov, head of laboratory "Semiconductor Physics" (ISPM) for the useful advices and practical help of creating thermal sensors in this study.

Conflict of Interest

The authors declare that there is no conflict of interest regarding the publication of this paper.

ORCID

Sharifa B. Utamuradova, <https://orcid.org/0000-0002-1718-1122>

Dilmurod A. Rakhmanov, <https://orcid.org/0000-0003-1275-5999>

Afsun S. Abiyev, <https://orcid.org/0009-0009-9377-7567>

REFERENCES

- [1] Sh.B. Utamuradova, D.A. Rakhmanov, P.L. Tuan, A.S. Doroshkevich, R.Sh. Isayev, and A.S. Abiyev, "Studying the Influence of Proton Irradiation on the Distribution Profile of Pt and Cr in Surface Layers n-Si<Pt>, n-Si<Cr> Using Ellipsometric Spectroscopy," *Advanced Physical Research*, **6**(2), 83 (2024). http://jomardpublishing.com/UploadFiles/Files/journals/APR/V6N2/Utamuradova_et_al.pdf
- [2] M.K. Bakhadyrkhanov, S.A. Valiev, S.S. Nasriddinov, and S.A. Tachilin, "Sensitive thermal sensors based on highly compensated silicon," *Electronic processing of materials*, **43**(6), 111 (2007). <https://eom.ifa.md/ru/journal/download/752>. (in Russian)
- [3] Sh.B. Utamuradova, Sh.Kh. Daliev, D.A. Rakhmanov, S.F. Samadov, and A.S. Doroshkevich, "Investigation of Radiation Defect Formation of Irradiated n-Si<Pt>," *Advanced Physical research*, **5**(3), 183 (2023). <http://jomardpublishing.com/UploadFiles/Files/journals/APR/V5N3/7.Utamuradova.pdf>
- [4] Utamuradova, Sh.B., Matchonov, Kh.J., Khamdamov, J.J., & Utemuratova, Kh.Y. X-ray diffraction study of the phase state of silicon single crystals doped with manganese. *New Materials, Compounds and Applications*, **7**(2), 93-99, (2023). http://jomardpublishing.com/UploadFiles/Files/journals/NMCA/v7n2/Utamuradova_et_al.pdf
- [5] Sh.B. Utamuradova, Sh.Kh. Daliev, A.V. Stanchik, and D.A. Rakhmanov, "Raman spectroscopy of silicon, doped with platinum and irradiated by protons," *E3S Web of conferences*, **402**, 14014 (2023). <https://doi.org/10.1051/e3sconf/202340214014>

- [6] Kh.S. Daliev, Z.E. Bahronkulov, J.J. Hamdamov, "Investigation of the Magnetic Properties of Silicon Doped with Rare-Earth Elements," East Eur. J. Phys. (4), 167 (2023), <https://doi.org/10.26565/2312-4334-2023-4-18>
- [7] Sh.B. Utamuradova, Sh.Kh. Daliev, D.A. Rakhmanov, A.S. Doroshkevich, V.A. Kinev, O.Yu. Ponamareva, et al., Advanced Physical research, 5(2), 73-80 (2023). http://jomardpublishing.com/UploadFiles/Files/journals/APR/V5N2/Utamuradova_et_al.pdf
- [8] Sh.B. Utamuradova, A.V. Stanchik, K.M. Fayzullaev, B.A. Bakirov, Applied Physics, 2, 33–38 (2022). (in Russian).
- [9] N.A. Turgunov, E.Kh. Berkinov, and D.X. Mamajonova, "Decay of Impurity Clusters of Nickel and Cobalt Atoms in Silicon under the Influence of Pressure," Journal of Nano- and Electronic Physics, 13(5), 05006 (2021). [https://doi.org/10.21272/jnep.13\(5\).05006](https://doi.org/10.21272/jnep.13(5).05006)
- [10] Sh.B. Utamuradova, D.A. Rakhmanov, A.S. Doroshkevich, I.G. Genov, P.L. Tuan, and A. Kirillov, "Processes of Defect Formation in Silicon Diffusion-Doped with Platinum and Irradiated with Protons," Eurasian physical technical journal, 20(3), 35 (2023). <https://doi.org/10.31489/2023No3/35-42>. (in Russian)
- [11] Z.T. Azamatov, M.A. Yuldoshev, N.N. Bazarbayev, and A.B. Bakhromov, "Investigation of Optical Characteristics of Photochromic Materials," Physics AUC, 33, 139-145 (2023). https://cis01.central.ucv.ro/pauc/vol/2023_33/13_PAUC_2023_139_145.pdf
- [12] Sh.B. Utamuradova, D.A. Rakhmanov, and A.S. Abiyev, "Influence of Different Types of Radiation on the Crystal Structure of Silicon Monocrystals n-Si," East Eur. J. Phys. (2), 380 (2024). <https://doi.org/10.26565/2312-4334-2024-2-47>
- [13] L. So, and S.K. Ghandhi, "The energy levels of palladium in silicon," Solid-State Electronics, 20, 113-117 (1977). [https://doi.org/10.1016/0038-1101\(77\)90059-4](https://doi.org/10.1016/0038-1101(77)90059-4)
- [14] M.A. Alanazi, "Development and experimental testing of an innovative nondestructive thermal sensor utilizing the thermal interrogation method for detecting leakage in water plastic pipes," Flow Measurement and Instrumentation, 98, 102646 (2024). <https://doi.org/10.1016/j.flowmeasinst.2024.102646>
- [15] O. Quldashov, Sh. Ergashev, G. Kochkorova, I. Tishabayeva, M. Teshaboyev, and N. Tashlanova, "Stand-alone solar optic device based on aps-photodeciver," E3S Web of Conferences, 508, 01010 (2024). <https://doi.org/10.1051/e3sconf/202450801010>
- [16] A.S. Rysbaev, M.T. Normuradov, A.M. Rakhimov, Z.A. Tursunmetova, and A.K. Tashatov, Journal of Surface Investigation, (11), 61 (2020). <https://doi.org/10.31857/S102809602011014X>
- [17] O. Kuldashov, O. Rayimdjanova, B. Djalilov, Sh. Ergashev, S. Toxirova, and A. Muhammadjonov, "Stabilization of parameters of optoelectronic devices on semiconductor emitters," E3S Web of Conferences, 508, 01001 (2024). <https://doi.org/10.1051/e3sconf/202450801001>

ДОСЛІДЖЕННЯ ЧУТЛИВИХ ТЕРМОСЕНСОРІВ НА ОСНОВІ Si<Pt> і Si<Pd>

Шаріфа Б. Утамурадова^а, Ділмурод А. Рахманов^а, Афсун С. Абієв^б

^аІнститут фізики напівпровідників і мікроелектроніки Національного університету Узбекистану,

100057, Ташкент, Узбекистан, вул. Янги Алмазар, 20

^бЗахідно-Каспійський університет, Баку, AZ1001, Азербайджан

У цій роботі розроблено нові чутливі термосенсори на основі Si<Pt> і Si<Pd>. Для дослідження використовували монокристалічні зразки кремнію n- і р-типу, леговані фосфором і бором під час росту. Ці зразки спочатку легували платиною і паладієм, потім піддавали омичному контакту з нікелем. Для виготовлення датчиків температури на основі n-Si<Pd> та отримання омичного контакту цей матеріал піддавався відповідній механічній та хімічній обробці. На його поверхню хімічно осаджували металевий нікель товщиною $d = 1$ мкм з наступним термічним відпадом у вакуумі при $T = 400-450^\circ\text{C}$ протягом $t = 10 - 15$ хвилин. Для порівняння створених датчиків температури був розроблений спеціальний вимірювальний прилад – термостат, який забезпечує рівномірний теплообмін.

Ключові слова: датчик температури; кремній; платина; паладій; легування; чутливість

DEVELOPMENT OF A CAPACITIVE PRESSURE SENSOR BASED ON NANOPOROUS ANODIC ALUMINIUM OXIDE

Trishna Moni Das^a, Devabrata Sarmah^b, Sankar Moni Borah^a, Sunandan Baruah^b

^aDepartment of Applied Sciences, Gauhati University, Jalukbari, Guwahati-781014, India

^bCentre of Excellence in Nanotechnology, Assam down town University, Guwahati -781026, India

*Corresponding Author e-mail: trishnamani.das@gmail.com

Received June 18, 2024; revised July 17, 2024; accepted August 12, 2024

Capacitive pressure sensors make pressure sensing technology more accessible to a wider range of applications and industries, including consumer electronics, automotive, healthcare etc. However, developing a capacitive pressure sensor with brilliant performance using a low-cost technique remains a difficulty. In this work, the development of a capacitive pressure sensor based on nanoporous Anodic Aluminium Oxide (AAO) fabricated by a two-step anodization approach which offers a promising solution for precise pressure measurement is fabricated by a two-step anodization approach. A parallel plate capacitive sensor was fabricated by placing two AAO deposited sheets are placed face to face, with the non-anodized aluminum component at the base functioning as the top and bottom electrodes. A variation in the capacitance value of the as fabricated sensor was observed over an applied pressure range (100 Pa-100 kPa). This change in capacitance can be attributed to the decrease in the distance between the two plates and the non-homogenous distribution of contact stress and strain due to the presence of nanoporous AAO structure. In this pressure range the sensor showed high sensitivity, short response time and excellent repeatability which indicates a promising future of the fabricated sensor in consumer electronics, intelligent robotics etc.

Keywords: Capacitive pressure sensor; Anodic Aluminium Oxide (AAO); Anodization; Sensitivity; Response time; Repeatability

PACS: 84.32.Tt, 07.07.Df

1. INTRODUCTION

In recent years, the field of sensor technology has witnessed a significant breakthrough with the emergence of Anodic Aluminium Oxide (AAO) based sensors. These sensors have demonstrated exceptional potential in various applications, including pressure sensing, biomedical monitoring, and environmental detection. The unique properties of AAO, including its highly ordered porous structure, high dielectric constant, and mechanical robustness, make it an ideal material for developing electrical and optical sensors that can operate accurately and reliably in harsh environments. As the demand for advanced sensors continues to grow, AAO based sensors are poised to play a critical role in revolutionizing various industries. One of the most significant advantages of AAO-based sensors is their ability to accurately measure capacitance and resistance variations. By depositing a thin metal coating on the surface of AAO, these sensors can detect even the slightest changes in pressure, making them ideal for a wide range of applications. The highly ordered porous structure of AAO allows for a high surface area-to-volume ratio, which enables the sensors to detect pressure changes with high sensitivity and accuracy. Moreover, AAO's high dielectric constant and mechanical robustness ensure that these sensors can operate accurately and reliably in harsh environments, making them ideal for industrial and aerospace applications.

Pressure sensors are classified into five types based on their sensing techniques, which include piezoelectricity, piezoresistivity, capacitance, triboelectricity, and transistors [1-17]. The capacitive pressure sensor is one type that has received much attention because of its stable structure, low pressure need, rapid dynamic reaction, and minimal temperature drift [18]. As the dielectric layer in a capacitive pressure sensor plays a vital role, therefore, incorporation of a porous dielectric material into a capacitive pressure sensor in place of a normal dielectric material would be more advantageous as it will provide increased sensitivity, low hysteresis, reduced stiffness, improved response time, lightweight, customizable properties and wide range applications. Developing a simple cost effective, controllable method to create a capacitive pressure sensor with excellent sensitivity, quick response and wide detection extent continues to be a formidable obstacle [18-28].

In this paper, we have reported the development of a pliable capacitive type sensor formed on nanoporous AAO. The conventional two-step anodization method is adopted to fabricate AAO layer over a commercially available aluminium sheet. As the thickness of the dielectric material has an inverse relationship with the capacitance of a parallel plate capacitor, we have prioritized the development of a thicker AAO layer in a short period of time. The hard anodization method is used for this purpose because it has proven to be a fast fabrication method. Two pieces of AAO on Al substrate are joined together where the AAO layers get stuck face to face to form a parallel plate capacitor. The pressure sensing response of aforesaid capacitor is studied here as a function of the capacitance.

2. MATERIALS AND METHODS

The studies were carried out using commercially available Al sheets. The 0.5 mm thick Al sheet was cut into the appropriate sizes for anodization. Al sheets were cleaned with acetone and deionized water for 10 minutes, then

annealed at 250°C for 4 hours. To dissolve the naturally occurring oxide layer, the aluminium sheets were electropolished in a solution of H₃PO₄, H₂SO₄ and deionized water at a weight ratio of 2:2:1. The Al sheets were then cleaned with deionized water numerous times before being dried and used as anodes in the as developed AAO fabrication setup. The nanoporous AAO structures were created using a simple two-step hard anodization procedure with a Pb sheet serving as the cathode. The anodization process was performed at a voltage of 140 V and a temperature of ~5°C. Here, 0.3M H₂C₂O₄ was used as the electrolyte. The morphology of nanoporous AAO has been proven to be affected by different parameters for instance the anodization time, anodization voltage, type and concentration of the electrolyte, and the temperature of the electrolytic bath. In this work a sample H1 was synthesized by keeping the anodization time 1 minute. The morphology of the as-prepared AAO structures was examined using a ZEISS Sigma 300 field emission scanning electron microscope (FESEM).

The pressure sensing ability of the nanoporous AAO structure was investigated by fabricating a flexible parallel plate capacitor, where, two nanoporous AAO deposited sheets of same size (Length=1 cm, Breadth= 1 cm, Height= 0.5 mm) are placed face to face, with the non-anodized aluminium component at the base functioning as the top and bottom electrodes. In this parallel plate capacitor arrangement, AAO layer serves as the dielectric layer. The capacitance variations of the as fabricated sensor were observed under a pressure range (100Pa-100 kPa) applied over the sensor. Responses were recorded by connecting the AAO sensor to a LCR meter. Figure 1 shows a schematic of the experimental sequence.

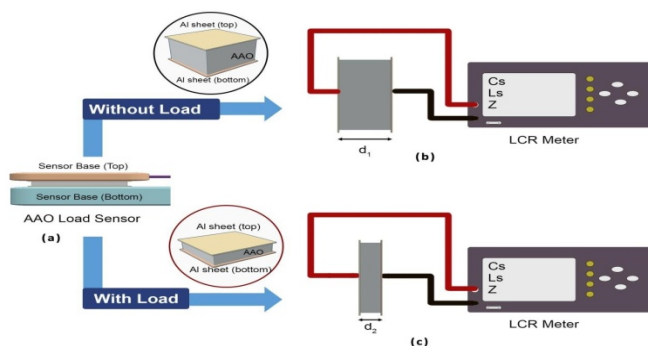
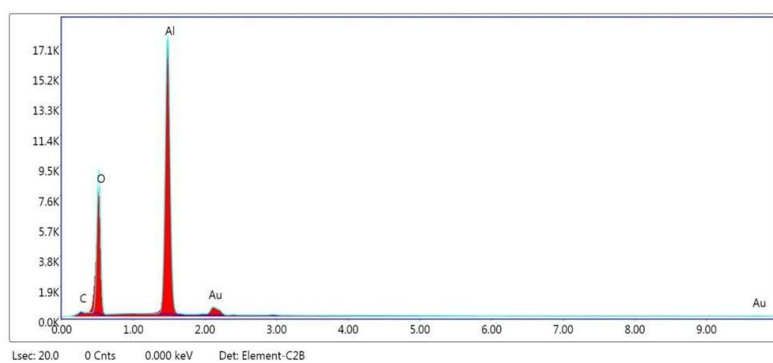
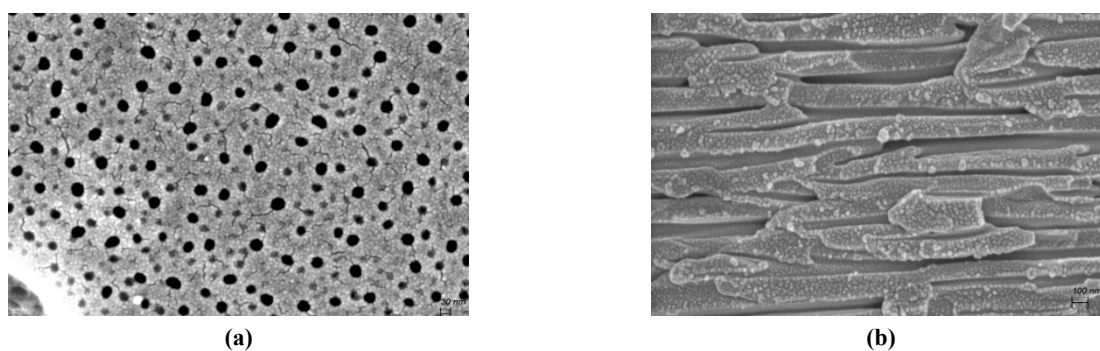


Figure 1. Schematic representation of the (a) as prepared AAO based capacitive sensor (b) Sensor without applying any load (c) Sensor with load where the distance between the two Al plates are decreasing

3. RESULTS AND DISCUSSION

The Scanning Electron Microscopy (SEM) photographs of the sample H1 are depicted in Figure 2(a) and (b). Figure 2(a) depicts the top view of the sample, while Figure 2(b) represents cross sectional view of the sample.



Element	Weight %	Atomic %
CK	1.69	3.10
OK	37.16	51.35
AlK	54.71	44.83
AuM	6.44	0.72

Figure 2. (a-b) SEM micrograph (Top view and Cross-sectional view) of the sample H1. (c) EDS pattern of the sample H1 (d) Atomic percentages of the different elements from the EDS.

The SEM micrograph (Top view) of sample H1 (Figure 2(a)) shows the extended-range ordering, homogeneity, shape, and size of the pores. This micrograph can reveal a variety of structural morphological details for instance pore diameter, inter-pore distance, porosity, and so on. Values were averaged over 20 measurements. The diameter of the pores is determined by the electrolyte type, anodization time, and anodization voltage. The porosity P of the hexagonal cell nanoporous AAO with a pore within each hexagon can be expressed as follows (with each pore assumed to be a perfect circle) [29]

$$P = \frac{\text{pore area}}{\text{hexagon area}} = \frac{\pi}{2\sqrt{3}} \left(\frac{D_p}{D_i}\right)^2, \quad (1)$$

where, D_p and D_i are the diameter of the pores and the inter-pore distance of the nanoporous AAO respectively, as shown in Figure 2 (a). The pore density, n of the porous AAO with a hexagonal distribution of pores can be described as the overall quantity of pores present in the 1 cm^2 surface area of the porous AAO, and expressed as follows [29]:

$$n = \frac{10^{14}}{A_{\text{hex}}} = \frac{2 \times 10^{14}}{\sqrt{3} D_i^2}. \quad (2)$$

Where A_{hex} represents the surface area of a single hexagonal cell (measured in nm^2). These structural parameters for the as prepared sample are analyzed through ImageJ software from the SEM micrographs and calculated using equations (1) and (2). The average diameter of pores (D_p), inter-pore distance (D_i), porosity (P) and the density of the pores (n) of the sample H1 are found to be 38 nm, 83nm, 18.95% and 1.7×10^{28} pore/ cm^2 respectively. The Energy dispersive X-ray spectroscopy (EDS) micrograph of sample H1, as depicted in figure 2 (c), confirms the presence of Al and O in the sample. Figure 2(d) represents the atomic percentages of the different elements present in the sample H1 from EDS. External loads were applied to the as-fabricated sensor in increasing order, generating pressures ranging from 100 Pa to 100 kPa, and the corresponding change in capacitance was observed. To evaluate the effectiveness of a pressure sensor, the pressure sensitivity (S) plays an important role and is represented by [30].

$$S = \frac{\delta(\Delta C/C_0)}{\delta P} \quad (3)$$

Here, C_0 denotes the initial capacitance without external pressure, ΔC denotes the relative change in capacitance ($C - C_0$), and P denotes the applied external pressure. The equation demonstrates how the slope of the tangent to the graph of pressure-capacitance can be used to calculate the sensor's sensitivity. Figure 3(a) shows the variation in relative capacitance of a sensor formed on nanoporous AAO over a wide pressure range. For example, when the pressure is around 40 kPa, the sensitivity of the as-fabricated sensor can reach 0.02 kPa^{-1} .

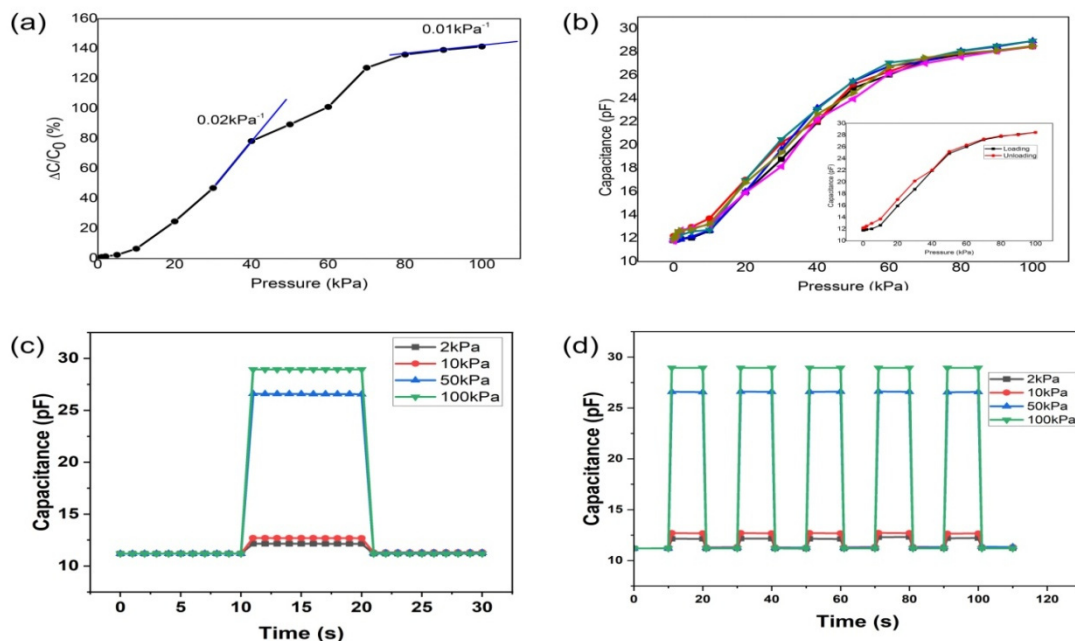


Figure 3. (a) The variation in the relative capacitance of the as fabricated sensor formed on nanoporous AAO. (b) Capacitance response by the as fabricated sensor with respect to pressure change for three loading/unloading cycles (inset is the single loading/unloading cycle). (c) The response of the sensor and the time of recovery when subjected to a pressure of 2, 10, 50 and 100kPa. (d) The sensor's capacitance response to repeated mechanical loads at pressures of 2, 10, 50 and 100kPa.

The sensitivity decreases to 0.01 kPa^{-1} when the pressure is increased above 80 kPa. Figure 3(b) clearly shows an apparent variation in capacitance response with regard to pressure change of the as-fabricated sensor during the loading/unloading process. When it comes to the application of flexible pressure sensors in various fields, short response as well as recovery time, in addition to high sensitivity, plays a vital role. The aforementioned features were also assessed by loading and unloading pressure on the as-fabricated pressure sensor. As demonstrated in Figure 3(c), putting on a pressure of 50 kPa causes the capacitance of the sensor to rapidly grow from its initial value to a steady value within 1 second. By releasing the loading force, the capacitance returns to its original value in around 1s. The repeatability of the sensor under 3 loading/unloading cycles is illustrated in Figure 3(d). Figure 3(b) shows that the capacitance response throughout the operation is quite uniform, with very little hysteresis, showing the sensor's stability. The capacitance of a parallel plate capacitive pressure sensor can be expressed as

$$c \propto \epsilon A/d \quad (4)$$

Where ϵ signifies the dielectric layer's dielectric constant, A represents the overlapping area of the two plates, and d represents the distance between the two plates [30]. Again, ϵ can be expressed as

$$\epsilon = \epsilon_0 \epsilon_r \quad (5)$$

where ϵ_0 stands for dielectric constant of free space and ϵ_r stands for relative dielectric constant [30].

Here, under vertical stress, the overlapping area remains practically constant; therefore, the value of the capacitance of the fabricated flexible capacitor is dependent on the dielectric constant and distance between the two plates. Since the two plates of AAO grown on Al are placed face to face to form the parallel plate capacitor, therefore, the value of dielectric constant will not affect the capacitance. Hence, capacitance will be primarily influenced by the separation distance. With the increase of external pressure, the gap between the two plates of the parallel plate capacitor decreases, and an enhanced capacitance response was observed for the as fabricated flexible capacitive pressure sensor formed on AAO. Also, the capacitance value of the as fabricated capacitive pressure sensor may be affected by the porous structure of the AAO. In a study, it was demonstrated that under the same applied pressure, a structured dielectric layer (nanopillars based on AAO) provided much higher strain concentration and contact stress in its territory, where the highest value was recorded at the deformation area when compared to a structure less dielectric layer, where stress and strain are distributed uniformly at the conjoined point of the electrode and the film [1].

4. CONCLUSION

This work describes the successful build out of a capacitive type pliable pressure sensor based on nanoporous AAO which was fabricated using a simple two step anodization method. The novelty of the as fabricated capacitive type pressure sensor lies in its construction, where two plates of AAO grown on Al are simply placed face to face. The Al on either side of these two AAO plates serves as the metal electrodes for the as fabricated parallel plate capacitor. The sensor shows excellent repeatability, high sensitivity, better stability and a very less hysteresis loss over the applied pressure range (100 Pa – 100 kPa). The mechanism behind the increase in capacitance with an increase in pressure for the as fabricated sensor is the decrease in the gap between the two AAO based plates and also the nanoporous structure of AAO, which offers enormous contact stress and strain. We hope that this strategic effort will pave way for the advancement of pliable pressure sensors, as well as be of great interest to many pressure sensing device applications.

Acknowledgements

The authors express their gratitude to Gauhati University and Assam Downtown University for providing them with access to their laboratory and equipment facilities.

Funding. The authors declare that no funds, grants, or other support were received during the preparation of this manuscript.

Competing Interests. The authors have no relevant financial or non-financial interests to disclose.

Author Contributions. All authors contributed to the study conception and design. Material preparation, data collection and analysis were performed by Trishna Moni Das and Devabrata Sarmah. The first draft of the manuscript was written by Trishna Moni Das and all authors commented on previous versions of the manuscript. All authors read and approved the final manuscript.

ORCID

©Trishna Moni Das, <https://orcid.org/0000-0001-5754-5608>; ©Sankar Moni Borah, <https://orcid.org/0000-0002-7891-270X>
©Sunandan Baruah, <https://orcid.org/0000-0003-2963-6128>

REFERENCES

- [1] W. Wu, X. Wen, and Z.L. Wang, "Taxel-Addressable Matrix of Vertical-Nanowire Piezotronic Transistors for Active and Adaptive Tactile Imaging," *Science* **340**, 952 (2013). <https://doi.org/10.1126/science.1234855>
- [2] C. Pan, L. Dong, G. Zhu, S. Niu, R. Yu, Q. Yang, Y. Liu, and Z.L. Wang, "High-resolution electroluminescent imaging of pressure distribution using a piezoelectric nanowire LED array," *Nature Photon* **7**, 752 (2013). <https://doi.org/10.1038/nphoton.2013.191>
- [3] E. Kar, N. Bose, B. Dutta, N. Mukherjee, and S. Mukherjee, "Ultraviolet- and Microwave-Protecting, Self-Cleaning e-Skin for Efficient Energy Harvesting and Tactile Mechanosensing," *ACS Appl. Mater. Interfaces* **11**, 17501 (2019). <https://doi.org/10.1021/acsami.9b06452>

- [4] K. Wang, Z. Lou, L. Wang, L. Zhao, S. Zhao, D. Wang, W. Han, et al., "Bioinspired Interlocked Structure-Induced High Deformability for Two-Dimensional Titanium Carbide (MXene)/Natural Microcapsule-Based Flexible Pressure Sensors," *ACS Nano* **13**, 9139 (2019). <https://doi.org/10.1021/acsnano.9b03454>
- [5] L.-Q. Tao, K.-N. Zhang, H. Tian, Y. Liu, D.-Y. Wang, Y.-Q. Chen, Y. Yang, et al., "Graphene-Paper Pressure Sensor for Detecting Human Motions," *ACS Nano* **11**, 8790 (2017). <https://doi.org/10.1021/acsnano.7b02826>
- [6] S. Zhang, H. Liu, S. Yang, X. Shi, D. Zhang, C. Shan, L. Mi, et al., "Ultrasensitive and Highly Compressible Piezoresistive Sensor Based on Polyurethane Sponge Coated with a Cracked Cellulose Nanofibril/Silver Nanowire Layer," *ACS Appl. Mater. Interfaces* **11**, 10922 (2019). <https://doi.org/10.1021/acsnano.7b02826>
- [7] D.J. Lipomi, M. Vosgueritchian, B.C.-K. Tee, S.L. Hellstrom, J.A. Lee, C.H. Fox, et al., "Skin-like pressure and strain sensors based on transparent elastic films of carbon nanotubes," *Nature Nanotech* **6**, 788 (2011). <https://doi.org/10.1038/nnano.2011.184>
- [8] G.Y. Bae, J.T. Han, G. Lee, S. Lee, S.W. Kim, S. Park, J. Kwon, et al., "Pressure/Temperature Sensing Bimodal Electronic Skin with Stimulus Discriminability and Linear Sensitivity," *Adv. Mater* **30**, 1803388 (2018). <https://doi.org/10.1002/adma.201803388>
- [9] C.M. Boutry, L. Beker, Y. Kaizawa, C. Vassos, H. Tran, A.C. Hinckley, R. Pfattner, et al., "Biodegradable and flexible arterial-pulse sensor for the wireless monitoring of blood flow," *Nat. Biomed. Eng.* **3**, 47 (2019). <https://doi.org/10.1038/s41551-018-0336-5>
- [10] S. Wang, Y. Xie, S. Niu, L. Lin, and Z.L. Wang, "Freestanding Triboelectric-Layer-Based Nanogenerators for Harvesting Energy from a Moving Object or Human Motion in Contact and Non-contact Modes," *Adv. Mater.* **26**, 2818 (2014). <https://doi.org/10.1002/adma.201305303>
- [11] A. Yu, Y. Zhu, W. Wang, and J. Zhai, "Progress in Triboelectric Materials: Toward High Performance and Widespread Applications," *Adv. Funct. Materials* **29**, 1900098 (2019). <https://doi.org/10.1002/adfm.201900098>
- [12] Q. Guan, G. Lin, Y. Gong, J. Wang, W. Tan, D. Bao, Y. Liu, et al., "Highly efficient self-healable and dual responsive hydrogel-based deformable triboelectric nanogenerators for wearable electronics," *J. Mater. Chem. A* **7**, 13948 (2019). <https://doi.org/10.1039/C9TA02711D>
- [13] S. Wang, J. Xu, W. Wang, G.-J.N. Wang, R. Rastak, F. Molina-Lopez, J.W. Chung, et al., "Skin electronics from scalable fabrication of an intrinsically stretchable transistor array," *Nature* **555**, 83 (2018). <https://doi.org/10.1038/nature25494>
- [14] K. Takei, T. Takahashi, J.C. Ho, H. Ko, A.G. Gillies, P.W. Leu, R.S. Fearing, et al., "Nanowire active-matrix circuitry for low-voltage macroscale artificial skin," *Nature Mater.* **9**, 821 (2010). <https://doi.org/10.1038/nmat2835>
- [15] Y. Zang, F. Zhang, D. Huang, X. Gao, C. Di, and D. Zhu, "Flexible suspended gate organic thin-film transistors for ultra-sensitive pressure detection," *Nat. Commun.* **6**, 6269 (2015). <https://doi.org/10.1038/ncomms7269>
- [16] C.-A. Ku, C.-W. Hung, and C.-K. Chung, "Influence of Anodic Aluminum Oxide Nanostructures on Resistive Humidity Sensing," *Nanomanufacturing* **4**, 58 (2024). <https://doi.org/10.3390/nanomanufacturing4010004>
- [17] G.-H. Lim, I.-Y. Kim, J.-Y. Park, Y.-H. Choa, and J.-H. Lim, "Anodic Aluminum Oxide-Based Chemi-Capacitive Sensor for Ethanol Gas," *Nanomaterials* **14**, 70 (2023). <https://doi.org/10.3390/nano14010070>
- [18] R.K. Nahar, "Study of the performance degradation of thin film aluminum oxide sensor at high humidity," *Sens. Actuators B: Chem.* **63**, 49 (2000). [https://doi.org/10.1016/S0925-4005\(99\)00511-0](https://doi.org/10.1016/S0925-4005(99)00511-0)
- [19] S.W. Chen, O.K. Khor, M.W. Liao, and C.K. Chung, "Sensitivity evolution and enhancement mechanism of porous anodic aluminum oxide humidity sensor using magnetic field," *Sens. Actuators B: Chem.* **199**, 384 (2014). <https://doi.org/10.1016/j.snb.2014.03.057>
- [20] C.K. Chung, O.K. Khor, C.J. Syu, and S.W. Chen, "Effect of oxalic acid concentration on the magnetically enhanced capacitance and resistance of AAO humidity sensor," *Sens. Actuators B: Chem.* **210**, 69 (2015). <https://doi.org/10.1016/j.snb.2014.12.096>
- [21] Z. He, L. Yao, M. Zheng, L. Ma, S. He, and W. Shen, "Enhanced humidity sensitivity of nanoporous alumina films by controlling the concentration and type of impurity in pore wall," *Phys. E: Low-Dimens. Syst. Nanostruct.* **43**, 366 (2010). <https://doi.org/10.1016/j.physe.2010.08.013>
- [22] M.A. Kashi, A. Ramazani, H. Abbasian, and A. Khayyatian, "Capacitive humidity sensors based on large diameter porous alumina prepared by high current anodization," *Sens. Actuators A: Phys.* **174**, 69 (2012). <https://doi.org/10.1016/j.sna.2011.11.033>
- [23] C.K. Chung, O.K. Khor, E.H. Kuo, and C.A. Ku, "Total effective surface area principle for enhancement of capacitive humidity sensor of thick-film nanoporous alumina," *Mater. Lett.* **260**, 126921 (2020). <https://doi.org/10.1016/j.matlet.2019.126921>
- [24] K. Sharma, and S.S. Islam, "Optimization of porous anodic alumina nanostructure for ultra-high sensitive humidity sensor," *Sens. Actuators B: Chem.* **237**, 443 (2016). <https://doi.org/10.1016/j.snb.2016.06.041>
- [25] M. Balde, A. Vena, and B. Sorli, "Fabrication of porous anodic aluminium oxide layers on paper for humidity sensors," *Sens. Actuators B: Chem.* **220**, 829 (2015). <https://doi.org/10.1016/j.snb.2015.05.053>
- [26] R. Andika, F. Aziz, Z. Ahmad, M. Doris, V. Fauzia, T.M. Bawazeer, N. Alsenany, et al., "Organic nanostructure sensing layer developed by AAO template for the application in humidity sensors," *J. Mater. Sci.: Mater. Electron.* **30**, 2382 (2019). <https://doi.org/10.1007/s10854-018-0511-1>
- [27] C.C. Yang, T.H. Liu, and S.H. Chang, "Relative humidity sensing properties of indium nitride compound with oxygen doping on silicon and AAO substrates," *Mod. Phys. Lett. B* **33**, 1940044 (2019). <https://doi.org/10.1142/S021798491940044X>
- [28] Y. Kim, B. Jung, H. Lee, H. Kim, K. Lee, and H. Park, "Capacitive humidity sensor design based on anodic aluminum oxide," *Sens. Actuators B: Chem.* **141**, 441 (2009). <https://doi.org/10.1016/j.snb.2009.07.007>
- [29] J.O. Carneiro, A. Ribeiro, F. Miranda, I.R. Segundo, S. Landi, V. Teixeira, and M.F.M. Costa, "Development of Capacitive-Type Sensors by Electrochemical Anodization: Humidity and Touch Sensing Applications," *Sensors* **21**, 7317 (2021). <https://doi.org/10.3390/s21217317>
- [30] Y. Guo, S. Gao, W. Yue, C. Zhang, and Y. Li, "Anodized Aluminum Oxide-Assisted Low-Cost Flexible Capacitive Pressure Sensors Based on Double-Sided Nanopillars by a Facile Fabrication Method," *ACS Appl. Mater. Interfaces* **11**, 48594 (2019). <https://doi.org/10.1021/acsnano.9b03454>

РОЗРОБКА ЄМНІСНОГО ДАТЧИКА ТИСКУ НА ОСНОВІ НАНОПОРИСТОГО АНОДНОГО ОКСИДУ АЛЮМІНІЮ

Трішна Моні Дас^a, Девабрата Сармах^b, Санкар Моні Борах^a, Сунандан Баруах^b

^aДепартамент прикладних наук, Університет Гаухаті, Джалукбарі, Гувахаті-781014, Індія

^bЦентр передового досвіду в області нанотехнологій, Університет міста Асам, Гувахаті -781026, Індія

Ємнісні датчики тиску роблять технологію вимірювання тиску більш доступною для ширшого спектру застосувань і галузей промисловості, включаючи побутову електроніку, автомобілебудування, охорону здоров'я тощо. Однак розробка ємнісного датчика тиску з блискучою продуктивністю за допомогою недорогої техніки залишається складною. У цій роботі розробка ємнісного датчика тиску на основі нанопористого анодного оксиду алюмінію (ААО), виготовленого за допомогою двоетапного підходу анодування, який пропонує перспективне рішення для точного вимірювання тиску, виготовлено за допомогою двоетапного підходу анодування. Паралельний пластинчастий ємнісний датчик був виготовлений шляхом розміщення двох нанесених ААО листів лицем один до одного, причому неанодований алюмінієвий компонент у основі функціонував як верхній і нижній електроди. Спостерігалася зміна значення ємності готового датчика в діапазоні прикладеного тиску (100–100 кПа). Цю зміну ємності можна пояснити зменшенням відстані між двома пластинами та неоднорідним розподілом контактної напруги та деформації через наявність нанопористої структури ААО. У цьому діапазоні тиску датчик показав високу чутливість, короткий час відгуку та чудову повторюваність, що вказує на багатообіцяюче майбутнє виготовлених датчиків у побутовій електроніці, інтелектуальній робототехніці тощо.

Ключові слова: ємнісний датчик тиску; анодний оксид алюмінію (ААО); анодування; чутливість; час відгуку; повторюваність